2014

Advancements in active surface wave methods: modeling, testing, and inversion

Shibin Lin
Iowa State University

Advancements in active surface wave methods: modeling, testing, and inversion

by

Shibin Lin

A dissertation submitted to the graduate faculty

in partial fulfillment of the requirements for the degree of

DOCTOR OF PHILOSOPHY

Major: Civil Engineering (Geotechnical Engineering)

Program of Study Committee:
Jeramy Ashlock, Major Professor
Igor Beresnev
Halil Ceylan
Thomas Rudolphi
R. Christopher Williams

Iowa State University

Ames, Iowa

2014

DEDICATION

To the memories of Qiumei Li (1915-2008) and Quanhang Huang (1935-2008).

TABLE OF CONTENTS

LIST OF TABLES

LIST OF FIGURES

ACKNOWLEDGEMENTS

I would like to thank my advisor, Dr. Jeramy Ashlock for his help, patience, guidance and inspiration. He shows me a role model as an excellent researcher and dedicated teacher, from whom I can definitely continue to study and benefit after the PhD program. I am grateful for the opportunity that he offered to study abroad, which significantly expanded my vision and extended my research interests.

I especially appreciate the discussion, help and materials from many researchers including Dr. Choon Park, Dr. Nils Ryden, Mr. Sudhish Kumar Bakku, Dr. Vitantonio Roma and a long list of names which I cannot fit here. Their works have paved a solid research path for me to explore my curiosity.

I am grateful to Professors Igor Beresnev, R. Christopher Williams, Halil Ceylan, and Thomas Rudolphi for serving on my thesis committee.

Thanks to Bing Yu, Chao Chen, and Ji Lu for their assistance in the surface wave field tests. I would like to say thanks for the help and encouragement from my officemates Mohammad Fotouhi-Ardakani, Jacob Phipps, and Theodore Bechtum.

Without the love and encouragement of my wife Yujin and the support of her and my families, this work would not have been possible. I owe a lot of gratitude to my wife for allowing me to study abroad for a long time, during which period she was strong and brave.

ABSTRACT

This study focuses on advancements in three broad aspects of active surface wave methods: modeling, testing, and inversion. Transfer matrix, global matrix, and stiffness matrix methods were employed to comprehensively model layered structures with half-space boundary conditions for soil structures with increasing/anomalous stiffness profiles, or pavement structures with decreasing stiffness profiles and leaky waves. All three methods were programmed in MATLAB as forward algorithms. The finite element method was adopted to simulate surface wave testing for various half-space site structures with absorbing layers using increasing damping technique. An improved experimental dispersion analysis scheme was developed by scanning phase-velocity and intercept-time followed by a power-spectrum analysis to minimize side lobes and increase sharpness of dispersion images. The multichannel simulation with one receiver (MSOR) method was applied to capture the dispersion characteristics of soil sites. The reciprocity principle for surface Rayleigh waves was verified by comparing dispersion images from MSOR and multichannel analysis of surface waves (MASW) testing at the same site with the same testing system. A multichannel surface wave acquisition system was developed to improve the accuracy of measuring high-frequency and high-velocity dispersion data on pavement sites. A minimally-invasive multimodal surface wave (MMSW) method was proposed to measure multi-mode dispersion data of Rayleigh waves by using either embedded receivers at various depths to record surface wave motions generated from moving impacts on the ground surface or using a multichannel seismograph with an array of geophones on the soil surface for measuring surface wave motions caused by Standard Penetration Test hammer blows at various depths in a

borehole. Stiffness matrix and finite element simulations of the MMSW method were employed to identify the critical geophone depths for optimum measurement of higher-mode motions. A hybrid genetic-simulated-annealing (GSA) algorithm was applied to solve multiple minimization and non-linear optimization problems to match the theoretical dispersion curves against their experimental counterparts. Results from simulation and real-world studies demonstrate that the advancements made in the three aspects of surface wave methods can improve the accuracy of surface wave testing results with higher resolution of experimental dispersion data, more complete multi-modal dispersion data, and higher certainty of inversion.

CHAPTER 1. INTRODUCTION

Many civil engineering problems involve layered media, such as soil sites, pavements, bridge decks, and floor slabs. Nondestructive surface wave testing encompasses a variety of methods to determine the material properties or conditions of such media. Applications of surface wave testing include seismic site profiling for seismic design of foundations and structures, and condition assessment of existing pavements and structural members. Therefore, the ability to nondestructively determine the stiffness profile of layered media is critical for engineering design, safety assessment, and quality assurance/quality control.

As an effective nondestructive technique for stiffness profiling, active surface wave methods typically consist of three steps—testing, modeling, and inversion. Each step plays a significant role in the accuracy of the final estimated stiffness profiles. This chapter includes a background and literature review on current approaches and limitations to each of these steps, and presents research objectives and organization of the dissertation.

1.1 Background

In 1885, Lord Rayleigh first predicted the existence of Rayleigh surface waves, which are commonly recognized as the most destructive type of waves in earthquakes. Significant advances in understanding these surface waves were contributed through persistent studies by Sezawa (1938), Picket (1945), Van der Poel (1951), Jones (1955, 1958, 1962), Press and Dobrin (1956), Heukelom and Foster (1960), and Vidale (1964), whose works led to the development of the steady state vibration method, also referred to as the Continuous Surface Wave (CSW) method. The CSW method was a milestone that

marked the beginning of tests to employ active nondestructive surface waves. However, research interest in this method did not grow significantly until the beginning of the 1980s, many years after development of the Fast Fourier Transform (FFT) algorithm by Cooley and Tukey (1965) led to a boom in research applications which remains strong today.

Employing tools of the FFT and modern computer hardware, a research team at The University of Texas at Austin developed the Spectral Analysis of Surface Waves (SASW) method, which is still used widely in geotechnical engineering, pavement engineering, and near-surface seismology (e.g., see Heisey et al. 1982, Nazarian 1984, Rix 1988, and Stokoe et al. 1994). The University of Kansas, as detailed in studies by Park et al. (1998, 1999a), and Xia et al. (1999), developed a more recent improved technique named the Multichannel Analysis of Surface Waves (MASW) method.

1.2 Literature Review

1.2.1 Rayleigh waves

Rayleigh (1885) first investigated the behavior of surface waves travelling along the traction-free surface of a half-space medium, and noticed the importance of the waves in earthquakes and the dynamic behavior of elastic solids. The generalized Rayleigh waves include Stoneley, Scholte, and quasi-Rayleigh waves. Stoneley (1924) proved that a type of wave can exist at solid-solid interfaces under very restricted conditions. Scholte (1947) found that Rayleigh-type waves also travelled along fluid-solid interfaces. Viktorov (1967) demonstrated that quasi-Rayleigh waves exist in an elastic finite layer, due to the interaction of the A0 and S0 modes of Lamb waves. The current research study

will primarily make use of Rayleigh waves for application to seismic site profiling of soils and quasi-Rayleigh waves for application to condition assessment of pavements.

1.2.2 Surface wave testing methods and experimental dispersion analysis

Before Cooley and Tukey (1965) developed the FFT algorithm to decompose arbitrarily time-varying signals into harmonic components, Van der Poel (1951), Heukelom and Foster (1960), Jones (1955, 1958, and 1962) and Vidale (1964) first developed the steady state vibration CSW method for geotechnical-scale seismic site characterization. The CSW method involves recording the harmonic ground surface velocity, using a receiver, due to continuous excitation caused by a harmonic vibrator operating at a fixed frequency (f). The receiver is incrementally moved away from the vibrator to determine the corresponding wavelength (λ) of surface motion, indicated by the smallest distance for which two measurement points vibrate in-phase. The test is then repeated over a range of frequencies to obtain the dispersion curve, which characterizes the phase velocity (V_{ph}) as a function of frequency through the relation $V_{ph} = \lambda f$.

Making use of the FFT algorithm, Heisey et al. (1982), Nazarian (1984), Rix (1988), and Stokoe et al. (1994) developed the SASW method, which employs two receivers at a predetermined separation (ΔD) to record the signals generated by a transient impact. The cross-power spectrum of the receivers is then used to determine the phase difference ($\Delta\Phi_f$) between the two signals as a function of frequency, from which the dispersion curve is calculated as $V_{ph} = \Delta D / (\Delta\Phi_f / (360° \times f))$. The separation distance is then varied to measure surface waves with various wavelengths that depend upon the properties of media at various depths.

Park et al. (1998, 1999a) proposed the MASW method to speed up surface wave testing by borrowing concepts from refraction testing in seismology. The MASW method requires a string of a dozen or more receivers to simultaneously record signals from a transient impact (i.e., shot gathers), from which the dispersion curve is calculated using a phase-velocity scanning scheme (Park et al. 1998). This is still the most popular algorithm used in surface wave programs, such as SurfSeis (KGS 2010) and SeisImager/SW (Geometics 2013).

When the length of testing spread has the same order of magnitude as the testing depth of interest, all of the above methods can only provide a single apparent dispersion curve, which is comprised of a fundamental-mode or a combination of several modes (e.g., Nazarian 1984, Guncunski and Woods 1992, Stokoe et al. 1994, Park et al. 1999a). In MASW testing, the experimental dispersion image is usually accompanied by many side lobes and aliasing (e.g., Park et al. 2001a, Ryden et al. 2004, Tran and Hiltunen 2008, Obando et al. 2010).

1.2.3 Inversion

Using the CSW method, Heukelom and Forster (1960) first determined experimentally the direct relationship between the dispersion curve and the media profile (i.e., shear-wave velocity and layer thickness), as shown in Figure 1.1.

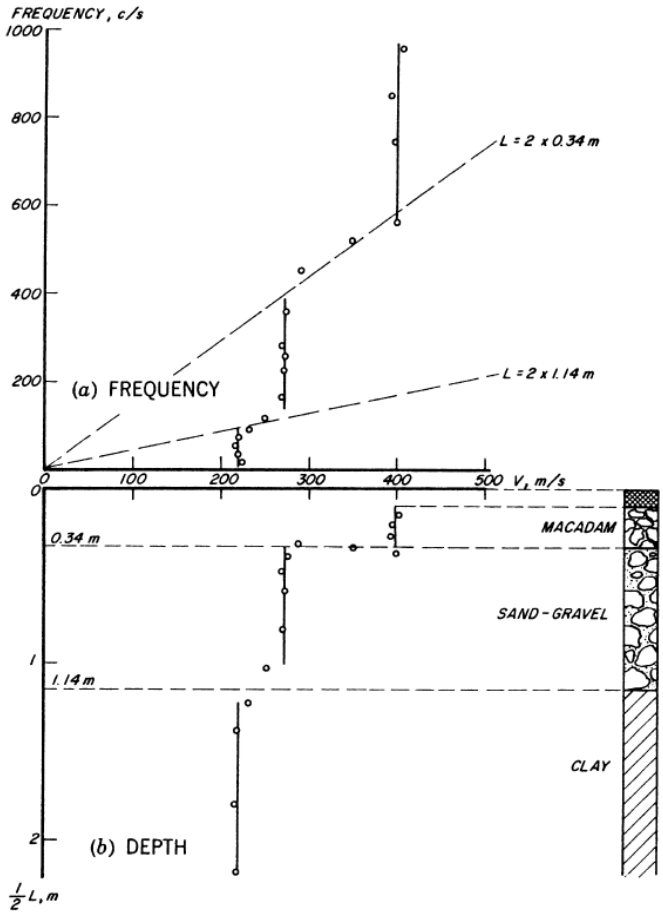

Figure 1.1 Wave velocity observed on stratified soil, as a function of frequency and depth (from Heukelum and Foster 1960). The transitions in phase velocity occur at wavelengths of approximately twice the depth of the interfaces.

A more comprehensive scheme is to calculate a theoretical dispersion image by forward modeling for an initial estimate of the material profile (e.g., Nazarian 1984, Lowe 1995, Ryden and Park 2006), then match the theoretical dispersion image to the experimental counterpart through optimization algorithms, such as the Levenberg-Marquardt (L-M) method (e.g., Nazarian et al. 1995, Xia et al. 1999), genetic algorithm (GA) method (e.g., Yamanaka and Ishida 1996, Yamanaka 2005, Pezeshk and Zarrabi 2005), or simulated annealing (SA) method (e.g., Iglesias et al. 2001, Ryden and Park

2006). The parameters typically varied in the optimization schemes include layer thicknesses, shear wave velocities, and number of layers.

Inverting the assumed material profiles to obtain the theoretical dispersion images presents a number of challenges that must be overcome, such as numerical instability at high frequencies, accounting for complex wavenumbers for leaky waves, and the requirement for computationally intensive algorithms. Much progress has been made in forward matrix modeling by Sezawa (1938), Pickett (1945), Haskell (1951), Jones (1962), Knopoff (1964), Vidale (1964), Dunkin (1965), Kausel (1981), Lowe (1995), Ryden and Park (2006), and Supranata (2006). The result of the forward matrix modeling is the theoretical dispersion curve (or dispersion image), which is the solution in terms of wavenumber (k) or phase velocity (V_{ph}) of the Rayleigh dispersion equation, $\Delta(\omega,k)$, for a given frequency (ω) in the linear eigenproblem:

$$\Delta(\omega, k) = 0 \tag{1.1}$$

The solution of dispersion images in pavements requires a two-dimensional search over real and imaginary components of complex wavenumbers, due to the significant energy in leaky modes (e.g., Jones 1962, Vidale 1964). Lowe (1995) proposed a method for two-dimensional searching over the complex wavenumber domain. Ryden and Park (2006) combined the phase-velocity scanning technique, fast Fourier transforms, and Hankel transforms to obtain theoretical dispersion images without the need for computationally-intensive two-dimensional searches. Since soils do not exhibit the phenomena of leaky waves or nonlinear strains in surface-wave testing, the imaginary component of the wave number may be neglected without an appreciable loss of accuracy (Ryden 2004). Therefore, generating dispersion images for soils requires only a one-

dimensional bisection searching technique (Nazarian 1984) or finding the minimum absolute value of a determinant (Supranata 2006).

After generating theoretical dispersion curves, a search method is typically used in an inversion procedure to minimize the difference between theoretical and experimental dispersion curves. Traditionally, perhaps the most widely used inversion method has been the Levenberg-Marquardt (L-M) method (Levenberg 1944, Marquardt 1963), which employs partial derivatives to determine the gradient towards a minimum error (e.g., Nazarian 1984, Xia 1999). Although the L-M method can provide a unique solution, it may converge to a local minimum and fail to find the global minimum error. To overcome this disadvantage, a variety of global search methods have been employed, including the genetic algorithm (GA) (Yamanaka and Ishida 1996, Iglesias et al. 2001, Pezeshk and Zarrabi 2005) and simulated annealing (SA) (Iglesias et al. 2001, Ryden and Park 2006). These global methods can ensure convergence to the true minimum within a specified domain, but at significant computational cost.

1.3 Objectives and Significance of the Dissertation

To advance the field of nondestructive surface wave testing of soils and pavements, this study focuses on developing improved NDT techniques with capacities for comprehensive modeling, multimode and high-resolution testing, and fast inversion. Comprehensive modeling is achieved by the combination of three matrix methods with the finite element method. In the dissertation, the three matrix methods will be described in detail and programmed in MATLAB as forward algorithms for further inversion analysis. The forward algorithms are able to deal with so-called “irregular” soil structures (defined as those having embedded high- or low-velocity layers), and pavement

structures requiring complex wavenumbers for leaky waves. The challenge of simulating half-space boundary conditions for surface wave analysis via FEM will be addressed by applying the absorbing layers using increasing damping (ALID) technique (Liu and Jerry 2003, Drozdz 2008) in the finite element software Abaqus 6.10-1.

Aimed at improving the resolution of experimental dispersion images by minimizing side lobes and increasing sharpness, a high-resolution phase-velocity and intercept-time scanning (PIS) scheme will also be presented. To provide cost savings and improve the efficiency of active surface wave 3-D stiffness profiling of soil and pavement sites, this study will make use of the multichannel simulation with one receiver (MSOR) method recently demonstrated by the research group to be equivalent to the MASW method for imaging dispersion curves for soils, and also shown to obey the reciprocity principle for surface Rayleigh waves. To improve the accuracy of measuring high-frequency and high-velocity dispersion data in pavement sites, this study will develop a multichannel surface wave acquisition system using MATLAB software and National Instruments hardware. To measure more complete multi-mode dispersion data of Rayleigh waves, using a relatively short receiver spread for minimizing lateral variation, a minimally-invasive multimodal surface wave (MMSW) method will be developed which uses either embedded receivers at various depths to record surface waves generated from moving impacts on the ground surface or a multichannel seismograph with an array of geophones on the soil surface for measuring surface wave motions caused by Standard Penetration Test hammer blows at various depths in a borehole. To estimate the ranges of optimum geophone depths for higher modes, stiffness matrix method and finite element-based simulations of the MMSW method will be

performed to identify the relationships between critical geophone depths and apparent cut-off frequencies.

The final inversion step will then infer the stiffness profile of the soil or pavement medium by employing a fast hybrid genetic-simulated-annealing (GSA) algorithm to solve multiple minimization and non-linear optimization problems to match the theoretical dispersion images against their experimental counterparts.

1.4 Dissertation Organization

This dissertation will be divided into three parts. Part I will contain background information and discussion of the numerical modeling of Rayleigh waves in a half-space medium by three matrix methods and an ALID FE method. The numerical models can produce theoretical dispersion images for given material profiles, and provide insight into aspects of wave generation and propagation. Part II will describe (1) an improved experimental dispersion analysis PIS scheme, (2) an economical and high-resolution surface wave testing method using one receiver and a moving source previously developed by Ryden (2004) for testing asphalt pavement and adapted by this research group for use on soils, (3) a new custom-programmed data acquisition system for MASW and MSOR testing using MATLAB software and National Instruments hardware, (4) a new minimally-invasive multimodal surface wave (MMSW) method for measuring multi-mode Rayleigh waves using an embedded receiver and moving surface source or a borehole impact and multichannel surface receivers, and (5) a procedure to identify critical depths for higher modes. Part III will introduce a hybrid GSA optimization method for improved inversion of surface wave dispersion data.

CHAPTER 2. RAYLEIGH WAVE MODELING BY ANALYTICAL AND COMPUTATIONAL METHODS

This chapter covers the formulation of Rayleigh-wave equations, forward matrix methods for modeling layered continua, techniques for calculating theoretical dispersion curves, and finite element simulation of Rayleigh wave propagation in a layered half-space.

2.1. Introduction

Rayleigh waves are disturbances that travel and transfer energy through solid media having a free surface, and contain information about geometrical and mechanical properties of the media. The continuous nature of the media makes wave propagation possible and enables the use of nondestructive testing to determine its material properties. For homogeneous media, Rayleigh waves are non-dispersive, but in heterogeneous media such as layered soil structures, Rayleigh waves are dispersive, meaning that the phase velocity of wave propagation varies with frequency. The dispersion characteristics of Rayleigh wave motion contain information on the stiffness profile of the media (i.e., layer thicknesses and associated shear moduli or shear wave velocities). Many geophysical methods have therefore been developed in the past several decades which use Rayleigh wave motion to infer the stiffness profiles of geological deposits.

2.2. Generation of Rayleigh Waves

Stress waves in solid media include body waves and surface waves. Body waves can be separated into P waves (referred to as primary, compressional, or dilatational) and S waves (secondary, shear, distortional, transverse, or equivoluminal). The direction of particle motion for P waves is parallel to the direction of wave propagation, while particle

motion for S waves is transverse to the propagation direction (Figure 2.1). S waves can therefore be decomposed into horizontally polarized (SH) and vertically polarized (SV) types, for which the transverse particle motion is in horizontal or vertical planes, respectively. Body waves are non-dispersive, meaning that their wave speed (also known as phase velocity) is independent of wavelength (or alternatively, frequency). When body waves impinge upon a free-surface or an interface between two materials, waves will be reflected and refracted and mode conversions may occur. Specifically, incident P waves will generate reflected and refracted P and SV waves, incident SV waves will generate reflected and refracted P and SV waves, and incident SH waves will generate only reflected and refracted SH waves. The reflection and refraction properties of body waves have been widely used in geophysical survey methods for many decades.

Surface waves are generated by the interaction of body waves along the interface of two media, at least one of which must be a solid. A characteristic of surface waves is that their motion decays with depth, and their rate of decay with distance along the surface is slower than that of body waves. SH waves are transformed to Love waves when trapped in a layer overlying another layer or half-space of higher wave speed. Similar to the SH waves from which they are generated, Love wave particle motion is confined to horizontal planes. Rayleigh waves result from the interaction between P and SV waves at the traction-free surface of a solid, and the resulting elliptical particle motion is therefore confined to vertical planes (Figure 2.2). Near the surface, the particle motion forms a retrograde ellipse, meaning that particle motion is counterclockwise for a wave traveling from left to right. Below a depth of approximately 20% of the Rayleigh wavelength, the phase of the horizontal component reverses and the motion becomes

prograde. Rayleigh waves are non-dispersive for a homogeneous half-space, but dispersive for vertically heterogeneous half-spaces, such as the layered soil models commonly used in geophysics and studied herein.

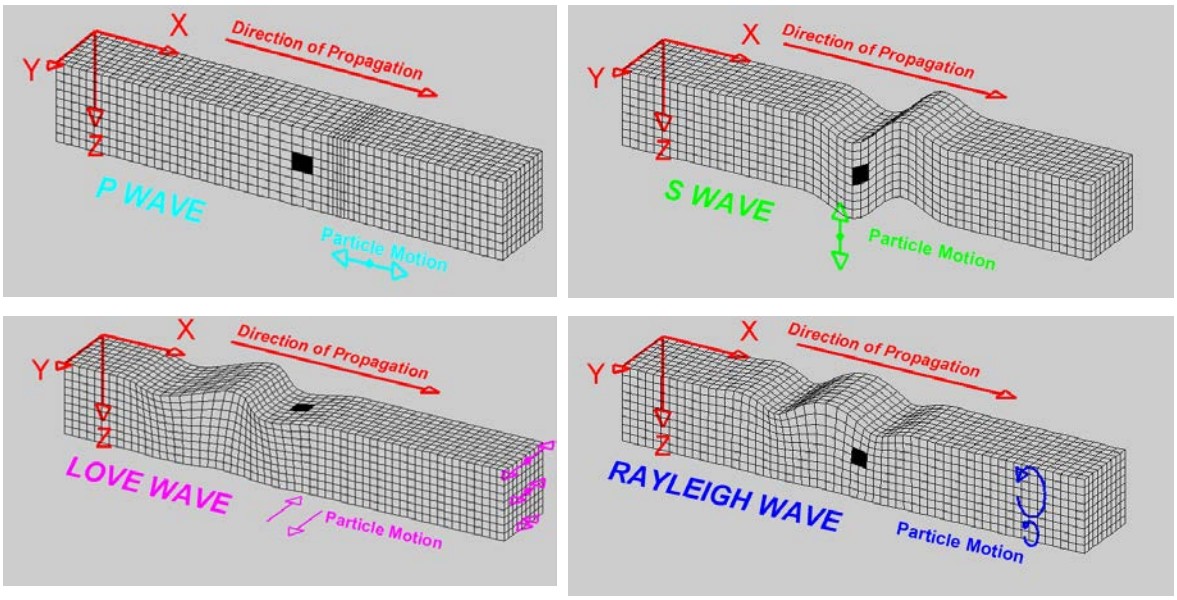

Figure 2.1 Horizontally propagating body waves (P and SV) and surface waves (Love and Rayleigh). (from Braile 2004)

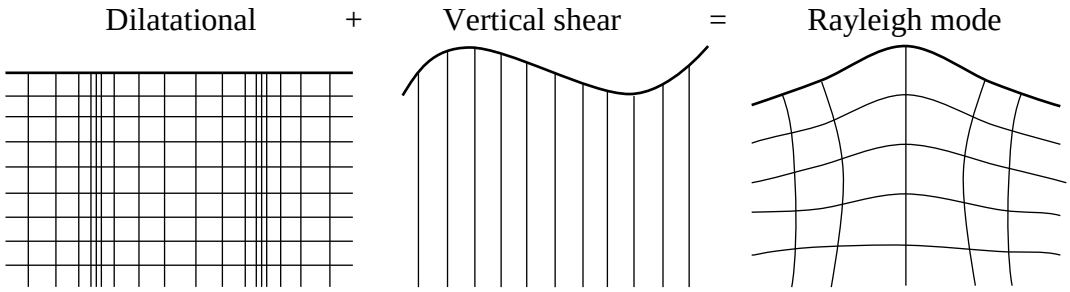

Figure 2.2 Interaction of P and SV waves to form Rayleigh waves at the traction-free surface of a solid. (after Viktorov 1967)

When an SV wave is incident at a traction-free surface of a solid, only reflected P and SV waves are generated. When the incidence angle

$$\beta_c = \sin^{-1}\left(\frac{V_S}{V_P}\right) \tag{2.1}$$

exceeds the critical angle, no reflected P waves propagate back into the half-space and P-waves only graze along the surface, thus part of the wave energy is trapped along the free surface (Figure 2.3). This phenomenon is called post-critical reflection, and suggests the existence of surface waves with a portion of their energy confined near the free surface.

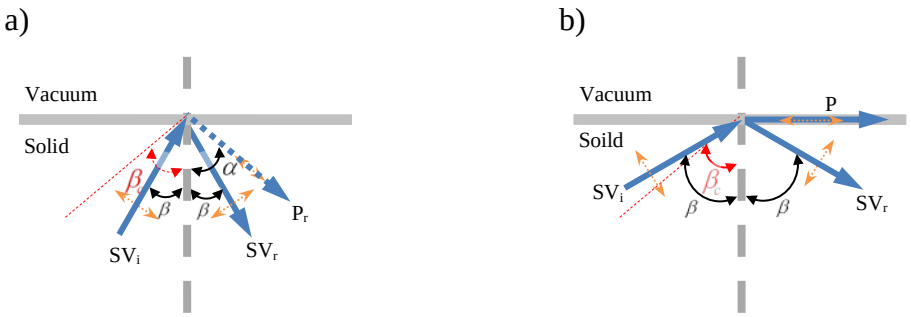

Figure 2.3 Incident SV wave and reflected SV and P waves: a) Pre-critical reflection; b) Post-critical reflection. (after Van Der Hilst 2014)

Lamb waves are guided waves in plates with traction-free surfaces, and have an infinite number of antisymmetric (A) and symmetric (S) modes. Rayleigh waves, on the other hand, can only exist in a half-space solid that has a traction-free surface. For finite plates, however, if the wavelength of a surface wave is much shorter than the thickness of the plate (e.g., less than half the plate thickness *d*), then the coupled motion of the fundamental antisymmetric (A_0) and symmetric (S_0) modes of Lamb waves can be thought of as quasi-Rayleigh waves (Viktorov 1967). Furthermore, at high frequencies, the phase velocities of the A_0 and S_0 Lamb waves in a plate asymptotically approach the phase velocity of Rayleigh waves of a homogeneous half-space having the same material properties as the plate (Figure 2.4). Additionally, the distribution of displacements with depth is similar for Lamb and Rayleigh waves (Figure 2.5).

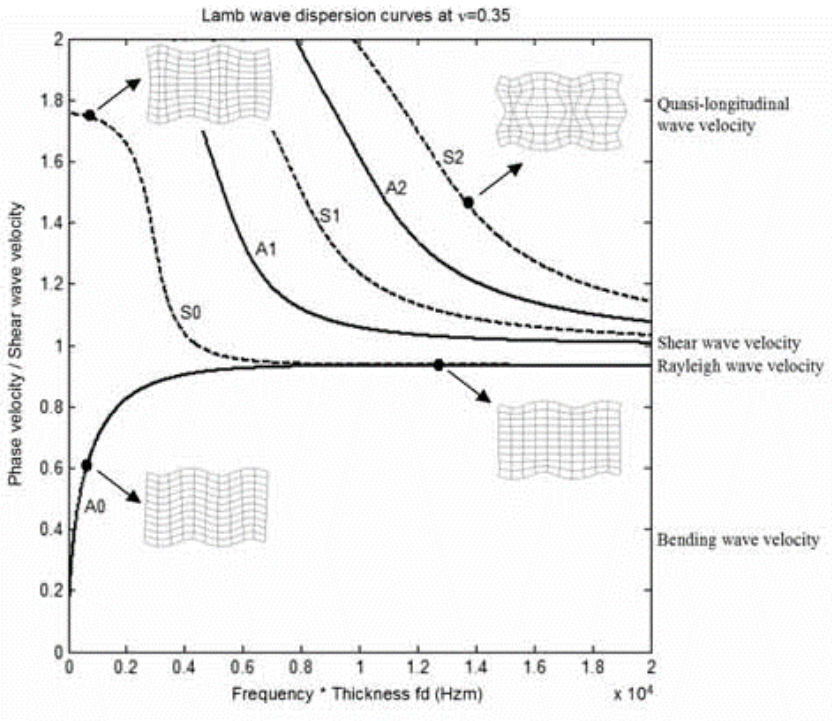

Figure 2.4 Lamb wave dispersion curves for a plate. (from Ryden and Park 2004)

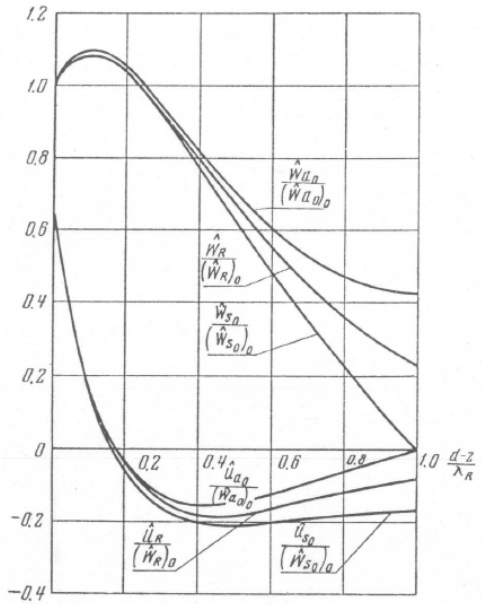

$\hat{W}_{a0}$: vertical displacement of A0 mode;

$\hat{W}_{s0}$: vertical displacement of S0 mode;

$\hat{W}_{R0}$: vertical displacement of Rayleigh waves;

$\hat{u}_{a0}$: horizontal displacement of A0 mode;

$\hat{u}_{s0}$: horizontal displacement of S0 mode;

$\hat{u}_R$: vertical displacement of Rayleigh waves;

d: thickness of the plate;

λ_R: wavelength of Rayleigh waves.

Figure 2.5 Amplitudes of A0 and S0 Lamb waves for a plate of thickness *d*, and Rayleigh waves for a homogeneous half-space. (from Viktorov 1967)

Having approximately equal amplitudes and phases, the A_0 and S_0 modes of Lamb waves in a plate interfere with each other. At the upper surface, the displacement of the A_0 and S_0 modes are in the same direction and interfere constructively, while at the

lower surface the displacements are in opposite directions and interfere destructively (Figure 2.6a). Thus their total acoustic field is similar to the Rayleigh wave acoustic field (Figure 2.6b), and the combined A_0 and S_0 displacements along depth are very similar to those of Rayleigh waves for both vertical and horizontal components (Figure 2.7).

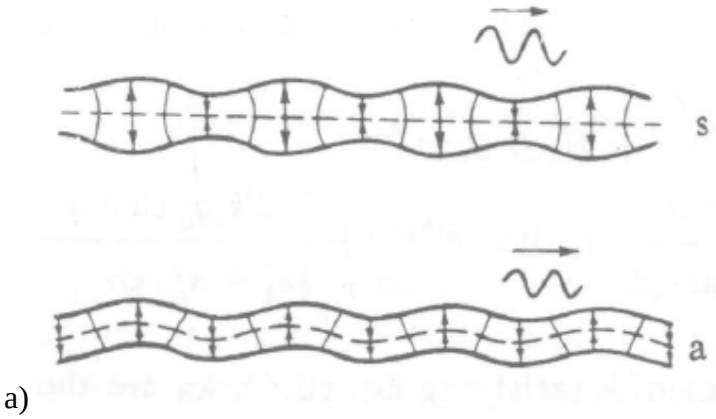

a)

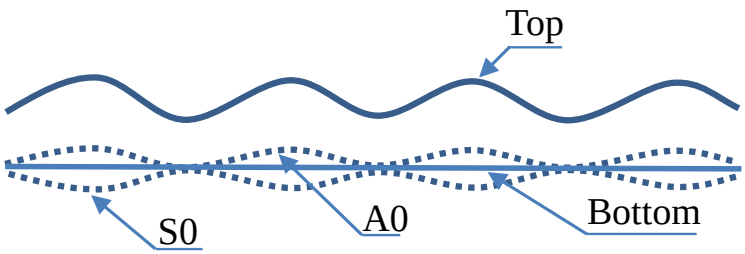

b)

Figure 2.6 a) Symmetric (S0) and antisymmetric (A0) fundamental Lamb-wave deformation modes of a plate (from Viktorov 1967); b) Superpostion of the A0 and S0 modes to form quasi-Rayleigh waves.

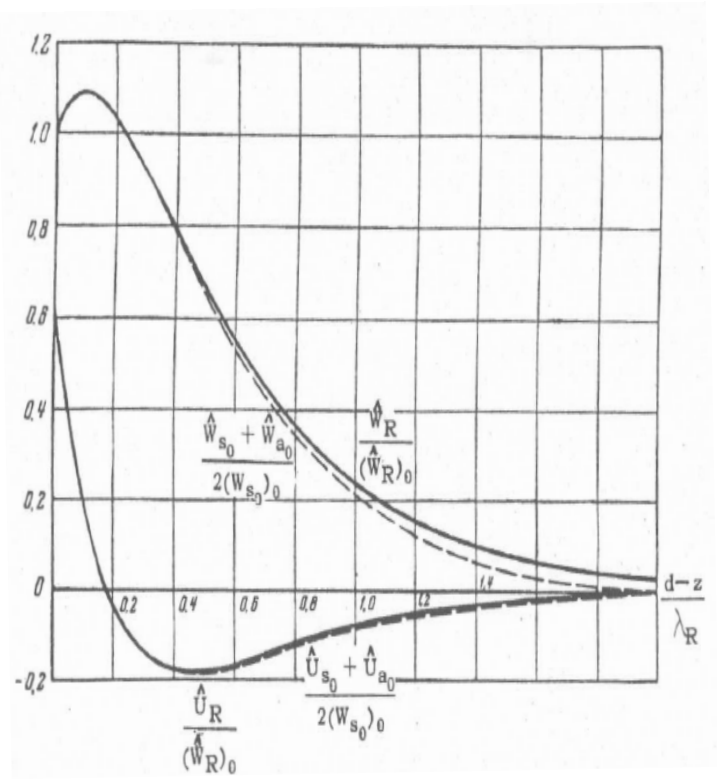

$\hat{W}_{a0}$: vertical displacement of A0 mode;

$\hat{W}_{s0}$: vertical displacement of S0 mode;

$\hat{W}_{R0}$: vertical displacement of Rayleigh waves;

$\hat{U}_{a0}$: horizontal displacement of A0 mode;

$\hat{U}_{s0}$: horizontal displacement of S0 mode;

$\hat{U}_R$: vertical displacement of Rayleigh waves;

d: thickness of the plate;

λ_R: wavelength of Rayleigh waves.

Figure 2.7 Horizontal and vertical displacement amplitudes for quasi-Rayleigh waves in a free plate of thickness d, and Rayleigh waves in a homogeneous half-space. (from Viktorov, 1967)

Generalized Rayleigh waves include Stoneley, Scholte, and tube waves. Stoneley waves exist at solid-solid interfaces only under very restricted conditions (Sheriff and Geldart 1982). Scholte waves exist at fluid-solid interfaces (Sheriff and Geldart 1982). Tube waves are a type of Stoneley acoustic wave at fluid-solid interfaces such as walls of fluid-filled boreholes, derived from the interaction of compressional waves in the liquid and shear waves in the solid. In this thesis, only Rayleigh and Lamb waves will be studied in detail, and the generalized surface waves will not be examined.

2.3. Basic Assumptions for Analysis of Rayleigh Waves

Basic assumptions are needed to enable Rayleigh-wave modeling in complex solid media and to capture their dispersion characteristics. The media are first assumed to be horizontally layered structures (Nazarian 1984, Stokoe et al. 1994, Park et al. 1999a).

Although the actual media might have significant horizontal variation (e.g., dipping interfaces, faults, folds), the horizontally-layered assumption is generally considered valid owing to another assumption that the inverted stiffness profile represents the middle point of the testing spread (e.g., Luo et al. 2009). Each layer of the media is treated as a homogeneous, isotropic, elastic solid, because the strains in soil, rock, and pavement are typically very small in geophysical testing (Figure 2.8), and the microstructure size of particles is relatively small compared to the wavelength of propagating waves and size of macrostructure of the media.

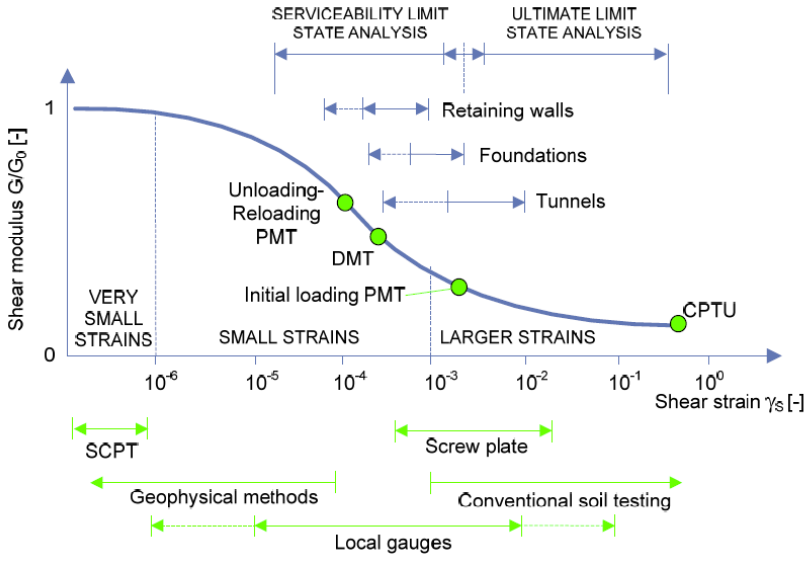

a)

Figure 2.8 Range and applicability of dynamic field and laboratory tests of soils: a) from Obrzud (2010). (continued on next page)

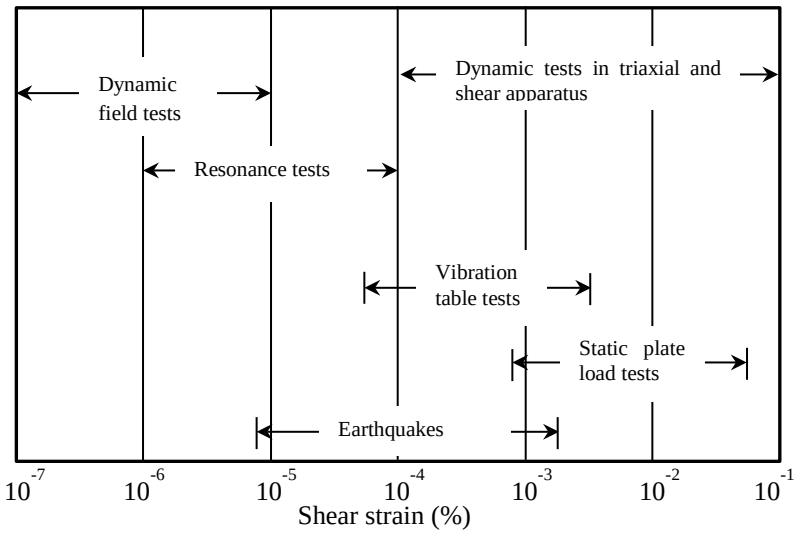

b)

Figure 2.8 (continued) b) after Das (2011).

Since the deformations are very small in geophysical field testing ($<10^{-5}$%), the modulus remains within the maximum range (Figure 2.9a) and the damping within the minimum range (Figure 2.9b).

Rayleigh waves generated by a point impact will propagate with cylindrical wavefronts, but can be treated as plane waves when measured beyond a certain distance along a straight line starting at the impact point (Park et al. 1999a). Figure 2.10 illustrates the relative amplitudes and velocities of P, SV, and Rayleigh wavefronts emanating from a circular footing vibrating vertically on the surface of a homogeneous half-space. Approximately 67% of the energy along the surface is carried by Rayleigh waves, making them relatively easy to generate and effective for seismic profiling.

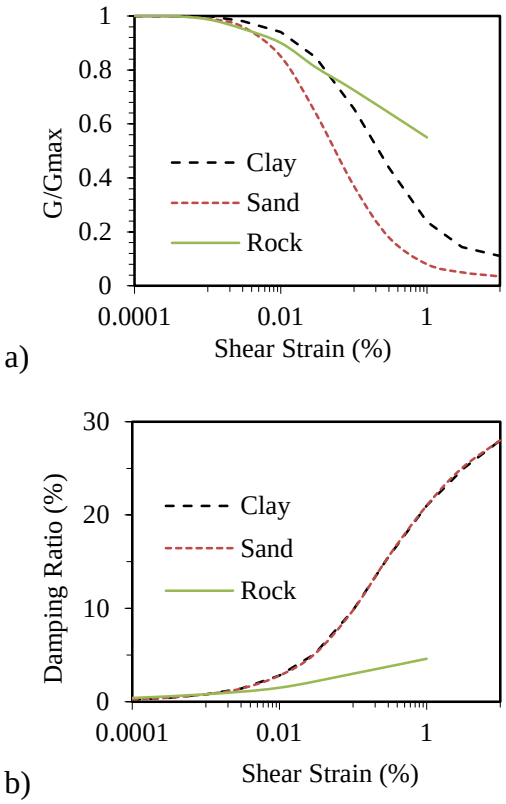

Figure 2.9 Representative dynamic properties for clay, sand, and rock: (a) Secant shear modulus versus shear strain amplitude; (b) damping ratio versus shear strain amplitude. (after Bardet et al. 2000)

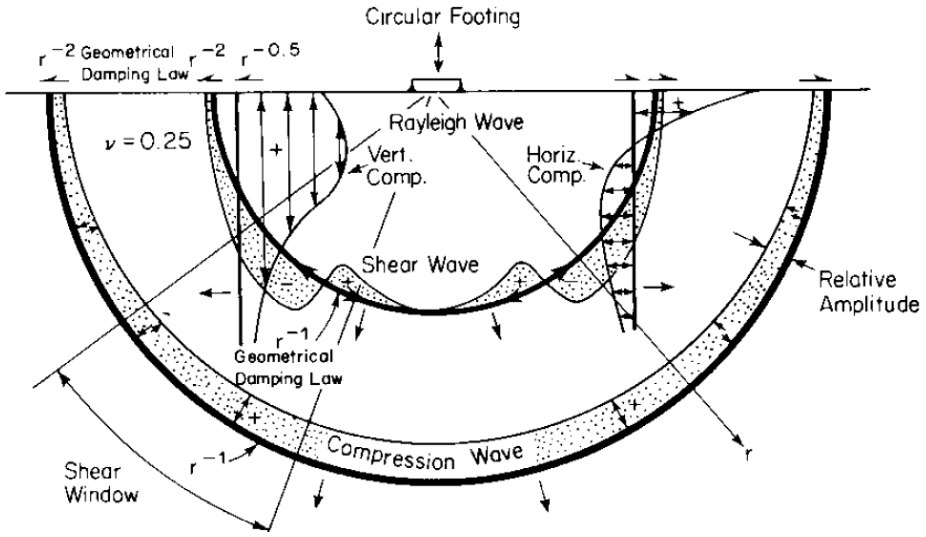

Figure 2.10 P, SV, and Rayleigh wavefronts emanating from a vertically vibrating circular footing on a homogeneous, isotropic, elastic half-space. (from Richart et al. 1970)

2.4. Rayleigh Wave Solutions for a Homogeneous, Isotropic, Elastic Half-space

2.4.1. Equations of motion

Figure 2.11 shows the normal and shear stresses acting on a differential element, with the stresses acting in the x-direction labeled. The element has dimensions dx, dy and dz, and tensile normal stresses are taken to be positive.

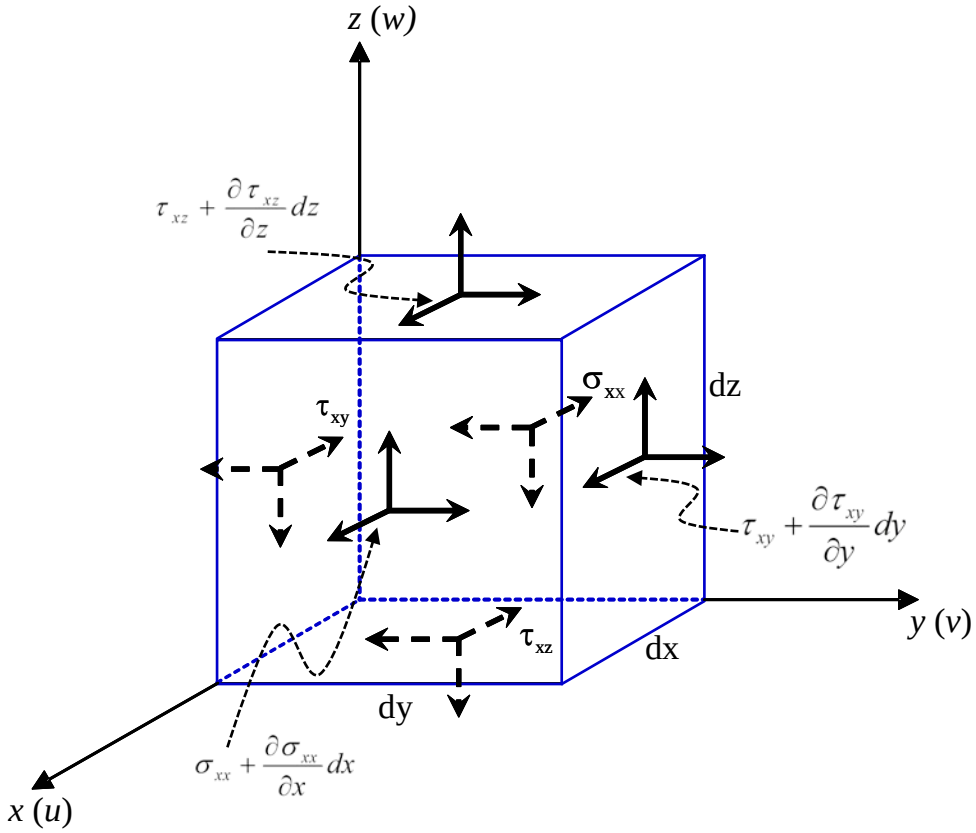

Figure 2.11 Normal and Shear tresses in x-direction on an infinitesimal element of a homogeneous elastic medium.

In the x direction, the dynamic equilibrium equation is

$$\left(\sigma_{xx} + \frac{\partial \sigma_{xx}}{\partial x} dx\right) dy\, dz - \sigma_{xx}\, dy\, dz + \left(\tau_{xy} + \frac{\partial \tau_{xy}}{\partial y} dy\right) dx\, dz - \tau_{xy}\, dx\, dz + \left(\tau_{xz} + \frac{\partial \tau_{xz}}{\partial z} dz\right) dx\, dy - \tau_{xz}\, dx\, dy = \rho\, dx\, dy\, dz \frac{\partial^2 u}{\partial t^2} \tag{2.2}$$

where σ_{xx} is normal stress in the x direction, τ_{xy} is shear stress in the x direction acting on the x-y plane, τ_{xz} is shear stress in the x direction acting on the x-z plane, u is displacement in the x direction, ρ is mass density of the differential element, and t is time. The above equation can be simplified to

$$\rho \frac{\partial^2 u}{\partial t^2} = \frac{\partial \sigma_{xx}}{\partial x} + \frac{\partial \tau_{xy}}{\partial y} + \frac{\partial \tau_{xz}}{\partial z} \tag{2.3}$$

The same operations in the y and z directions give

$$\rho \frac{\partial^2 v}{\partial t^2} = \frac{\partial \tau_{yx}}{\partial x} + \frac{\partial \sigma_{yy}}{\partial y} + \frac{\partial \tau_{yz}}{\partial z} \tag{2.4}$$

$$\rho \frac{\partial^2 w}{\partial t^2} = \frac{\partial \tau_{zx}}{\partial x} + \frac{\partial \tau_{zy}}{\partial y} + \frac{\partial \sigma_{zz}}{\partial z} \tag{2.5}$$

where v and w are displacements in the x and z directions, respectively. Eqs. (2.3)–(2.5) represent three-dimensional equations of motion of an elastic solid element.

For a linear, isotropic, elastic medium, the equations of motion can be written in terms of strains and displacements using the constitutive (stress-strain) and kinematic (strain-displacement) relationships. The stress-strain relationships (generalized 3D Hooke's law) can be expressed as

$$\begin{aligned}
&\sigma_{xx} = \lambda\bar{\varepsilon} + 2\mu\varepsilon_{xx} \qquad && \tau_{xy} = \tau_{yx} = \mu\gamma_{xy} \\
&\sigma_{yy} = \lambda\bar{\varepsilon} + 2\mu\varepsilon_{yy} \qquad && \tau_{yz} = \tau_{zy} = \mu\gamma_{yz} \\
&\sigma_{zz} = \lambda\bar{\varepsilon} + 2\mu\varepsilon_{zz} \qquad && \tau_{zx} = \tau_{xz} = \mu\gamma_{zx} \\
&\mu = \frac{E}{2(1+\upsilon)} \qquad && \lambda = \frac{\upsilon E}{(1+\upsilon)(1-2\upsilon)}
\end{aligned} \tag{2.6}$$

where, $\bar{\varepsilon}$ $(= \varepsilon_x + \varepsilon_y + \varepsilon_z)$ is volumetric strain, λ and μ are Lamé's constants, E is Young's modulus, μ is shear modulus, and υ is Poisson's ratio.

The strain-displacement relationships are

$$\begin{aligned}
\varepsilon_{xx} &= \frac{\partial u}{\partial x} \qquad \varepsilon_{xy} = \frac{1}{2}\left(\frac{\partial v}{\partial x} + \frac{\partial u}{\partial y}\right) \qquad \gamma_{xy} = 2\varepsilon_{xy} \qquad \Omega_x = \frac{1}{2}\left(\frac{\partial w}{\partial y} - \frac{\partial v}{\partial z}\right) \\
\varepsilon_{yy} &= \frac{\partial v}{\partial y} \qquad \varepsilon_{yz} = \frac{1}{2}\left(\frac{\partial w}{\partial y} + \frac{\partial v}{\partial z}\right) \qquad \gamma_{yz} = 2\varepsilon_{yz} \qquad \Omega_y = \frac{1}{2}\left(\frac{\partial u}{\partial z} - \frac{\partial w}{\partial x}\right) \\
\varepsilon_{zz} &= \frac{\partial w}{\partial z} \qquad \varepsilon_{zx} = \frac{1}{2}\left(\frac{\partial u}{\partial z} + \frac{\partial w}{\partial x}\right) \qquad \gamma_{zx} = 2\varepsilon_{zx} \qquad \Omega_z = \frac{1}{2}\left(\frac{\partial v}{\partial x} - \frac{\partial u}{\partial y}\right)
\end{aligned} \tag{2.7}$$

where γ_{ij} are the engineering shear strains and Ω_{ij} are the rotations. Substituting Eqs. (2.6) and (2.7) into Eqs. (2.3)–(2.5) and simplifying gives Navier's equations;

$$\rho\frac{\partial^2 u}{\partial t^2} = (\lambda + \mu)\frac{\partial \bar{\varepsilon}}{\partial x} + \mu\nabla^2 u \tag{2.8}$$

$$\rho\frac{\partial^2 v}{\partial t^2} = (\lambda + \mu)\frac{\partial \bar{\varepsilon}}{\partial y} + \mu\nabla^2 v \tag{2.9}$$

$$\rho\frac{\partial^2 w}{\partial t^2} = (\lambda + \mu)\frac{\partial \bar{\varepsilon}}{\partial z} + \mu\nabla^2 w \tag{2.10}$$

where ∇^2 is the Laplacian operator defined as $\nabla^2 = \frac{\partial^2}{\partial x^2} + \frac{\partial^2}{\partial y^2} + \frac{\partial^2}{\partial z^2}$.

2.4.2. Solution of Navier's equations of motion for Rayleigh waves

Navier's equations can be solved using the Helmholtz decomposition:

$$\mathbf{u} = \nabla\Phi - \nabla\times\boldsymbol{\psi} \tag{2.11}$$

where Φ represents the scalar potential of compressional (P wave) motion, $\boldsymbol{\psi}$ represents the vector potential of shear (S wave) motion, and $\mathbf{u}$ is the displacement vector, such that

$$\mathbf{u} = \begin{Bmatrix} u & v & w \end{Bmatrix}^T$$

$$\nabla\Phi = \begin{Bmatrix} \frac{\partial\Phi}{\partial x} & \frac{\partial\Phi}{\partial y} & \frac{\partial\Phi}{\partial z} \end{Bmatrix}^T$$

$$\nabla\times\boldsymbol{\psi} = \begin{vmatrix} i & j & k \\ \frac{\partial}{\partial x} & \frac{\partial}{\partial y} & \frac{\partial}{\partial z} \\ \psi_x & \psi_y & \psi_z \end{vmatrix} = \begin{Bmatrix} \frac{\partial\psi_z}{\partial y} - \frac{\partial\psi_y}{\partial z} & \frac{\partial\psi_x}{\partial z} - \frac{\partial\psi_z}{\partial x} & \frac{\partial\psi_y}{\partial x} - \frac{\partial\psi_x}{\partial y} \end{Bmatrix}^T$$

Eq. (2.11) demonstrates that the Rayleigh wave is from the superposition of P and SV waves. Expansion of Eq. (2.11) gives

$$u = \frac{\partial \Phi}{\partial x} - \frac{\partial \psi_z}{\partial y} + \frac{\partial \psi_y}{\partial z} \tag{2.12}$$

$$v = \frac{\partial \Phi}{\partial y} - \frac{\partial \psi_x}{\partial z} + \frac{\partial \psi_z}{\partial x} \tag{2.13}$$

$$w = \frac{\partial \Phi}{\partial z} - \frac{\partial \psi_y}{\partial x} + \frac{\partial \psi_x}{\partial y} \tag{2.14}$$

Considering a Rayleigh wave as a plane wave (Figure 2.12) that travels in the x direction and has zero displacement in the y direction (v=0, $\partial \psi_z / \partial y = 0$, $\partial \psi_x / \partial y = 0$), the above equations can be simplified to

$$u = \frac{\partial \Phi}{\partial x} + \frac{\partial \Psi}{\partial z} \tag{2.15}$$

$$w = \frac{\partial \Phi}{\partial z} - \frac{\partial \Psi}{\partial x} \tag{2.16}$$

where Ψ represents ψ_y.

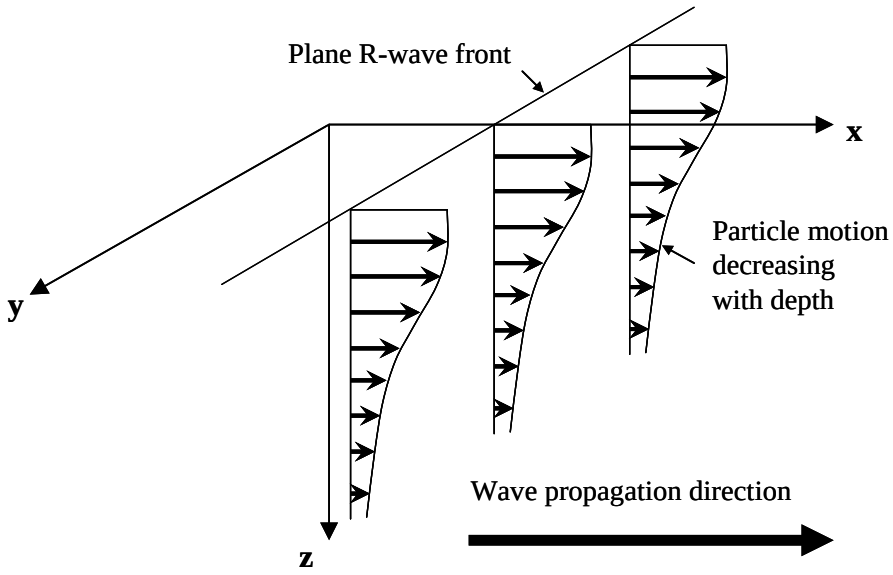

Figure 2.12 Plane Rayleigh wave in homogeneous elastic half-space. (from Supranata 2006)

For the plane wave, the volumetric strain (dilation) thus reduces to

$$\overline{\varepsilon} = \varepsilon_{xx} + \varepsilon_{zz} = \frac{\partial u}{\partial x} + \frac{\partial w}{\partial z} \tag{2.17}$$

The only nonzero rotation is

$$2\Omega_y = \frac{\partial u}{\partial z} - \frac{\partial w}{\partial x} \tag{2.18}$$

Substituting Eqs. (2.15) and (2.16) into Eqs. (2.17) and (2.18) gives

$$\overline{\varepsilon} = \varepsilon_{xx} + \varepsilon_{zz} = \frac{\partial^2 \Phi}{\partial x^2} + \frac{\partial^2 \Phi}{\partial z^2} = \nabla^2 \Phi \tag{2.19}$$

$$2\Omega_y = \frac{\partial^2 \Psi}{\partial x^2} + \frac{\partial^2 \Psi}{\partial z^2} = \nabla^2 \Psi \tag{2.20}$$

The above two equations illustrate that Φ and Ψ are related to dilation and rotation (shear deformation), respectively. For the plane wave, Navier's equations simplify to Eqs. (2.8) and (2.10). Substituting Eqs. (2.15)–(2.17) into Eqs. (2.8) and (2.10) gives

$$\rho \frac{\partial^2}{\partial t^2}\left(\frac{\partial \Phi}{\partial x} + \frac{\partial \Psi}{\partial z}\right) = (\lambda + \mu)\frac{\partial(\nabla^2 \Phi)}{\partial x} + \mu \nabla^2\left(\frac{\partial \Phi}{\partial x} + \frac{\partial \Psi}{\partial z}\right) \tag{2.21}$$

$$\rho \frac{\partial^2}{\partial t^2}\left(\frac{\partial \Phi}{\partial z} - \frac{\partial \Psi}{\partial x}\right) = (\lambda + \mu)\frac{\partial(\nabla^2 \Phi)}{\partial z} + \mu \nabla^2\left(\frac{\partial \Phi}{\partial z} - \frac{\partial \Psi}{\partial x}\right) \tag{2.22}$$

which can be rearranged to

$$\rho \frac{\partial}{\partial x}\left(\frac{\partial^2 \Phi}{\partial^2 t}\right) + \rho \frac{\partial}{\partial z}\left(\frac{\partial^2 \Psi}{\partial^2 t}\right) = (\lambda + 2\mu)\frac{\partial(\nabla^2 \Phi)}{\partial x} + \mu \frac{\partial(\nabla^2 \Psi)}{\partial z} \tag{2.23}$$

$$\rho \frac{\partial}{\partial z}\left(\frac{\partial^2 \Phi}{\partial^2 t}\right) - \rho \frac{\partial}{\partial x}\left(\frac{\partial^2 \Psi}{\partial^2 t}\right) = (\lambda + 2\mu)\frac{\partial(\nabla^2 \Phi)}{\partial z} - \mu \frac{\partial(\nabla^2 \Psi)}{\partial x} \tag{2.24}$$

Subtracting the partial derivative of Eq. (2.24) with respect to x from the partial derivative of Eq. (2.23) with respect to z gives

$$\rho \frac{\partial^2}{\partial x^2}\left(\frac{\partial^2 \Psi}{\partial^2 t}\right) + \rho \frac{\partial^2}{\partial z^2}\left(\frac{\partial^2 \Psi}{\partial^2 t}\right) = \mu \frac{\partial(\nabla^2 \Psi)}{\partial z^2} + \mu \frac{\partial(\nabla^2 \Psi)}{\partial x^2} \tag{2.25}$$

which can be rearranged to

$$\frac{\partial^2}{\partial x^2}\left(\rho \frac{\partial^2 \Psi}{\partial^2 t} - \mu \nabla^2 \Psi\right) = \frac{\partial}{\partial z^2}\left(\mu \nabla^2 \Psi - \rho \frac{\partial^2 \Psi}{\partial^2 t}\right) \tag{2.26}$$

The above equation is satisfied if the vector potential satisfies the wave equation

$$\nabla^2\Psi = \frac{1}{V_S^2}\frac{\partial^2\Psi}{\partial^2 t} \tag{2.27}$$

where $V_S = \sqrt{\mu/\rho}$ is the shear wave velocity. The sum of the partial derivative of Eq. (2.23) with respect to x and the partial derivative of Eq. (2.24) with respect to z gives

$$\rho\frac{\partial^2}{\partial x^2}(\frac{\partial^2\Phi}{\partial^2 t}) + \rho\frac{\partial^2}{\partial z^2}(\frac{\partial^2\Phi}{\partial^2 t}) = (\lambda+2\mu)\frac{\partial(\nabla^2\Phi)}{\partial x^2} + (\lambda+2\mu)\frac{\partial(\nabla^2\Phi)}{\partial z^2} \tag{2.28}$$

which can be rearranged as

$$\frac{\partial^2}{\partial x^2}(\rho\frac{\partial^2\Phi}{\partial^2 t} - (\lambda+2\mu)\nabla^2\Phi) = \frac{\partial}{\partial z^2}((\lambda+2\mu)\nabla^2\Phi - \rho\frac{\partial^2\Phi}{\partial^2 t}) \tag{2.29}$$

The above equation is satisfied if the scalar potential satisfies the wave equation

$$\nabla^2\Phi = \frac{1}{V_P^2}\frac{\partial^2\Phi}{\partial^2 t} \tag{2.30}$$

where $V_P = \sqrt{(\lambda+2\mu)/\rho}$ is the dilatational wave velocity. If the plane Rayleigh wave is harmonic with circular frequency ω and wavenumber k_R, the wave velocity is

$$V_R = \omega / k_R \tag{2.31}$$

The displacement potentials which are the solutions to Eqs. (2.27) and (2.30) can thus be assumed to have the form of harmonic plane waves propagating in the +*x* direction;

$$\Phi = f(z)e^{i(\omega t - k_R x)} \tag{2.32}$$

$$\Psi = g(z)e^{i(\omega t - k_R x)} \tag{2.33}$$

where *f*(*z*) and *g*(*z*) describe the variation of dilatational and rotational components of Rayleigh waves with depth. Substituting the above two equations into the wave Eqs. (2.27) and (2.30) gives

$$-\frac{\omega^2}{V_P^2}f(z) = -k_R^2 f(z) + \frac{d^2 f(z)}{dz^2} \tag{2.34}$$

$$-\frac{\omega^2}{V_S^2}g(z) = -k_R^2 g(z) + \frac{d^2 g(z)}{dz^2} \tag{2.35}$$

which can be rearranged to

$$\frac{d^2 f(z)}{dz^2} - \left(k_R^2 - \frac{\omega^2}{V_P^2}\right) f(z) = 0 \tag{2.36}$$

$$\frac{d^2 g(z)}{dz^2} - \left(k_R^2 - \frac{\omega^2}{V_S^2}\right) g(z) = 0 \tag{2.37}$$

In order for the solutions to be non-harmonic with depth, we must have

$$k_R^2 - \frac{\omega^2}{V_P^2} > 0 \tag{2.38}$$

$$k_R^2 - \frac{\omega^2}{V_S^2} > 0 \tag{2.39}$$

Thus,

$$V_R < V_S < V_P$$

and the Rayleigh wave travels slower than the shear and dilatational waves. The general solutions to $f(z)$ and $g(z)$ can be written in the form

$$f(z) = Ae^{-qz} + Be^{qz} \tag{2.40}$$

$$g(z) = Ce^{-sz} + De^{sz} \tag{2.41}$$

where

$$q^2 = k_R^2 - \omega^2 / V_P^2 \tag{2.42}$$

$$s^2 = k_R^2 - \omega^2 / V_S^2 \tag{2.43}$$

Then the potentials Φ and Ψ can be written as

$$\Phi = (Ae^{-qz} + Be^{qz})e^{i(\omega t - k_R x)} \tag{2.44}$$

$$\Psi = (Ce^{-sz} + De^{sz})e^{i(\omega t - k_R x)} \tag{2.45}$$

in which A and C are coefficients of horizontally propagating plane waves with amplitudes that decay exponentially with depth, while B and D are similar coefficients for

waves with amplitudes that grow exponentially with depth. For a semi-infinite half-space, displacement must be bounded as $z \to \infty$. Therefore, *B* and *D* must be zero, and the potential functions can be simplified to

$$\Phi = Ae^{-qz}e^{i(\omega t - k_R x)} \tag{2.46}$$

$$\Psi = Ce^{-sz}e^{i(\omega t - k_R x)} \tag{2.47}$$

The surface is traction-free, and therefore

$$\sigma_{zz} = \lambda\bar{\varepsilon} + 2\mu\varepsilon_{zz} = \lambda\bar{\varepsilon} + 2\mu\frac{\partial w}{\partial z} = 0 \tag{2.48}$$

$$\tau_{xz} = \mu\gamma_{zx} = \mu\left(\frac{\partial u}{\partial z} + \frac{\partial w}{\partial x}\right) = 0 \tag{2.49}$$

Substituting Eqs. (2.15)–(2.17) and (2.19) into the above equations gives

$$\sigma_{zz} = \lambda\nabla^2\Phi + 2\mu\left(\frac{\partial^2\Phi}{\partial z^2} - \frac{\partial^2\Psi}{\partial x\partial z}\right) = 0 \tag{2.50}$$

$$\tau_{xz} = \mu\left(\frac{\partial}{\partial z}\left(\frac{\partial\Phi}{\partial x} + \frac{\partial\Psi}{\partial z}\right) + \frac{\partial}{\partial x}\left(\frac{\partial\Phi}{\partial z} - \frac{\partial\Psi}{\partial x}\right)\right) = 0 \tag{2.51}$$

Substituting the Rayleigh wave potential functions Eqs. (2.46) and (2.47) into the above two equations gives

$$\sigma_{zz} = \lambda(-k_R^2 + q^2)\Phi + 2\mu\left(q^2\Phi - ik_R s\Psi\right) = 0 \tag{2.52}$$

$$\tau_{xz} = \mu\left(2\frac{\partial^2\Phi}{\partial x\partial z} + \frac{\partial^2\Psi}{\partial z^2} - \frac{\partial^2\Psi}{\partial x^2}\right) = \mu\left(2ik_R q\Phi + (s^2 + k_R^2)\Psi\right) = 0 \tag{2.53}$$

When *z* is zero, the potential functions become $\Phi = Ae^{i(\omega t - k_R x)}$ and $\Psi = Ce^{i(\omega t - k_R x)}$, which can be substituted into the above equations to give

$$\sigma_{zz} = A[(\lambda + 2\mu)q^2 - \lambda k_R^2] - C(2i\mu k_R s) = 0 \tag{2.54}$$

$$\tau_{xz} = A(2ik_R q) + C(s^2 + k_R^2) = 0 \tag{2.55}$$

which can be combined to give

$$(s^2 + k_R^2)[(\lambda + 2\mu)q^2 - \lambda k_R^2] = 4\mu k_R^2 sq \tag{2.56}$$

Substituting q and s into the above equation gives

$$(2k_R^2-\frac{\omega^2}{V_S^2})[(\lambda+2\mu)\times\left(k_R^2-\frac{\omega^2}{V_P^2}\right)-\lambda k_R^2]=4\mu k_R^2\sqrt{k_R^2-\frac{\omega^2}{V_S^2}}\times\sqrt{k_R^2-\frac{\omega^2}{V_P^2}} \tag{2.57}$$

which can be rearranged as

$$\frac{1}{\mu k_R^2}(2k_R^2-\frac{\omega^2}{V_S^2})[2\mu k_R^2-(\lambda+2\mu)\frac{\omega^2}{V_P^2}]=4\sqrt{k_R^2-\frac{\omega^2}{V_S^2}}\times\sqrt{k_R^2-\frac{\omega^2}{V_P^2}} \tag{2.58}$$

Squaring both sides of the above equation and simplifying gives

$$\left(2-\frac{\omega^2}{V_S^2k_R^2}\right)^2\left(2-\frac{\lambda+2\mu}{\mu}\frac{\omega^2}{V_P^2k_R^2}\right)^2=16\left(1-\frac{\omega^2}{V_S^2k_R^2}\right)\left(1-\frac{\omega^2}{V_P^2k_R^2}\right) \tag{2.59}$$

Defining the ratio of the Rayleigh wave velocity to the shear wave velocity as

$$K_{RS}=\frac{V_R}{V_S}=\frac{\omega}{V_Sk_R} \tag{2.60}$$

and the ratio of the Rayleigh wave velocity to the P wave velocity as

$$\frac{V_R}{V_P}=\frac{\omega}{V_Pk_R}=\sqrt{\frac{1-2\upsilon}{2-2\upsilon}}\,\frac{\omega}{V_Sk_R}=\alpha K_{RS} \tag{2.61}$$

where

$$\alpha=\frac{V_S}{V_P}=\sqrt{\frac{\mu}{\lambda+2\mu}}=\sqrt{\frac{1-2\upsilon}{2-2\upsilon}} \tag{2.62}$$

Note that for all real media, Poisson's ratio will be in the range $0\le\upsilon\le0.5$, and α will therefore be between $\alpha(\upsilon=0.5)=0$ and $\alpha(\upsilon=0)=1/\sqrt{2}$. After substituting Eqs. (2.60) and (2.62) into Eq. (2.59), the latter can be rewritten as

$$\left(2-K_{RS}^2\right)^2\left(2-\frac{1}{\alpha^2}\alpha^2K_{RS}^2\right)^2=16\left(1-K_{RS}^2\right)\left(1-\alpha^2K_{RS}^2\right) \tag{2.63}$$

which can be rearranged with $x=K_{RS}^2$ to give the characteristic Rayleigh wave equation:

$$x^3-8x^2+(24-16\alpha^2)x+16(\alpha^2-1)=0 \tag{2.64}$$

While multiple real or complex-valued roots can exist for this equation, it can be shown for all real media for which $0 \le \upsilon \le 0.5$ that Eq. (2.64) has only one real root (Viktorov 1967). If V_R=0 (i.e., x=0), the left hand side of this equation becomes $16(\alpha^2 - 1)$ which will always be less than zero, and this condition is therefore not possible. Similarly, if V_R=V_S (i.e., x=1), the left hand side becomes 1, and this condition is also not possible. Therefore, Eq. (2.64) has only one real root in the range

$$0 < x < 1 \text{ or } 0 < V_R / V_S < 1$$

which is shown in Figure 2.13. For given values of Poisson's ratio, Eq. (2.64) can be used to find real-valued roots to obtain the Rayleigh wave velocity. Also, the equation is independent of frequency, meaning that R-waves in a homogeneous half-space are non-dispersive. The variation of velocity ratio with Poisson's ratio is shown in Figure 2.14, from which it can be seen that V_R / V_S ranges between 0.87 and 0.96 as reported by Knopoff (1952). An approximate expression for this ratio is provided by Viktorov (1967);

$$\frac{V_R}{V_s} = \frac{0.87 + 1.12\upsilon}{1 + \upsilon} \tag{2.65}$$

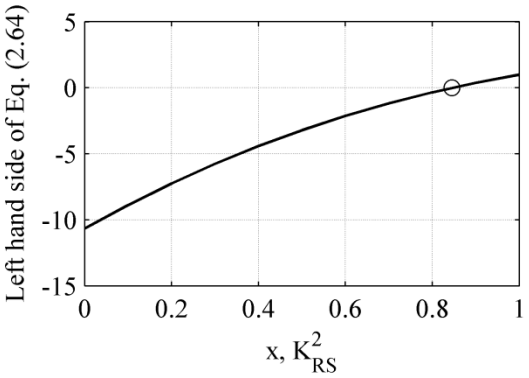

Figure 2.13 Value of the left-hand side of Eq. (2.64) showing one real root.

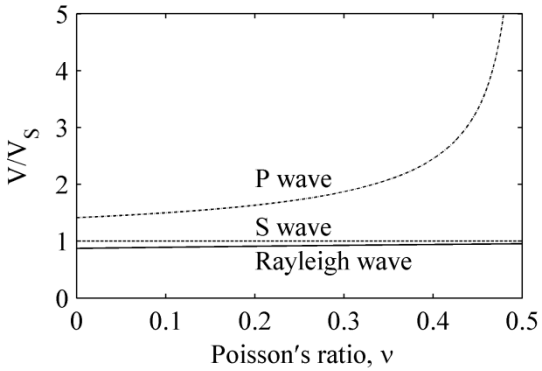

Figure 2.14 Variation of velocity ratio with Poisson's ratio. (after Richart et al. 1970)

Substituting the potential functions, Eqs. (2.46) and (2.47), into the displacement functions, Eqs. (2.15) and (2.16), gives

$$u = -Aik_R e^{-qz} e^{i(\omega t - k_R x)} - Cse^{-sz} e^{i(\omega t - k_R x)} \tag{2.66}$$

$$w = -qAe^{-qz} e^{i(\omega t - k_R x)} + Cik_R e^{-sz} e^{i(\omega t - k_R x)} \tag{2.67}$$

Applying the boundary condition of zero shear stress on the free surface from Eq. (2.55) gives

$$C = -\frac{2k_R qi}{s^2 + k_R^2} A \tag{2.68}$$

Substituting C into u and w in the above two equations gives

$$u = A\left(-k_R e^{-qz} + \frac{2k_R qs}{s^2 + k_R^2} e^{-sz} \right) ie^{i(\omega t - k_R x)} \tag{2.69}$$

$$w = A\left(-qe^{-qz} + \frac{2k_R^2 q}{s^2 + k_R^2} e^{-sz} \right) e^{i(\omega t - k_R x)} \tag{2.70}$$

These displacements are shown in Figure 2.15 normalized by their values at z=0. The ratio of vertical to horizontal displacement can be written as

$$\frac{w}{u} = \frac{-qe^{-qz} + \frac{2k_R^2 q}{s^2 + k_R^2} e^{-sz}}{-k_R e^{-qz} + \frac{2k_R qs}{s^2 + k_R^2} e^{-sz}} i \tag{2.71}$$

The imaginary unit i in Eqs. (2.69) and (2.71) indicates that the horizontal and vertical displacements are out of phase by 90°. The variation of $w(z=0)/u(z=0)$ with Poisson's ratio is shown in Figure 2.16, from which it can be seen that the vertical component is always larger than the horizontal one at the free surface. Figure 2.17 shows an example of the vertical displacement $w(x,t)$ at z=0 in the space and time domains, which is periodic in time with period $T = 1/f$ and periodic in space with wavelength $\lambda = 2\pi / k_R$.

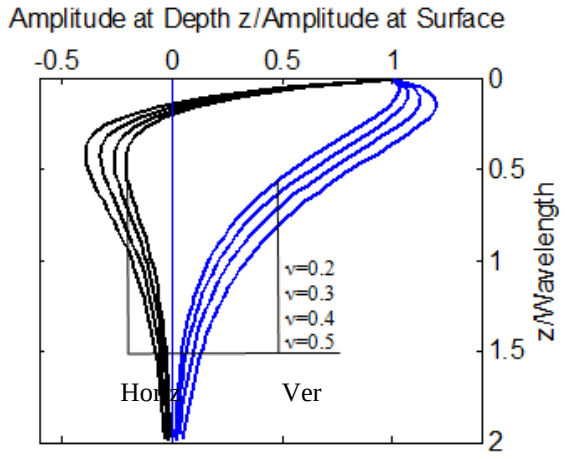

Figure 2.15 Normalized amplitudes of Rayleigh wave displacement components with depth (after Richart et al., 1970).

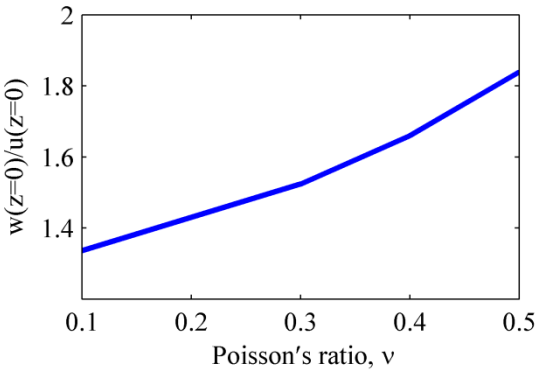

Figure 2.16 Ratio of vertical to horizontal Rayleigh wave displacement at free surface versus Poisson's ratio.

a) b)

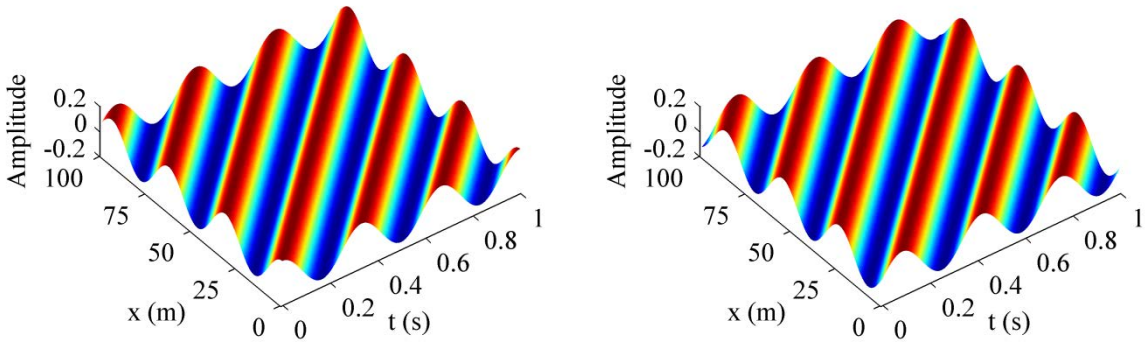

Figure 2.17 Vertical displacement $w(x,t)/A$ at z=0 in space and time domains for plane Rayleigh wave having frequency 3 Hz and wavelength 31.4 m calculated by Eq. (2.70): a) real part; b) imaginary part.

Figure 2.18 shows theoretical and experimentally measured Rayleigh wave particle motions. For a homogeneous, isotropic half-space, the particle motion decays exponentially with depth, and is elliptical and retrograde near the surface, changing to prograde below a depth of approximately 20% of the Rayleigh wavelength. Although the retrograde/prograde rotation direction behavior is often cited, Haskell (1953) demonstrated that the behavior does not hold true at all frequencies for vertically

heterogeneous layered soils, and damping and nonlinearity in real soils also causes the ellipse axes to be inclined, both of which are evident in Figure 2.18b.

a)

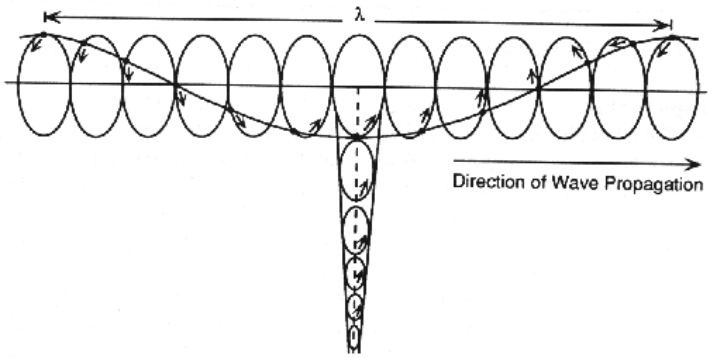

b)

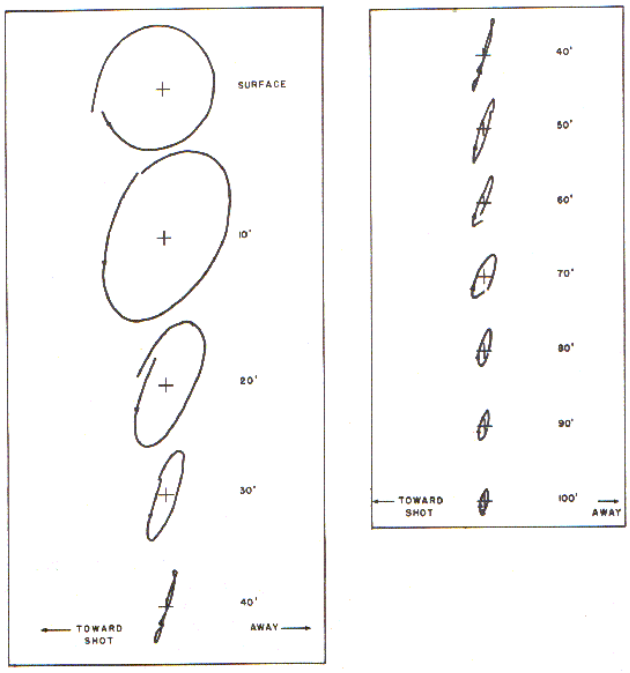

Figure 2.18 Particle motion: a) theoretical; b) experimentally measured in soil (from Igel, 2012).

2.5. Computational Modeling of Rayleigh Wave Motion and Dispersion Behavior in Layered Media

As discussed above, Rayleigh waves are dispersive in layered media. For analytical and computational modeling, each layer in the assumed soil medium model has horizontal interfaces and is homogeneous, isotropic, and elastic. Considering a Rayleigh

wave as a plane wave propagating in a 2-D medium, the model can be described in a 2-D coordinate system as shown in Figure 2.19. The x-axis is directed along the ground surface and is the wave propagation direction, while the z-axis is taken as positive downward into the medium.

For such vertically inhomogeneous layered soil profiles, the phase velocity for harmonic Rayleigh or Love waves is a function of wave frequency (or alternatively, wave length or wave period), and therefore the surface waves are dispersive. The dependence of surface wave phase velocity on frequency (or wave length) is referred to as the dispersion relationship, which can be represented by dispersion curves or by images of dispersion curves, as will be explained in subsequent chapters. The dispersion curves depend on the material properties (Poisson's ratio, shear modulus, density) and geometry (e.g., layer thicknesses, dipping, faulting) of the layered media. Thus, the dispersion curves of a given layered medium can be considered a unique representation of the physical properties of the medium, and are most sensitive to the shear modulus and layer thickness profiles. Due to the complexity of the equations involved, dispersion curves for layered media are usually calculated using numerical methods. Propagation of Rayleigh waves in layered media and the derivation of the dispersion functions are detailed in the following sections using the transfer matrix, global matrix, and stiffness matrix methods.

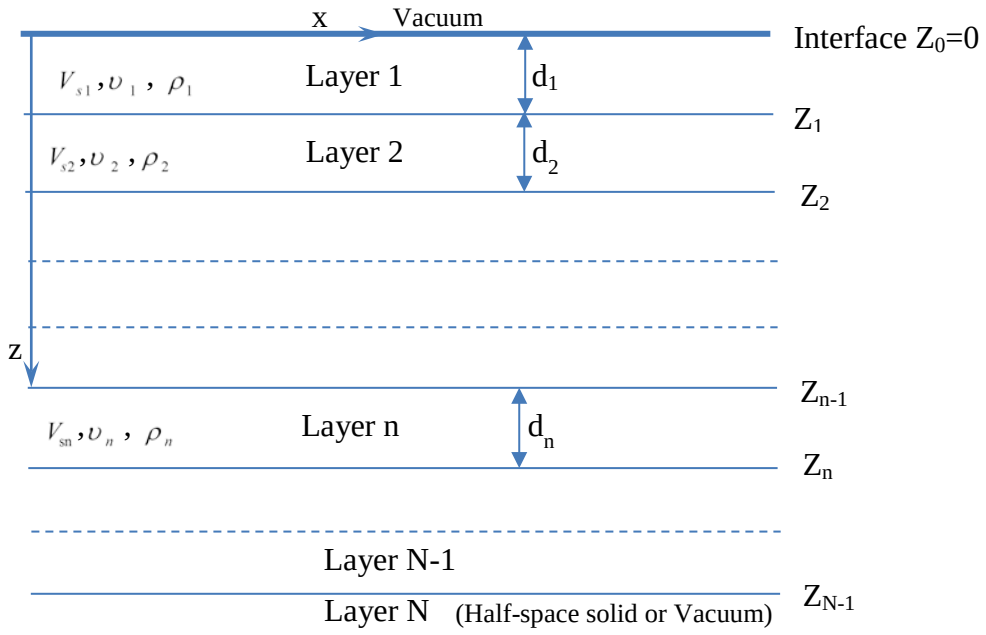

Figure 2.19 Notation for layered soil structure with horizontal interfaces.

2.5.1. Transfer matrix method

The transfer matrix method for solution of the dispersion problem of layered media was first introduced by Thomson (1950), and later modified and corrected by Haskell (1953). A number of further works to treat numerical difficulties in the transfer matrix method are detailed in Nazarian (1984). A brief overview of the method and a potential degeneration of the solution for application to the case of wave propagation in layered plates is presented herein.

In Section 2.4, the propagation of Rayleigh waves was demonstrated as the combination of two potential functions Φ and Ψ representing dilatational and shear waves, respectively. In general, layered media can posess not only downward propagating waves from surface sources (such as a hammer impact on the free surface), but also upward propagating waves from seismic sources or from refraction and reflection of upward and downward waves from the layer interfaces. Therefore, in a

general formulation including body waves, each potential function can have two parts describing both downward and upward propagating waves, which can be represented by complex exponentials in z of the form $e^{i(\omega t \pm kz)}$. In the Rayleigh-wave formulation of the previous sections, however, such terms were replaced by real-valued exponential functions describing standing waveforms with exponential growth or decay in the z-direction.

Considering an ideal elastic medium with N-1 layers overlying a half-space, with z=0 at the free surface, the potential functions for the n^{th} layer can be written as

$$\Phi_n = (A_n e^{-q_n(z-Z_{n-1})} + B_n e^{q_n(z-Z_{n-1})}) e^{i(\omega t - k_R x)} \tag{2.72}$$

$$\Psi_n = (C_n e^{-s_n(z-Z_{n-1})} + D_n e^{s_n(z-Z_{n-1})}) e^{i(\omega t - k_R x)} \tag{2.73}$$

where Z_{n-1} is the depth of the $(n\text{-}1)^{th}$ layer interface at the top of layer n , and $Z_{n-1} \le z \le Z_n$ is the depth from the ground surface. A_n and C_n are coefficients of downward decaying waves, and B_n and D_n are coefficients of upward decaying waves. The potential functions can therefore be decomposed into upward and downward decaying components as

$$\Phi_n = \Phi_n^U + \Phi_n^D \tag{2.74}$$

$$\Psi_n = \Psi_n^U + \Psi_n^D \tag{2.75}$$

$$\Phi_n^U = B_n e^{q_n(z-Z_{n-1})} e^{i(\omega t - k_R x)} \tag{2.76}$$

$$\Phi_n^D = A_n e^{-q_n(z-Z_{n-1})} e^{i(\omega t - k_R x)} \tag{2.77}$$

$$\Psi_n^U = D_n e^{s_n(z-Z_{n-1})} e^{i(\omega t - k_R x)} \tag{2.78}$$

$$\Psi_n^D = C_n e^{-s_n(z-Z_{n-1})} e^{i(\omega t - k_R x)} \tag{2.79}$$

where q_n, s_n and $(z\text{-}Z_{n-1})$ are positive. Substituting the above four potential equations into displacement and stress functions (Eqs. (2.6), (2.15) and (2.16)) and using Eq. (2.19) gives

$$u_n = \frac{\partial \Phi_n}{\partial x} + \frac{\partial \Psi_n}{\partial z} = [-ik_R \;\; s_n \;\; -ik_R \;\; -s_n][\Phi_n^U \;\; \Psi_n^U \;\; \Phi_n^D \;\; \Psi_n^D]^T \tag{2.80}$$

$$w_n = \frac{\partial \Phi_n}{\partial z} - \frac{\partial \Psi_n}{\partial x} = [q_n \;\; ik_R \;\; -q_n \;\; ik_R][\Phi_n^U \;\; \Psi_n^U \;\; \Phi_n^D \;\; \Psi_n^D]^T \tag{2.81}$$

$$\sigma_{zz,n} = \lambda\bar{\varepsilon} + 2\mu\varepsilon_{zz} = [\mu a_n \;\; 2i\mu k_R s_n \;\; \mu a_n \;\; -2i\mu k_R s_n][\Phi_n^U \;\; \Psi_n^U \;\; \Phi_n^D \;\; \Psi_n^D]^T \tag{2.82}$$

$$\tau_{xz,n} = \mu\gamma_{xz} = [-2i\mu k_R q_n \;\; \mu a_n \;\; 2i\mu k_R q_n \;\; \mu a_n][\Phi_n^U \;\; \Psi_n^U \;\; \Phi_n^D \;\; \Psi_n^D]^T \tag{2.83}$$

where T denotes the transpose, and

$$a_n = \left(2k_R^{\,2} - \omega^2 \Big/ \left(V_S^n\right)^2\right) \tag{2.84}$$

Defining the following two vectors and transformation matrix for the n^{th} layer:

$$S_n(z) = [u_n(z) \;\; w_n(z) \;\; \sigma_{zz,n}(z) \;\; \tau_{xz,n}(z)]^T \tag{2.85}$$

$$P_n(z) = [\Phi_n^U(z) \;\; \Psi_n^U(z) \;\; \Phi_n^D(z) \;\; \Psi_n^D(z)]^T \tag{2.86}$$

$$T_n = \begin{bmatrix} -ik_R & s_n & -ik_R & -s_n \\ q_n & ik_R & -q_n & ik_R \\ \mu a_n & 2i\mu k_R s_n & \mu a_n & -2i\mu k_R s_n \\ -2i\mu k_R q_n & \mu a_n & 2i\mu k_R q_n & \mu a_n \end{bmatrix} \tag{2.87}$$

The displacement and stress functions in Eqs. (2.80)–(2.83) at any point z within the layer can be rewritten as

$$S_n(z) = T_n P_n(z) \tag{2.88}$$

by which the potential function vector can be determined from the stresses and displacements as

$$P_n(z) = T_n^{-1} S_n(z) \tag{2.89}$$

The relationship between two potential function vectors at top and bottom interfaces of the n^{th} layer can be written as

$$\begin{aligned} \Phi_n^U(Z_n) &= B_n e^{q_n(Z_n - Z_{n-1})} e^{i(\omega t - k_R x)} \\ &= e^{q_n d_n} B_n e^{q_n(Z_{n-1} - Z_{n-1})} e^{i(\omega t - k_R x)} \\ &= e^{q_n d_n} \Phi_n^U(Z_{n-1}) \end{aligned} \tag{2.90}$$

where $d_n = Z_n - Z_{n-1}$ is the thickness of the n^{th} layer. A similar procedure results in the following three equations:

$$\Phi_n^D(Z_n) = e^{-q_n d_n}\Phi_n^D(Z_{n-1}) \tag{2.91}$$

$$\Psi_n^U(Z_n) = e^{s_n d_n}\Psi_n^U(Z_{n-1}) \tag{2.92}$$

$$\Psi_n^D(Z_n) = e^{-s_n d_n}\Psi_n^U(Z_{n-1}) \tag{2.93}$$

Upon defining the matrix

$$E_n = \begin{bmatrix} e^{q_n d_n} & 0 & 0 & 0 \\ 0 & e^{s_n d_n} & 0 & 0 \\ 0 & 0 & e^{-q_n d_n} & 0 \\ 0 & 0 & 0 & e^{-s_n d_n} \end{bmatrix} \tag{2.94}$$

the above four relations between potential functions at the top and bottom of layer *n* can be expressed as

$$P_n(Z_n) = E_n P_n(Z_{n-1}) \tag{2.95}$$

Enforcing equality of the stresses and displacements at the interface of layers *n* and (*n*+1) gives

$$\begin{aligned} S_{n+1}(Z_n) &= S_n(Z_n) \text{ (continuity boundary condition)} \\ &= T_n P_n(Z_n) \text{ (Eq. (2.88) is used.)} \\ &= T_n E_n P_n(Z_{n-1}) \text{ (Eq. (2.95) is used.)} \\ &= T_n E_n T_n^{-1} S_n(Z_{n-1}) \text{ (Eq. (2.89) is used.)} \end{aligned} \tag{2.96}$$

Defining

$$G_n = T_n E_n T_n^{-1} \tag{2.97}$$

Eq. (2.96) can be written as

$$S_n(Z_n) = S_{n+1}(Z_n) = G_n S_n(Z_{n-1}) \tag{2.98}$$

which gives the displacements and stresses at the bottom of layer *n* given the properties of the layer and displacements/stresses at its top. Equation (2.98) can be applied

recursively to establish the relationship between displacements and stresses at the free surface and those at the interface at depth Z_{n-1}:

$$S_n(Z_{n-1}) = \prod_{i=n-1}^{1} G_i S_1(Z_0) \tag{2.99}$$

2.5.1.1. Case 1: Layered soil system with traction-free top surface overlying a half-space

Equation (2.99) can be substituted into Eq. (2.89) to relate the potentials at the top of any layer *n* to the displacements and stresses at the free surface:

$$P_n(Z_{n-1}) = T_n^{-1} S_n(Z_{n-1}) = T_n^{-1} \prod_{i=n-1}^{1} G_i S_1(Z_0) = T_n^{-1} R_n S_1(Z_0) \tag{2.100}$$

where

$$R_n = \prod_{i=n-1}^{1} G_i \tag{2.101}$$

With the surface of the top layer being traction-free, $S_1(Z_0)$ becomes

$$S_1(Z_0) = \left[u_1(0) \;\; w_1(0) \;\; 0 \;\; 0\right]^{\mathrm{T}} \tag{2.102}$$

If the load is applied only at the free surface of the top layer, then the potentials in the half-space must be bounded as $z \to \infty$. Thus, the potential vector for the half-space is

$$\begin{aligned} P_N(Z_{N-1}) &= [\Phi_N^U(Z_{N-1}) \;\; \Psi_N^U(Z_{N-1}) \;\; \Phi_N^D(Z_{N-1}) \;\; \Psi_N^D(Z_{N-1})]^T \\ &= [0 \;\; 0 \;\; \Phi_N^D(Z_{N-1}) \;\; \Psi_N^D(Z_{N-1})]^T \end{aligned} \tag{2.103}$$

Using the two boundary conditions in Eqs. (2.102) and (2.103), Eq. (2.100) can be written in matrix form as

$$\begin{bmatrix} 0 \\ 0 \\ \hline \Phi_N^D(Z_{N-1}) \\ \Psi_N^D(Z_{N-1}) \end{bmatrix} = \left[\begin{array}{cc:cc} r_{11} & r_{12} & r_{13} & r_{14} \\ r_{21} & r_{22} & r_{23} & r_{24} \\ \hdashline r_{31} & r_{32} & r_{33} & r_{34} \\ r_{41} & r_{42} & r_{43} & r_{44} \end{array}\right] \begin{bmatrix} u_1(0) \\ w_1(0) \\ \hline 0 \\ 0 \end{bmatrix} \tag{2.104}$$

The above matrix can be partitioned into sub-matrices as indicated by the dashed lines, giving

$$\begin{bmatrix} \mathbf{0} \\ A \end{bmatrix} = \begin{bmatrix} R_{11} & R_{12} \\ R_{21} & R_{22} \end{bmatrix} \begin{bmatrix} B \\ \mathbf{0} \end{bmatrix} \tag{2.105}$$

which gives the equations

$$\begin{aligned} R_{11} \cdot B &= \mathbf{0} \\ A &= R_{21} \cdot B \end{aligned} \tag{2.106}$$

From the first of the above equations,

$$\begin{bmatrix} r_{11} & r_{12} \\ r_{21} & r_{22} \end{bmatrix} . \begin{bmatrix} u_1(0) \\ w_1(0) \end{bmatrix} = \begin{bmatrix} 0 \\ 0 \end{bmatrix} \tag{2.107}$$

The displacements at the free surface depend on the imparted energy, and therefore can be non-zero in general. Thus, for a nontrivial solution, the determinant of R_{11} must be zero. The determinant $|R_{11}| = 0$ is a function of k and ω, and is called the characteristic (dispersion) function;

$$\Delta(\omega, k) = |R_{11}| = \begin{vmatrix} r_{11} & r_{12} \\ r_{21} & r_{22} \end{vmatrix} = 0 \tag{2.108}$$

Solving for the roots of the dispersion function at a given frequency yields the wavenumber and thus phase velocity of the Rayleigh wave at that frequency for the layered soil system. Solving for phase velocity over a range of frequencies then yields the dispersion curves. In general, multiple roots of the dispersion function may exist at a given frequency, corresponding to multiple modes of Rayleigh wave propagation. Numerical methods for determining the roots are discussed in later sections.

2.5.1.2. Case 2: Degeneration of solution for a layered, free plate

The solution for a free plate consisting of N-1 layers can be obtained by considering a medium for which the bottom half-space (layer N) is a vacuum. Equation

(2.99) indicates that the stresses and displacements at the bottom of the last layer (N-1) are related to those on the free surface of the top layer through

$$S_N(Z_{N-1}) = S_{N-1}(Z_{N-1}) = R_N S_1(Z_0) \tag{2.109}$$

where $R_N = \prod_{i=N-1}^{1} G_i$ according to Eq. (2.101).

The bottom and top of the plate are both free surfaces, so the stress components are zero:

$$S_{N-1}(Z_{N-1}) = [u_{N-1}(Z_{N-1}) \;\; w_{N-1}(Z_{N-1}) \;\; 0 \;\; 0]^T \tag{2.110}$$

$$S_1(0) = [u_1(0) \;\; w_1(0) \;\; 0 \;\; 0]^T \tag{2.111}$$

Eq. (2.109) can thus be written in matrix form as

$$\begin{bmatrix} u_{N-1}(Z_{N-1}) \\ w_{N-1}(Z_{N-1}) \\ \hdashline 0 \\ 0 \end{bmatrix} = \left[\begin{array}{cc:cc} r_{11} & r_{12} & r_{13} & r_{14} \\ r_{21} & r_{22} & r_{23} & r_{24} \\ \hdashline r_{31} & r_{32} & r_{33} & r_{34} \\ r_{41} & r_{42} & r_{43} & r_{44} \end{array}\right] \begin{bmatrix} u_1(0) \\ w_1(0) \\ \hdashline 0 \\ 0 \end{bmatrix} \tag{2.112}$$

which can be partitioned into sub-matrices as indicated by the dashed lines;

$$\begin{bmatrix} A \\ \mathbf{0} \end{bmatrix} = \begin{bmatrix} R_{11} & R_{12} \\ R_{21} & R_{22} \end{bmatrix} \begin{bmatrix} B \\ \mathbf{0} \end{bmatrix} \tag{2.113}$$

which gives

$$R_{21} \cdot B = \mathbf{0} \tag{2.114}$$

or

$$\begin{bmatrix} r_{31} & r_{32} \\ r_{41} & r_{42} \end{bmatrix} . \begin{bmatrix} u_1(0) \\ w_1(0) \end{bmatrix} = \begin{bmatrix} 0 \\ 0 \end{bmatrix} \tag{2.115}$$

Again, for a nontrivial solution with non-zero displacements at the plate's top surface, the determinant of R_{21} must be zero, giving the characteristic (dispersion) function for quasi-Rayleigh wavenumber or velocity as

$$\Delta(\omega, k) = |R_{21}| = \begin{vmatrix} r_{31} & r_{32} \\ r_{41} & r_{42} \end{vmatrix} = 0 \tag{2.116}$$

Note that wave propagation in a free plate will actually consist of Lamb waves for which the characteristic dispersion function is different from the one above (e.g., Lamb 1917, Ryden and Park 2004, Ryden et al. 2004). However, given the similarity of the composite A_0 and S_0 Lamb-wave modes to Rayleigh waves as discussed in Section 2.2, the Rayleigh wave approximation given in Eq. (2.116) may be useful for application to pavements. This topic is recommended for further study.

As demonstrated in this section, the transfer matrix method is useful for determining theoretical dispersion curves for layered soil systems by solving for the roots of the scalar characteristic dispersion functions. However, the method does not directly provide the stresses and displacements at the layer interfaces within the soil profile. To determine these quantities, the formulation above can be modified to produce a global matrix, which is then converted to a global stiffness matrix. The formulations are presented in the following sections.

2.5.2. Global matrix method

To relate the vectors of displacements, stresses, and potentials at each layer interface, the equations presented above can be employed to formulate a global matrix in the frequency-wavenumber (ω–k) domain. The global matrix method can be traced back to Knopoff (1964), and is discussed further in Lowe (1995). The formulation for the cases of a layered soil profile overlying a half-space and a traction-free layered plate are presented below.

2.5.2.1. Case 1: Layered soil system with traction-free top surface overlying a half-space

At the free surface of the first layer, Eq. (2.88) relates the potential function vector to the displacement and stress vector;

$$S_1(Z_0) = T_1 P_1(Z_0) \tag{2.117}$$

which gives the potential vector at the top of the layer as

$$P_1(Z_0) = T_1^{-1} S_1(Z_0) \tag{2.118}$$

Equation (2.95) then relates the potential function vectors at the top and bottom of the first layer:

$$P_1(Z_1) = E_1 P_1(Z_0) \tag{2.119}$$

which gives

$$P_1(Z_0) = E_1^{-1} P_1(Z_1) \tag{2.120}$$

Combination of Eqs. (2.118) and (2.120) gives

$$T_1^{-1} S_1(Z_0) = E_1^{-1} P_1(Z_1) \tag{2.121}$$

which can be rearranged to

$$[T_1^{-1} \quad -E_1^{-1}] \begin{bmatrix} S_1(Z_0) \\ P_1(Z_1) \end{bmatrix} = \mathbf{0} \tag{2.122}$$

For the intermediate layers $2 \le n \le N\text{-}1$, the stresses and displacements on the interface of the $(n\text{-}1)^{th}$ and n^{th} layers at depth $Z_{n\text{-}1}$ are equal:

$$S_n(Z_{n-1}) = S_{n-1}(Z_{n-1}) \tag{2.123}$$

which can be expanded and related to potential function vectors using Eq. (2.88):

$$S_{n-1}(Z_{n-1}) = T_{n-1} P_{n-1}(Z_{n-1}) \tag{2.124}$$

$$S_n(Z_{n-1}) = T_n P_n(Z_{n-1}) \tag{2.125}$$

Substituting Eqs. (2.124) and (2.125) into Eq. (2.123) gives

$$T_n P_n(Z_{n-1}) = T_{n-1} P_{n-1}(Z_{n-1}) \tag{2.126}$$

Recalling that Eq. (2.95) relates two potential function vectors at Z_{n-1} and Z_n, one may write

$$P_n(Z_{n-1}) = E_n^{-1} P_n(Z_n) \tag{2.127}$$

Substituting Eq. (2.127) into Eq. (2.126) gives

$$T_n E_n^{-1} P_n(Z_n) = T_{n-1} P_{n-1}(Z_{n-1}) \tag{2.128}$$

which can be rearranged to

$$\begin{bmatrix} T_{n-1} & -T_n E_n^{-1} \end{bmatrix} \begin{bmatrix} P_{n-1}(Z_{n-1}) \\ P_n(Z_n) \end{bmatrix} = \mathbf{0} \tag{2.129}$$

Enforcing continuity of stresses and displacements on the interface of the last layer and the half-space gives

$$S_N(Z_{N-1}) = S_{N-1}(Z_{N-1}) \tag{2.130}$$

which can be written in terms of potential vectors according to Eq. (2.126) as

$$T_N P_N(Z_{N-1}) = T_{N-1} P_{N-1}(Z_{N-1}) \tag{2.131}$$

and expressed in matrix form as

$$\begin{bmatrix} T_{N-1} & -T_N \end{bmatrix} \begin{bmatrix} P_{N-1}(Z_{N-1}) \\ P_N(Z_{N-1}) \end{bmatrix} = \mathbf{0} \tag{2.132}$$

Assembling the matrices for the top layer from Eq. (2.122), intermediate layers from Eq. (2.129), and last layer and half-space from Eq. (2.132) gives the global matrix,

$$\begin{bmatrix} T_1^{-1} & -E_1^{-1} & & & & & & & \\ & T_1 & -T_2E_2^{-1} & & & & & & \\ & & T_2 & -T_3E_3^{-1} & & & & & \\ & & & \ddots & \ddots & & & & \\ & & & & T_{N-3} & -T_{N-2}E_{N-2}^{-1} & & & \\ & & & & & T_{N-2} & -T_{N-1}E_{N-1}^{-1} & & \\ & & & & & & T_{N-1} & -T_N \end{bmatrix} \begin{bmatrix} S_1(Z_0) \\ P_1(Z_1) \\ P_2(Z_2) \\ P_3(Z_2) \\ \vdots \\ P_{N-3}(Z_{N-3}) \\ P_{N-2}(Z_{N-2}) \\ P_{N-1}(Z_{N-1}) \\ P_N(Z_{N-1}) \end{bmatrix} = \mathbf{0} \tag{2.133}$$

The above system of equations has $4N$ individual equations and $4(N+1)$ unknowns. Four additional equations must be provided to solve the system. Considering the boundary conditions that the top layer is traction-free and the bottom (N^{th}) layer is a half-space gives the additional equations:

$$\begin{aligned} S_1(Z_0) &= [u_1(Z_0)\ \ w_1(Z_0)\ \ \sigma_{zz,1}(Z_0)\ \ \tau_{xz,1}(Z_0)]^T \\ &= \left[u_1(0)\ \ w_1(0)\ \ 0\ \ 0\right]^{\mathrm{T}} \end{aligned} \tag{2.134}$$

$$\begin{aligned} P_N(Z_{N-1}) &= [\Phi_N^U(Z_{N-1})\ \ \Psi_N^U(Z_{N-1})\ \ \Phi_N^D(Z_{N-1})\ \ \Psi_N^D(Z_{N-1})]^T \\ &= [0\ \ 0\ \ \Phi_N^D(Z_{N-1})\ \ \Psi_N^D(Z_{N-1})]^T \end{aligned} \tag{2.135}$$

Substituting Eqs. (2.134) and (2.135) into Eq. (2.133) and eliminating the zero components gives the $4N$ by $4N$ matrix,

$$\begin{bmatrix} T_1^{-1}{}_{(:,[1,2])} & -E_1^{-1} & & & & & & & \\ & T_1 & -T_2E_2^{-1} & & & & & & \\ & & T_2 & -T_3E_3^{-1} & & & & & \\ & & & \ddots & \ddots & & & & \\ & & & & T_{N-3} & -T_{N-2}E_{N-2}^{-1} & & & \\ & & & & & T_{N-2} & -T_{N-1}E_{N-1}^{-1} & & \\ & & & & & & T_{N-1} & -T_{N(:,[3,4])} \end{bmatrix} \begin{bmatrix} S_1(Z_0)_{(1,2)} \\ P_1(Z_1) \\ P_2(Z_2) \\ P_3(Z_3) \\ \vdots \\ P_{N-3}(Z_{N-3}) \\ P_{N-2}(Z_{N-2}) \\ P_{N-1}(Z_{N-1}) \\ P_N(Z_{N-1})_{(3,4)} \end{bmatrix} = \mathbf{0} \tag{2.136}$$

where $T_1^{-1}{}_{(:,[1,2])}$ denotes all rows and the first two columns of T_1^{-1}.

The above square matrix equation can be written as

$$[\mathbf{S}][\mathbf{A}] = \mathbf{0} \tag{2.137}$$

which can be viewed as an eigenvalue problem, for which the characteristic (dispersion) function.

$$\Delta(\omega,k) = |\mathbf{S}| = \begin{vmatrix} T_1^{-1}{}_{(:,[1,2])} & -E_1^{-1} & & & & & & & \\ & T_1 & -T_2E_2^{-1} & & & & & & \\ & & T_2 & -T_3E_3^{-1} & & & & & \\ & & & \ddots & \ddots & & & & \\ & & & & T_{N-3} & -T_{N-2}E_{N-2}^{-1} & & & \\ & & & & & T_{N-2} & -T_{N-1}E_{N-1}^{-1} & & \\ & & & & & & T_{N-1} & -T_{N(:,[3,4])} \end{vmatrix} = 0 \tag{2.138}$$

at a given frequency will give the solution for Rayleigh wavenumber k, and thus phase velocity.

2.5.2.2. Case 2: Degeneration of solution for a layered, free plate

If the bottom layer is also traction-free, the medium becomes a layered, free plate. For the top layer, Eq. (2.120) can be written for this case as

$$\begin{bmatrix} I & -E_1^{-1} \end{bmatrix} \begin{bmatrix} P_1(Z_0) \\ P_1(Z_1) \end{bmatrix} = \mathbf{0} \tag{2.139}$$

where I is the 4×4 identity matrix. For the bottom layer (N-1) of the plate, Eq. (2.129) with $n = N$-1 relates the potential vectors at the top and bottom of the layer. Assembling all layers together gives the global matrix,

$$\begin{bmatrix} I & -E_1^{-1} & & & & & \\ & T_1 & -T_2E_2^{-1} & & & & \\ & & T_2 & -T_3E_3^{-1} & & & \\ & & & \ddots & \ddots & & \\ & & & & T_{N-3} & -T_{N-2}E_{N-2}^{-1} & \\ & & & & & T_{N-2} & -T_{N-1}E_{N-1}^{-1} \end{bmatrix} \begin{bmatrix} P_1(Z_0) \\ P_1(Z_1) \\ P_2(Z_2) \\ P_3(Z_3) \\ \vdots \\ P_{N-3}(Z_{N-3}) \\ P_{N-2}(Z_{N-2}) \\ P_{N-1}(Z_{N-1}) \end{bmatrix} = \mathbf{0} \tag{2.140}$$

Waves propagating along the free plate have no external energy input. Thus the conditions on the potentials for the top and bottom layers can be written as,

$$\begin{aligned} P_1(Z_0) &= [\Phi_1^U(Z_0)\ \Psi_1^U(Z_0)\ \Phi_1^D(Z_0)\ \Psi_1^D(Z_0)]^T \\ &= [\Phi_1^U(Z_0)\ \Psi_1^U(Z_0)\ \ 0\ \ 0]^T \end{aligned} \tag{2.141}$$

$$\begin{aligned} P_{N-1}(Z_{N-1}) &= [\Phi_{N-1}^U(Z_{N-1})\ \Psi_{N-1}^U(Z_{N-1})\ \Phi_{N-1}^D(Z_{N-1})\ \Psi_{N-1}^D(Z_{N-1})]^T \\ &= [0\ \ 0\ \Phi_{N-1}^D(Z_{N-1})\ \Psi_{N-1}^D(Z_{N-1})]^T \end{aligned} \tag{2.142}$$

Inserting these boundary conditions into Eq. (2.140) and eliminating the zero components gives the 4*N* by 4*N* matrix,

$$\begin{bmatrix} I_{(:,[1,2])} & -E_1^{-1} & & & & & \\ & T_1 & -T_2E_2^{-1} & & & & \\ & & T_2 & -T_3E_3^{-1} & & & \\ & & & \ddots & \ddots & & \\ & & & & T_{N-3} & -T_{N-2}E_{N-2}^{-1} & \\ & & & & & T_{N-2} & -T_{N-1}E_{N-1(:[3,4])}^{-1} \end{bmatrix} \begin{bmatrix} P_1(Z_0)_{(1,2)} \\ P_1(Z_1) \\ P_2(Z_2) \\ P_3(Z_3) \\ \vdots \\ P_{N-3}(Z_{N-3}) \\ P_{N-2}(Z_{N-2}) \\ P_{N-1}(Z_{N-1})_{(3,4)} \end{bmatrix} = \mathbf{0} \tag{2.143}$$

which can be written as

$$[\mathbf{S}][\mathbf{A}] = \mathbf{0} \tag{2.144}$$

The characteristic (dispersion) function for this case is

$$\Delta(\omega,k)=|\mathbf{S}|=\begin{vmatrix} I_{(:,[1,2])} & -E_1^{-1} & & & & & \\ & T_1 & -T_2E_2^{-1} & & & & \\ & & T_2 & -T_3E_3^{-1} & & & \\ & & & \ddots & \ddots & & \\ & & & & T_{N-3} & -T_{N-2}E_{N-2}^{-1} & \\ & & & & & T_{N-2} & -T_{N-1}E_{N-1(:[3,4])}^{-1} \end{vmatrix}=0 \tag{2.145}$$

The characteristic function can also be derived from the boundary conditions of traction-free top and bottom surfaces of the free plate. For the last layer, Eq. (2.88) relates the potential function vector at the Z_{N-1} interface to the displacement and stress vector at the Z_N free surface:

$$\begin{aligned} S_{N-1}(Z_{N-1}) &= T_{N-1}P_{N-1}(Z_{N-1}) \\ &= T_{N-1}E_{N-1}P_{N-1}(Z_{N-2}) \\ &= T_{N-1}E_{N-1}T_{N-1}^{-1}T_{N-2}P_{N-2}(Z_{N-2}) \end{aligned} \tag{2.146}$$

which can be written as

$$\begin{bmatrix} T_{N-1}E_{N-1}T_{N-1}^{-1}T_{N-2} & -I \end{bmatrix}\begin{bmatrix} P_{N-2}(Z_{N-2}) \\ S_{N-1}(Z_{N-1}) \end{bmatrix}=\mathbf{0} \tag{2.147}$$

Assembling all layers together gives a global matrix,

$$\begin{bmatrix} T_1^{-1} & -E_1^{-1} & & & & & \\ & T_1 & -T_2E_2^{-1} & & & & \\ & & T_2 & -T_3E_3^{-1} & & & \\ & & & \ddots & \ddots & & \\ & & & & T_{N-3} & -T_{N-2}E_{N-2}^{-1} & \\ & & & & & T_{N-1}E_{N-1}T_{N-1}^{-1}T_{N-2} & -I \end{bmatrix}\begin{bmatrix} S_1(Z_0) \\ P_1(Z_1) \\ P_2(Z_2) \\ P_3(Z_3) \\ \vdots \\ P_{N-3}(Z_{N-3}) \\ P_{N-2}(Z_{N-2}) \\ S_{N-1}(Z_{N-1}) \end{bmatrix}=\mathbf{0} \tag{2.148}$$

Enforcing zero shear and normal stress on the top and bottom surfaces of the plate;

$$S_1(Z_0) = \left[u_1(0)\ \ w_1(0)\ \ 0\ \ 0\right]^{\mathrm{T}} \tag{2.149}$$

$$S_{N-1}(Z_{N-1}) = \left[u_{N-1}(Z_{N-1})\ \ w_{N-1}(Z_{N-1})\ \ 0\ \ 0\right]^{\mathrm{T}} \tag{2.150}$$

Applying these boundary conditions and eliminating the zero components in Eq. (2.148) gives the $4N$ by $4N$ matrix,

$$\begin{bmatrix} T_1^{-1}{}_{(:,[1,2])} & -E_1^{-1} & & & & & & \\ & T_1 & -T_2E_2^{-1} & & & & & \\ & & T_2 & -T_3E_3^{-1} & & & & \\ & & & \ddots & \ddots & & & \\ & & & & T_{N-3} & -T_{N-2}E_{N-2}^{-1} & & \\ & & & & & T_{N-1}E_{N-1}T_{N-1}^{-1}T_{N-2} & -I_{(:,[1,2])} & \end{bmatrix} \begin{bmatrix} S_1(Z_0)_{(1,2)} \\ P_1(Z_1) \\ P_2(Z_2) \\ P_3(Z_3) \\ \vdots \\ P_{N-3}(Z_{N-3}) \\ P_{N-2}(Z_{N-2}) \\ S_{N-1}(Z_{N-1})_{(1,2)} \end{bmatrix} = \mathbf{0} \tag{2.151}$$

which can be written as

$$[\mathbf{S}][\mathbf{A}] = \mathbf{0} \tag{2.152}$$

The characteristic (dispersion) function is

$$\Delta(\omega,k) = |\mathbf{S}| = \begin{vmatrix} T_1^{-1}{}_{(:,[1,2])} & -E_1^{-1} & & & & & & \\ & T_1 & -T_2E_2^{-1} & & & & & \\ & & T_2 & -T_3E_3^{-1} & & & & \\ & & & \ddots & \ddots & & & \\ & & & & T_{N-3} & -T_{N-2}E_{N-2}^{-1} & & \\ & & & & & T_{N-1}E_{N-1}T_{N-1}^{-1}T_{N-2} & -I_{(:,[1,2])} & \end{vmatrix} = 0 \tag{2.153}$$

2.5.3. Stiffness matrix method

The above global matrix method involves displacements, stresses and potentials at the layer interfaces. The potentials can be eliminated to obtain a global stiffness matrix relating only stresses and displacements at the layer interfaces, similar to a finite element

force-displacement stiffness matrix. The stiffness matrix approach was presented by Kausel and Roesset (1981), Gucunski and Woods (1992), and Ganji et al. (1998). Its formulation is detailed below.

2.5.3.1. Case 1: Layered soil system with traction-free top surface overlying a half-space

Recalling Eqs. (2.97) and (2.98), the stresses and displacements on the top (Z_{n-1}) and bottom (Z_n) interfaces of layer n can be related by

$$S_n(Z_n) = G_n S_n(Z_{n-1}) \tag{2.154}$$

Using the expressions for T_n and E_n in Eqs. (2.87) and (2.94), the inverse and matrix products in the above equation can be derived as

$$T_n^{-1} = \frac{1}{a_n - 2k_R^2}\begin{bmatrix} -ik_R & \frac{a_n}{2q_n} & \frac{1}{2\mu} & -\frac{ik_R}{2q_n\mu} \\ \frac{a_n}{2s_n} & ik_R & \frac{ik_R}{2s_n\mu} & \frac{1}{2\mu} \\ -ik_R & -\frac{a_n}{2q_n} & \frac{1}{2\mu} & \frac{ik_R}{2q_n\mu} \\ -\frac{a_n}{2s_n} & ik_R & -\frac{ik_R}{2s_n\mu} & \frac{1}{2\mu} \end{bmatrix}$$

$$T_n E_n = \begin{bmatrix} -ik_R & s_n & -ik_R & -s_n \\ q_n & ik_R & -q_n & ik_R \\ \mu a_n & 2i\mu k_R s_n & \mu a_n & -2i\mu k_R s_n \\ -2i\mu k_R q_n & \mu a_n & 2i\mu k_R q_n & \mu a_n \end{bmatrix}\begin{bmatrix} e^{q_n d_n} & 0 & 0 & 0 \\ 0 & e^{s_n d_n} & 0 & 0 \\ 0 & 0 & e^{-q_n d_n} & 0 \\ 0 & 0 & 0 & e^{-s_n d_n} \end{bmatrix}$$

$$= \begin{bmatrix} -ik_R e^{q_n d_n} & s_n e^{s_n d_n} & -ik_R e^{-q_n d_n} & -s_n e^{-s_n d_n} \\ q_n e^{q_n d_n} & ik_R e^{s_n d_n} & -q_n e^{-q_n d_n} & ik_R e^{-s_n d_n} \\ \mu a_n e^{q_n d_n} & 2i\mu k_R s_n e^{s_n d_n} & \mu a_n e^{-q_n d_n} & -2i\mu k_R s_n e^{-s_n d_n} \\ -2i\mu k_R q_n e^{q_n d_n} & \mu a_n e^{s_n d_n} & 2i\mu k_R q_n e^{-q_n d_n} & \mu a_n e^{-s_n d_n} \end{bmatrix}$$

and G_n can be written as

$$G_n = \frac{1}{a_n - 2k_R^2}\begin{bmatrix} -ik_R e^{q_n d_n} & s_n e^{s_n d_n} & -ik_R e^{-q_n d_n} & -s_n e^{-s_n d_n} \\ q_n e^{q_n d_n} & ik_R e^{s_n d_n} & -q_n e^{-q_n d_n} & ik_R e^{-s_n d_n} \\ \mu a_n e^{q_n d_n} & 2i\mu k_R s_n e^{s_n d_n} & \mu a_n e^{-q_n d_n} & -2i\mu k_R s_n e^{-s_n d_n} \\ -2i\mu k_R q_n e^{q_n d_n} & \mu a_n e^{s_n d_n} & 2i\mu k_R q_n e^{-q_n d_n} & \mu a_n e^{-s_n d_n} \end{bmatrix}\begin{bmatrix} -ik_R & \frac{a_n}{2q_n} & \frac{1}{2\mu} & -\frac{ik_R}{2q_n\mu} \\ \frac{a_n}{2s_n} & ik_R & \frac{ik_R}{2s_n\mu} & \frac{1}{2\mu} \\ -ik_R & -\frac{a_n}{2q_n} & \frac{1}{2\mu} & \frac{ik_R}{2q_n\mu} \\ -\frac{a_n}{2s_n} & ik_R & -\frac{ik_R}{2s_n\mu} & \frac{1}{2\mu} \end{bmatrix}$$

from which

$$\begin{aligned} G_n(1,1) &= \frac{1}{a_n - 2k_R^2}\left[\frac{a_n e^{s_n d_n}}{2} - \frac{k_R^2}{e^{q_n d_n}} - k_R^2 e^{q_n d_n} + \frac{a_n}{2e^{s_n d_n}}\right] \\ &= \frac{1}{a_n - 2k_R^2}\left[\frac{a_n}{2}\left(e^{s_n d_n} + \frac{1}{e^{s_n d_n}}\right) - k_R^2\left(\frac{1}{e^{q_n d_n}} + e^{q_n d_n}\right)\right] \\ &= \frac{1}{a_n - 2k_R^2}\left[a_n \cos(is_n d_n) - 2k_R^2 \cos(iq_n d_n)\right] \end{aligned}$$

$$\begin{aligned} G_n(1,2) &= \frac{k_R i}{a_n - 2k_R^2}\left[s_n e^{s_n d_n} - \frac{s_n}{e^{s_n d_n}} - \frac{a_m e^{q_n d_n}}{2q_n} + \frac{a_n}{2q_{\mathrm{m}} e^{q_n d_n}}\right] \\ &= \frac{k_R i}{a_n - 2k_R^2}\left[s_n\left(e^{s_n d_n} - \frac{1}{e^{s_n d_n}}\right) - \frac{a_n}{2q_n}\left(e^{q_n d_n} - \frac{1}{e^{q_n d_n}}\right)\right] \\ &= \frac{-k_R}{a_n - 2k_R^2}\left[-2s_n \sin(is_n d_n) + \frac{a_n}{q_n}\sin(iq_n d_n)\right] \end{aligned}$$

$$\begin{aligned} G_n(1,3) &= \frac{k_R i}{(a_n - 2k_R^2)\mu}\left[-\frac{e^{q_n d_n}}{2} - \frac{1}{2e^{q_n d_n}} + \frac{e^{s_n d_n}}{2} + \frac{1}{2e^{s_n d_n}}\right] \\ &= \frac{k_R i}{(a_n - 2k_R^2)\mu}\left[\frac{1}{2}\left(e^{s_n d_n} + \frac{1}{e^{s_n d_n}}\right) - \frac{1}{2}\left(e^{q_n d_n} + \frac{1}{e^{q_n d_n}}\right)\right] \\ &= \frac{k_R i}{(a_n - 2k_R^2)\mu}\left[\cos(is_n d_n) - \cos(iq_n d_n)\right] \end{aligned}$$

$$G_n(1,4)=\frac{1}{(a_n-2k_R^2)\mu}[\frac{s_n e^{s_n d_n}}{2}-\frac{s_n}{2e^{s_n d_n}}-\frac{k_R^2 e^{q_n d_n}}{2q_n}+\frac{k_R^2}{2q_n e^{q_n d_n}}]$$
$$=\frac{1}{(a_n-2k_R^2)\mu}\left[\frac{s_n}{2}\left(e^{s_n d_n}-\frac{1}{e^{s_n d_n}}\right)-\frac{k_R^2}{2q_n}\left(e^{q_n d_n}-\frac{1}{e^{q_n d_n}}\right)\right]$$
$$=\frac{i}{(a_n-2k_R^2)\mu}\left[-s_n\sin(is_n d_n)+\frac{k_R^2}{q_n}\sin(iq_n d_n)\right]$$

$$G_n(2,1)=\frac{k_R i}{a_n-2k_R^2}[-q_n e^{q_n d_n}+\frac{q_n}{e^{q_n d_n}}+\frac{a_n e^{s_n d_n}}{2s_n}-\frac{a_n}{2s_n e^{s_n d_n}}]$$
$$=\frac{k_R i}{a_n-2k_R^2}\left[\frac{a_n}{2s_n}\left(e^{s_n d_n}-\frac{1}{e^{s_n d_n}}\right)-q_n\left(e^{q_n d_n}-\frac{1}{e^{q_n d_n}}\right)\right]$$
$$=\frac{-k_R}{a_n-2k_R^2}\left[-\frac{a_n}{s_n}\sin(is_n d_n)+2q_n\sin(iq_n d_n)\right]$$

$$G_n(2,2)=\frac{1}{a_n-2k_R^2}[\frac{a_n e^{q_n d_n}}{2}-\frac{k_R^2}{e^{s_n d_n}}-k_R^2 e^{s_n d_n}+\frac{a_n}{2e^{q_n d_n}}]$$
$$=\frac{1}{a_n-2k_R^2}\left[-k_R^2\left(e^{s_n d_n}+\frac{1}{e^{s_n d_n}}\right)+\frac{a_n}{2}\left(e^{q_n d_n}+\frac{1}{e^{q_n d_n}}\right)\right]$$
$$=\frac{1}{a_n-2k_R^2}\left[-2k_R^2\cos(is_n d_n)+a_n\cos(iq_n d_n)\right]$$

$$G_n(2,3)=\frac{1}{a_n-2k_R^2}[\frac{q_n e^{q_n d_n}}{2\mu}-\frac{q_n}{2\mu e^{q_n d_n}}-\frac{k_R^2 e^{s_n d_n}}{2\mu s_n}+\frac{k_R^2}{2\mu s_n e^{s_n d_n}}]$$
$$=\frac{1}{a_n-2k_R^2}\left[-\frac{k_R^2}{2\mu s_n}\left(e^{s_n d_n}-\frac{1}{e^{s_n d_n}}\right)+\frac{q_n}{2\mu}\left(e^{q_n d_n}-\frac{1}{e^{q_n d_n}}\right)\right]$$
$$=\frac{i}{a_n-2k_R^2}\left[\frac{k_R^2}{\mu s_n}\sin(is_n d_n)-\frac{q_n}{\mu}\sin(iq_n d_n)\right]$$

$$G_n(3,1)=\frac{a_n\mu k_R i}{a_n-2k_R^2}[-e^{q_n d_n}-\frac{1}{e^{q_n d_n}}+e^{s_n d_n}+\frac{1}{e^{s_n d_n}}]$$
$$=\frac{a_n\mu k_R i}{a_n-2k_R^2}\left[\left(e^{s_n d_n}+\frac{1}{e^{s_n d_n}}\right)-\left(e^{q_n d_n}+\frac{1}{e^{q_n d_n}}\right)\right]$$
$$=\frac{2a_n\mu k_R i}{a_n-2k_R^2}\left[\cos(is_n d_n)-\cos(iq_n d_n)\right]$$

$$G_n(3,2)=\frac{\mu}{a_n-2k_R^2}[\frac{a_n^2e^{q_nd_n}}{2q_n}-\frac{a_n^2}{2q_ne^{q_nd_n}}-2k_R^2s_ne^{s_nd_n}+\frac{2k_R^2s_n}{e^{s_nd_n}}]$$

$$=\frac{\mu}{a_n-2k_R^2}\left[-2k_R^2s_n\left(e^{s_nd_n}-\frac{1}{e^{s_nd_n}}\right)+\frac{a_n^2}{2q_n}\left(e^{q_nd_n}-\frac{1}{e^{q_nd_n}}\right)\right]$$

$$=\frac{\mu i}{a_n-2k_R^2}\left[4k_R^2s_n\sin(is_nd_n)-\frac{a_n^2}{q_n}\sin(iq_nd_n)\right]$$

$$G_n(4,1)=\frac{\mu}{a_n-2k_R^2}[\frac{a_n^2e^{s_nd_n}}{2s_n}-\frac{a_n^2}{2s_ne^{s_nd_n}}-2k_R^2q_ne^{q_nd_n}+\frac{2k_R^2q_n}{e^{q_nd_n}}]$$

$$=\frac{\mu}{a_n-2k_R^2}\left[\frac{a_n^2}{2s_n}\left(e^{s_nd_n}-\frac{1}{e^{s_nd_n}}\right)-2k_R^2q_n\left(e^{q_nd_n}-\frac{1}{e^{q_nd_n}}\right)\right]$$

$$=\frac{\mu i}{a_n-2k_R^2}\left[-\frac{a_n^2}{s_n}\sin(is_nd_n)+4k_R^2q_n\sin(iq_nd_n)\right]$$

$$G_n(2,4)=G_n(1,3) \qquad G_n(3,3)=G_n(2,2) \qquad G_n(3,4)=G_n(1,2)$$

$$G_n(4,2)=G_n(3,1) \qquad G_n(4,3)=G_n(2,1) \qquad G_n(4,4)=G_n(1,1)$$

Equation (2.154) can be expanded as

$$\begin{bmatrix}u_n(Z_n)\\w_n(Z_n)\\\sigma_{zz,\mathrm{n}}(Z_n)\\\tau_{xz,\mathrm{n}}(Z_n)\end{bmatrix}=\begin{bmatrix}G_{11}^n & G_{12}^n & G_{13}^n & G_{14}^n\\G_{21}^n & G_{22}^n & G_{23}^n & G_{24}^n\\G_{31}^n & G_{32}^n & G_{33}^n & G_{34}^n\\G_{41}^n & G_{42}^n & G_{43}^n & G_{44}^n\end{bmatrix}\begin{bmatrix}u_n(Z_{n-1})\\w_n(Z_{n-1})\\\sigma_{zz,\mathrm{n}}(Z_{n-1})\\\tau_{xz,\mathrm{n}}(Z_{n-1})\end{bmatrix} \tag{2.155}$$

Defining the following two vectors and four sub-matrices:

$$\overline{U}_n=[u_n(z)\ \ w_n(z)]^T \qquad \overline{S}_m=[\sigma_{zz,\mathrm{n}}(z)\ \ \tau_{xz,\mathrm{n}}(z)]^T$$

$$H_{11}^n=\begin{bmatrix}G_{11}^n & G_{12}^n\\G_{21}^n & G_{22}^n\end{bmatrix} \qquad H_{12}^n=\begin{bmatrix}G_{13}^n & G_{14}^n\\G_{23}^n & G_{24}^n\end{bmatrix}$$

$$H_{21}^n=\begin{bmatrix}G_{31}^n & G_{32}^n\\G_{41}^n & G_{42}^n\end{bmatrix} \qquad H_{22}^n=\begin{bmatrix}G_{33}^n & G_{34}^n\\G_{43}^n & G_{44}^n\end{bmatrix}$$

Equation (2.155) can be written as

$$\begin{bmatrix}\overline{U}_n(Z_n)\\\overline{S}_n(Z_n)\end{bmatrix}=\begin{bmatrix}H_{11}^n & H_{12}^n\\H_{21}^n & H_{22}^n\end{bmatrix}\begin{bmatrix}\overline{U}_n(Z_{n-1})\\\overline{S}_n(Z_{n-1})\end{bmatrix} \tag{2.156}$$

Upon defining the external loadings

$$\bar{p}_n(Z_{n-1}) = \bar{S}_n(Z_{n-1}) \tag{2.157}$$

at the upper interface, and

$$\bar{p}_n(Z_n) = -\bar{S}_n(Z_n) \tag{2.158}$$

at the lower interface, Eq. (2.156) can be expressed in terms of external loads as

$$\begin{bmatrix} \bar{U}_n(Z_n) \\ -\bar{p}_n(Z_n) \end{bmatrix} = \begin{bmatrix} H_{11}^n & H_{12}^n \\ H_{21}^n & H_{22}^n \end{bmatrix} \begin{bmatrix} \bar{U}_n(Z_{n-1}) \\ \bar{p}_n(Z_{n-1}) \end{bmatrix} \tag{2.159}$$

The first equation is

$$\bar{U}_n(Z_n) = H_{11}^n \bar{U}_n(Z_{n-1}) + H_{12}^n \bar{p}_n(Z_{n-1}) \tag{2.160}$$

which gives the loading vector in terms of the displacement and stress vectors as

$$\bar{p}_n(Z_{n-1}) = \begin{bmatrix} -(H_{12}^n)^{-1} H_{11}^n & (H_{12}^n)^{-1} \end{bmatrix} \begin{bmatrix} \bar{U}_n(Z_{n-1}) \\ \bar{U}_n(Z_n) \end{bmatrix} \tag{2.161}$$

The second equation in (2.159) is

$$-\bar{p}_n(Z_n) = H_{21}^n \bar{U}_n(Z_{n-1}) + H_{22}^n \bar{p}_n(Z_{n-1}) \tag{2.162}$$

Substituting Eq. (2.161) into Eq. (2.162) gives

$$\begin{aligned} -\bar{p}_n(Z_n) &= H_{21}^n \bar{U}_n(Z_{n-1}) + H_{22}^n [-(H_{12}^n)^{-1} H_{11}^n \bar{U}_n(Z_{n-1}) + (H_{12}^n)^{-1} \bar{U}_n(Z_n)] \\ &= (H_{21}^n - H_{22}^n (H_{12}^n)^{-1} H_{11}^n) \bar{U}_n(Z_{n-1}) + H_{22}^n (H_{12}^n)^{-1} \bar{U}_n(Z_n)) \end{aligned}$$

or in matrix form,

$$\bar{p}_n(Z_n) = \begin{bmatrix} -H_{21}^n + H_{22}^n (H_{12}^n)^{-1} H_{11}^n & -H_{22}^n (H_{12}^n)^{-1} \end{bmatrix} \begin{bmatrix} \bar{U}_n(Z_{n-1}) \\ \bar{U}_n(Z_n) \end{bmatrix} \tag{2.163}$$

Assembling Eq. (2.161) and Eq. (2.163) gives the stiffness matrix relating external loadings to displacements at the layer interfaces;

$$\begin{bmatrix} \bar{p}_n(Z_{n-1}) \\ \bar{p}_n(Z_n) \end{bmatrix} = \begin{bmatrix} -(H_{12}^n)^{-1} H_{11}^n & (H_{12}^n)^{-1} \\ -H_{21}^n + H_{22}^n (H_{12}^n)^{-1} H_{11}^n & -H_{22}^n (H_{12}^n)^{-1} \end{bmatrix} \begin{bmatrix} \bar{U}_n(Z_{n-1}) \\ \bar{U}_n(Z_n) \end{bmatrix} \tag{2.164}$$

or finally,

$$\begin{bmatrix} \bar{p}_n(Z_{n-1}) \\ \bar{p}_n(Z_n) \end{bmatrix} = \begin{bmatrix} K_{11}^n & K_{12}^n \\ K_{21}^n & K_{22}^n \end{bmatrix} \begin{bmatrix} \bar{U}_n(Z_{n-1}) \\ \bar{U}_n(Z_n) \end{bmatrix} \tag{2.165}$$

where the 2×2 sub-matrices are

$$K_{11}^n = -(H_{12}^n)^{-1} H_{11}^n \qquad K_{12}^n = (H_{12}^n)^{-1}$$

$$K_{21}^n = -H_{21}^n + H_{22}^n (H_{12}^n)^{-1} H_{11}^n \qquad K_{22}^n = -H_{22}^n (H_{12}^n)^{-1}$$

For the last interface at depth Z_{N-1}, Eq. (2.88) can be used to relate the half-space potential vector to the vector of displacements and stresses:

$$S_N(Z_{N-1}) = T_N P_N(Z_{N-1}) \tag{2.166}$$

where T_N is given by Eq. (2.87), and $P_{N-1}(Z_{N-1})$ satisfying the half-space condition is given by Eq. (2.135). The above equation can therefore be written as

$$\begin{bmatrix} u_N(Z_{N-1}) \\ w_N(Z_{N-1}) \\ \sigma_{zz,N}(Z_{N-1}) \\ \tau_{xz,N}(Z_{N-1}) \end{bmatrix} = \begin{bmatrix} -ik_R & s_N & -ik_R & -s_N \\ q_N & ik_R & -q_N & ik_R \\ \mu a_N & 2i\mu k_R s_N & \mu a_N & -2i\mu k_R s_N \\ -2i\mu k_R q_N & \mu a_N & 2i\mu k_R q_N & \mu a_N \end{bmatrix} \begin{bmatrix} 0 \\ 0 \\ \Phi_N^D(Z_{N-1}) \\ \Psi_N^D(Z_{N-1}) \end{bmatrix} \tag{2.167}$$

Defining the following three vectors and two sub-matrices:

$$\bar{U}_N(Z_{N-1}) = [u_N(Z_{N-1}) \;\; w_N(Z_{N-1})]^T$$

$$\bar{S}_N(Z_{N-1}) = [\sigma_{zz,N}(Z_{N-1}) \;\; \tau_{xz,N}(Z_{N-1})]^T \qquad H_{12}^N = \begin{bmatrix} T_{13}^N & T_{14}^N \\ T_{23}^N & T_{24}^N \end{bmatrix} \qquad H_{22}^N = \begin{bmatrix} T_{33}^N & T_{34}^N \\ T_{43}^N & T_{44}^N \end{bmatrix}$$

$$\bar{Q}_N(Z_{N-1}) = [\Phi_N^D(Z_{N-1}) \;\; \Psi_N^D(Z_{N-1})]^T$$

and eliminating zero components in Eq. (2.167) gives

$$\begin{bmatrix} \bar{U}_N(Z_{N-1}) \\ \bar{S}_N(Z_{N-1}) \end{bmatrix} = \begin{bmatrix} H_{12}^N \\ H_{22}^N \end{bmatrix} \bar{Q}_N(Z_{N-1}) \tag{2.168}$$

from which the potential vector can be expressed in terms of the displacement vector and stress vector, respectively, as

$$\bar{Q}_N(Z_{N-1}) = (H_{12}^N)^{-1} \bar{U}_N(Z_{N-1}) \tag{2.169}$$

$$\overline{Q}_N(Z_{N-1}) = (H_{22}^N)^{-1}\overline{S}_N(Z_{N-1}) \tag{2.170}$$

The above two equations can be combined to eliminate the potential vector, giving the stress vector in terms of the displacement vector as

$$\overline{S}_N(Z_{N-1}) = H_{22}^N(H_{12}^N)^{-1}\overline{U}_N(Z_{N-1}) \tag{2.171}$$

Defining the external loading $\overline{p}_N(Z_{N-1}) = \overline{S}_N(Z_{N-1})$ at the Z_{N-1} interface, Eq. (2.171) can be rewritten in stiffness-matrix form as

$$\overline{p}_N(Z_{N-1}) = K^N\overline{U}_N(Z_{N-1}) \tag{2.172}$$

where

$$K^N = H_{22}^N(H_{12}^N)^{-1} \tag{2.173}$$

By combining Eqs. (2.165) and (2.172), the $2(N\text{-}1)\times 2(N\text{-}1)$ global stiffness matrix for the entire layered structure can be assembled as $\boldsymbol{p} = K\boldsymbol{u}$, where

$$K = \begin{bmatrix}
K_{11}^1 & K_{12}^1 & 0 & 0 & 0 & 0 & 0 & 0 \\
K_{21}^1 & K_{22}^1 + K_{11}^2 & K_{12}^2 & 0 & 0 & 0 & 0 & 0 \\
0 & K_{21}^2 & K_{22}^2 + K_{11}^3 & K_{12}^3 & 0 & 0 & 0 & 0 \\
0 & 0 & K_{21}^3 & K_{22}^3 + K_{11}^4 & K_{12}^4 & 0 & 0 & 0 \\
0 & 0 & 0 & \ddots & \ddots & \ddots & 0 & 0 \\
0 & 0 & 0 & 0 & K_{21}^{N-3} & K_{22}^{N-3} + K_{11}^{N-2} & K_{12}^{N-2} & 0 \\
0 & 0 & 0 & 0 & 0 & K_{21}^{N-2} & K_{22}^{N-2} + K_{11}^{N-1} & K_{12}^{N-1} \\
0 & 0 & 0 & 0 & 0 & 0 & K_{21}^{N-1} & K_{22}^{N-1} + K^N
\end{bmatrix} \tag{2.174}$$

and the global vector of external loads applied at the layer interfaces is

$$\boldsymbol{p} = [\,p_0 \quad p_1 \quad \cdots \quad p_{N-1}\,]^T$$

where superposition of the interfacial loads from the layers above and below gives the total resultant load vector at each layer interface, i.e.

$$p_0 = \overline{p}_1(Z_0) \quad \text{for interface} \quad n = 0$$
$$p_n = \overline{p}_n(Z_n) + \overline{p}_{n+1}(Z_n) \quad \text{for interfaces} \quad 1 \le n \le N-1$$

For the case of vertical loading $\sigma_{zz} = p_{0v}$ at the free surface as in seismic surface wave testing, the first 2×1 vector element in the global loading vector is

$$p_0 = \bar{p}_1(Z_0) = \bar{S}_1(Z_0) = [\sigma_{zz}(0) \quad \tau_{xz}(0)]^T = [p_{0v} \quad 0]^T$$

while all other elements are zero:

$$\begin{aligned} p_n = \bar{p}_n(Z_n) + \bar{p}_{n+1}(Z_n) &= -\bar{S}_n(Z_n) + \bar{S}_{n+1}(Z_n) \\ &= -\bar{S}_n(Z_n) + \bar{S}_n(Z_n) = [0 \quad 0]^T, \qquad 1 \le n \le N-1 \end{aligned}$$

in which continuity of stresses at the interfaces was invoked in the next to last step. Therefore, for analyzing surface wave tests in which vertical loads are applied only at the surface, the global stiffness matrix for the entire soil model is

$$\begin{bmatrix} p_0 \\ \hline 0 \\ 0 \\ 0 \\ \vdots \\ 0 \\ 0 \\ 0 \end{bmatrix} = \left[\begin{array}{c|cccccccccc} K_{11}^1 & K_{12}^1 & & & & & & & & \\ K_{21}^1 & K_{22}^1 + K_{11}^2 & K_{12}^2 & & & & & & & \\ & K_{21}^2 & K_{22}^2 + K_{11}^3 & K_{12}^3 & & & & & & \\ & & K_{21}^3 & K_{22}^3 + K_{11}^4 & \ddots & & & & & \\ & & & \ddots & \ddots & \ddots & & & & \\ & & & & & K_{21}^{N-3} & K_{22}^{N-3} + K_{11}^{N-2} & K_{12}^{N-2} & & \\ & & & & & & K_{21}^{N-2} & K_{22}^{N-2} + K_{11}^{N-1} & K_{12}^{N-1} & \\ & & & & & & & K_{21}^{N-1} & K_{22}^{N-1} + K^N & \end{array}\right] \begin{bmatrix} u_0 \\ \hline u_1 \\ u_2 \\ u_3 \\ u_4 \\ \vdots \\ u_{N-4} \\ u_{N-3} \\ u_{N-2} \\ u_{N-1} \end{bmatrix}$$

where $p_0 = [p_{0v} \quad 0]^T$ and $u_n = \bar{U}_{n+1}(Z_n) = [u_{n+1}(Z_n) \quad w_{n+1}(Z_n)]^T$. Dividing the above into sub-matrices as indicated by the dashed lines gives

$$\begin{bmatrix} p_0 \\ \boldsymbol{0} \end{bmatrix} = \begin{bmatrix} \mathcal{K}_{11} & \mathcal{K}_{12} \\ \mathcal{K}_{21} & \mathcal{K}_{22} \end{bmatrix} \begin{bmatrix} u_0 \\ \boldsymbol{u} \end{bmatrix} \tag{2.175}$$

The propagation of a plane Rayleigh wave in semi-infinite layered media means that displacements can exist without loading at the free surface nor incoming waves from the half-space. Thus, the solution for Rayleigh waves must satisfy $K\boldsymbol{u} = \boldsymbol{0}$, and the characteristic (dispersion) function is therefore

$$\Delta(\omega, k) = |K| = 0 \tag{2.176}$$

2.5.3.2. Case 2: Degeneration of solution for a layered, free plate

If the bottom layer above the half-space is also considered traction-free on its bottom (i.e., the half-space is a vacuum), the layered system becomes a free plate. The stiffness matrix for the entire layered structure will then be the same as in Eq. (2.174), but with $K^N = 0$

$$K = \begin{bmatrix} K_{11}^1 & K_{12}^1 & 0 & 0 & 0 & 0 & 0 \\ K_{21}^1 & K_{22}^1 + K_{11}^2 & K_{12}^2 & 0 & 0 & 0 & 0 \\ 0 & K_{21}^2 & K_{22}^2 + K_{11}^3 & K_{12}^3 & 0 & 0 & 0 \\ 0 & 0 & K_{21}^3 & K_{22}^3 + K_{11}^4 & K_{12}^4 & 0 & 0 \\ 0 & 0 & 0 & \ddots & \ddots & \ddots & 0 \\ 0 & 0 & 0 & 0 & K_{21}^{N-2} & K_{22}^{N-2} + K_{11}^{N-1} & K_{12}^{N-1} \\ 0 & 0 & 0 & 0 & 0 & K_{21}^{N-1} & K_{22}^{N-1} \end{bmatrix} \quad (2.177)$$

2.6. Matrix Modeling Theoretical Dispersion Curves

Numerical solutions can be obtained for any of the matrix methods presented in the preceding sections to yield theoretical dispersion curves for a layered structure having known properties. This procedure is referred to as the forward analysis. In searching for the roots to the characteristic dispersion equations, four main solution techniques are typically used. These include the bisection searching technique (Nazarian 1984), two dimensional searching technique (Lowe 1995), smallest absolute determinant (Supranata 2006), and phase-velocity scanning technique (Ryden and Park 2006).

The bisection searching technique attempts to find an appropriate pair of ω and *k* (real wavenumber) to make the real part of the determinant in the characteristic function equal to zero. Because the imaginary part of the determinant is typically very small compared to the real part, the imaginary part can usually be neglected without an

appreciable loss of accuracy. The two dimensional searching technique attempts to find an appropriate pair of ω and *k* (complex wavenumber) to make both the real and imaginary parts of the determinant in the characteristic function equal to zero. When the imaginary part is significant, two dimensional searching is needed to find the complex wavenumber root, which accounts for energy loss through attenuation and/or leaky wave modes. The solution of the characteristic function can also be determined by searching for the smallest absolute determinant in place of the zero determinant. Application of the phase-velocity scanning technique for calculating theoretical dispersion curves can avoid the need for time-consuming two-dimensional searches and some associated numerical instabilities.

2.6.1. Zero determinant: bisection searching technique for real wavenumber

It is generally not possible to find the roots of the dispersion function analytically, as it contains many complicated functions of two independent variables. Therefore, one common solution technique is to fix the value of one variable and use mathematical optimization methods to solve for the value of the other variable numerically. If the frequency ω is fixed, one dimensional searching techniques can be used to solve for values of wavenumber *k* (roots) which satisfy the dispersion function $\Delta(\omega,k)=0$. During this solution process, the dispersion function may be complex-valued for some combinations of ω and *k*, with no real-valued solutions for ω and *k* values satisfying the complex-valued $\Delta(\omega,k)$. In such cases, only the real part of the dispersion function is considered to obtain a dispersion curve over the frequency range of interest. As the Rayleigh wave velocity is related to wavenumber and frequency through $V_R=\omega/k_R$, the

dispersion relationship between frequency and phase velocity can be built by repeating the above search over a range of wavenumbers.

For a given frequency, there can be multiple roots for wavenumber *k*, in which case the corresponding phase velocities correspond to multiple modes. The lowest velocity corresponds to the fundamental mode (M0) and each of the next higher velocities correspond to the next higher modes (first higher mode M1, second higher mode M2, etc.). An example of multi-mode theoretical dispersion curves in shown in Figure 2.20 in both the frequency-phase velocity and frequency-wavenumber domains. The real and imaginary components of the corresponding dispersion function at 15 Hz are shown for a searched range of wavenumbers in Figure 2.21, illustrating that the range of the real part is significantly larger than that of the imaginary part. The variation of the real part with wavenumber is illustrated in Figure 2.22, showing two wavenumber roots where the sign changes at k_1=0.207 rad/m and k_2=0.148 rad/m. These two wavenumbers can be seen in the dispersion curves of Figure 2.20b at a frequency of 15 Hz for modes M0 and M1, with the corresponding phase velocities $V_{R1} = \omega / k_1 = 455$ m/s and $V_{R2} = \omega / k_2 = 637$ m/s apparent in Figure 2.20a.

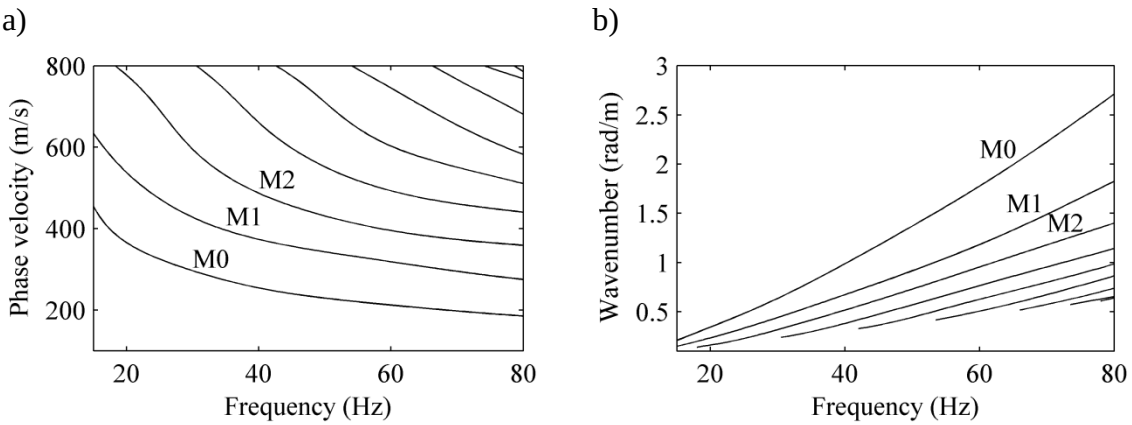

Figure 2.20 Multi-mode dispersion curves in a) frequency and phase-velocity domain, b) frequency and wavenumber domain

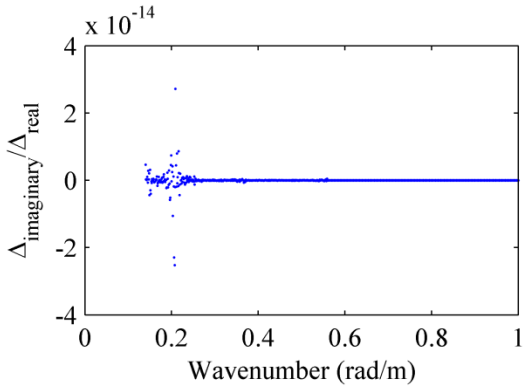

Figure 2.21 Real and imaginary parts of dispersion function for a search range of wavenumber.

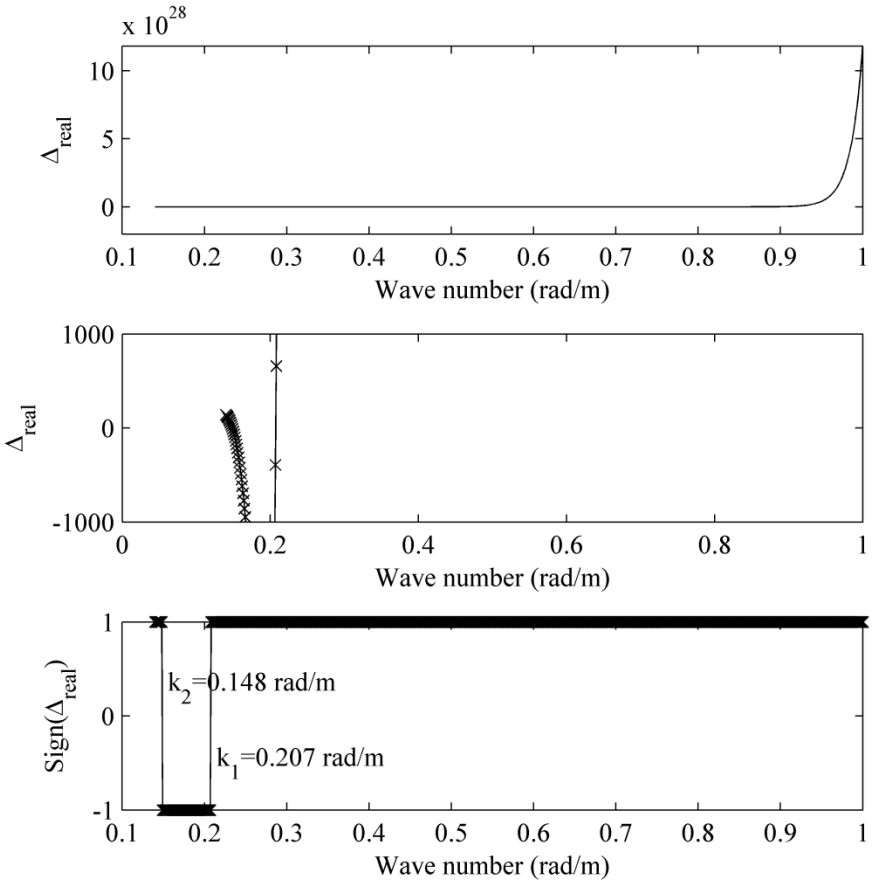

Figure 2.22 Variation of real part of dispersion function with wavenumber at frequency of 15 Hz. (a): full range plot, (b): close-up showing zero crossings, (c): normalized real part $\mathrm{Re}(\Delta)/|\mathrm{Re}(\Delta)| = Sign(\Delta_{real})$ indicating two wavenumber roots $\mathrm{Re}(\Delta) = 0$ where sign changes.

2.6.2. Zero determinant: two dimensional searching technique for complex wavenumber

Lowe (1995) proposed a two dimensional searching technique that fixes one real variable (frequency or real wavenumber) and solves for the remaining real variable and the imaginary wavenumber. The solution can be found by iteratively locating the minimum of the absolute value of the characteristic function, alternately varying one of the unknowns and holding the others constant, as illustrated in Figure 2.23. The search starts with a sweep of frequency at a fixed imaginary wavenumber, for which a minimum of the absolute value of the function is found at point A. The frequency is then fixed and the imaginary wavenumber is varied to find a new minimum at point B. Alternating searches over frequency and imaginary wavenumber are continued to find a minimum which is acceptably close to the origin and makes both parts of the characteristic function close to zero.

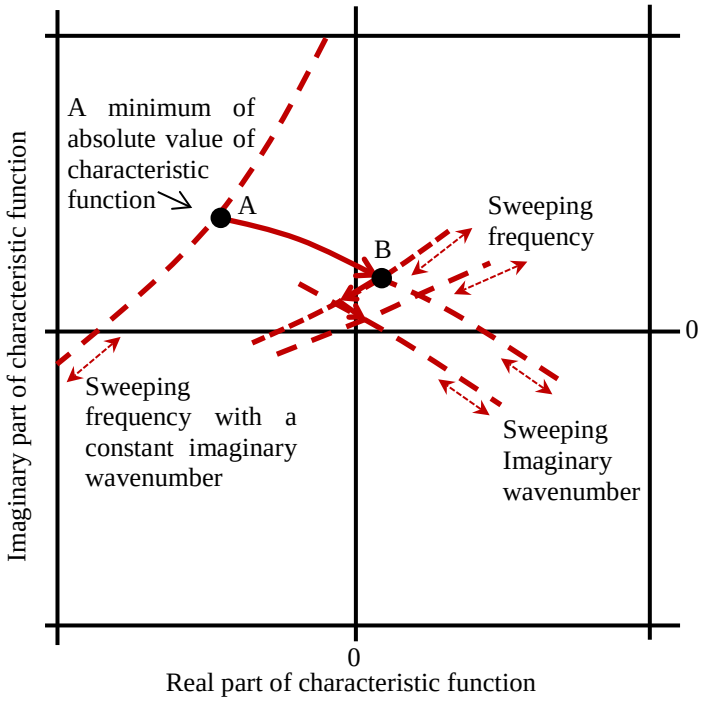

Figure 2.23 Two dimensional search technique (after Lowe, 1995).

2.6.3. Smallest absolute determinant technique

Supranata (2006) argued that the determinant is not a good measure of singularity of a matrix, because it can be difficult to compute accurately as its value tends to be very small or very large. He proposed that the singularity of a matrix can better be characterized by its minimum absolute eigenvalue. Figure 2.24 shows an example of the variation of absolute eigenvalues with wave velocities for a theoretical soil model, for which the local minimum values correspond to the roots of the characteristic dispersion function. In Supranata's work, the use of the determinant for the theoretical soil model produced errors in the roots resulting in incorrect dispersion functions. However, the determinant was used for the characteristic function in this study to calculate the dispersion curves for the same soil model, resulting in duplication of Supranata's "correct" dispersion curves. The incorrect curves could not be duplicated using the determinant. Therefore, the minimum absolute eigenvalue method was not studied further.

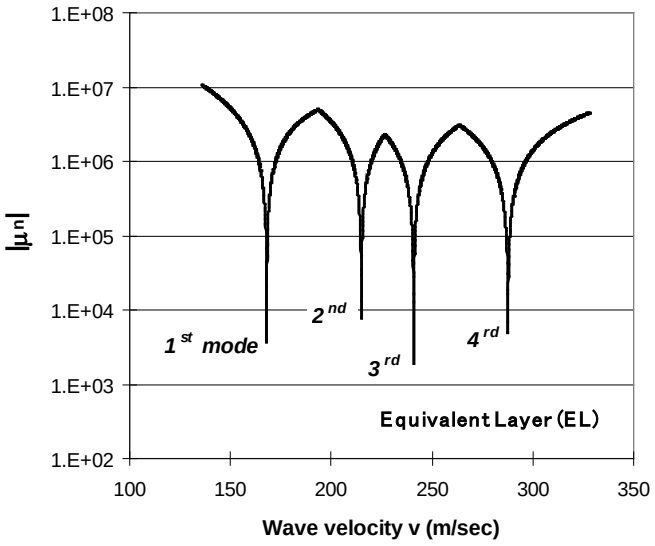

Figure 2.24 Multi-mode dispersion image characterized by minimum absolute eigenvalues. (from Supranata 2006)

2.6.4. Phase-velocity scanning technique

The phase-velocity scanning technique was originally introduced in Park et al. (1998) as a wavefield transformation method for processing multichannel field seismograph records. Ryden and Park (2006) combined the phase-velocity scanning technique with fast Fourier transforms and Hankel transforms to obtain theoretical dispersion images without the need for computationally intensive and time-consuming searches and their associated numerical instabilities. The phase-velocity scanning technique for constructing experimental dispersion images from actual and simulated field data will be detailed in Chapter 3. A brief overview of its application to theoretical dispersion images is presented below.

The static condensation method can be used to solve the partitioned stiffness matrix equation given in Eq. (2.175):

$$\begin{bmatrix} \boldsymbol{p}_0 \\ \boldsymbol{0} \end{bmatrix} = \begin{bmatrix} \boldsymbol{K}_{11} & \boldsymbol{K}_{12} \\ \boldsymbol{K}_{21} & \boldsymbol{K}_{22} \end{bmatrix} \begin{bmatrix} \boldsymbol{u}_0 \\ \boldsymbol{u} \end{bmatrix}$$

The first sub-equation is

$$\boldsymbol{K}_{11}\boldsymbol{u}_0 + \boldsymbol{K}_{12}\boldsymbol{u} = \boldsymbol{p}_0 \tag{2.178}$$

and the second equation is

$$\boldsymbol{K}_{21}\boldsymbol{u}_0 + \boldsymbol{K}_{22}\boldsymbol{u} = \boldsymbol{0} \tag{2.179}$$

From the second equation, the displacement below the ground surface can be expressed in terms of the displacement on the ground surface as

$$\boldsymbol{u} = -\boldsymbol{K}_{22}^{-1}\boldsymbol{K}_{21}\boldsymbol{u}_0 \tag{2.180}$$

Substituting Eq. (2.180) into Eq. (2.178) gives

$$(\boldsymbol{K}_{11} - \boldsymbol{K}_{12}\boldsymbol{K}_{22}^{-1}\boldsymbol{K}_{21})\boldsymbol{u}_0 = \boldsymbol{p}_0 \tag{2.181}$$

from which the displacement on the ground surface is

$$\boldsymbol{u_0} = (\boldsymbol{K_{11}} - \boldsymbol{K_{12}}\boldsymbol{K_{22}^{-1}}\boldsymbol{K_{21}})^{-1}\,\boldsymbol{p_0} \tag{2.182}$$

Substituting Eq. (2.182) into Eq. (2.180) then gives the displacement at the internal layer interfaces:

$$\boldsymbol{u} = -\boldsymbol{K_{22}^{-1}}\boldsymbol{K_{21}}(\boldsymbol{K_{11}} - \boldsymbol{K_{12}}\boldsymbol{K_{22}^{-1}}\boldsymbol{K_{21}})^{-1}\,\boldsymbol{p_0} \tag{2.183}$$

Combining Eqs. (2.182) and (2.183) gives the interfacial displacements for the entire model:

$$\begin{aligned}\tilde{u}(k,\omega_n) &= [\boldsymbol{u_0} \quad \boldsymbol{u}]^T \\ &= \begin{bmatrix} (\boldsymbol{K_{11}} - \boldsymbol{K_{12}}\boldsymbol{K_{22}^{-1}}\boldsymbol{K_{21}})^{-1} \\ -\boldsymbol{K_{22}^{-1}}\boldsymbol{K_{21}}(\boldsymbol{K_{11}} - \boldsymbol{K_{12}}\boldsymbol{K_{22}^{-1}}\boldsymbol{K_{21}})^{-1} \end{bmatrix}\boldsymbol{p_0}\end{aligned} \tag{2.184}$$

For surface wave testing with vertical impacts at the soil surface, the applied loading can be mathematically approximated as uniform, axisymmetric and vertical with intensity P_0 and radius R_0. The load can then be transformed from the time-spatial domain ($p(r,t)$) to the frequency-spatial domain ($p(r,\omega_n)$) using the Fourier transform (see Appendix):

$$p(r,\omega_n) = \int_{-\infty}^{\infty} p(r,t)e^{-i\omega_n t}dt \tag{2.185}$$

The Hankel transform can then be used to transform from the spatial domain to the wavenumber domain (see Appendix):

$$p(k,\omega_n) = -\int_0^{\infty} p(r,\omega_n)J_0(kr)rdr \tag{2.186}$$

where J_0 is the Bessel function of the first kind of order 0. Using the following fundamental property of Bessel functions (Wylie and Barrett 1982, p. 592):

$$\int_0^{x_1} J_0(x)xdx = x_1 J_1(x_1) \tag{2.187}$$

for the loading with uniform intensity and uniform spectral content $p(r,\omega_n) = P_0$ and radius $r = R_0$, the integral of Eq.(2.186) can be evaluated as:

$$\begin{aligned} p(k,\omega_n) &= -\int_0^{\infty} p(r,\omega_n) J_0(kr) r dr \\ &= -\frac{1}{k^2}\int_0^{R_0} P_0 J_0(kr)(kr) d(kr) \\ &= -\frac{P_0}{k^2} kR_0 J_1(kR_0) \\ &= -\frac{P_0 R_0}{k} J_1(kR_0) \end{aligned} \tag{2.188}$$

The above equation shows that the loading in the frequency-wavenumber domain has uniform frequency content, and varies with wavenumber according to the Bessel function of the first kind of order 1. If the impact loading is only in the vertical direction, the loading vector at the surface $\boldsymbol{p_0}$ becomes

$$\boldsymbol{p_0} = [-\frac{P_0 R_0}{k} J_1(kR_0) \quad 0]^T \tag{2.189}$$

For propagation of Rayleigh waves, the free surface outside of the small loading area has zero stress:

$$\overline{S}_1(Z_0) = [0 \quad 0]^T \tag{2.190}$$

The resultant of the applied load and zero stress is therefore

$$\overline{p}_1(Z_0) = \boldsymbol{p_0} + \overline{S}_1(Z_0) = [-\frac{P_0 R_0}{k} J_1(kR_0) \quad 0]^T \tag{2.191}$$

Denoting the displacement on the ground surface due to a unit vertical loading in Eq. (2.184) as $\boldsymbol{u_0} = [\tilde{u}_0 \;\; \tilde{w}_0]^T$, the total vertical displacement at the surface under the action of the loading $\boldsymbol{p_0}$ can be expressed as

$$w_{0t} = -\frac{P_0 R_0}{k} J_1(kR_0)\tilde{w}_0 \tag{2.192}$$

The inverse Hankel transform can then be used to transform the displacements from the wavenumber domain back to the spatial domain:

$$
\begin{aligned}
U(r,\omega_n) &= \int_0^\infty w_{0t} k J_0(kr) dk \\
&= \int_0^\infty \left[-\frac{P_0 R_0}{k} J_1(kR_0) \tilde{w}_0 \right] k J_0(kr) dk \\
&= -P_0 R_0 \int_0^\infty J_1(kR_0) J_0(kr)) \tilde{w}_0 dk
\end{aligned}
\tag{2.193}
$$

In the phase-velocity scanning method (Park 1998), the above displacements at different offsets (r) are normalized by their maximum values, which discards the amplitude (i.e., attenuation) information but preserves phase information. The normalized displacements are denoted as

$$
\bar{U}(r,\omega_n) = \frac{U(r,\omega_n)}{\max(U(r,\omega_n))} \tag{2.194}
$$

The phase-velocity scanning procedure then transforms the normalized displacement in the spatial-frequency domain to spectral values in the phase velocity-frequency domain:

$$
\bar{A}_f(V_{ph}) = \bar{A}(V_{ph},\omega_n) = \int_0^\infty \bar{U}(r,\omega_n) e^{-i\omega r/V_{ph}} dr \tag{2.195}
$$

where the subscript f denotes the summed (integrated) amplitude $\bar{A}_f(V_{ph})$ at the specific frequency $\omega_n = 2\pi f$ for a trial value of scanning phase velocity V_{ph}. For theoretical dispersion calculations, the integral in the above equation can be performed numerically with r being a continuous variable. For actual field data with a finite number of sensor offsets, the integral is replaced with a summation over the discrete receiver offsets r_n, hence the term "summed amplitude".

For the same fixed frequency, varying the scanning phase-velocity in Eq. (2.195) gives different spectral values of summed amplitude. The spectral values are then also normalized by their maximum values as

$$
\bar{\bar{A}}_f(V_{ph}) = \frac{\left|\bar{A}_f(V_{ph})\right|}{\max(\left|\bar{A}_f(V_{ph})\right|)} \tag{2.196}
$$

The procedures of Eqs. (2.193)–(2.196) are then repeated for other frequencies of interest, and the normalized summed amplitudes $\overline{\overline{A}}_f(V_{ph})$ are plotted as color contour surfaces in the frequency vs. phase-velocity domain (referred to as dispersion images), the peaks of which correspond to the multi-mode dispersion curves.

2.7. Finite Element Modeling of Surface-wave Testing on a Half-space Media

Although the matrix methods presented above can be used to model theoretical dispersion behavior of plane Rayleigh wave propagation, they cannot account for complex wave propagation phenomena in real-world situations, including 3D wave propagation, near/far field effects, cylindrical wave fronts, non-horizontal interfaces, and anomalies. To overcome such challenges for Rayleigh wave modeling, the finite element method was employed in this study to simulate surface-wave testing on a layered half-space. Simulation of the half-space boundary (radiation) conditions by the finite element method requires specific strategies, such as infinite elements (Motamed et al. 2009), the perfectly matched layer (PML) technique (Berenger 1994, Drozdz 2008), or the absorbing layers using increasing damping (ALID) technique (Liu and Jerry 2003, Drozdz 2008).

The infinite element technique can only handle incident waves that meet the Sommerfeld radiation condition (e.g., Drozdz 2008). FEM simulation of a transient impact on the traction-free surface does not meet this requirement, and causes noticeable reflected energy from the infinite element boundary (Drozdz 2008). Therefore, the infinite element technique is not suitable for modeling complex wave propagation in surface-wave testing of 2D/3D media, although it is a readily available modeling tool in

some commercial FE programs. For example, Abaqus offers the infinite element CINPE4 for plane strain.

The PML method is limited to the frequency domain using implicit solvers, and an inverse Fourier transform is needed to recover the time domain signal. Although PML requires a smaller model size than ALID, it is reported that simulation using PML in COMSOL is not more efficient than using ALID in ABAQUS (Drozdz 2008).

The ALID method is implemented by simply surrounding the region of interest by additional material zones which have damping values that gradually increase with distance. The method is reported to have several advantages. First, users have the convenience of using ALID without any complex derivation and extra theory (Liu and Jerry 2003, Drozdz 2008, Bian et al. 2012). Second, users have a wide range of choices to simulate Rayleigh damping and/or recover time domain signals (Liu and Jerry 2003, Drozdz 2008, Bian et al. 2012). Third, users have the flexibility of implementing ALID in any available FE software for any 2D/3D complex model (Drozdz 2008, Bian et al. 2012). Fourth, an explicit solver can be used (e.g., the central difference algorithm in ABAQUS) to simulate large models with greater speed and memory efficiency than an implicit solver when time domain results are needed (Drozdz 2008). Results of benchmark tests and surface wave test simulations using the ALID technique are presented in the following sections.

2.7.1 FEM simulation of a homogeneous half-space with ALID

To absorb energy and minimize unwanted reflections from artificial bottom and side boundaries of a finite-sized soil model, the ALID method was employed using the finite element program Abaqus 6.10-1 to simulate surface wave testing on a half-space.

The FEM model was axisymmetric and a vertical transient point impact was applied on the soil's top surface along the axis of symmetry, as denoted by the red arrow in the figure. Analyses were performed using three different damping scenarios within a 10-meter wide extended region consisting of ten one-meter wide sub-regions surrounding the region of study (Figure 2.25). The three damping scenarios in the extended region employed different Rayleigh damping ratios and are referred to as uniformly slightly damped, uniformly moderately damped, and gradually damped (ALID) cases, as detailed in Table 2.1. Rigid boundary conditions were applied outside the extended region, which normally causes incoming waves to be reflected, thus violating the half-space radiation condition. An example of the wave propagation simulation for the gradually damped model is shown in Figure 2.26, illustrating the high resolution of the study.

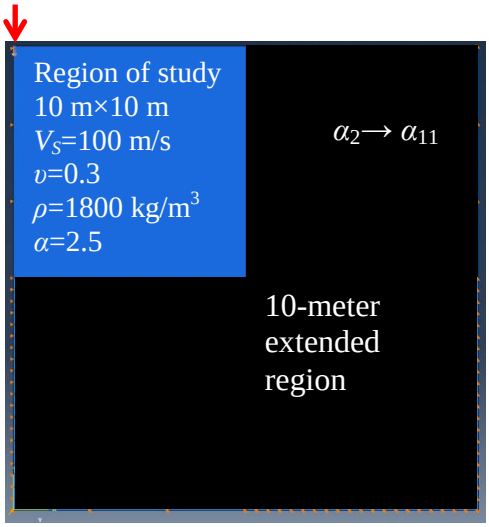

Figure 2.25 Axisymmetric FEM soil model with ALID extended region.

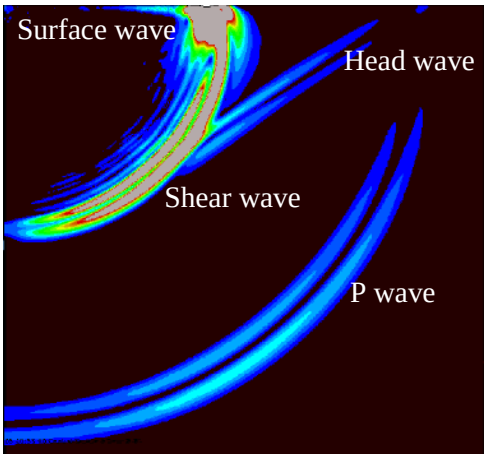

Figure 2.26 Wave propagating in the FEM model. Wavefront shown is von Mises stress.

Table 2.1 Rayleigh damping coefficients for soil model using three damping scenarios.

Treatment	Rayleigh damping coefficient, α (Damping ratio= α/2ω)										
	Region of study	Extended region (1-meter wide zones)									
Slightly damped	2.5	2.5	2.5	2.5	2.5	2.5	2.5	2.5	2.5	2.5	2.5
Moderately damped	2.5	100	100	100	100	100	100	100	100	100	100
Gradually damped	2.5	4	8	16	32	64	128	256	512	1024	2048

The impact was imposed by specifying a step-function for nodal velocity over a patch, which was found to help minimize high-frequency problems caused by suddenly applied nodal forces. Surface velocity results of the FEM analysis indicate that the ALID technique is able to simulate the half space boundary condition reasonably well, by using a gradually damped region to absorb energy and minimize the reflection of waves from the artificial boundary (Figure 2.27 and Figure 2.28). Specifically, the vertical velocity on the soil surface at a distance of 9 m from the impact shows arrivals of P and S-waves, followed by R-wave arrivals near the expected time of 0.0971 s calculated using a Rayleigh-wave phase velocity of 92.7 m/s determined using the velocity ratio V_R/V_S=0.927 from Figure 2.14. Reflections from the rigid boundaries are clearly evident for the slightly damped case (Figure 2.27). The reflections are greatly reduced but still evident for the moderately damped case, and effectively removed for the gradually damped case. Figure 2.28 also indicates that the gradually damped boundary results in less artificial attenuation of motion than a moderately damped boundary region, thus reducing the sharp contrast in particle-velocity attenuation rate at the interface of the two regions. Figure 2.29 illustrates results of a parametric study of the problem domain size, indicating little change in response when the absorbing boundaries are moved further

away from the impact point by increasing the area of study from $(10\ m)^2$ to $(20\ m)^2$ with a 10-meter wide extended region outside.

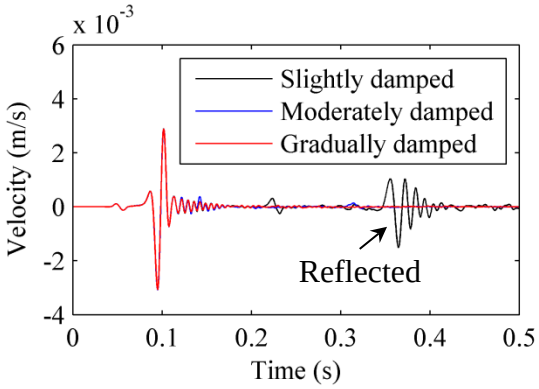

Figure 2.27 Vertical velocity on soil surface 9 meters away from impact source.

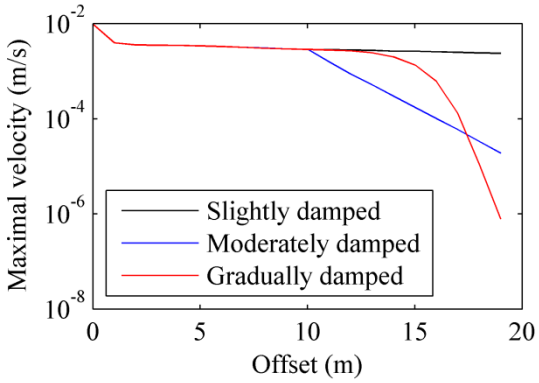

Figure 2.28 Attenuation of velocity motion.

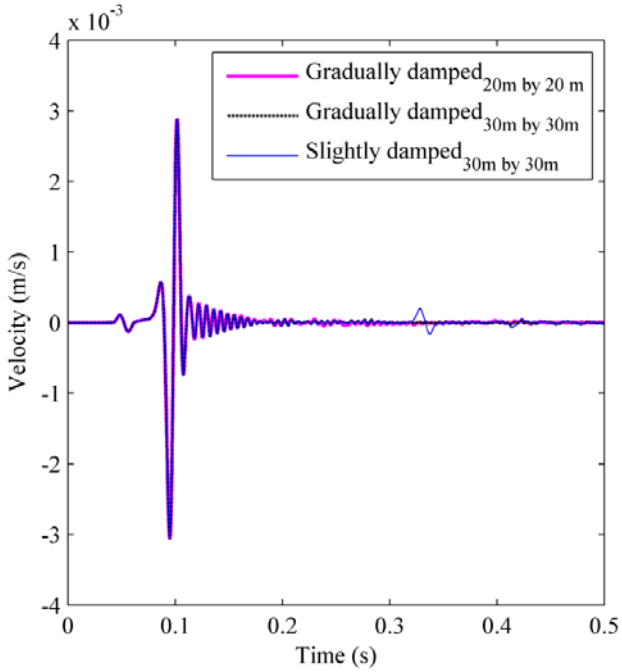

Figure 2.29 Effect of increasing the size of the region of study.

The normalized velocity traces in the offset-time domain and corresponding simulated experimental dispersion images are shown in Figure 2.30 for the three damping scenarios. Since the medium is homogeneous and therefore non-dispersive, the dispersion images exhibit a constant phase velocity with frequency. The slightly damped case shows

significant reflections from the rigid boundary (Figure 2.30a), causing its dispersion image to suffer significant aliasing (Figure 2.30b). The moderately and gradually damped cases have no noticeable reflection waves (Figures 2.30c and e); and both dispersion images become clearer and smoother with reduced aliasing, especially for the gradually damped case (Figures 2.30d and f).

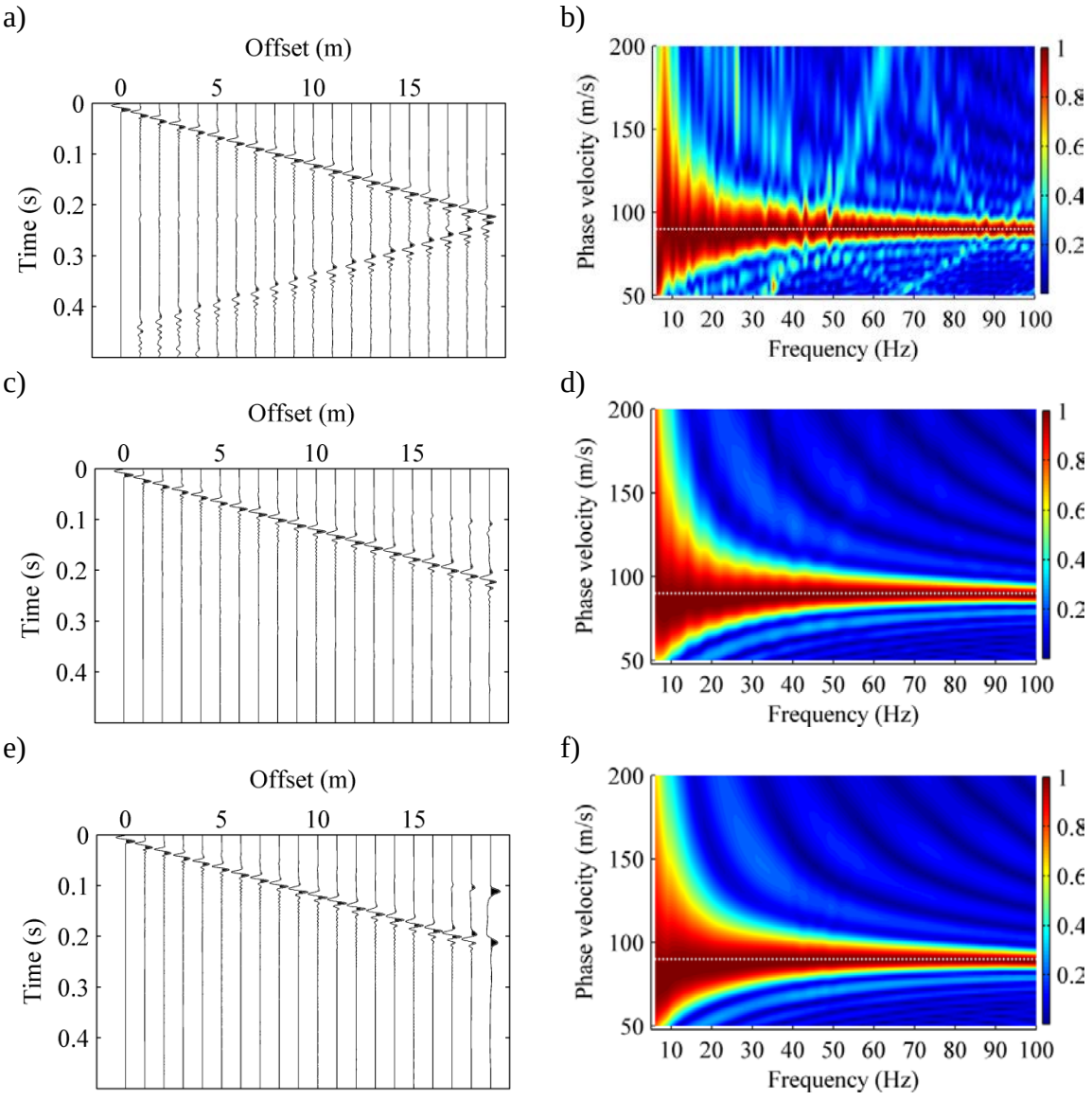

Figure 2.30 Normalized vertical surface velocity traces and corresponding dispersion images: a) and b) slightly damped, c) and d) moderately damped, e) and f) gradually damped. Theoretical dispersion "curves" shown as white dots.

2.7.2 Simulation of surface wave test on a layered soil system using FEM with ALID

The ALID method was applied using the finite element program Abaqus 6.10-1 to simulate surface wave testing on the layered medium defined in Table 2.2. A vertical transient impact was applied on the top of the FE model along the axis of symmetry, as indicated by the red arrow in Figure 2.31. Vertical velocity was monitored along the free surface at 24 "geophone" locations having a horizontal spacing of 1 m and first offset of 2 m. To model half-space radiation conditions, ALID with Rayleigh damping coefficients for the gradually damped case of Table 2.1 were used on the right lateral boundary as well as underneath the bottom layer. The extents of the entire model were 160 m by 40 m, including a 10-meter wide extended region on the right side and bottom. The normalized vertical velocity signals at the geophone stations are plotted in Figure 2.32a to form multichannel records, from which dispersion data were calculated using the phase-velocity intercept-time scanning method introduced in Chapter 3, resulting in the images of dispersion curves shown in Figure 2.32b. The results show that the FEM simulation with the ALID region results in a clear dispersion image that is sharp and smooth, with minimal aliasing.

Table 2.2 Parameters of layered soil model.

Layer #	V_S (m/s)	Poisson's ratio, ν	Density, ρ (kg/m^3)	Layer thickness, h (m)
1	150	0.30	1800	2
2	200	0.30	1800	3
3	400	0.30	1900	∞ (half space)

Figure 2.31 FEM simulation of MASW test on layered soil model of Table 2.2 with damping in extended region from gradually damped case of Table 2.1. Wavefront shown is von Mises stress.

a) b)

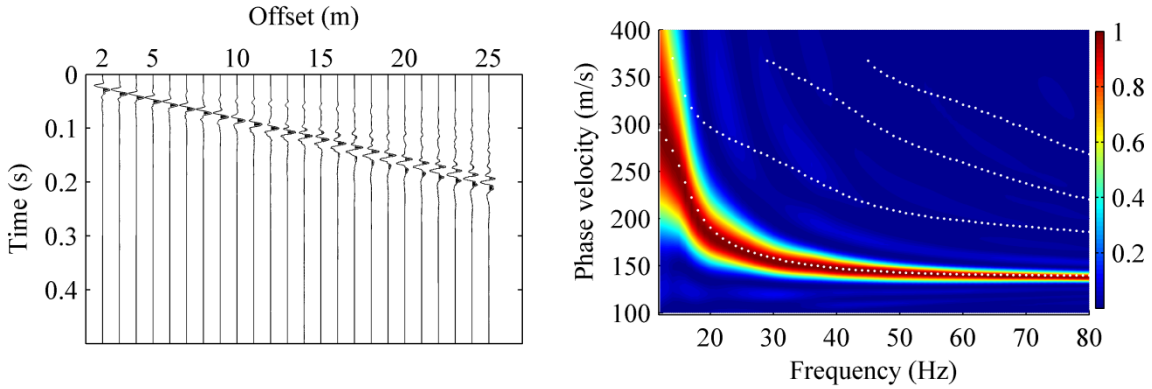

Figure 2.32 a) Normalized velocity traces from FEM simulation; b) simulated experimental dispersion image (FEM results in color contour) vs. theoretical dispersion curves (transfer matrix results in white dots).

2.8. Conclusions

This chapter provided a theoretical background on surface wave propagation in homogenous and layered media. The transfer matrix, global matrix, and stiffness matrix methods for calculating theoretical dispersion curves and displacements of ideal layered soil systems possessing uniform horizontal layers were detailed. Numerical issues in solving for roots of the characteristic dispersion functions were highlighted, and the effectiveness of the ALID method for FEM simulation of wave propagation in more general semi-infinite layered media types was demonstrated. The FEM simulation results

indicate that the ALID can simulate the half-space boundary well by using gradually increasing damping to absorb incident energy. The FEM models including the extended damping regions are of reasonable size, enabling acceptable computation times. The energy of reflected waves from the ALID extended region is much smaller than that of the surface waves, and the simulated dispersion images are therefore very smooth and clear with minimal aliasing. As will be examined in a later chapter, the FEM models with ALID regions can therefore be used to study wave propagation in more general layered soil systems, such as those possessing dipping layers, faults, folds, voids, inclusions, inhomogeneity, or anisotropy.

CHAPTER 3. PHASE-VELOCITY AND INTERCEPT-TIME SCANNING (PIS) TECHNIQUE FOR IMAGING SURFACE WAVE DISPERSION CHARACTERISTICS

3.1 Abstract

In geophysical surface wave methods, the ability to extract the true dispersion trends from surface wave field data is critical for inferring accurate stiffness profiles. However, dispersion images such as those generated by the widely used multichannel analysis of surface wave (MASW) wavefield transformation method of Park et al. (1998) are usually accompanied by numerical artifacts including side-lobes and aliasing, both of which decrease the dispersion image resolution and may lead to misinterpretation of dispersion modes. For example, the side lobes can be misinterpreted as higher or lower modes, which would introduce additional errors into the inverted stiffness profiles. To improve the resolution and sharpness of dispersion images by minimizing the side lobes, a new experimental dispersion analysis method is presented in this chapter. The new method employs scanning of the phase-velocities and intercept-times of a series of harmonic signals obtained by Fourier transformation of raw multichannel data in the space-time (x-t) domain. Results obtained from synthetic and real field data demonstrate that the newly developed method can yield high-quality dispersion images compared to those of the conventional MASW wavefield transformation method. In addition, the new method does not rely on the assumption that the impact point is the generation point of the Rayleigh waves, which is needed for the MASW wavefield transformation method.

3.2 Introduction

As commonly applied in MASW analyses (e.g., Park et al. 1999a, Xia et al. 2000, 2003, Song et al. 2007), experimental dispersion images can be extracted from multichannel surface wave data to obtain apparent dispersion curves, which are used to infer the site structure (e.g., soil layer thickness and stiffness). Thus, a high-resolution dispersion image is of critical importance for accurate soil profiling via surface wave testing. Historically, experimental dispersion analysis methods have developed along two main branches: (1) the frequency-wavenumber (*f-k*) transform (e.g., Horike 1985, Gabriels et al. 1987, Santamarina and Fratta 1998) and (2) the slowness-frequency (*p-f*) transform (e.g., McMechan and Yedlin 1981, Park et al. 1998, Louie 2001, Obando et al. 2010, O'Connell and Turner 2011).

The *f-k* transform applies a 2D Fourier transform to the space-time field data. The time Fourier transform converts the data from the time (t) to the frequency (f) domain, and the spatial Fourier transform converts the data from the spatial (x) to the wavenumber (k) domain. The *f-k* method can be used to characterize the fundamental and higher modes of surface waves in the *f-k* domain. However, it typically requires numerous receivers because the total receiver spread (X) controls the wavenumber resolution $\Delta k = \pi/X$, whereas the geophone spacing Δx controls the highest obtainable wavenumber $k_{max} = \pi/\Delta x_{min}$ (Foti 2002, Stokoe et al. 2004, Tran 2008).

The *p-f* transform employs the slant-stack scheme to extract dispersion information from the field data. It was developed by McMechan and Yedlin (1981) for active-source testing using two linear transforms: (1) the p-τ (phase slowness-time intercept) transform, which can be thought of as applying the slant-stack scheme to sum

field data along trial phase slowness ($p = 1/V_{ph}$) lines with various intercept times, yielding traces with the summed amplitude as the vertical coordinate and the time intercept as the horizontal coordinate; and (2) the time Fourier transform of the p-τ traces, which provides a dispersion image in the form of spectral peaks (i.e., ridges of a contour plot) in the p-f domain.

In addition to the two main f-k and p-f transforms, several variations and other methods have become popular in the past few decades. Park et al. (1998) proposed the active MASW wavefield transformation method using a similar phase-velocity scanning scheme, which first constructs harmonic signals from field data via the time Fourier transform, then slant-stacks the amplitudes of the harmonic signals along trial phase slowness lines which have a zero intercept time. Louie (2001) proposed the Refraction Microtremor (ReMi) method for use with passive seismic sources by applying p-τ (Thorson and Claerbout 1985) and p-f (McMechan and Yedlin 1981) transforms on recorded microtremors in both forward and reverse directions. Obando et al. (2010) improved the p-f transform as a phase-scanning approach to correct inaccurate time-shifts in the surface-wave walk-away method and to eliminate false apparent higher modes. O'Connell et al. (2011) proposed the IMASW (Interferometric Multichannel Analysis of Surface Waves) method by combining the p-f transform with interferometric time-domain dispersion analysis to improve the resolution of dispersion images at low frequencies.

From the above review of existing methods, the following conclusions may be drawn: (1) all f-k and p-f methods apply the Fourier transform to the raw field data with respect to the recording time (e.g., McMechan and Yedlin 1981, Horike 1985, Gabriels et al. 1987, Santamaria and Fratta 1998, Park et al. 1998, Obando et al. 2010, O'Connell

2011), or to the slant-stacked data with respect to the intercept time (e.g., Louie 2001); and (2) all *p-f* methods apply the slant-stack scheme either to the field data directly (e.g., McMechan and Yedlin 1981, Louie 2001) or to the harmonic signals extracted from the field data (e.g., Park et al. 1998, Obando et al. 2010, O'Connell 2011). Thus, the Fourier transform and the slant-stack scheme are two effective techniques for extracting dispersion data. It is demonstrated herein that an appropriate combination of the two techniques in a new way can lead to experimental dispersion analysis methods with improved resolution and accuracy.

An extensive review of literature on the subject reveals that experimental MASW dispersion images are typically accompanied by many side lobes as a result of spectral leakage, and also suffer from spatial aliasing effects (e.g., Park et al. 2001a, Ryden et al. 2004, Park et al. 2005, Tran and Hiltunen 2008, Obando et al. 2010, O'Connell and Turner 2011, Park 2012). As mentioned above, these numerical artifacts decrease the resolution of dispersion images, and can lead to misidentification of dispersion modes. To overcome these deficiencies, a new experimental dispersion analysis method termed the Phase-velocity and Intercept-time Scanning (PIS) method is developed herein, which combines 2D Fourier transforms with the slant-stack scheme. In the PIS method, the time Fourier transform is first applied to the space-time (*x-t*) field data to obtain an array of harmonic motions in the space-frequency (*x-f*) domain that contains dispersion information (i.e., phase velocity for each discrete frequency component), as is done for the MASW method. Second, the slant-stack scheme is used to stack (i.e., sum) amplitudes of each of the individual harmonic motion components along trial "scanning" values of slowness, with scanned intercept times (τ) as well, providing a new series of

harmonic curves in the p-τ plane. Third, another Fourier transform is applied to the new curves, followed by auto-power spectrum analysis to yield the dispersion image in the form of spectral values. The key differences in the new method relative to conventional MASW analysis are (1) the additional dimension of scanning the intercept time, whereas the conventional analysis assumes an intercept time of zero, and (2) the use of auto-power spectrum analysis, which presents the dispersion image amplitude in terms of power to greatly reduce effects of side lobes and aliasing. The performance of the newly developed PIS method is demonstrated below using both synthetic and real field data.

3.3 Phase-velocity and Intercept-time Scanning (PIS) Method

3.3.1 Synthetic data

Parameters of a hypothetical soil model used to study the new PIS method are listed in Table 3.1. The theoretical fundamental-mode dispersion curve of the hypothetical model is shown in Figure 3.1, as obtained by the transfer matrix method described in Chapter 2. The theoretical dispersion curve was then used to define a set of synthetic sinusoidal surface wave displacements at each discrete frequency f as

$$\bar{u}_f(x,t) = \sin\left[2\pi f\left(t - \frac{x}{V_{ph}(f)}\right)\right] \tag{3.1}$$

where $V_{ph}(f)$ is the frequency-dependent phase velocity from the theoretical dispersion curve, and x are the distances from the source to the receivers. The synthetic sinusoidal signals obtained from Eq. (3.1) are used instead of field data to demonstrate the performance of the PIS method for pure data that is not influenced by environmental noise, air waves, body waves, and near-field or far-field effects.

Table 3.1 Parameters of layered soil model.

Layer #	V_S (m/s)	Poisson's ratio, ν	Density, ρ (kg/m^3)	Layer thickness, h (m)
1	122.5	0.45	1800	1
2	250.0	0.45	1800	2
3	380.0	0.45	1800	5
4	560.0	0.45	1800	5
5	735.0	0.45	1800	6
6	850.0	0.45	1900	6
7	900.0	0.45	1900	5
8	1100.0	0.45	1900	5
9	1308.0	0.45	2000	∞

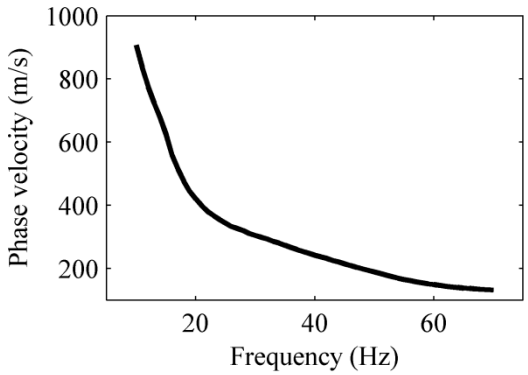

Figure 3.1 Fundamental-mode dispersion curve of the soil model in Table 3.1 calculated by the transfer matrix method of Chapter 2**.**

3.3.2 Fourier transform to extract harmonic signals from field data

The frequency content of the field data can be determined by applying the Fourier transform as the first step in MASW data analysis (Park et al. 1998, Obando et al. 2010, O'Connell et al. 2011). The raw field displacement (or alternatively, velocity or acceleration) data $u(x^a, t)$ are thus converted to the displacement spectra $U(x^a, f)$ at each offset distance by the finite-range continuous-time Fourier transform;

$$U(x^a, f) = \int_0^{t_t} u(x^a, t) e^{-i2\pi ft} dt \tag{3.2}$$

where x^a is the receiver offset with respect to the source point of Rayleigh wave generation, t_t is the total recording time, dt is the differential time interval, and f is frequency in Hz. In reality, the field data are sampled at discrete times and offsets, so the fast Fourier transform (FFT) is used to numerically approximate Eq. (3.2).

According to Euler's formula, Eq. (3.2) can be written as

$$\begin{aligned} U(x^a, f) &= \int_0^{t_t} u(x^a, t)[\cos(2\pi ft) - i\sin(2\pi ft)]dt \\ &= \int_0^{t_t} u(x^a, t)\cos(2\pi ft)dt - i\int_0^{t_t} u(x^a, t)\sin(2\pi ft)dt \\ &= c - id \\ &= \sqrt{c^2 + d^2}\left(\frac{c}{\sqrt{c^2 + d^2}} - i\frac{d}{\sqrt{c^2 + d^2}}\right) \end{aligned} \tag{3.3}$$

where $c = c(x^a, f) = \int_0^{t_t} u(x^a, t)\cos(2\pi ft)dt$ and $d = d(x^a, f) = \int_0^{t_t} u(x^a, t)\sin(2\pi ft)dt$.

The Fourier spectra $U(x^a, f)$ for each receiver offset x^a are complex valued, and can therefore be expressed as the product of their amplitude $A(x^a, f)$ and phase $P(x^a, f)$ components as

$$U(x^a, f) = A(x^a, f)P(x^a, f) \tag{3.4}$$

where

$$A(x^a, f) = \sqrt{c^2 + d^2} \tag{3.5}$$

$$P(x^a, f) = \frac{c}{\sqrt{c^2 + d^2}} - i\frac{d}{\sqrt{c^2 + d^2}} = e^{-i\theta^a} \tag{3.6}$$

and

$$\theta^a = \tan^{-1}\left(\frac{d}{c}\right) = 2\pi f \frac{x^a}{V_{ph}^a(f)} \tag{3.7}$$

Also, it is assumed that each spectral component propagates at its own frequency-dependent phase velocity (or velocities for multiple modes) that does not vary

with distance. The phase $P(x^a, f)$ thus contains dispersion information, as it is a function of frequency (f), receiver offset with respect to the source point of Rayleigh wave generation (x^a), and the actual phase velocity $V_{ph}^a(f)$ which is frequency-dependent for a dispersive medium. The amplitude $A(x^a, f)$ contains information on spherical divergence and attenuation, which vary with offset and frequency, and can be useful for other analytical approaches that consider these effects. However, since the amplitude does not include any information on dispersion, the amplitudes $A(x^a, f)$ for each receiver offset x^a can be normalized with respect to their maximum values without negatively affecting the dispersion analysis as

$$\overline{A}(x^a, f) = A(x^a, f) / \left|A(x^a, f)\right| = 1 \tag{3.8}$$

Noting that $\left|U(x^a, f)\right| = \left|A(x^a, f)\right|$ in Eq. (3.4), the normalized displacement spectra can be obtained from Eq. (3.4) as

$$\begin{aligned} \overline{U}(x^a, f) &\equiv U(x^a, f) / \left|\mathrm{U}(x^a, f)\right| \\ &= \underbrace{\overline{A}(x^a, f)}_{=1} P(x^a, f) \\ &= e^{-i\theta^a} \\ &= e^{-i2\pi f x^a / V_{ph}^a(f)} \end{aligned} \tag{3.9}$$

where f is known, and x^a is assumed to be equal to the receiver offset from the impact location (x) in conventional MASW analysis (Park et al. 1998). However, because Rayleigh waves are produced by the interaction of *P*- and *S*-waves with the free surface, they develop beyond a finite distance from the source point in actual tests. As a result, the distance from a receiver to the generation point of Rayleigh waves can be less than the receiver-to-impact location distance, i.e. $x^a < x$. This phenomenon, together with the fact that the spherical wavefronts can only be approximated as planar beyond a finite distance,

are referred to as the "near-field effects". Near-field effects must be carefully considered when acquiring experimental data in field tests. However, the synthetic displacement signals in Eq. (3.1) define perfectly planar theoretical Rayleigh wavefronts that originate at the source point x=0 and are free of near-field effects. If the impact point is assumed to be the generation point of the Rayleigh waves (x=x^a, which may be an approximation for certain field test geometries), then the only unknown for real or simulated field data in Eq. (3.9) is the phase velocity, which can be determined by using the proposed PIS or conventional MASW phase-scanning methods.

3.3.3 MASW wavefield transformation method

The MASW wavefield transformation method (alternatively referred to as the MASW phase-velocity scanning scheme) was proposed for experimental dispersion analysis of active-source multichannel seismograph records (Park et al. 1998). Conceptually, this scheme can be thought of as summing the amplitudes of harmonic signals plotted in the space-time domain (for a given frequency) along a straight-line defined by a trial scanning phase velocity V_{ph}^{s}, (or equivalently, scanning phase slowness $p_s = 1/V_{ph}^{s}$).

In conventional MASW analysis, all trial phase slowness lines are chosen to go through the origin, which imposes a fixed zero intercept time, τ=0. In actual implementation, the calculations are performed in the frequency rather than the time domain for improved efficiency and accuracy. The frequency-domain calculations are implemented by first multiplying Eq. (3.9) by $e^{i2\pi fx/V_{ph}^{s}}$, which gives the value of the harmonic Fourier component $\overline{U}(x^a, f)$ if it were plotted in the x-t domain, at its

intersection with the scanning phase slowness line at time $t = x / V_{ph}^{s}$. In practice, this is actually performed in the frequency domain by forming the following product with the Fourier-transformed field data of Eq. (3.9):

$$\overline{U}(x^a, f)e^{i2\pi fx/V_{ph}^{s}} = e^{-i2\pi f(x^a/V_{ph}^{a}(f)-t)} \tag{3.10}$$

where

$$t = x / V_{ph}^{s} \tag{3.11}$$

In terms of the actual phase angle θ^a of the field data and the assumed scanning phase angle defined as

$$\theta^s = 2\pi f \frac{x}{V_{ph}^{s}} \tag{3.12}$$

the product in Eq. (3.10) may be expressed as

$$\overline{U}(x^a, f)e^{i2\pi fx/V_{ph}^{s}} = e^{-i(\theta^a-\theta^s)} \tag{3.13}$$

For a single channel, this product will have a maximum real component equal to 1 and minimum imaginary component equal to 0 when $x = x^a$ and $V_{ph}^{s} = V_{ph}^{a}$, or equivalently, when the actual and scanning phase velocities coincide, i.e. $\theta^a = \theta^s$.

To find the optimum V_{ph}^{s} considering the traces recorded at all offsets, the slant-stack summation along the scanning phase velocity line (V_{ph}^{s}) at a certain frequency (*f*) is then calculated as

$$A_f(V_{ph}^{s}) = \int_{x_1}^{x_N} e^{i2\pi fx_n/V_{ph}^{s}} \overline{U}(x^a, f)dx \tag{3.14}$$

where x_n is the distance between the impact point and the nth receiver. When the scanning phase velocity V_{ph}^{s} is equal to the actual phase velocity V_{ph}^{a} for a given frequency, the

stacked amplitude $A_f(V_{ph}^s)$ will have a maximum. For real field data sampled at a finite number of offset locations, Eq. (3.14) can be written in discrete form as

$$\begin{aligned} A_f(V_{ph}^s) &= \sum_{x_n=x_1}^{x_N} e^{i2\pi f x_n/V_{ph}^s}\overline{U}(x_n^a, f) \\ &= \sum_{x_n=x_1}^{x_N} e^{i2\pi f x_n/V_{ph}^s} e^{-i2\pi f x_n^a/V_{ph}^a(f)} \\ &= \sum_{x_n=x_1}^{x_N} e^{i2\pi f x_n(1/V_{ph}^s - 1/V_{ph}^a(f))} \end{aligned} \tag{3.15}$$

where the impact point was assumed to be the generation point of the Rayleigh waves, i.e. $x_n^a = x_n$ (Park et al. 1998, 2001a).

The stacked amplitudes of the harmonic signals are calculated for a range of scanning phase velocities at each frequency of interest using Eq. (3.15). As will be shown below, a 2D dispersion image is then constructed in the form of a contour plot of the normalized stacked amplitude

$$\overline{A}_f(V_{ph}^s) = \frac{A_f(V_{ph}^s)}{\max(A_f(V_{ph}^s))} \tag{3.16}$$

versus phase velocity and frequency. Theoretically, when the scanning phase velocity is perfectly equal to the actual velocity, $A_f(V_{ph}^s)$ will be equal to $Ne^{-i0} = N\cdot(1-i0)$. For real experimental data, however, the exponent in Eq. (3.15) will not be equal to zero due to discretization and a range of physical imperfections, and the numerically calculated value of $A_f(V_{ph}^s)$ will be complex-valued with a small imaginary part. In the phase velocity scanning approach, a logical choice would therefore be to maximize the real part of Eq. (3.15) while minimizing the imaginary part towards zero. In practice, however, the

complex modulus (or 'magnitude') $\left|A_f(V_{ph}^s)\right|$ is commonly used in Eq. (3.16) to generate the 2D dispersion image:

$$\overline{A}_f(V_{ph}^s) = \frac{\left|A_f(V_{ph}^s)\right|}{\max(\left|A_f(V_{ph}^s)\right|)} \tag{3.17}$$

A further analysis of the MASW phase-velocity scanning scheme is presented here to demonstrate that the only dispersion information used from the field data is the relative phase difference between receivers, and not the absolute phase difference relative to the source point. Thus the assumption that the impact point is the generation point of the Rayleigh waves (x=x^a), is actually not necessary. For this purpose, the distance between the impact point and the n^{th} receiver can be decomposed into two parts:

$$x_n = x_1 + \Delta x_n \tag{3.18}$$

where x_1 is the offset from the first receiver to the impact point, and Δx_n is the distance between the n^{th} and first receivers. Substituting Eq. (3.18) into Eq. (3.14) gives

$$\begin{aligned} A_f(V_{ph}^s) &= \int_{x_1}^{x_N} e^{i2\pi f[x_1+\Delta x_n]/V_{ph}^s}\overline{U}(x_n^a, f)dx \\ &= e^{i2\pi f x_1/V_{ph}^s}\int_{x_1}^{x_N} e^{i2\pi f \Delta x_n/V_{ph}^s}\overline{U}(x_n^a, f)dx \\ &= e^{i2\pi f x_1/V_{ph}^s}A_{f1}(V_{ph}^s) \end{aligned} \tag{3.19}$$

where $e^{i2\pi f x_1/V_{ph}^s}$ does not contain any multichannel dispersion information and thus the variation of x_1 does not change the magnitude of the dispersion image, it only applies a linear phase shift with frequency that is proportional to x_1. The fact that the closest-to-source offset x_1 does not change the magnitude of the dispersion image for the same set of field data with an artificially varied x_1 was demonstrated empirically by Park et al. (2001a) and Park (2012). The above equation now provides a theoretical explanation for

these empirical observations. If the actual x_1 is physically varied in a field setup, then the dispersion characteristics of the field data in $\overline{U}(x_n^a, f)$ will also change (e.g., Park et al. 2000), which may be attributable to separation of higher modes, near-field effects, and attenuation.

The term

$$A_{f1}(V_{ph}^s) = \int_{x_1}^{x_N} e^{i2\pi f \Delta x_n / V_{ph}^s} \overline{U}(x_n^a, f)dx \tag{3.20}$$

contains the necessary dispersion information and can be further analyzed by substituting Eq. (3.9) to give

$$A_{f1}(V_{ph}^s) = \int_{x_1}^{x_N} e^{i2\pi f \Delta x_n / V_{ph}^s} e^{-i2\pi f x_n^a / V_{ph}^a(f)}dx \tag{3.21}$$

The distance between the actual generation point of the Rayleigh waves and the n^{th} receiver can similarly be decomposed into two parts:

$$x_n^a = x_1^a + \Delta x_n \tag{3.22}$$

where x_1^a is the offset from the first receiver to the generation point of the Rayleigh waves and Δx_n is again the distance between the n^{th} and first receivers. Substituting Eq. (3.22) into Eq. (3.21) gives

$$\begin{aligned} A_{f1}(V_{ph}^s) &= \int_{x_1}^{x_N} e^{i2\pi f \Delta x_n / V_{ph}^s} e^{-i2\pi f (x_1^a + \Delta x_n)/V_{ph}^a(f)}dx \\ &= e^{-i2\pi f x_1^a / V_{ph}^a(f)} \int_{x_1}^{x_N} e^{i2\pi f \Delta x_n \left(1/V_{ph}^s - 1/V_{ph}^a(f)\right)}dx \\ &= e^{-i2\pi f x_1^a / V_{ph}^a(f)} A_{f2}(V_{ph}^s) \end{aligned} \tag{3.23}$$

where $e^{-i2\pi f x_1^a / V_{ph}^a(f)}$ does not contain any multichannel dispersion information, whereas

$$A_{f2}(V_{ph}^s) = \int_{x_1}^{x_N} e^{i2\pi f \Delta x_n \left(1/V_{ph}^s - 1/V_{ph}^a(f)\right)}dx \tag{3.24}$$

contains all the necessary multichannel dispersion information and is independent of the first receiver offsets x_1 and x_1^a. When the scanning phase velocity V_{ph}^s is equal to the actual phase velocity V_{ph}^a for a given frequency, the stacked amplitude $A_{f2}(V_{ph}^s)$ will have a maximum. Substituting Eq. (3.23) into Eq. (3.19) gives

$$A_f(V_{ph}^s) = e^{i2\pi f\left(x_1/V_{ph}^s - x_1^a/V_{ph}^a(f)\right)} A_{f2}(V_{ph}^s) \tag{3.25}$$

where x_1^{a} is unknown. Therefore, the term $e^{i2\pi f\left(x_1/V_{ph}^s - x_1^{\mathrm{a}}/V_{ph}^a(f)\right)}$ can be eliminated as $e^{-i2\pi f x_1^a/V_{ph}^a} = e^{-i\theta_a}$, which is known from the Fourier-transformed field data by Eq. (3.9). From Eq. (3.25), it is immediately evident that $\left|A_f(V_{ph}^s)\right| = \left|A_{f2}(V_{ph}^s)\right|$, so a dispersion image using the complex magnitude $\left|A_{f2}(V_{ph}^s)\right|$, i.e.

$$\bar{A}_{f2}(V_{ph}^s) = \frac{\left|A_{f2}(V_{ph}^s)\right|}{\max\left(\left|A_{f2}(V_{ph}^s)\right|\right)} \tag{3.26}$$

will be identical to that using $\left|A_f(V_{ph}^s)\right|$. However, the use of $\left|A_{f2}(V_{ph}^s)\right|$ has better conceptual clarity and can clearly demonstrate that the critical factor affecting the dispersion image is the relative phase difference between receivers. On the other hand, according to the discussion of Eq. (3.16), the real component should be maximized and the imaginary component minimized in the phase-scanning approach. Dispersion images defined using the real parts i.e.,

$$\bar{A}_f^{\mathrm{Re}}(V_{ph}^s) = \frac{\mathrm{Re}\left(A_f(V_{ph}^s)\right)}{\max\left(\mathrm{Re}\left(A_f(V_{ph}^s)\right)\right)} \tag{3.27}$$

and

$$\overline{A}_{f2}^{\mathrm{Re}}(V_{ph}^{s}) = \frac{\mathrm{Re}\left(A_{f2}(V_{ph}^{s})\right)}{\max\left(\mathrm{Re}\left(A_{f2}(V_{ph}^{s})\right)\right)} \tag{3.28}$$

would therefore be different according to Eq. (3.25), and may prove useful as alternative dispersion images.

3.3.4 Phase-velocity and intercept-time scanning (PIS) analysis

As will be demonstrated below, the phase-velocity and intercept time scanning (PIS) technique proposed herein can remove the requirement for the assumption $x=x^a$, and also reduce the side lobes and thereby the uncertainty in dispersion images. For the conceptual *x*-*t* domain interpretation of the MASW phase scanning approach (e.g., Park et al. 1999a, Ryden et al. 2004, Park 2011), the proposed PIS technique allows each scanning phase slowness line to also be offset along the time axis by a scanned intercept time τ_s in Eq. (3.14), i.e.,

$$t = \tau_s + \frac{x}{V_{ph}^{s}} \tag{3.29}$$

The final step in the PIS method is to perform an auto-power spectral analysis of the slant-stacked harmonic signals obtained via applying the phase-velocity and intercept-time scanning scheme to the harmonic signals. A synthetic example of phase-velocity and intercept-time scanning on a 55 Hz pure sinusoidal signal defined by Eq. (3.1) is shown in Figure 3.2a. Three scanning phase-velocity lines are shown for velocities of 155, 165, and 175 m/s, all with the same intercept-time of τ=0.0227 s. The actual velocity for this example is $V_{ph}^{a} = 165$ m/s. Figure 3.2b shows the normalized amplitudes along the three scanning lines;

$$\overline{U}(x, f)e^{i2\pi f(\tau_s + x/V_{ph}^{s})} \tag{3.30}$$

When the scanning velocity is equal to the actual phase velocity of 165 m/s, the normalized amplitude along the scanning line is a constant and a maximum.

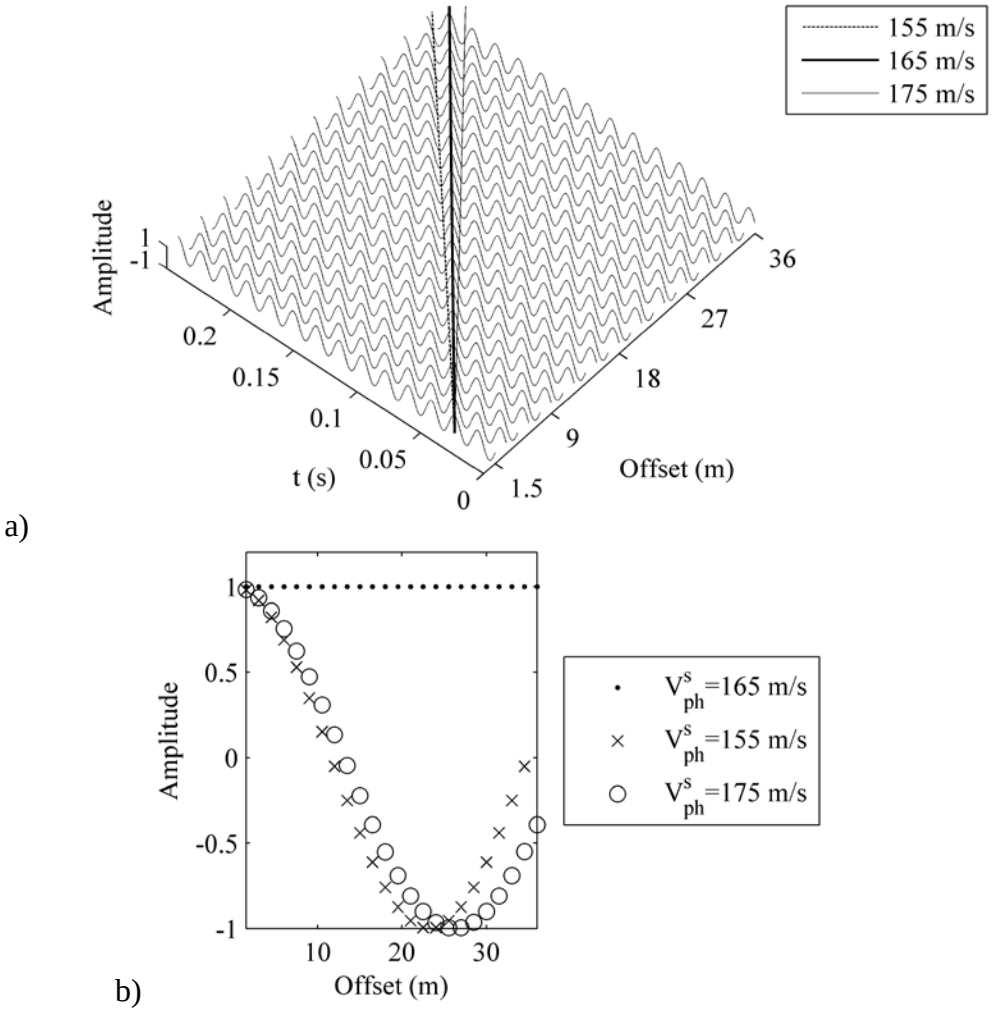

Figure 3.2 (a) Phase-velocity and time-intercept (PIS) scanning scheme shown in *x*-*t* domain for harmonic 55 Hz component, with scanning phase velocity varied and scanning intercept time fixed; (b) Amplitude $\overline{U}(x, f)$ of harmonic components along the three trial scanning lines.

For actual field test data, the normalized amplitude of Eq. (3.30) is then summed along the scanning line at the discrete receiver offsets (x_n) to obtain the slant-stack summation. For the present theoretical example, the sum can be replaced with an integral, corresponding to an infinitesimal receiver spacing *dx*, giving the summed amplitude

$$A_f(V_{ph}^s, \tau_s) = \int_{x_1}^{x_N} \overline{U}(x, f) e^{i2\pi f(\tau_s + x/V_{ph}^s)} dx \tag{3.31}$$

where x is the offset, τ_s is the scanning intercept time, V_{ph}^s is the scanning phase velocity, and the calculation is for a particular frequency component of the Fourier transform in Eq. (3.2). For actual field tests, Eq. (3.31) is replaced with the summation

$$\begin{aligned} A_f(V_{ph}^s, \tau_s) &= \sum_{x=x_1}^{x_N} \overline{U}(x, f) e^{i2\pi f\left(\tau_s + x/V_{ph}^s\right)} = \sum_{x=x_1}^{x_N} \underbrace{\overline{A}(x, f)}_{=1} e^{i2\pi f(\tau_s + x/V_{ph}^s - x^a/V_{ph}^a)} \\ &= e^{i2\pi f\tau_s} \sum_{x=x_1}^{x_N} e^{i2\pi f(x/V_{ph}^s - x^a/V_{ph}^a)} \end{aligned} \tag{3.32}$$

For instructional purposes, plotting the resulting summed normalized amplitudes versus the scanned intercept time (τ_s) provides a new time-domain waveform, as shown in Figure 3.3. This plot allows the optimum scanning phase velocity to be identified as that which produces the largest waveform amplitude. For the present theoretical example, the optimum phase velocity is the actual value of 165 m/s. In practice, the optimum intercept time can be found by simply programming another loop over intercept time in Eq. (3.32) and searching for the maximum $A_f(V_{ph}^s, \tau_s)$. It should be noted that the effect of τ_s on the summed amplitude in the above equation is similar to that of x_1 / V_{ph}^s in Eq. (3.19).

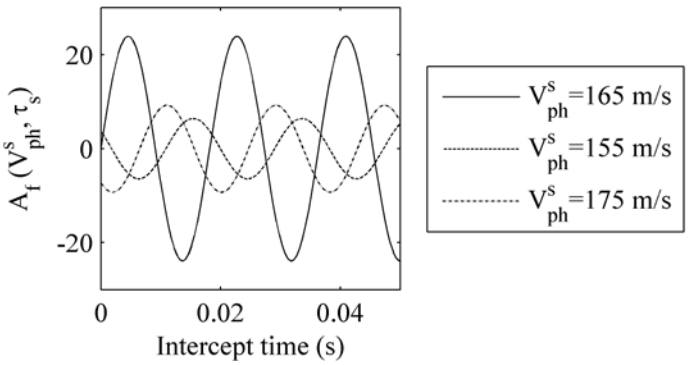

Figure 3.3 Waveforms of summed normalized amplitude $A_f(V_{ph}^s, \tau_s)$ produced by varying the scanning intercept time τ_s for three scanning phase velocities V_{ph}^s.

3.3.5 Auto power spectral analysis

The dispersion information needs to be extracted from the summed amplitude $A_f(V_{ph}^s, \tau_s)$, which varies with the scanning phase velocity and scanning intercept time. As shown conceptually in Figure 3.3, $A_f(V_{ph}^s, \tau_s)$ for different scanning velocities results in different waveforms, the amplitudes of which are dispersion-information measurements of the scanning velocities. The amplitude discrepancy among scanning velocities can be further magnified by taking a 1D Fourier transform of the amplitude waveforms followed by an auto power spectrum analysis. The first 1D Fourier transform converts Eq. (3.31) from the intercept-time domain to the frequency domain:

$$F_f(V_{ph}^s, f_\tau) = \int_\tau A_f(V_{ph}^s, \tau) e^{-i2\pi f_\tau \tau} d\tau \tag{3.33}$$

and the auto power spectrum analysis of Eq. (3.33) then provides the spectral value,

$$S_f(V_{ph}^s, f_\tau) = F_f^*(V_{ph}^s, f_\tau) F_f(V_{ph}^s, f_\tau) \tag{3.34}$$

where * denotes the complex conjugate. Figure 3.4 shows the three auto power spectra for the three scanning velocities of the present theoretical example. As expected, the auto power spectra peaks are at the examined frequency of 55 Hz (i.e., $f_\tau = f$) for all of the scanning phase velocities, and the maximum spectral value occurs when the scanning velocity is equal to the actual phase velocity of the sinusoidal signal (165 m/s).

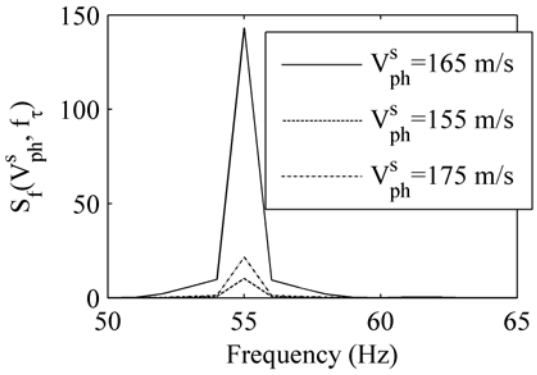

Figure 3.4 Auto power spectra (spectral value vs. frequency).

The peak amplitudes for different scanning velocities in Figure 3.4 can be used to construct a plot of auto-power spectrum values vs. scanning velocities for the corresponding optimum intercept-times. For a harmonic signal at a certain frequency (*f*) obtained by the Fourier transform of Eq. (3.2), varying the phase velocity in Eq. (3.34) in the scanning range provides auto-power spectrum values which vary with V^s_{ph};

$$S_f(V^s_{ph}) = \max(S_f(V^s_{ph}, f_\tau)), \qquad V^s_{ph} \in (V^s_{ph,\min}, V^s_{ph,\max}) \tag{3.35}$$

this auto power spectral analysis is useful to extract the peak information in Figure 3.3 in order to magnify the difference among scanning velocities and thus increases the contrast of dispersion images. The auto-power spectrum is then plotted as a function of V^s_{ph} in the form of a 2-D slice dispersion image and then repeated for different frequencies (*f*) to obtain the complete 3-D dispersion image of the PIS analysis. It should be noted for conventional MASW analyses that a similar improvement in dispersion image quality can be obtained by plotting the auto-power spectrum (the square of the complex magnitude) of the summed amplitude in Eq. (3.16). This finding was an additional benefit enabled by the formulation of the PIS approach presented above.

3.3.6 Spectral ratio

At each frequency of interest, all slowness values (or equivalently, phase velocities) of interest are scanned in Eq. (3.35) by first replacing Eq. (3.33) with a Fast Fourier Transform evaluated for the range $0 < \tau < 2/f$. Then, the resulting summed spectral values can be normalized with respect to the maximum value as

$$R(V_{ph}^{s}, f) = \frac{S_f(V_{ph}^{s})}{\max(S_f(V_{ph}^{s}))} \tag{3.36}$$

In the PIS method, the dispersion image is then constructed as a 3D or contour plot of R in Eq. (3.36) against the scanning phase velocities and the frequency of the Fourier transform of Eq. (3.9).

A slice of one such normalized dispersion image for a frequency of 55 Hz is shown in Figure 3.5 for the conventional MASW analysis and the new MASW-PIS method presented herein. Figure 3.5 shows a slice through a dispersion image after applying the phase-velocity scanning scheme to the synthetic 55 Hz sinusoidal signals in Figure 3.2a. As mentioned above, the synthetic signals are free from noise and near- or far-field effects. Despite this ideal situation, the dispersion imaging scheme results in many side lobes distributed throughout the phase-velocity scanning range using the conventional MASW analysis method (Figure 3.5). Similar phenomena can also be observed in Park et al. 2001a, Ryden et al. 2004, and Park 2012. The spectral side-lobe leakage phenomenon of Fourier transforms is a consequence of discretizing the frequency spectrum and the implied rectangular window, for which the Fourier transform is a sinc function with many side-lobes (e.g., see Bendat and Piersol 1996). The product of the signal and the window in the time-domain becomes a convolution of their respective

Fourier transforms in the frequency domain. Here, side-lobe leakage also occurs along the phase-velocity axis in Figure 3.5 due to discretization of the phase-velocity spectrum. The side lobes decrease the resolution of the main lobe which identifies the apparent dispersion trend, and in some instances, may be misidentified as higher and/or lower modes. As shown in the figure, the new MASW-PIS method significantly reduces the amplitudes of the sidelobes, thus improving the resolution of the main peak from which the phase velocity is determined for the given frequency. The comparison of two full dispersion images in Figures 3.6a and 3.6b demonstrates the MASW-PIS method can yield experimental dispersion images with much greater clarity than conventional MASW analysis due to drastically reduced side lobes. This is primarily a result of the power-spectrum analysis step of the PIS method, and can therefore be easily applied to conventional MASW analyses to immediately improve the quality of dispersion images by plotting the square of the complex magnitude of Eq. (3.16).

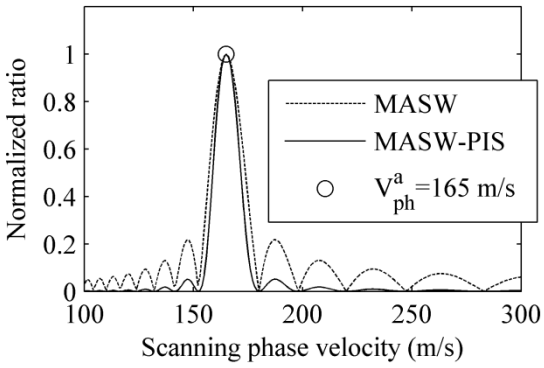

Figure 3.5 Dispersion image slices at 55 Hz using MASW method, and MASW-PIS method resulting in reduced side lobes.

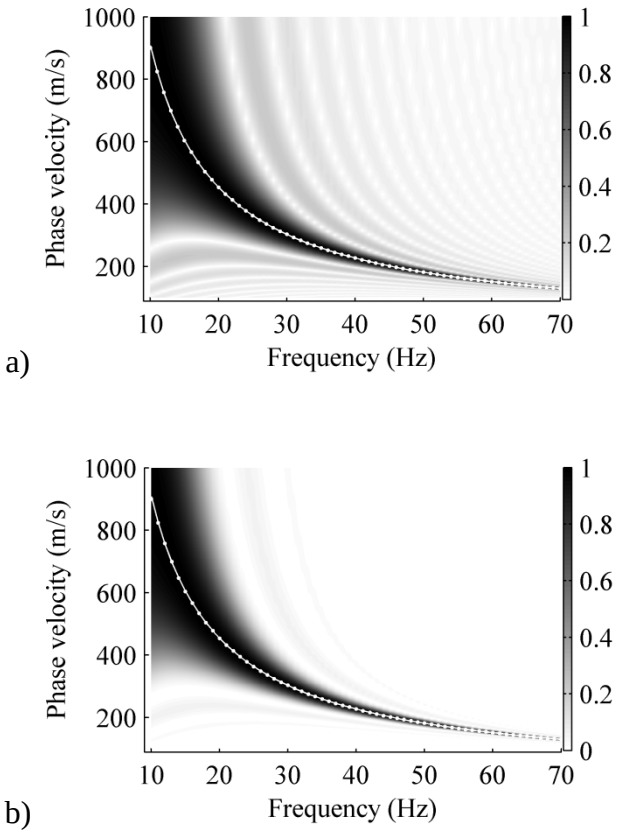

Figure 3.6 Synthetic experimental dispersion images: a) using MASW and b) using MASW-PIS.

3.4 Case Studies

To examine the relative performance of the conventional MASW and new MASW-PIS analysis methods, data from two different field sites and a finite element simulation are used in this section. The raw data are from: (1) multichannel simulation with one-receiver (MSOR) testing at a soil site in Iowa (Lin and Ashlock 2011), (2) active-source MASW testing at the National Geotechnical Experimental Site (NGES) at Texas A&M University from the SASW benchmarking data set (GEC 2011, Tran and Hiltunen 2011), and (3) a finite element simulation of surface waves in a three-layer soil model using Abaqus 6.10-1.

3.4.1 MSOR Tests at East River Valley site

A single 4.5 Hz vertical geophone and triggered 10 lb sledgehammer source impacting a 1 in. thick aluminum plate were used for multichannel simulation with one receiver (MSOR) tests at this site. A 4-channel LDS Photon II dynamic signal analyzer was used for data acquisition, with a sampling interval of 0.78125 msec and anti-aliasing filtering for a maximum frequency of 500 Hz. A 12 ft station separation over an offset range from 18–258 ft was utilized. Twenty impacts were recorded at each station for signal stacking. All stacked, normalized signals with filled positive amplitudes are assembled in Figure 3.7. A slice through the dispersion image at 12 Hz and the full experimental dispersion image are shown in Figures 3.8 and 3.9, respectively for both MASW and MASW-PIS analysis methods. The two methods yield similar dispersion images with consistent fundamental modes (Figures 3.9a and 3.9b). The slice through the dispersion image in Figure 3.8 as well as the images in Figure 3.9 exhibit significant reductions in aliasing and side lobe height for the new MASW-PIS method.

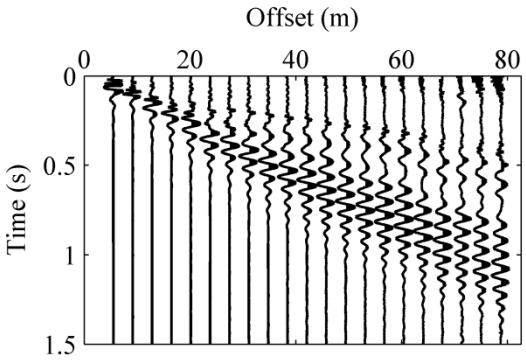

Figure 3.7 Field data for MSOR tests at East River Valley site.

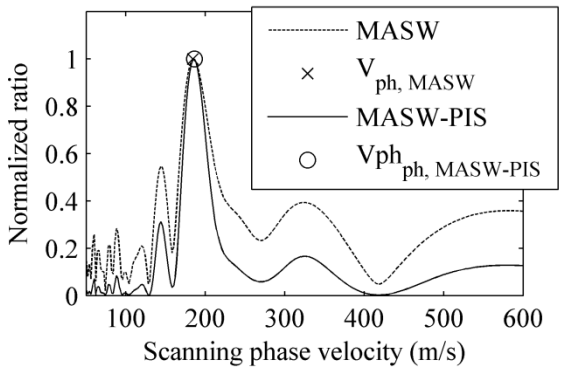

Figure 3.8 Slice of dispersion image at 12 Hz using MASW and MASW-PIS analyses for MSOR tests at East River Valley site.

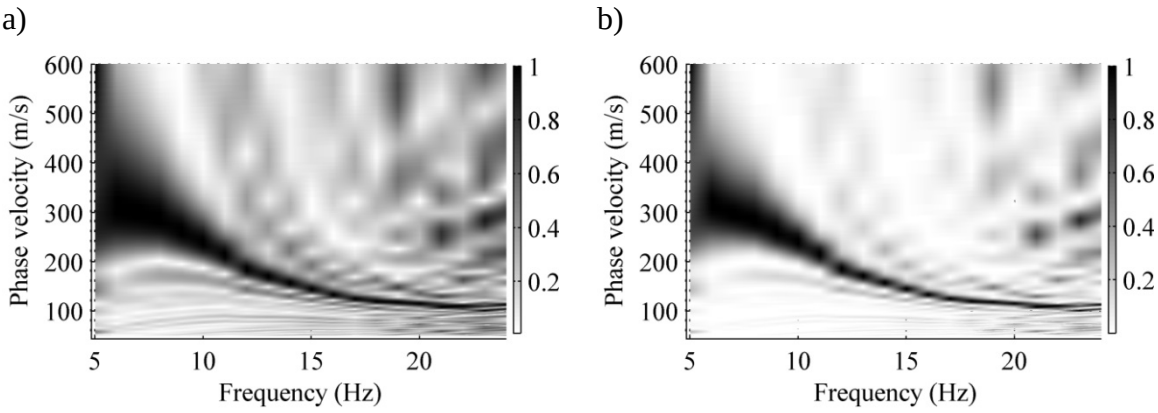

Figure 3.9 Experimental dispersion images: a) using MASW and b) using MASW-PIS for MSOR tests at East River Valley site.

3.4.2 MASW tests at NGES

For this analysis, one of the SASW benchmarking data sets from GEC (2011) was used, with receiver offsets from 98 to 220 ft and the impact point at 88 ft. The conventional multi-receiver MASW testing method was used with a total of sixty-two 4.5-Hz vertical geophones, a sampling interval of 0.78125 msec, and a triggered sledgehammer. Geophones were placed along a straight-line with 10-ft source offset and 2-ft spacing. The pre-trigger delay was about 10% of the 12.8-sec record time. A selected subset of the normalized signals with filled positive amplitudes are assembled in Figure 3.10. A slice at 40 Hz and the experimental dispersion images obtained from this data

using the conventional MASW and new MASW-PIS methods are shown in Figures 3.11 and 3.12. The relative performance of the two methods is similar to that shown for the MSOR tests in Figures 3.8 and 3.9; the MASW-PIS method significantly reduces side lobes and aliasing over the entire frequency range.

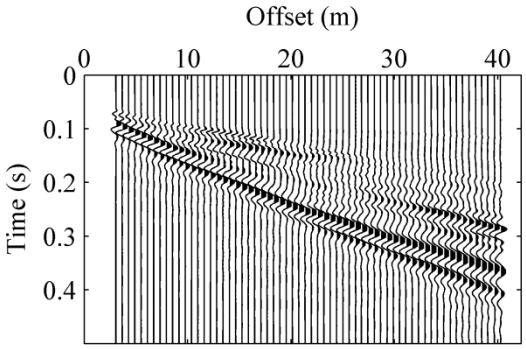

Figure 3.10 Field data from MASW tests at NGES.

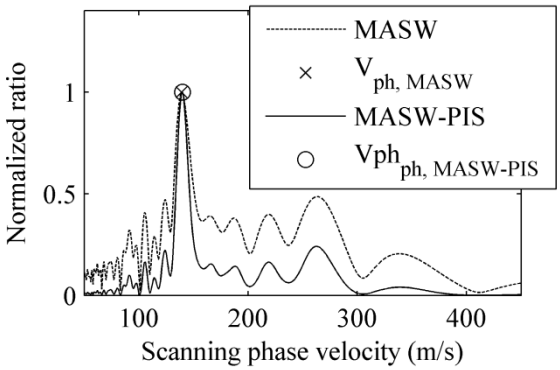

Figure 3.11 Slice of dispersion image at 40 Hz using conventional MASW and MASW-PIS analysis methods for MASW tests at NGES.

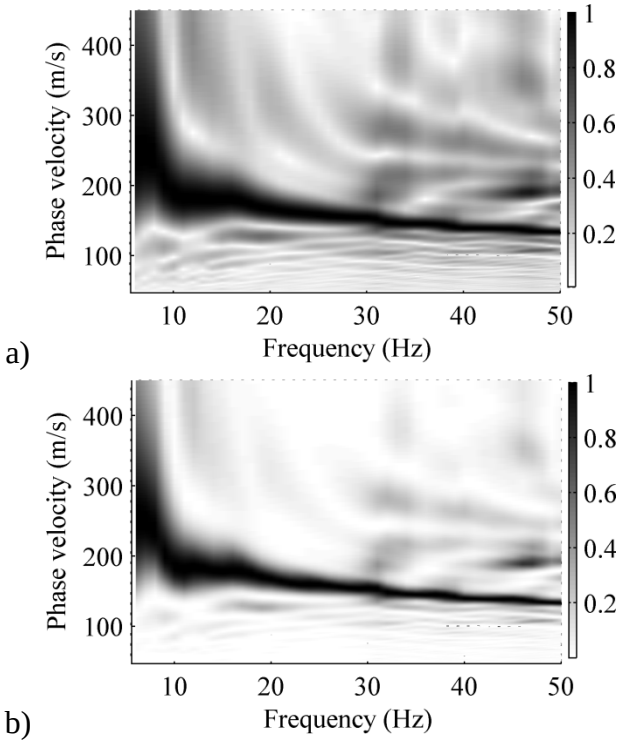

Figure 3.12 Experimental dispersion and inversion analysis: a) using MASW and b) using MASW-PIS for MASW tests at NGES.

3.4.3 Finite element simulation

MASW surface wave testing on a three-layer soil model was simulated using the finite element method in Abaqus 6.10-1 (Lin and Ashlock 2014a). The soil structure and properties for this analysis are shown in Table 3.2.

Table 3.2 Parameters of a layered soil model

Layer #	V_S (m/s)	Poisson's ratio, ν	Density, ρ (kg/m^3)	Layer thickness, h (m)
1	150	0.30	1800	2
2	200	0.30	1800	3
3	400	0.30	1900	∞ (half space)

The conventional MASW and new MASW-PIS experimental dispersion analyses of the simulated surface waves provide the dispersion images shown in Figure 3.13. The first three modes of the theoretical dispersion curves were calculated using the transfer

matrix method for the soil model in Table 3.2, and are shown for reference as continuous curves in Figure 3.13.

The results from this finite element simulation also demonstrate that the new MASW-PIS method produces dispersion images with significant reductions in side lobes and aliasing. It is important to note that the strong sidelobes shown in Figure 3.13a are not higher modes, as is clear from comparison to the theoretical dispersion curves shown. For similar dispersion images from field data cases, the strong side lobes may be incorrectly identified as apparent higher modes. The muted side lobes by the MASW-PIS method can therefore help to easily and correctly interpret experimental dispersion images, reducing misinterpretation of higher modes.

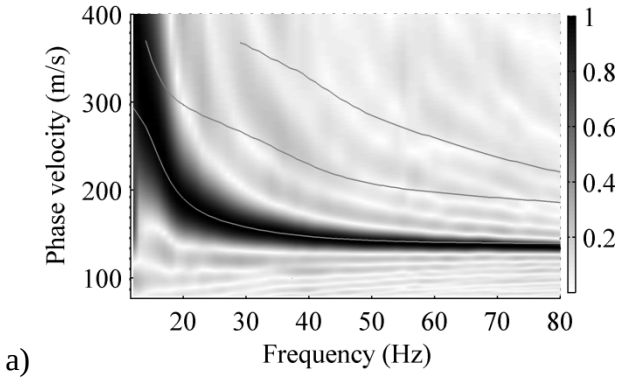

a)

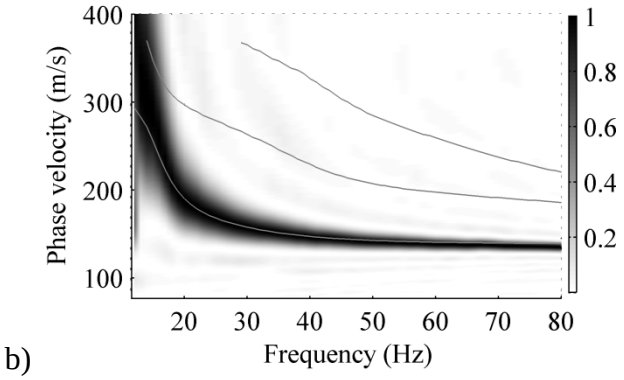

b)

Figure 3.13 Experimental dispersion images: a) using MASW and b) using MASW-PIS. (Solid grey lines are the first three-modes of theoretical dispersion curves.)

3.5 Conclusions

It was demonstrated in this chapter that dispersion images in the form of auto-power spectral values calculated using the new MASW-PIS method, which employs phase-velocity and intercept-time scanning schemes, have greater resolution and reduced side lobes relative to the conventional MASW analysis method, which features dispersion images in the form of stacked amplitude values obtained by the phase-velocity scanning scheme. Through one theoretical example, two field case studies, and one finite element simulation, it was demonstrated that the MASW-PIS method can significantly reduce side lobes and aliasing using the auto-power spectrum analysis, which can help minimize the misidentification of apparent higher and/or lower modes. Additionally, increasing the sharpness of dispersion image contours using the new method can improve certainty and increase confidence when manually picking the maxima, which is a common step in routine MASW data analysis. The application of the intercept-time scanning technique can eliminate the assumption that the impact point is the generation point of the Rayleigh waves, and therefore eliminate the need for a complex high-accuracy trigger system. As a result, a simpler synchronized trigger system could be used, or the first receiver could be used as a trigger.

CHAPTER 4. SURFACE-WAVE TESTING OF SOIL SITES USING MULTICHANNEL SIMULATION WITH ONE RECEIVER

4.1 Abstract

This chapter includes studies of soil stiffness profiling using the multichannel simulation with one-receiver (MSOR) method. The MSOR method reverses the roles of source and receiver in the multi-channel analysis of surface wave (MASW) method, based on the reciprocity theorem of mechanics. MSOR was originally developed for pavement sites, which tend to have relatively uniform horizontally layered structures compared to soil sites. To examine the feasibility and accuracy of utilizing MSOR for soil sites, the finite element method (FEM) is first employed to simulate MSOR testing for three soil profiles containing (1) horizontal interfaces, (2) a vertical fault, and (3) a dipping interface. The effect of variations in the moving impact locations on the uncertainty and repeatability of the dispersion results is then analyzed. Real-world case studies are carried out to examine the equivalency of MSOR and MASW testing in terms of characterizing dispersion data of soil profiles. From the computational simulations and field case studies, MSOR is demonstrated to be equivalent to MASW testing for practical purposes. In addition, MSOR has the advantages of reduced instrumentation cost, improved portability, enhanced ability to measure multi-mode dispersion curves by utilizing borehole geophones, and the potential for improving efficiency of 3-D stiffness profiling.

4.2 Introduction

Geophysical surface wave methods have been widely utilized to infer stiffness profiles of layered media by employing dispersion characteristics of surface waves (e.g.,

Nazarian 1984, Rix 1988, Park et al. 1999a, Xia et al. 1999, Louie 2001, Xia et al. 2003, Ryden 2004, Socco et al. 2010, Cox and Beekman 2011). Surface wave testing procedures for soil sites typically employ either the two-receiver spectral analysis of surface waves (SASW) method (e.g., Nazarian 1984, Stokoe et al. 1994), or a seismograph with an array of receivers in the multichannel analysis of surface waves (MASW) method (e.g., Park et al. 1998, 1999a). In the past few decades, the MASW method has gained increasing popularly for seismic profiling of soil sites (i.e., Park et al. 1999a, Xia et al. 1999, Louie 2001, Xia et al. 2004, Zywicki and Rix 2005, Song et al. 2007, Vanneste et al. 2011).

In this chapter, the feasibility and validity of using the MSOR method for soil sites is investigated computationally and experimentally. Successful application of MSOR testing for geophysical profiling of soils will expand the usefulness of surface methods for various scenarios, such as organizations and developing countries with budgets limited to only a few geophones and data acquisition systems having only a few channels, and increased portability for remote test sites with limited accessibility or emergency response after earthquakes.

The reciprocity principle has been widely used for interchanging source and receiver locations without affecting recorded seismic signals (e.g., Dahlen and Tromp 1998, Ikelle and Amundsen 2005, Burger et al. 2006). Arntsen and Carcione (2000) numerically demonstrated the feasibility of applying reciprocity with distributed sources instead of point sources. Wapenaar (1998) reported that the reciprocity principle is satisfactory with different characteristics of source and receiver, provided that the amplitude of the signal is not critical. Traditional active surface wave methods extract

frequency-related dispersion information from multichannel field data by employing an array of point receivers and a distributed active source. For near-surface profiling, the point receivers typically consist of 24 or 48 geophones coupled to soil by ground spikes, with the source consisting of a sledgehammer striking a 15-cm by 15-cm rectangular aluminum plate. If the multiple receivers with a single impact location are exchanged for multiple impact locations with a single receiver, the dispersion images of two testing procedures should theoretically be equivalent based on the reciprocity principle. Whether the principle of reciprocity holds in practice for actual soil profiles and testing conditions including the presence of external noise is examined in this chapter.

The single-receiver MSOR method has been successfully applied to nondestructive testing of pavements (e.g., Ryden et al. 2001, 2002a, 2006, Park et al. 2002, Olson and Miller 2010, Lin and Ashlock 2014b) and soils (e.g., Lin and Ashlock 2011, 2014a). It has several advantages compared to the multi-receiver methods such as MASW, including: (1) greatly reduced instrumentation costs, since only one sensor and a two-channel data acquisition system are required; (2) increased portability, as a multichannel seismograph with external battery source and string of geophones are not required; (3) enabling minimally invasive measurement of higher modes using a single borehole for downhole receiver measurements with moving impacts at the surface (Lin and Ashlock 2014a, Ashlock and Lin 2014); (4) the potential to be faster than MASW if a movable servo-electric impact source is used, as the set-up time for a string of geophones and cables is eliminated; and (5) ease in obtaining 3-D stiffness profiles, as the source can readily be moved along different horizontal lines, compared to reinstalling an entire

string of geophones multiple times to cover the entire testing area for MASW, as shown in Figure 6.4 in Chapter 6.

The MSOR method has two primary requirements: (1) repeatable impacts that can generate waves with consistent energy, timing, and triggering (Park et al. 2002) and (2) accurate and consistent impact locations. To exclude negative effects caused by these inconsistencies, an FEM simulation was first employed to study the reciprocity of dispersion images for MASW and MSOR methods for three types of site structures under ideal testing conditions. The cross-correlation function was then used to statistically analyze the distribution of sampling time-lags among stacking signals, which can arise from the impact inconsistencies mentioned above. To examine the potential errors caused by these inconsistencies, a uniform distribution of lags was employed to simulate the effect of variations in impact locations on the accuracy of dispersion data. One real-world case study was performed using MASW and MSOR at the same site to demonstrate their equivalence in terms of the reciprocal dispersion data.

4.3 FEM Simulations of MASW and MSOR at Soil Sites

To assess the feasibility of applying the MSOR testing procedure to various soil sites, the finite element method was utilized to simulate the MSOR method with moving impact locations and fixed geophones at the ground surface. The soil models defined in Tables 4.1, 4.2, and 4.3 were simulated in Abaqus 6.10-1, using infinite elements on the two lateral boundaries. A transient impact was applied to simulate the dynamic loading of a sledge hammer on the free surface at selected source locations, and the vertical velocity was recorded at the geophone locations. The velocity records were assembled to form multichannel records, from which the dispersion images were calculated using the Phase-

velocity and Intercept-time (PIS) Scanning procedure detailed in Chapter 3. The MASW test procedure was then simulated for the same models by reversing the geophone and source locations. Finally, dispersion images of MASW velocity data for each soil model were calculated and compared against their counterparts from MSOR data.

4.3.1 Case 1: Site with three horizontal layers

Case 1 consisted of a site with uniform horizontal layers, as assumed in the theoretical matrix method formulations presented in Chapter 2. The MSOR moving impacts were applied successively to the 24 source locations shown in Figure 4.1, which have a spacing of 1 m and a first offset of 2 m from the single geophone. Figure 4.2 shows that the dispersion curves of the MSOR and MASW simulations are in good agreement with each other, as well as their theoretical counterpart obtained via the transfer matrix method. Thus the equivalency of the MASW and MSOR testing approaches is demonstrated for this case of uniform horizontal layers and idealized testing conditions without impact inconsistencies or external noise. Slight variations in the FEM dispersion curves are apparent in the figure. It can be shown that simulations using the stiffness matrix method will produce much smoother curves, similar to that from the transfer matrix method in Figure 4.2. Therefore, the slight fluctuations in the FEM dispersion curves are likely due to numerical issues such as discretization error and modeling error for the finite boundaries.

Table 4.1 Properties of layered soil model for Case 1.

Layer #	V_S (m/s)	Poisson's ratio, ν	Density, ρ (kg/m^3)	Layer thickness, h (m)
1	150	0.30	1800	2
2	200	0.30	1800	3
3	400	0.30	1900	∞ (half space)

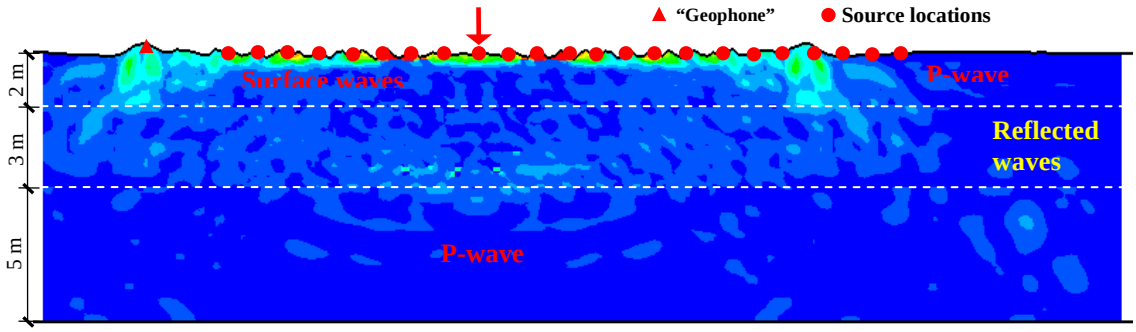

Figure 4.1 FEM simulation of wavefield propagation in layered soil model of Table 4.1 for MSOR test. (Vertical displacements exaggerated. Contour plot is snapshot of von Mises stress.)

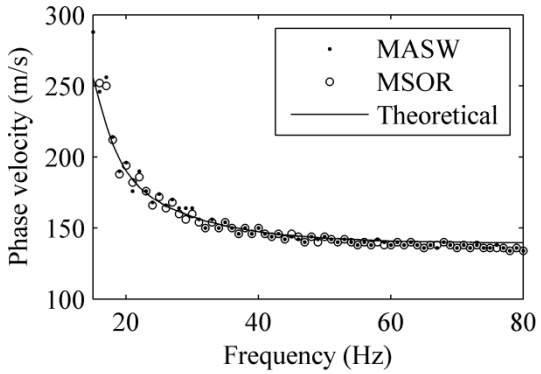

Figure 4.2 Experimental dispersion curves from FEM simulations of MASW and MSOR tests on horizontally layered site. (Theoretical curve from transfer matrix method).

4.3.2 Case 2: Site with a vertical fault

To further assess the feasibility of the MSOR method for more complex soil sites than can be handled by the matrix methods detailed in Chapter 2, the FEM was used to simulate the MSOR and MASW testing on a site with a vertical fault. The material properties of the soil model are given in Table 4.2. Impacts were applied successively from left to right at the 47 locations shown in Figure 4.3. The impact stations have a spacing of 0.5 m and a first offset of 2 m from the geophone. The 1st to 24th impacts were applied to the left of the fault, and are referred to as MSOR impact set I1. The 24th to 47th

impacts were applied to the right of the fault, and comprise MSOR impact set I2. The MSOR data for the I1 and I2 impact sets were assembled to form multichannel records and dispersion images, the peaks of which are plotted as hollow circles in Figures 4.4a and 4.4b.

Table 4.2 Properties of layered soil model with vertical fault for Case 2.

Layer #	V_S (m/s)	Poisson's ratio, ν	Density, ρ (kg/m^3)	Layer thickness, h (m)
1	150	0.30	1800	4 (left), 2 (right)
2	400	0.30	1900	∞ (half space)

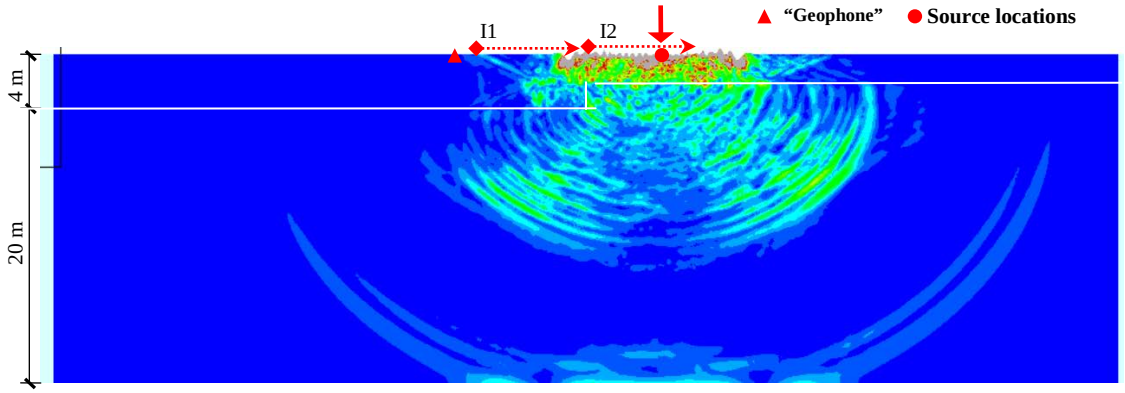

Figure 4.3 Simulation of MSOR testing at soil site with a vertical fault. (Vertical displacements exaggerated. Contour plot is snapshot of von Mises stress.)

The geophone and impact locations used in the MSOR simulation were then switched to perform an MASW simulation on the same model with one impact and 47 geophones. The 1st to 24th geophones and the 24th to 47th geophones comprise the first MASW geophone set (G1) and the second MASW geophone set (G2), respectively. The MASW data for geophone sets G1 and G2 were assembled to form two sets of multichannel records and dispersion images, the peaks of which are also plotted in Figures 4.4a and 4.4b as solid dots. Also shown in the figures are the theoretical dispersion curves evaluated by the matrix method for the vertical soil profiles at the centers of the corresponding geophone/impact spreads.

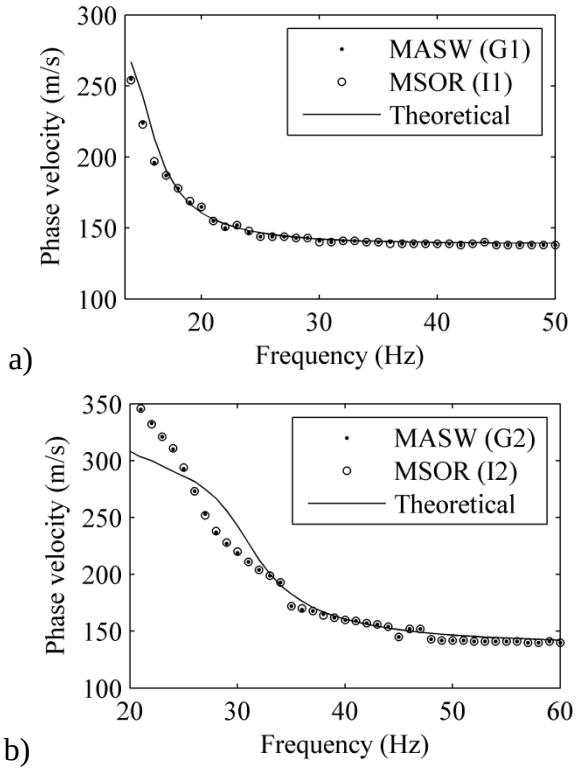

Figure 4.4 Experimental dispersion curves for soil site with vertical fault: a) simulated MASW of G1 and MSOR of I1, b) simulated MASW of G2 and MSOR of I2. (Theoretical curves from transfer matrix method at center of testing spreads).

Comparison of Figures 4.4a and 4.4b reveals that the experimental dispersion curves obtained using MSOR and MASW are in excellent agreement. This demonstrates that the two methods are equivalent for practical purposes, even for this more complicated case of a soil structure containing a fault. As mentioned in Chapter 3, the theoretical matrix methods required the assumption of perfectly uniform and horizontal layers, and are therefore unable to handle the faulted structure shown in Figure 4.3. This explains the good agreement between FEM and transfer matrix results in the above figure for lines I1/G1 located before the fault, and the discrepancies in the low-frequency range for lines I2/G2 which are located after the fault.

4.3.3 Case 3: Site with dipping interface

To further study more general site conditions than the matrix methods can handle, FEM simulations were performed for MSOR and MASW tests on a site with a dipping interface (Table 4.3). Moving impacts were applied successively to 24 locations having a spacing of 1 m and a first offset of 2 m from the geophone (Figure 4.5). As shown in the figure, two geophones were placed symmetrically on the left and right sides of the centerline. The MSOR data of the left and right geophones for the 24 impacts were assembled to form two sets of multichannel records, from which the two MSOR dispersion curves in Figure 4.6 were calculated. The geophone and impact locations were then switched to obtain the two MASW dispersion curves shown in the figure. The four simulated experimental dispersion curves from the forward and reverse MSOR and MASW tests are all in excellent agreement with the theoretical counterpart at the centerline of the profile. This agreement also validates the middle-of-receiver-spread assumption commonly assumed for the MASW method (e.g., Luo et al. 2009).

Table 4.3 Properties of soil site with dipping layer for Case 3.

Layer #	V_S (m/s)	Poisson's ratio, ν	Density, ρ (kg/m^3)	Layer thickness, h (m)
1	150	0.30	1800	7 (left), 4.5 (middle), 2 (right)
2	400	0.30	1900	∞ (half space)

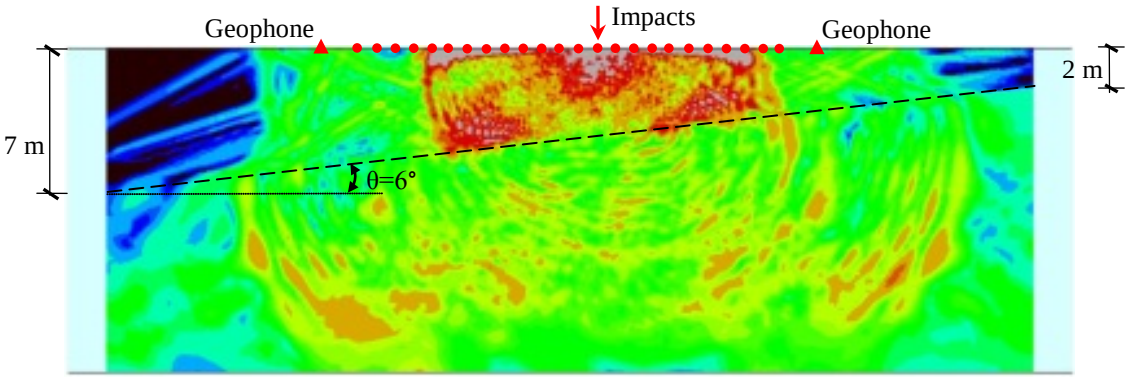

Figure 4.5 Simulation of MSOR testing at soil site with dipping interface. (Vertical displacements exaggerated. Contour plot is snapshot of von Mises stress.).

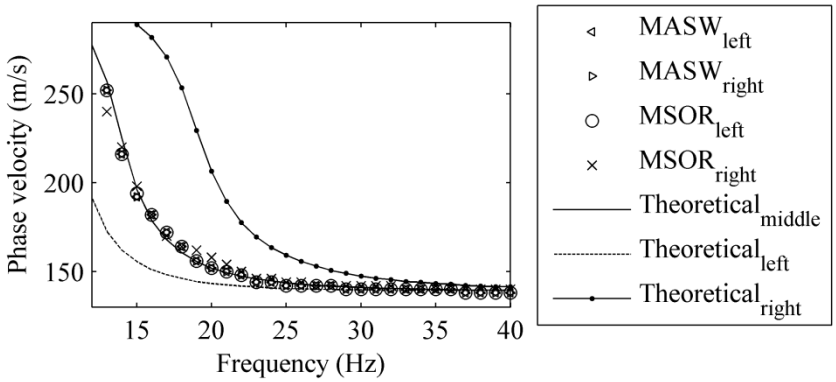

Figure 4.6 Experimental dispersion curves for FEM simulations of MASW and MSOR testing at soil site with dipping layer. (Theoretical curves from transfer matrix method at centerline).

From the preceding three FEM simulations, one can conclude the following: (1) in the absence of experimental error, the MSOR is theoretically equivalent to the MASW method in terms of experimental dispersion curves for soil sites, and (2) the reciprocity principle holds for surface Rayleigh waves in terms of the reciprocal dispersion curves, which depend only upon phase information but are independent of amplitude (i.e., attenuation).

4.4 Effect of Inconsistencies in MSOR Impact Locations

In the above numerical simulations, the idealized impacts are free from sources of experimental error and are thus exactly repeatable. However, due to slight variations in impact location, triggering, energy, and external noise, impacts in actual physical tests are not completely repeatable. Therefore, signals used for the common practice of stacking (i.e., summing) to reduce effects of random errors are not completely repeatable and exhibit variations in sampling time-lags, amplitude, and frequency content. As will be discussed in a later chapter, the consistency of impacts is critical for success of MSOR testing in pavements, because of the high frequencies (several kilohertz), high phase velocities, and small receiver spreads used. On the other hand, MSOR testing for soils typically employs frequencies less than 100 Hz, and is therefore much less sensitive to the repeatability of impacts, because low-frequency wave components are least affected by the inconsistencies (Park et al. 2002).

In this section, a quantitative study on the repeatability of impacts for MSOR soil testing was conducted using the cross-correlation function to quantify the number of sample lags between stacking signals from repeated impacts. Relative errors in dispersion curves were then examined to quantify their variability due to the imperfect repeatability of impacts.

4.4.1 Lags of stacking signals

The cross-correlation function is widely used to quantify the dependence of one signal on another (e.g., Bendat and Piersol 1986, Taghizadeh 2000):

$$R_{x_2x_1}(\tau) = \lim_{T\to\infty} \frac{1}{T} \int_0^T x_2(t) x_1(t+\tau) dt \,, \tag{4.1}$$

where x_1 and x_2 are two signals, and T is the observation time. For discretely sampled signals, Eq. (4.1) is defined as:

$$R_{x_2x_1}(m) = \frac{1}{N}\sum_{n=1}^{N-m} x_2(n)x_1(n+m), \tag{4.2}$$

where m=0, 1, 2, 3, …, N are sample lags (time shifts) and N is the number of discrete sample points. If x_1 and x_2 are identical, the cross-correlation will have a maximum at lag m=0. If x_2 is the same signal as x_1 with a shift of m lags, the cross-correlation will have a maximum at lag m. Thus, the cross-correlation function can quantify the variability of repeated impacts if they are of similar shape, in terms of time-shifts quantified by lags between stacking signals. If the impact and trigger are exactly repeatable, the geophone response signals will be identical with a maximum cross-correlation at lag m=0. In reality, the signals for stacking will exhibit variations in time breaks and amplitudes, as shown in Figure 4.7 for field data from 10 sledgehammer impacts on soil at 25.6 m (84 ft) from a geophone. For the field tests, 10 stacking signals were performed at each of 12 different impact stations ranging from 3.66 m (12 ft) to 43.89 m (144 ft) offset from the geophone, with 3.66 m (12 ft) station separations. More details on the tests can be found in Lin and Ashlock (2014a).

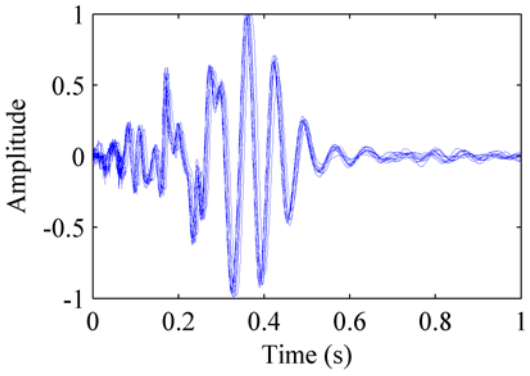

Figure 4.7 Ten geophone signals for stacking due to sledgehammer impacts on soil surface 25.6 m away in MSOR tests.

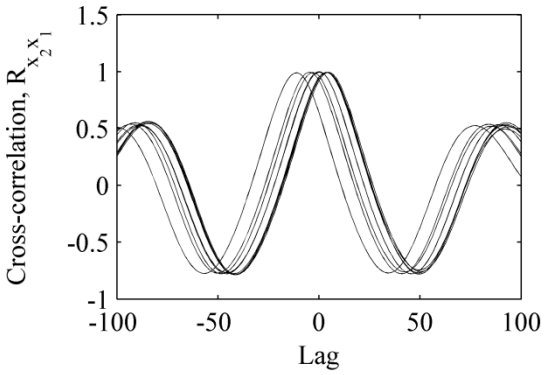

Figure 4.8 Cross-correlation between the first and all other signals in Figure 4.7.

The cross-correlation function between the first impact signal (x_1) in Figure 4.7 and all others (x_2) was calculated using Eq. (4.2), giving the results shown in Figure 4.8. The maximum coefficient of cross-correlation as well as the corresponding lags can be found from the peaks in Figure 4.8. The lags between the first stacking signal and the other nine are then plotted versus impact number in Figure 4.9. A positive or negative lag means the corresponding impact occurs later or earlier, respectively, than the first one. The signals from the 2nd, 3rd, 6th, and 9th impacts all have lag values of +4 with respect to the first signal, and are therefore considered to be the most repeatable signals.

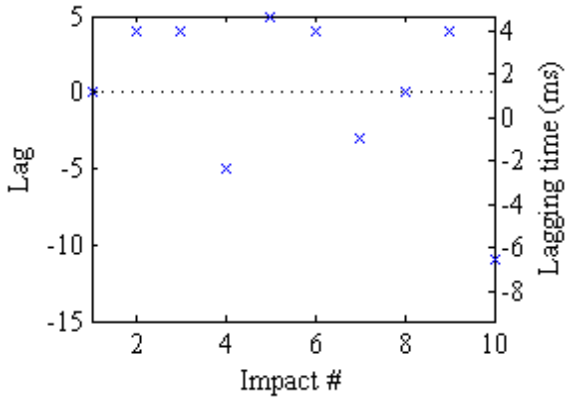

Figure 4.9 Lags between first signal and 9 others in Figure 4.8.

The cross-correlation analysis was then repeated using one of the most repeatable signals as x_1 for 10 signals at each of 12 impact stations with offsets ranging from 3.66 m (12 ft) to 43.89 m (144 ft), giving a total of 120 lags. All 120 lags are shown in the distribution in Figure 4.10, indicating that about 50% of the signals have zero lag and the maximum lag is around 15 samples, or a time of 15 samples × 0.78125 msec/sample = 11.7 msec. To examine the worst-case scenario for the influence of the sampling lags on the experimental dispersion image, the zero-lag signals were ignored, and a uniform distribution, $U(-15,15)$ was used to simulate the effect of inconsistent impacts by perturbing a set of MASW data.

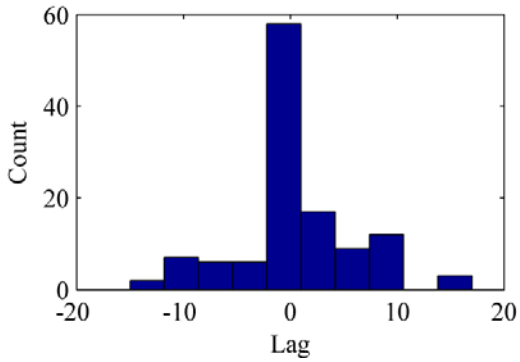

Figure 4.10 Frequency distribution of 120 lags from 10 stacking signals at each of 12 impact stations in MSOR field tests of soil site.

4.4.2 Effect of inconsistent impacts on dispersion curves

The set of MASW data shown in Figure 4.11 (which has zero lags, since all traces are for a common impact) was used to form synthetic MSOR data by perturbing each trace by a random number of lags according to the uniform probability distributions $U(-n,n)$, with n ranging from 1 to 15. The dispersion curves obtained as maxima of the dispersion images of the synthetic MSOR data are shown in Figure 4.12a. The curves are shown with and without stacking applied, and also compared against the dispersion curve of the original un-perturbed MASW data. The average errors of the simulated MSOR

dispersion curves relative to the MASW dispersion curve are calculated by Eq. (4.3) and shown in Figure 4.12b for *n* ranging from 1 to 15.

$$\text{Average error} = \frac{1}{N}\sum_{i=1}^{N}\frac{\left|V_{ph,i}^{\text{MSOR}} - V_{ph,i}^{\text{MASW}}\right|}{V_{ph,i}^{\text{MASW}}} \tag{4.3}$$

where $V_{ph,i}^{\text{MSOR}}$ and $V_{ph,i}^{\text{MASW}}$ are phase velocities at the i^{th} frequency from the dispersion curves with MSOR and MASW methods, respectively, and N is the total number of frequency points. As shown in these figures, the simulated MSOR dispersion curves, even with the most unfavorable distribution of sampling lags, are in good agreement with MASW, especially after stacking. The RMS error is less than 6% for the maximum distribution width of 15 samples, and drops well below 1% if stacking is used. From this study, one can conclude that the inconsistency of impacts in MSOR testing in the form of inconsistent break times, as might be caused by an inconsistent hammer trigger or slight variations in impact locations, does not appreciably affect experimental dispersion curves. However, the above stochastic approach of perturbing MASW data by uniform probability distributions of sampling lags does not account for other types of real impact inconsistencies, such as differences in environmental noise, impact energy, or frequency content. To account for these variables, a direct comparison between MSOR tests with stacking and MASW tests at the same site is presented in the next section.

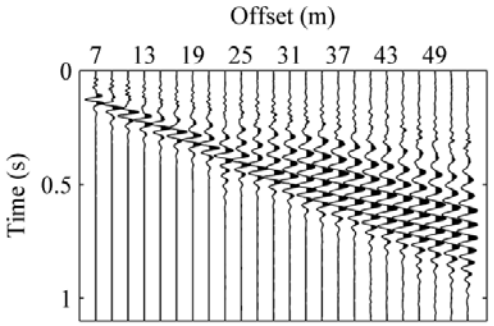

Figure 4.11 Velocity traces from MASW test with 24 receiver offsets.

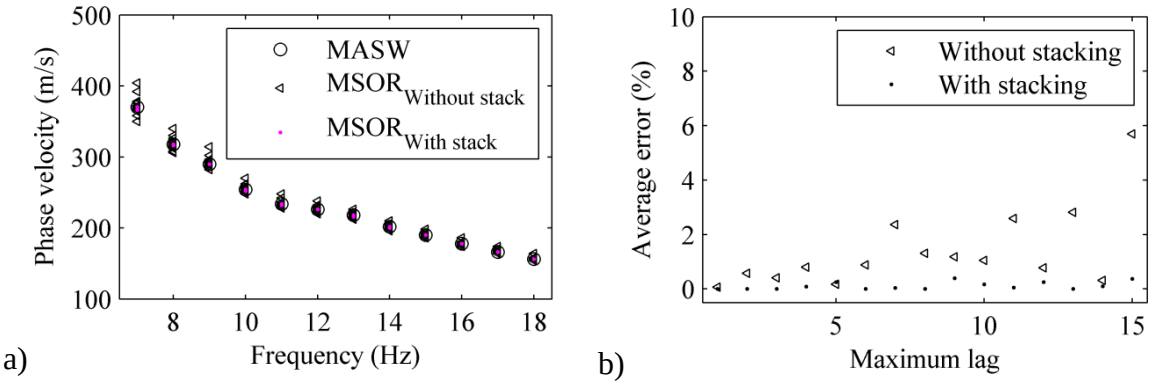

a) b)

Figure 4.12 a) Dispersion curves; b) Average error.

4.5 Field Case Studies of MSOR Testing for Soil Sites

For a direct comparison of MSOR and MASW tests at the same site, field tests were conducted at the East River Valley recreational site in Ames, Iowa (Figure 4.13a). Twenty-four 4.5 Hz vertical geophones were coupled to the soil surface using ground spikes. A triggered 10 lb sledgehammer source was used to generate Rayleigh waves by impacting an aluminum plate resting on the ground surface. A Geode 24-channel seismograph from Geometrics Inc. was utilized for data acquisition, with a sampling interval of 0.5 msec. A 2 m station separation was used over an offset range from 7 to 53 m, and 10 impacts were performed at an impact offset of 7 m from the first geophone for MASW signal stacking. Equivalent MSOR tests were then performed using the reciprocity principle, by placing the first geophone at the previous MASW impact location and performing 10 stacking impacts at each of the previous MASW receiver locations (Figure 4.13b). Figures 4.14a and 4.14b show the velocity traces of MASW and MSOR tests in the space-time (x-t) domain, and the corresponding FFT amplitudes from 7 to 18 Hz. The comparison indicates that the general agreement between MASW and MSOR in the x-t domain increases as the impact offset increases, and this fact is reflected in the x-f domain by FFT spectra that become closer with increasing offset. Figures 4.14c

and 4.14d show the dispersion images of MASW and MSOR, which are qualitatively in good agreement. The MSOR tests show slighty more low-frequency energy between 7 and 9 Hz. This is likely a result of many students moving around during the duration of MSOR testing which required 240 impacts, while the MASW test was quicker with only 10 impacts. The relative error of dispersion images, as shown in Figure 4.14e, decreases as the frequency increases; the average error is about six percent. The comparison of MASW and MSOR data in Figure 4.14 indicates that MSOR can detect similar dispersion data as MASW.

a) 

b) 

Figure 4.13 Field testing: (a) MASW and (b) MSOR (only data from the first geophone is used).

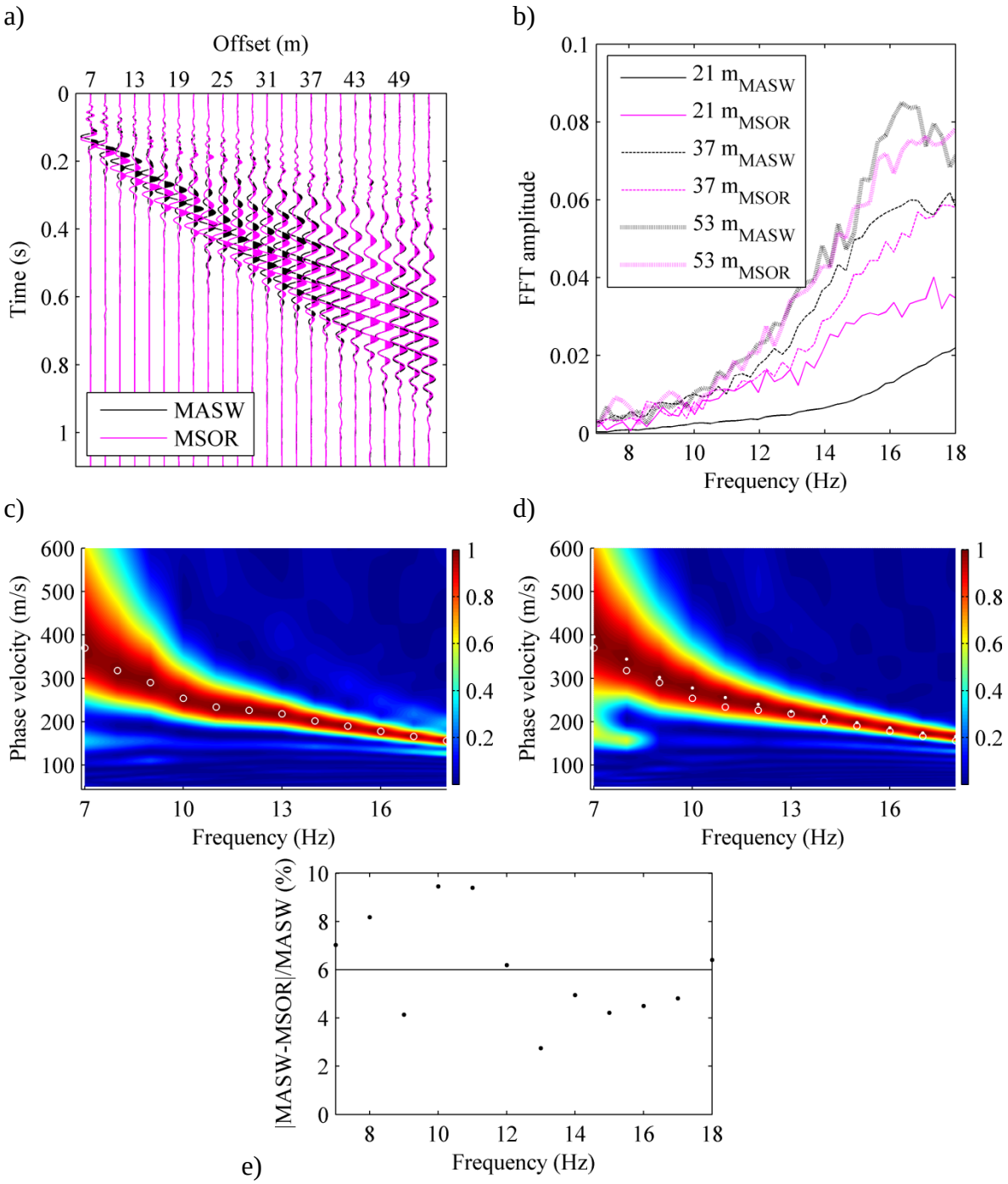

Figure 4.14 a) MASW and MSOR field data, b) FFT amplitude, c) Experimental dispersion image of MASW data (white circles are the maxima.), d) Experimental dispersion image of MSOR data (white circles are the maxima of MASW, white dots are the maxima of MSOR), e) error of MSOR dispersion image peaks relative to MASW.

4.6 Conclusions

The numerical simulations of MSOR tests and inconsistent impacts, and field tests presented herein demonstrate the feasibility of using the moving-source one-receiver method as an alternative surface wave testing procedure at soil sites. To characterize dispersion data, it was demonstrated that MSOR is practically equivalent to MASW testing if a consistent impact can be ensured. Consistent impacts require a repeatable trigger system and minimal variation of the impact locations. Using a single geophone and a two-channel dynamic signal analyzer powered by a USB cable from a laptop, the MSOR method is highly portable and can significantly reduce instrumentation cost. Thus, MSOR may be ideal for site investigation in remote sites and for post-earthquake characterization immediately after earthquakes before ground conditions change.

CHAPTER 5. SURFACE WAVE TESTING OF PAVEMENTS

5.1 Abstract

This chapter presents a computational and experimental study on seismic stiffness profiling of pavements using the multi-channel analysis of surface waves (MASW) and multi-channel simulation with one receiver (MSOR) testing procedures. Development of a new custom-programmed data acquisition system for MASW and MSOR testing using MATLAB software and National Instruments hardware are detailed. Effects of different receiver coupling methods on the test results are examined. The cross-correlation function is employed to statistically quantify the repeatability of impacts, which is critical for MSOR tests in which multi-channel records are simulated by performing multiple impacts over a range of incremental offsets from a single fixed receiver. Experimental dispersion data from MASW and MSOR tests performed at the same site with the same testing system are compared, and MASW is found to enable measurement of dispersion data to much higher frequencies than MSOR. Inversion results from MASW and MSOR data at the same site are compared, and it is found that MASW is able to provide measurements of the stiffness of the surface layer with reduced variability.

5.2 Introduction

Surface wave testing of pavements can be traced back to the continuous surface wave (CSW) method developed by Van der Poel (1951) and further advanced by Heukelom and Foster (1960), Jones (1955, 1958, and 1962) and Vidale (1964). After the popularization of the FFT in the 1960s, the CSW testing procedure evolved into the widely used SASW method developed by Heisey et al. (1982), Nazarian (1984), Rix (1988), and Stokoe et al. (1994). Following the success and wide usage of MASW in

near-surface stiffness profiling of soils (e.g., Park et al. 1999a), the method was also applied to pavements using multiple geophones by Park et al. (2001b), and later using multiple accelerometers by Tertre et al. (2010). To reduce the cost and inconvenience of coupling multiple receivers to pavement in MASW, the MSOR method was developed and applied to pavement stiffness profiling by Ryden et al. (2001), Ryden et al. (2002a, 2002b, 2006), Park et al. (2002), Olson and Miller (2010), and Lin and Ashlock (2011). In MSOR, synthetic multichannel records may be created by applying multiple impacts at a fixed source location while a single receiver is incrementally moved out to cover a range of offsets. Alternatively, the source and receiver in MSOR are more commonly reversed according to the reciprocity theorem of mechanics, such that the receiver is fixed while the impact location is moved out.

Due to the decreasing velocity (stiffness) of pavement layers with depth, phase velocity spectra from surface wave tests on pavements primarily show an increase in phase velocity with frequency. However, wave propagation in pavement layers is very complex. As detailed in Ryden et al. (2006), experimental phase velocity spectra actually consist of several branches that can be approximated as multiple modes of anti-symmetric and symmetric Lamb waves for a free plate corresponding to the material properties of the stiff surface layer. The correspondence to Lamb waves is approximate, as the surface layer is not truly free, but interacts with the underlying base and subgrade layers in the low-frequency regime to create partial branches of leaky quasi-Lamb waves. However, at high frequencies (typically above 10 kHz), the experimental phase velocities approach those of the fundamental anti-symmetric (A0) and symmetric (S0) modes of dispersive Lamb waves, which themselves asymptotically approach the surface layer's Rayleigh

wave velocity. To obtain accurate properties of the base and subgrade layers, inversion of the phase velocity dispersion data would require matching of the low-frequency branches generated by interaction of leaky quasi-Lamb waves in these layers. Alternatively, if only the properties (E-modulus and thickness) of the stiff top asphalt layer are desired, inversion can be avoided by using a simplified analysis in which experimental phase velocities are matched to fundamental anti-symmetric (A0) mode of Lamb waves in a free plate (as well as segments of the S0 mode, if detected), as described by Ryden et al. (2004, 2006).

Whether using a multi-layer inversion or the free-plate Lamb wave approximation, resolution of the top pavement layer properties requires accurate experimental measurement of the phase velocity spectrum at high frequencies. A high-resolution testing setup and delicate operation are required due to the high wave speeds, short wavelengths, and small motions involved. To reliably measure high-frequency dispersion characteristics, the MSOR method requires a repeatable impact source that can generate waves with consistent timing and triggering (Park et al. 2002), with minimal deviation from the intended impact locations. In the author's experience, the MASW method can provide more reliable measurement of high-frequency components owing to the fixed receiver locations and less-stringent requirement on impact repeatability. The primary drawbacks of MASW testing for pavements are the costs of multiple accelerometers and a multi-channel signal analyzer, and the time required for coupling and decoupling of multiple accelerometers.

To examine the performance of MSOR and MASW methods in acquiring high-frequency dispersion data, a new data acquisition system and program was developed in

this study using National Instruments hardware and MATLAB software, with PCB accelerometers used as receivers and triggers. The data acquisition system and program are described in the following section. The repeatability of impacts in experimental MSOR data is then quantified using the cross-correlation function. The inconsistency of impacts is modeled using a normal distribution of inconsistent time breaks in terms of their sampling time-lags. Perturbations to experimental MSOR and MASW data in the form of normal time-lag distributions are compared in terms of their effects on the phase-velocity spectra. A real-world case study is carried out with both MSOR and MASW tests on the same pavement to compare dispersion data and inverted shear-wave velocities of the surface layer from the two testing methods.

5.3 Surface Wave Testing Systems and Experimental Issues

The MASW testing system used in this study consists of nine PCB accelerometers (one model 621B51, six 353B33, and two 356B08), an impact hammer with one of the accelerometers mounted as a trigger, and a multichannel signal analyzer assembled from National Instruments (NI) hardware, as shown schematically in Figure 5.1a. The signal analyzer is comprised of an NI cDAQ-9172 USB chassis and three NI 9234 4-Channel, 24-Bit analog input modules having a maximum simultaneous sampling rate of 51.2 kHz. A 12-volt deep-cycle marine battery and pure sine-wave inverter were used to power the chassis in field tests. The MSOR testing equipment consists of the same impact hammer with accelerometer trigger, a single PCB 621B51 high-frequency accelerometer as a receiver, and a single NI 9234 input module in a USB-powered cDAQ-9171 single-slot chassis, shown schematically in Figure 5.1b. The NI hardware for the MSOR and MASW systems are also shown in Figure 5.2.

a) b)

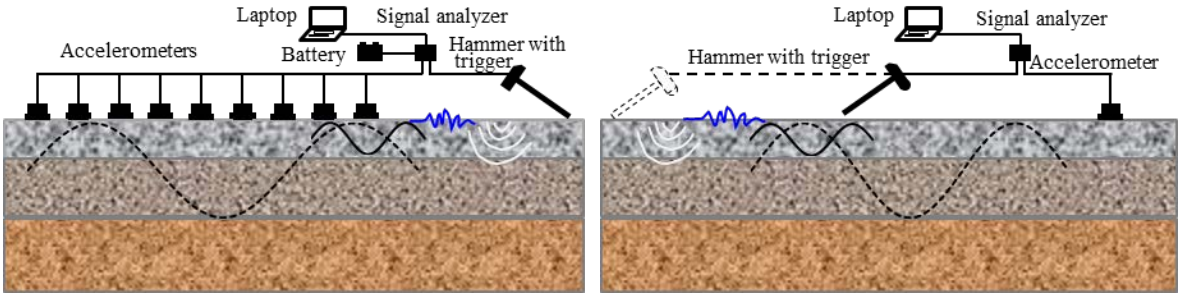

Figure 5.1 Schematic of setup for a) MASW and b) MSOR tests (after Ryden et al. 2002b).

a) b)

Figure 5.2 a) NI 9234 input module in a USB-powered cDAQ-9171 single-slot chassis; b) NI 9234 4-Channel input module and NI cDAQ-9172 USB chassis (from ni.com).

A short-duration transient impact over a small contact area has been widely employed to generate high frequency signals using rounded head ball-peen hammers (Ryden et al. 2001, 2002b, 2004, Park et al. 2001b, 2002, Nazarian 1984) or 8-mm diameter steel balls (Alzate-diaz and Popvics 2009). The mass of hammers used in the literature varies from 0.22 kg (8 oz) to 0.5 kg (18 oz) (Ryden et al. 2001, 2002b, 2004, Park et al. 2001b, 2002). As the interest of this chapter is on the surface asphalt layer, an 8-oz hammer was adopted to generate high frequency (>10 kHz) surface waves with wavelengths comparable to the thickness of surface layer, ranging from 4 to 6 inches.

A triggering system consisting of an accelerometer attached to a hammer was recommended by Ryden et al. (2001). In the present study, it was confirmed that such a

triggering system was more reliable than an off-the-shelf electric contact closure hammer switch from Geometrics, which was designed for much larger sledgehammer sources. Since the NI 9234 input modules do not feature a hardware analog triggering capability, a software trigger was programmed in MATLAB using a circular 3-slot buffer to constantly acquire sample records and extract those containing a trigger event (Figure 5.3). When the signal of the accelerometer mounted on the hammer meets the prescribed trigger level, the triggered records are extracted from the circular buffer with a user-selected number of pre-trigger samples (Figure 5.4). Zero padding in the first and third buffer slots of the trigger channel was used to prevent possible double triggering. The PCB accelerometers were used as high frequency receivers for measurements up to 25 kHz. The frequency range of accelerometers for surface wave measurement can exceed their natural resonance frequencies, because the critical information for the experimental dispersion data is not the magnitude of waves but their relative phase at different offsets (Ryden et al. 2002b).

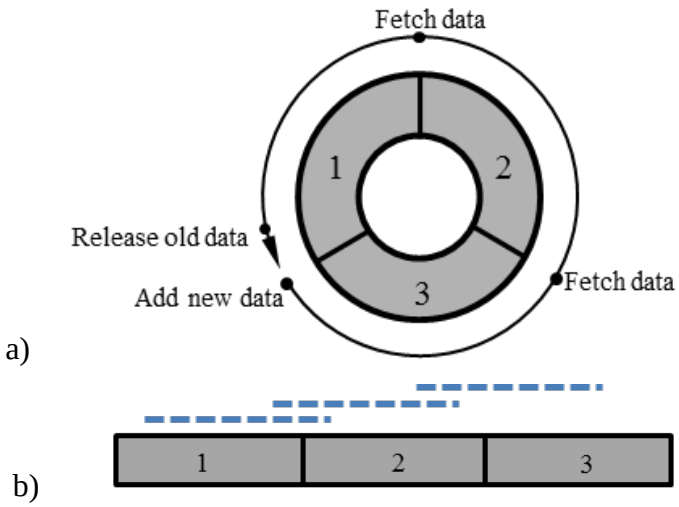

Figure 5.3 (a) circular 3-slot buffer, (b) unwrapped 3-slot buffer. Dashed lines show the possible distribution of signals of interest.

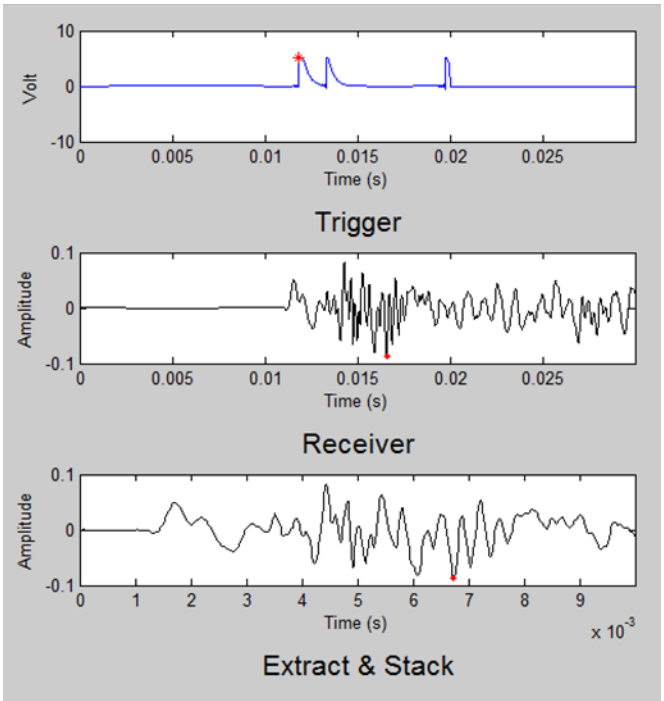

Figure 5.4 Trigger and receiver signals in the MATLAB data acquisition program (double trigger event shown).

A critical issue in surface wave testing of pavements is to ensure a proper coupling of the accelerometers to the pavement surface to achieve a high frequency bandwidth. Several coupling methods were examined in the present study, including plumber's putty, hot glue, superglue, epoxy, and a synthetic waterproof high temperature polymer grease with a working range of -20 to 500 °F (Green Grease brand). Sticky grease was reported by Ryden et al. (2001) to provide an appropriate coupling that can ensure the necessary frequency bandwidth for pavement testing. In the present study, plumber's putty was found to perform comparable to sticky grease, with the added convenience of easy coupling and decoupling. For MASW, a putty strip was formed around the accelerometers to hold them together, thus improving the efficiency of installing the accelerometers with the selected spacing. Coupling of the putty strip with

the pavement surface was improved by adding a thin layer of the polymer grease underneath.

The resonant frequency of the accelerometers is another important consideration for high frequency surface wave testing of pavements. Ryden et al. (2001) examined models having resonant frequencies of 50 kHz and 34 kHz, and reported that the 34 kHz model had the optimum combination of frequency response and sensitivity. The accelerometers used in this study have comparable resonant frequencies of 35 kHz (model 621B51), ≥22 kHz (model 353B33), and ≥20 kHz (model 356B08).

5.4 DAQ Program

A data acquisition and analysis program for MSOR surface wave testing of soils and pavements was developed using MATLAB software. A screen capture of the MASW program is shown in Figure 5.5. The left-most column is the control panel including pushbuttons, and parameter inputs for the experimental dispersion analysis. The middle three columns contain drop-down dialog boxes for selecting the trigger and receiver parameters, and additional parameter inputs for data acquisition. The user can review the signals after each triggered impact with the option to undo and redo. The same DAQ system is used for MSOR testing using only one active receiver.

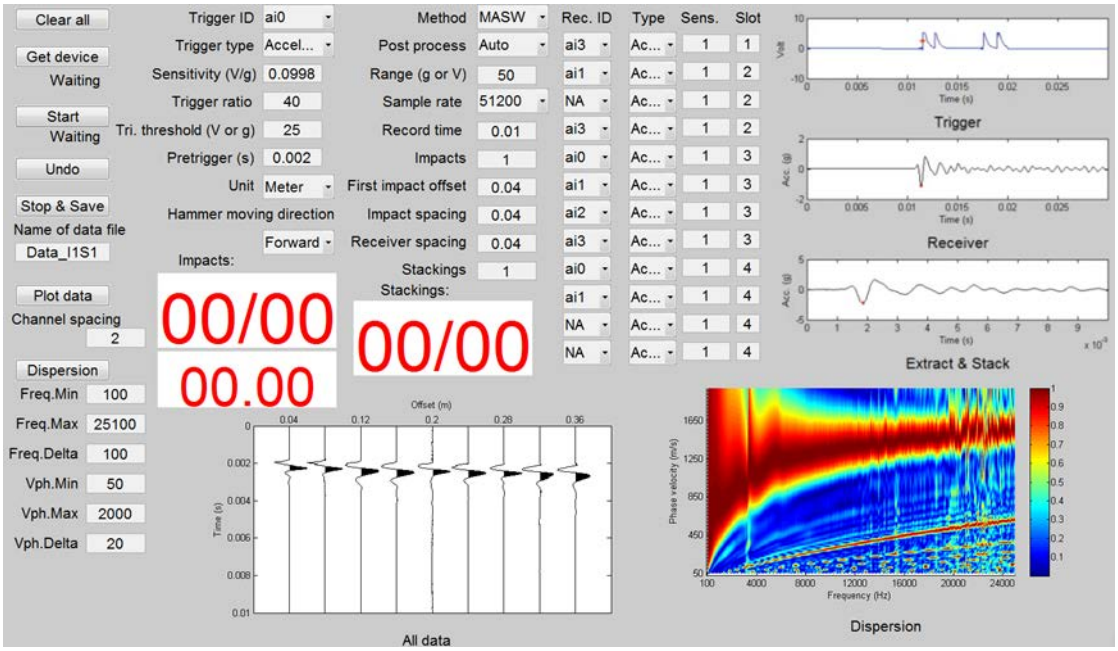

Figure 5.5 DAQ system program window for MASW and MSOR testing.

5.5 Consistency of Impacts

As discussed above, the consistency of impacts is critical for the success of MSOR testing in pavements due to the high frequencies involved, on the order of several kilohertz (Park et al., 2002). Since the accuracy of the digital trigger can be no better than one sample interval (Ryden et al. 2002b), and small variations in impact location are unavoidable when using a manual hammer, it is of interest to statistically quantify the effects of such variations on dispersion data. For this purpose, the cross-correlation function was employed to quantify the sample lags between stacked signals caused by slight variations in impact location, and the root-mean-square (RMS) difference used to measure the discrepancy of the resulting dispersion curves. It should be noted that other methods can also be used to minimize the variations in impact location, such as using a steel spike to couple the hammer to the pavement surface (e.g., Ryden et al. 2004), or correcting the slight differences in time breaks to force all first arrivals to have a

consistent velocity (Park et al. 2002). Although these two latter methods may improve lost resolution in MSOR tests due to slight variations in impact location, they do not address differences in the energy of each blow, whereas all sensors in MASW measure the motion of a common impact.

5.5.1 Lags of stacking signals

The cross-correlation function (e.g., Bendat and Piersol 1986, Taghizadeh 2000) was employed to measure the slight differences among signals used for stacking from repeated impacts at the same offset distance:

$$R_{x_2x_1}(m) = \frac{1}{N}\sum_{n=1}^{N-m} x_2(n)x_1(n+m) \tag{5.1}$$

where x_1 and x_2 are two discrete signals, m=0, 1, 2, 3, …, N are sample lags (time shifts), and N is the number of discrete sample points. If x_1 and x_2 are identical, the cross-correlation will have a maximum at lag m=0. If x_2 is the same signal as x_1 with a shift of m lags, the cross-correlation will have a maximum at lag m. Thus the cross-correlation function can quantify the inconsistency of repeated impacts in terms of lags of stacking signals. If the impact and trigger are exactly repeatable, the accelerometer response signals will be exactly the same with a maximum cross-correlation at lag m=0. In reality, the signals for stacking will exhibit variations in time breaks and amplitudes, as shown in Figure 5.6a for signals from 10 repeated impacts on an asphalt pavement surface at an offset of 0.2 m from the accelerometer, with a sampling interval of 0.02 ms (sample rate of 50 kHz). Figure 5.6b shows the cross-correlation between the first impact signal (x_1) and all others (x_2). The sample lags for each of the 10 signals can be found as the abscissas of the maximum peaks in Figure 5.6b.

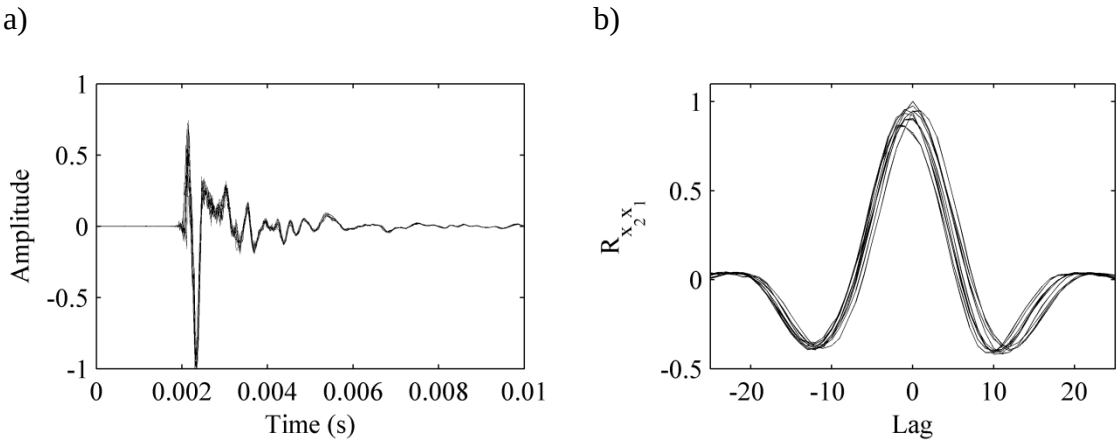

Figure 5.6 a) Ten signals for stacking obtained by hammer impacts 0.2 m away from accelerometer on pavement surface; b) Cross-correlation of the ten signals.

Figure 5.7a shows the lags and the corresponding lag times between the x_1 signal and the remaining nine x_2 signals. Having the same zero lag with respect to the first signal, the four signals from the 2nd, 4th, 6th, and 9th impacts are the most repeatable relative to 1st signal. Similar cross-correlation analyses were conducted for 10 signals at each of 9 impact-stations (a total of 90 signals), taking the most repeatable signal at each station as x_1. The resulting statistical frequency distribution all of 90 lags is shown in Figure 5.7b. Approximately 70 of the 90 signals have zero lag. The one signal having a lag of 10 samples was due to an inappropriate impact, which could be remedied by using the undo button in the DAQ program and repeating the impact. A normal probability distribution, $N(0.189,2.222)$, can be used to describe the distribution of lags, as shown by the solid curve in Figure 5.7b.

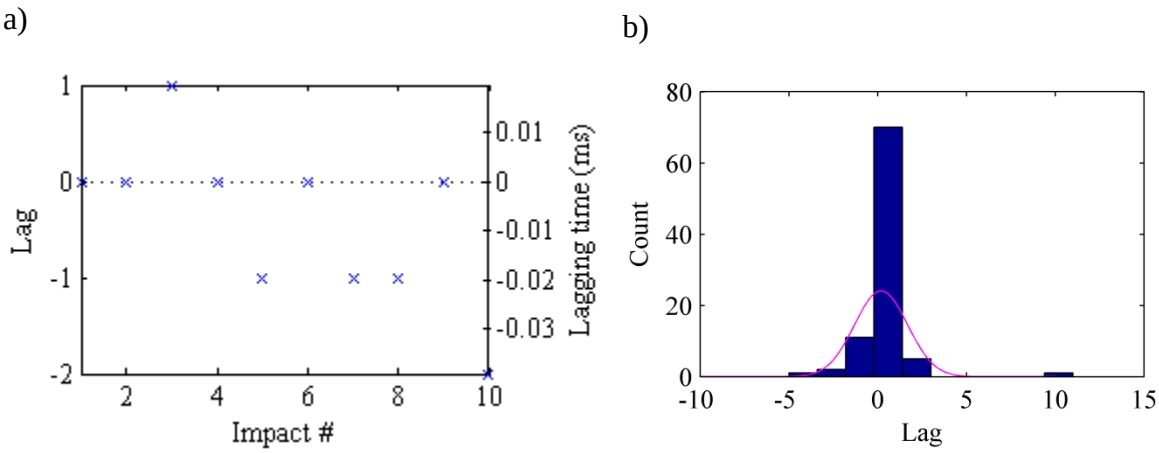

Figure 5.7 a) Lags between signals from 10 impacts at one impact station; b) statistical frequency distribution of 90 lags from 9 different impact stations.

5.5.2 Effect of inconsistent impacts on dispersion curves

To study the effect of inconsistent impacts on experimental dispersion data, the set of 9-channel MASW pavement data shown in Figure 5.8a was recorded for a single impact, then perturbed by injecting sampling lags with the normal distribution shown in Figure 5.7b to form synthetic MSOR data. The resulting dispersion trend of the simulated MSOR data is shown in Figure 5.8b with and without simulated stacking, along with the phase-velocity dispersion image of the unaltered MASW data. The comparison indicates that the high-frequency dispersion data of MSOR is not in good agreement with that of MASW, especially when stacking is not used (Figure 5.8b). The effect of the inconsistent impacts is to reduce the useful frequency range of the dispersion data from approximately 20 kHz to approximately 6 kHz.

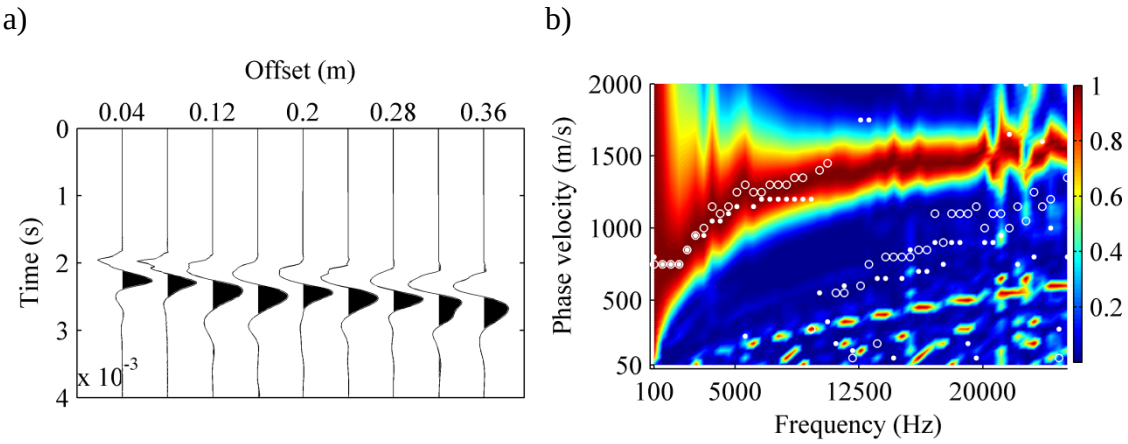

Figure 5.8 a) Field data of MASW test; b) Comparison of experimental dispersion trends for MASW data and simulated MSOR data obtained by applying normally distributed lags to MASW data. (MASW dispersion image in color contour; MSOR without stacking in white dots; MSOR with stacking in white circles.)

5.6 Real-world Case Study: MSOR vs. MASW Tests on Asphalt Pavement

The equipment and DAQ program developed for MASW and MSOR testing were used on an asphalt pavement on the Iowa State University campus (Figure 5.9). MSOR data were recorded with receiver stations from 0.08 to 0.40 m in 0.04 m increments (Figures 5.10a and 5.10c). MASW data were also recorded on the same pavement with impact stations from 0.04 to 0.36 m in 0.04 m increments (Figures 5.10b and 5.10d). The dispersion trend of the MSOR test is also overlaid in the form of white dots on the MASW dispersion image Figure 5.10d. The MSOR dispersion trend agrees with that of MASW up to approximately 7.5 kHz. Beyond this frequency, however, the MSOR phase-velocity spectrum does not exhibit a clear dispersion mode.

a) 

b) 

Figure 5.9 Typical field setups for pavement tests: (a) MSOR and (b) MASW.

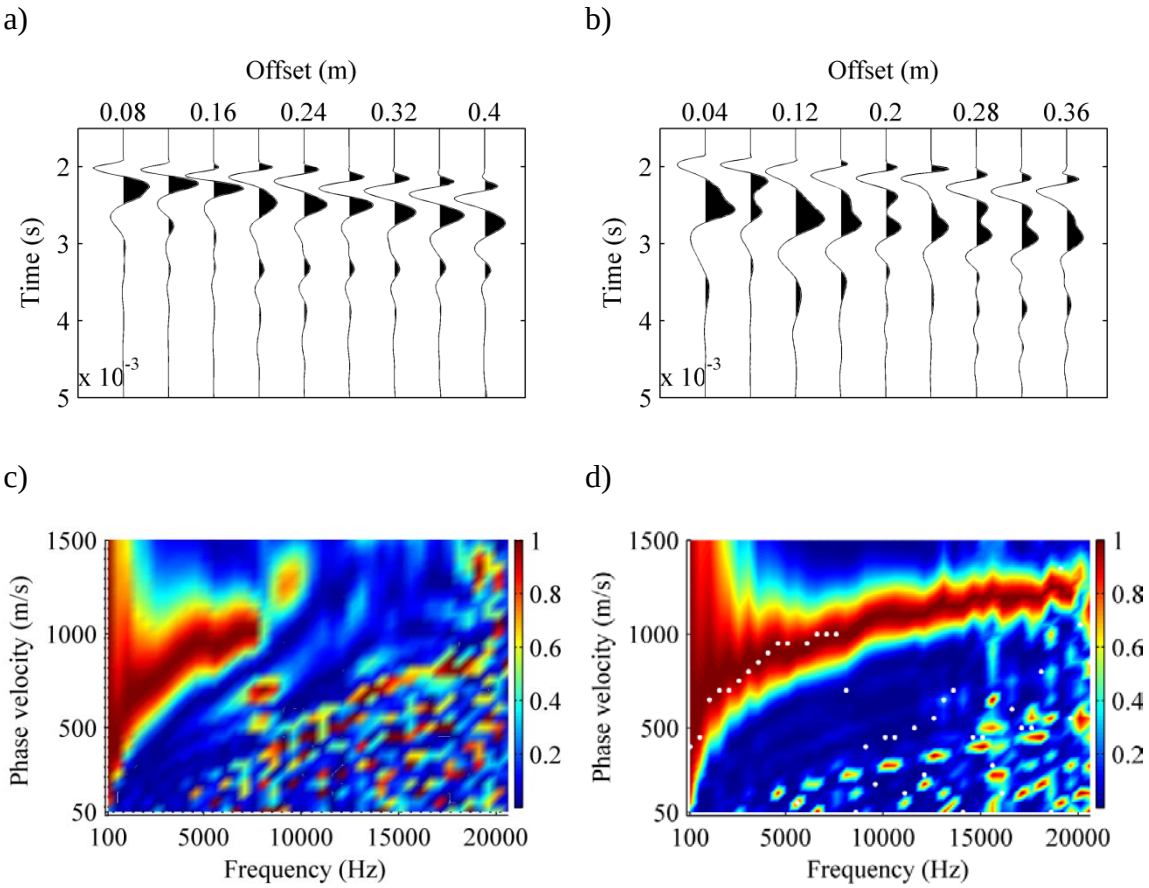

Figure 5.10 a) Field data of MSOR test; b) Field data of MASW test; c) Experimental dispersion image of MSOR test; d) Experimental dispersion image of MASW test (White dots are the MSOR maximum intensity at each frequency from 10c.).

The hybrid Genetic-Simulated Annealing (GSA) inversion program presented in Chapter 8 was used to back-calculate the pavement profile in terms of layer thickness and shear wave velocity, using the maxima of the MSOR and MASW experimental dispersion images of Figure 5.10c (up to 7.5 kHz) and Figure 5.10d (up to 20 kHz) as the target dispersion curves in the optimization. The target dispersion curves were then compared against the theoretical dispersion curves of the final converged profiles over a frequency range of 20 kHz (Figure 5.11a). In the high frequency range beyond 5 kHz, the theoretical dispersion curve of MSOR inversion has higher phase velocities than the experimental MASW dispersion curve, whereas the theoretical dispersion curve of

MASW inversion has better agreement with the experimental counterpart. A statistical analysis of the surface layer's shear-wave velocity was performed using the MASW and MSOR data with twenty inversion trials each. The MASW data resulted in a much smaller deviation in the estimated shear wave velocity than the MSOR data, although the average velocities are close for the two methods (Figure 5.11b).

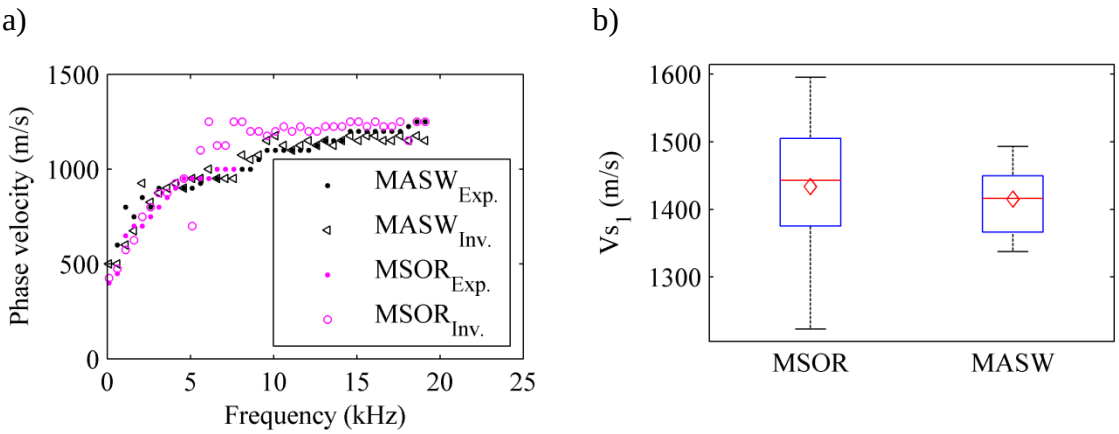

Figure 5.11 a) Comparison of dispersion curves; b) Boxplots of the shear wave velocity of the surface layer (V_{S1}) from MASW and MSOR inversions (central mark is median, diamond is mean, box edges are 25th and 75th percentiles, whiskers extend to most extreme data points not considered outliers).

5.7 Conclusions

The custom-developed equipment and DAQ program can enable surface wave testing of pavements with great efficiency and relatively low cost. Use of a putty strip with a grease coating offers advantages of effective coupling of accelerometers to pavement, convenient sensor locating, and simple decoupling. It was demonstrated that slight variations in impact locations in MSOR testing can have a significant effect on the high-frequency dispersion data. For the methods used in this study, MASW was found to enable measurement of dispersion data to much higher frequencies than MSOR. Inversion of MASW and MSOR dispersion data indicated that MASW tests result in less uncertainty in characterizing the stiffness (velocity) of the surface layer.

CHAPTER 6. MULTI-MODE RAYLEIGH WAVE PROFILING BY MINIMALLY-INVASIVE METHODS

6.1 Abstract

To improve the accuracy of shallow seismic shear-wave velocity profiling, a hybrid minimally-invasive multimodal surface wave (MMSW) method is proposed, which enhances the detection of higher modes of Rayleigh wave dispersion data. The new method combines techniques from the multi-channel analysis of surface waves and multi-channel simulation with one receiver (MSOR) methods to record components of Rayleigh wave motion at the surface as well as at shallow depths within the soil mass.

The performance of the proposed method is demonstrated through computational and experimental studies. It is shown that individual modes of Rayleigh waves can exhibit different dominant depths at which their motion is most significant. This is illustrated through a numerical study of eigenvectors of layered soil profiles via the stiffness matrix method detailed in Chapter 2, and confirmed by a finite element simulation of the apparent dispersion trends recorded at shallow depths using the MSOR testing method detailed in Chapter 4. Upon superimposing dispersion data recorded via the receivers at various depths in the soil, the resulting multi-mode dispersion data is used in a multi-objective inverse analysis, for which the difference between experimental and theoretical dispersive phase-velocity spectra are minimized for multiple modes simultaneously. In the numerical study, the resulting inverted profiles and theoretical dispersion data are shown to have improved accuracy relative to single-mode inversion. Preliminary field tests are performed using the new hybrid method, and the results are

shown to support the conclusions of the numerical study and confirm the feasibility of the proposed technique.

While the use of multiple modes in surface wave testing is not new, the proposed hybrid method can provide more accurate and complete multi-modal dispersion data than achieved with surface-only Rayleigh wave methods. As a result, errors due to misidentification or partial measurement of higher modes may be minimized, thus reducing statistical uncertainty in the inverted profiles.

By reversing the role of surface impacts and borehole receivers in the new MMSW method, an equivalent method employing standard penetration test (SPT) hammer blows as borehole impact sources was also developed. This variant is termed the MMSW-SPT method, and uses a multichannel seismograph with an array of geophones on the soil surface for measuring more complete multimode Rayleigh-wave motions caused by SPT impacts applied at the soil surface as well as at shallow depths within the soil. Due to the prevalence of SPT testing on construction sites, the hybrid MMSW-SPT method can enable more accurate and complete measurement of higher modes than surface-only methods such as MASW, with improved economy and efficiency relative to the single-receiver MSOR variant of the MMSW method.

6.2 Introduction

For surface-wave methods, the quality of experimental dispersion data is of critical importance to infer accurate site profiles in terms of layer thicknesses and shear-wave velocities. Layered soil profiles inherently possess multi-mode dispersion characteristics, which include complete information on the soil profile. However, in the analysis of dispersion data from surface-wave testing, if one selects only the Rayleigh-

wave component that is dominant at each frequency, then a single "apparent dispersion curve" will be obtained. The apparent dispersion curve is comprised of a fundamental-mode curve for "regular" soil sites for which velocity increases gradually with depth, or a combination of several modes for irregular profiles which contain velocity inversions, i.e., fast over slow layers (e.g., see Nazarian 1984, Gucunski and Woods 1992, Stokoe et al. 1994, Park et al. 1999a, Xia et al. 1999, Louie 2001, Ryden 2004, Lu et al. 2007, Wong et al. 2011). The single apparent dispersion curve contains only a fraction of the available information on the soil profile contained in the data, and thus limits the resolution and accuracy of the inversion results.

Previous studies have demonstrated that higher-mode Rayleigh waves not only provide information for greater depths than the fundamental mode, but also improve the accuracy of the inverted shear-wave velocity (V_S) profile, and improve the stability and resolution of the inversion calculations (e.g., Tokimatsu et al. 1992, Xia et al. 2000, 2003, Beaty et al. 2002, Song et al. 2007, Supranata 2006, Luo et al. 2007). However, non-invasive measurement of multi-mode dispersion data from surface waves is challenging for a number of reasons. First, wave trains can be very close together and can even overlap (Crampin and Bath 1965), and different modes may have approximately equal group velocities (Nolet and Panza 1976). Second, the presence of a rigid stratum or stiff layer can cause a higher Rayleigh mode to become dominant at low frequencies, shifting the apparent dispersion curve from the fundamental to the higher mode (Karray and Lefebvre 2010). Even when the fundamental mode appears to be clearly captured, its use in a fundamental-mode inversion can fail to accurately determine the velocity of bedrock (Casto et al. 2010). Analysis of higher modes is thus crucial for accurate determination of

bedrock depth as well as identification and isolation of the fundamental mode in general. Third, it can be difficult to measure higher modes because they can be much less energetic than the fundamental mode (Socco et al. 2010).

The frequency-wave number (*f-k*) method can be used to extract multi-mode dispersion data from measured surface waves, particularly if a long geophone array is used, which aids in separating higher modes with small differences in wavenumber (Gabriels et al. 1987, Stokoe et al. 2004). The *f-k* method can also be used with conventional arrays (e.g., 24 to 48 geophones with spacing of a few meters), although wavenumber resolution $\Delta k = \pi/X$ improves with increasing total array length X (Foti et al. 2002). If several hundred traces and large receiver spreads of several hundred meters are used, significant lateral variation in material properties may be incurred for the depth scales considered in near-surface profiling (Park et al. 1999b). Additionally, it can be seen from various studies that receiver arrays longer than 250 m (Stokoe et al. 2004), 330 m (Gabriels et al. 1987), 600 m (Vanneste et al. 2011), or 2000 m (Klein et al. 2005) can cause the layered profile assumption to become invalid, thus decreasing the reliability of the measurements.

Advantages of more time-consuming and costly borehole methods are their greater accuracy since they involve direct measurement of wave propagation times between two points, and the fact that they do not require an inversion analysis. The primary advantages of surface-wave methods are their non-invasive nature and resulting lower cost relative to borehole testing methods, as well as the ability of Rayleigh waves to yield soil stiffness information well below the sensor elevation, e.g., to depths on the order of 30-50 m for large impact sources, or 75 to over 200 m for Vibroseis sources.

However, solutions for V_S profiles from surface-wave inversion procedures are non-unique (e.g., Calderón-Macías and Luke 2007), and therefore possess statistical uncertainty. Furthermore, if higher modes are not resolved appropriately, they can contribute further to this uncertainty, as they may be mistaken for the fundamental mode. Significant effort has therefore been focused on detecting higher modes in surface wave data to minimize their influence or extract the fundamental mode (e.g., see Park et al. 2000).

The Multichannel Analysis of Surface Waves (MASW) method has been employed to measure multi-mode Rayleigh waves using relatively short geophone arrays of approximately 30 m (e.g., Park et al. 1999b, 2000, Xia et al. 2000, 2003, Song et al. 2007). However, the resulting multi-mode dispersion data are generally incomplete in the frequency range of interest (e.g., Xia et al. 2003, Bergamo et al. 2011), and are unclear at some frequencies (Song et al. 2007). Additionally, including such incomplete or unclear higher modes in the inversion process can result in an inferior fit of the fundamental mode (Casto et al. 2010). A similar technique named the "Modal Analysis of Surface Waves method" has also been used to measure higher modes, although this method appears to selectively skip many of the higher modes (Karray and Lefebvre 2010). The practice of manually picking multi-mode curves from the apparent dispersion data can also yield inaccurate target curves for the inversion analysis, introducing significant errors into the inverted profiles.

As is evident from the studies outlined above, the successful measurement and effective application of higher Rayleigh-wave modes is a challenge that requires advances in experimental and analytical techniques. To this end, a hybrid minimally-

invasive multimodal surface wave (MMSW) method is proposed herein, which combines techniques from MSOR testing, MASW analysis, and borehole or probing methods to limited depths. Using the hybrid method, the accuracy with which higher modes can be measured is improved relative to surface-only methods. The hybrid method can thus be viewed as an enhancement to surface-wave methods by the addition of limited-depth borehole measurements, or conversely, as an enhancement of borehole methods by the addition of surface-wave data, whereby use of Rayleigh waves extends the profiling depth of borehole methods (such as crosshole tests) or probing methods (such as seismic cone penetration test (CPT) tests) well below the maximum depth of the sensor.

6.3 Multi-mode Rayleigh Waves

Non-invasive surface wave methods employing sensors coupled to the ground surface have been widely used to measure Rayleigh waves since the 1980s. An advantage of surface wave methods is the relative ease with which Rayleigh wave motion can be measured, as this wave type comprises the majority of energy generated from a source on the surface. As depth increases, however, the dominant mode of the surface waves will attenuate quickly, while the other modes may become increasingly dominant with mode shapes that are strongly dependent on the soil profile. This is demonstrated below by examining the natural mode shapes of Rayleigh waves with depth, i.e. the natural mode shapes of vibration of the layered soil structure.

6.3.1 Natural mode shapes of Rayleigh waves with depth

To gain insight into mode shapes of Rayleigh waves with respect to depth, a layered soil system defined by the parameters in Table 6.1 was analyzed using the Dynamic Stiffness Method (DSM) of Kausel and Roësset (1981). Using the DSM, layer

stiffness matrices were calculated and assembled to form a global stiffness matrix as defined in Chapter 2, the eigenvectors of which correspond to the mode shapes of the soil system (e.g., see Supranata 2006). Theoretical dispersion curves calculated by the transfer matrix method (Chapter 2) for the same layered soil system are presented in Figure 6.1. The resulting phase velocities (V_{ph}) of four modes of the dispersion curves were determined at a frequency of 60 Hz, and the corresponding wavelengths were calculated (Table 6.2). Substituting these frequencies and wavelengths into the global stiffness matrix of the system gives the mode shapes for the fundamental and three higher modes shown in Figure 6.2.

Table 6.1 Parameters of layered soil model.

Layer #	V_S (m/s)	Poisson's ratio, v	Density, ρ (kg/m^3)	Layer thickness h (m)
1	150	0.30	1800	2
2	200	0.30	1800	3
3	400	0.30	1900	∞ (half space)

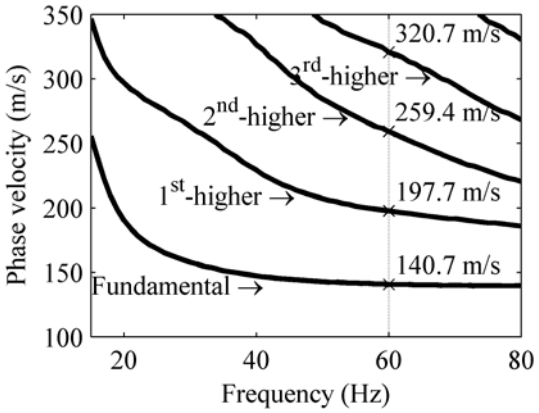

Figure 6.1 Theoretical dispersion curves for the layered soil model of Table 6.1.

Table 6.2 Phase velocity and wavelength of Rayleigh waves at 60 Hz for the soil model of Table 6.1.

Mode #	Phase velocity, V_{ph} (m/s)	Wavelength, $\lambda = V_{ph}/f$ (m)
1	140.7	2.34
2	197.7	3.29
3	259.4	4.32
4	320.7	5.36

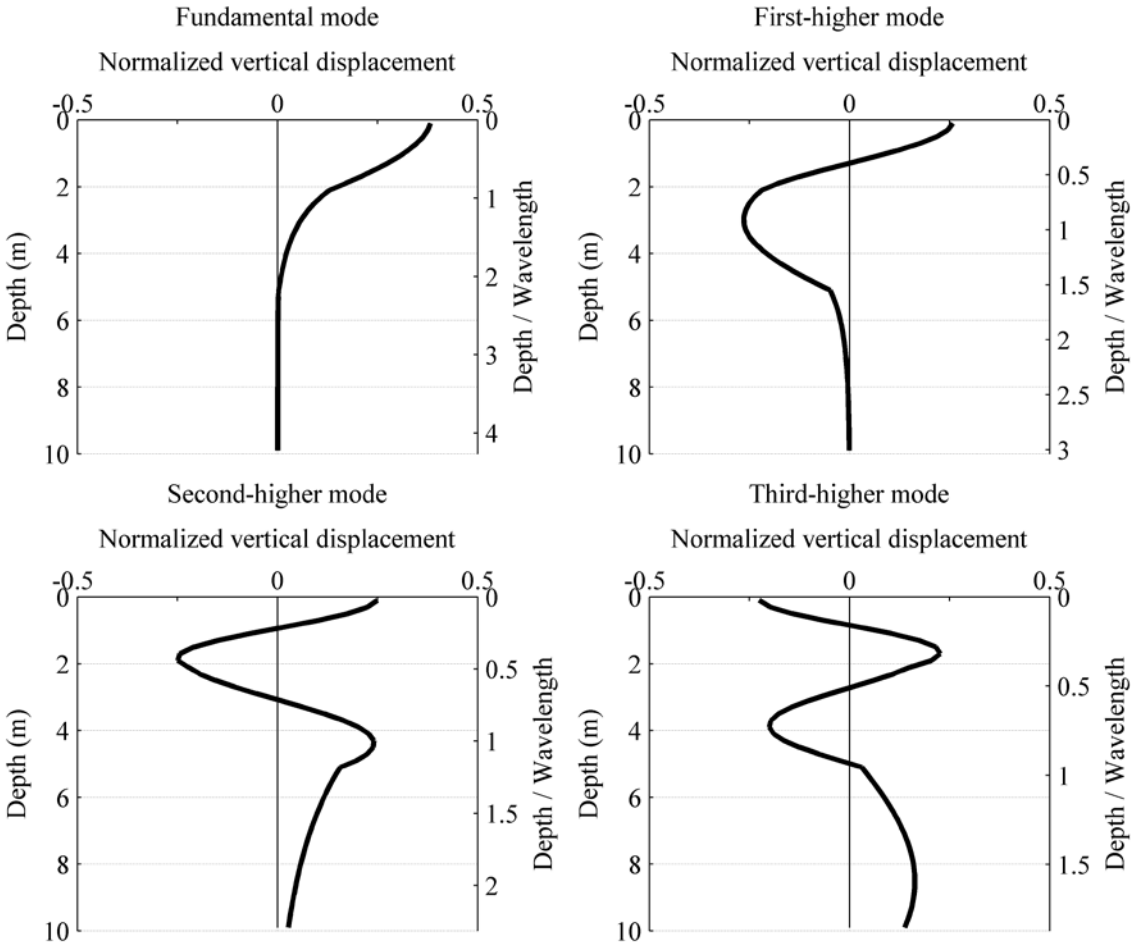

Figure 6.2 Natural mode shapes of Rayleigh waves at 60 Hz for the layered soil model of Table 6.1 (normalized vertical displacement vs. depth).

The fundamental mode attenuates exponentially with depth, as is expected for Rayleigh waves (e.g., Richart et al. 1970). Considering a superposition of all modes, it can be seen that the higher-modes will become dominant as depth increases due to the decay of the fundamental mode. Conceptually, depending upon the relative amplitudes of the various modes, a measurement of soil motion at depth may have significant energy contributed by the higher modes and negligible energy from the fundamental mode. Therefore, sensors placed at selected depths in the soil profile may be able to record the higher-mode Rayleigh waves with improved accuracy due to improved separation from the fundamental mode owing to higher signal-to-noise ratios. In contrast, attempting to

measure higher mode contributions at the soil surface for this layered system would typically result in the fundamental mode dominating the response, reducing the accuracy of the higher modes.

The hypothesis of this study is that sensors placed at shallow depths in the soil using a borehole or probe can enable more accurate resolution of higher-mode Rayleigh waves, thus improving the accuracy of final inverted V_S profiles. A hybrid method is therefore proposed which combines aspects of surface-wave and borehole methods. In contrast to borehole methods such as suspension logging or cross-hole testing, the approach does not limit the depth of profiling to the maximum sensor depth, and only a single borehole or probe sounding is needed. Because Rayleigh waves and concepts of surface-wave testing are employed, the maximum sensor depth is only a fraction of the maximum depth profiled, making the hybrid method more efficient and economical than borehole methods, yet possibly more accurate than surface-only methods.

6.3.2 Sensitivity of multi-mode dispersion images to soil structure

The Jacobian matrix can be used to assess the sensitivity of the dispersion data to soil model parameters (e.g., Xia et al. 1999 and 2003, Luo et al. 2007). The magnitude of the Jacobian matrices for the soil model of Table 6.1 demonstrate that the near-surface soil generally has the greatest influence on a given Rayleigh-wave mode, with the exception of the fundamental mode between 15 and 20 Hz (Figure 6.3). However, for any given depth, the higher-modes generally show a greater sensitivity to soil model parameters than lower-modes. If only the fundamental mode is used for inversion (Figure 6.3a), the deep soil structure will have very limited influence on the inversion results. That is, the uncertainty of the inverted V_S profile will be expected to be greater for the

deeper layers. If the higher modes (Figures 6.3b and 3c) are used in the inversion, then the deeper layers will exert a greater influence on the inversion results, and V_S will be expected to have lower uncertainty for the deeper layers.

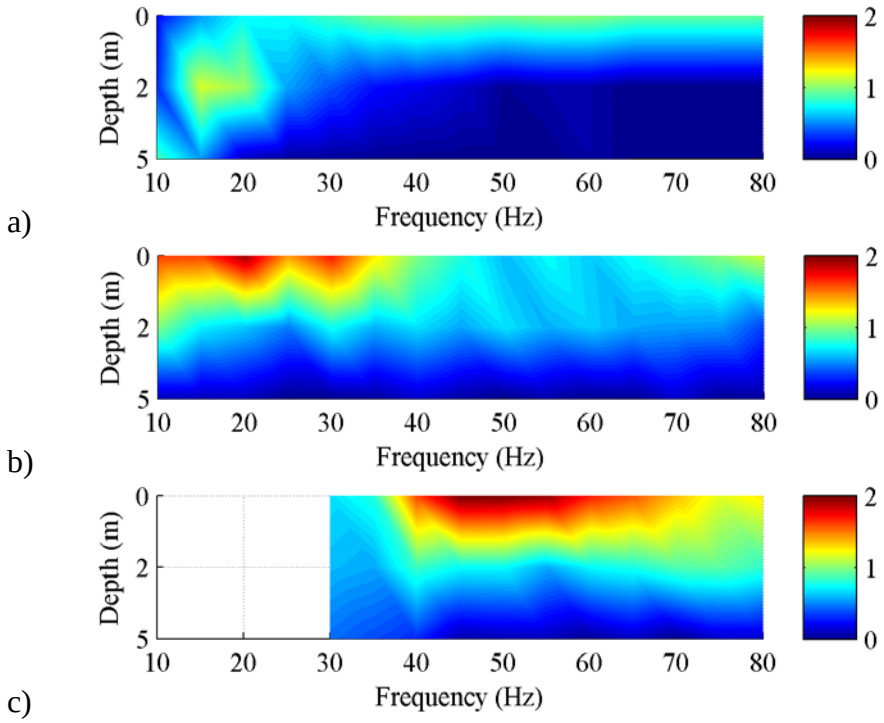

Figure 6.3 Magnitude of Jacobian matrices for the soil model of Table 6.1: a) fundamental mode, b) first-higher mode, c) second-higher mode.

6.4 Hybrid Surface-and-borehole Field Testing Procedure

6.4.1 Multichannel simulation with one-receiver (MSOR) method

To implement an economical and minimally-invasive field-testing approach for measuring higher Rayleigh-wave modes, the multichannel simulation with one-receiver (MSOR) method can be used instead of a multi-channel one-source method such as MASW. As described in Chapter 4, the MSOR method simply reverses the roles of source and receiver in the MASW method, and has been successfully applied to nondestructive testing of pavements (Ryden et al. 2002a, 2004, 2006, Olson and Miller 2010) and soils (Lin and Ashlock 2011). Compared to the MASW method, the MSOR

method has several advantages: 1) greatly reduced instrumentation costs as only one sensor is required; 2) cost savings for data acquisition systems as only two channels are needed (one for the geophone and the other for a trigger); 3) the potential to be faster than MASW if an automated moveable impact source is available, as set-up time for a string of geophones and cables is eliminated; 4) ease in obtaining a 3-D profile as the source can readily be moved along different horizontal lines as shown in Figure 6.4, compared to reinstalling an entire string of geophones multiple times to cover the whole testing area for MASW. The primary requirement of the MSOR method is to obtain a repeatable impact source that can generate waves with consistent timing (Park et al. 2002).

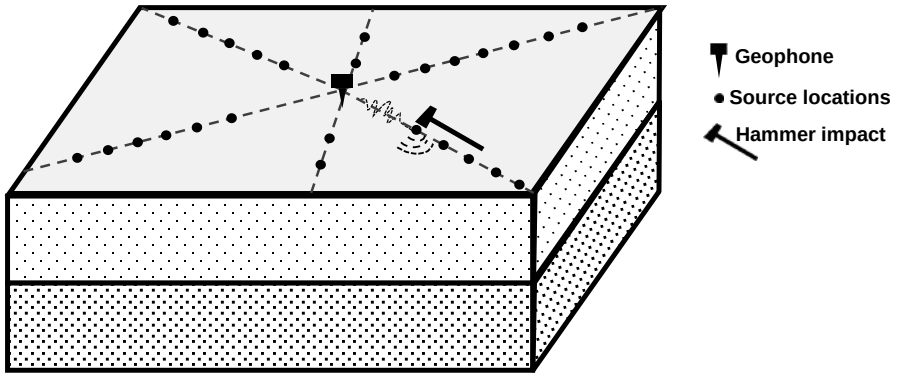

Figure 6.4 Schematic of multichannel simulation with one-receiver (MSOR) method.

6.4.2 Measurement of higher-mode Rayleigh wave motion within the soil

For measurement of the vertical Rayleigh wave motion at selected shallow depths in the soil, a borehole geophone may be used. One potential difficulty when using a borehole for such tests is the prospect of collapsing soils such as sands below the water table, which would normally require hollow-stem auguring or installation of casing. This problem might be avoided if a sensor were inserted in the soil by a probe and used measure the unimpeded free-field Rayleigh wave motion within the soil. A standard seismic CPT probe would not likely be usable, as the stiffness of CPT rods would

attenuate the motion and alter the dispersion data. However, a retractable CPT tip with embedded accelerometer or geophone which can be temporarily uncoupled from the CPT rods may be a useful alternative.

In the proposed hybrid MMSW method, a sensor is used to measure the ground motion at the surface, then at selected depths within the soil, due to surface impacts performed over a range of offsets. Alternatively, a string of borehole geophones could be used to measure the motion at several depths simultaneously to reduce testing time. The initial configuration with the sensor at the surface (before creating a borehole) is the same as an MSOR surface wave test. The resulting recorded ground motion can then be used to construct a dispersion image using standard MASW analysis procedures. The downhole sensor is then lowered to the first selected depth in the soil and the series of impacts repeated, giving another dispersion curve. As the sensor is lowered to greater depths, the higher modes will begin to dominate the dispersion curves (Figure 6.2). Detailed in the following sections are numerical simulations of the MMSW test procedure described above, followed by results and interpretation of preliminary field tests.

6.5 Numerical Simulations

6.5.1 Finite element simulation of multi-mode Rayleigh wave measurement by MMSW approach

To test the hypothesis that multi-mode Rayleigh waves can be effectively measured using the proposed minimally-invasive hybrid approach, the Finite Element Method (FEM) was used to simulate MSOR tests in Abaqus 6.10-1 with geophones embedded at depths of 0, 1.2, 2.4, and 3.6 meters (Figure 6.5). To model half-space radiation conditions, infinite elements were used on the two lateral boundaries as well as

underneath the bottom layer. A transient impact was imposed as a step-function for velocity over a patch, to simulate the dynamic loading of a sledge hammer on the free surface at 24 source locations having a horizontal spacing of 1 m and a first offset of 2 m, while the vertical velocity was calculated at the embedded geophone locations. Rayleigh waves as well as primary, reflected, and head waves can be clearly seen in the displacements (Figure 6.5), although the half-space conditions cannot be simulated perfectly by FEM. The resulting MSOR velocity data for the 24 source locations were assembled to form multichannel records for each geophone depth, from which dispersion data were calculated using the phase-scanning wavefield transformation method of Park et al. (1998) to give the dispersion images of Figure 6.6.

From the simulated dispersion data, apparent Rayleigh wave modes are obtained for each geophone measurement depth, and the higher-modes clearly become more dominant at higher frequencies as geophone depth increases due to the decay of lower-mode Rayleigh wave motion. The maxima of the dispersion-images correspond to the apparent dispersion curves for each geophone depth (Figure 6.6). It should be noted that the dispersion data for the surface sensor corresponds to MASW testing by reciprocity with the MSOR method, and does not contain a clear branch of the higher modes (Figure 6.6a). The apparent dispersion data were superimposed to construct multi-mode dispersion curves (Figure 6.7), which are in good agreement with their theoretical counterparts from Figure 6.1 obtained via the transfer matrix method. This numerical simulation clearly demonstrates that the proposed MMSW testing method for measuring multi-mode Rayleigh waves is feasible, provided that an effective field testing procedure can be developed.

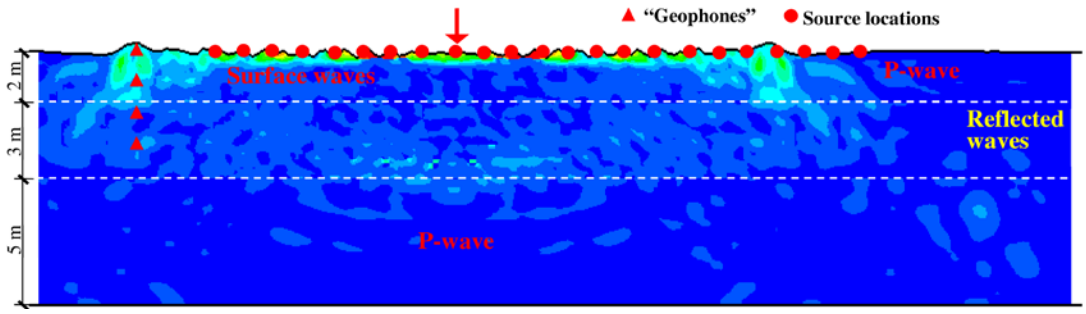

Figure 6.5 Soil model geometry and instantaneous vertical displacements from FEM simulation of wavefield propagation in the layered soil model of Table 6.1 for MSOR testing with embedded "geophones" (red triangles) and moving source (red dots).

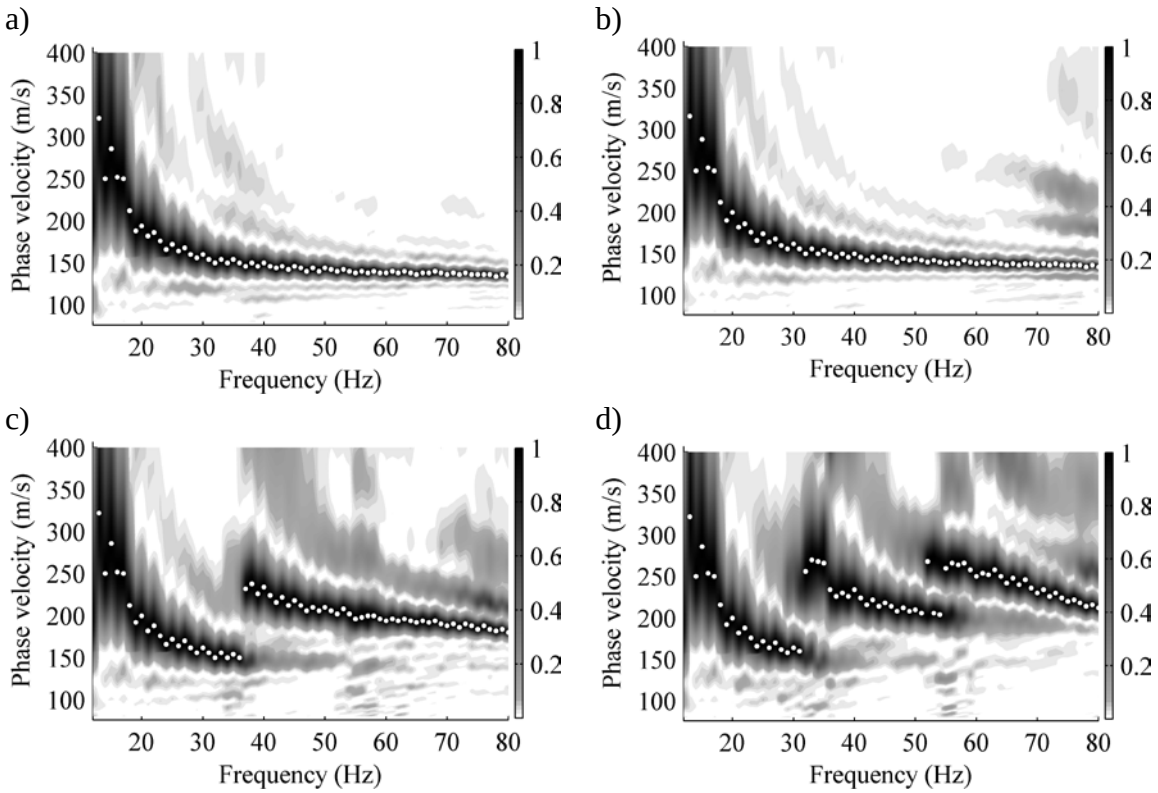

Figure 6.6 Dispersion images from FEM simulation of geophones at four depths: a) 0 m, b) 1.2 m, c) 2.4 m, d) 3.6 m. White dots are the maxima.

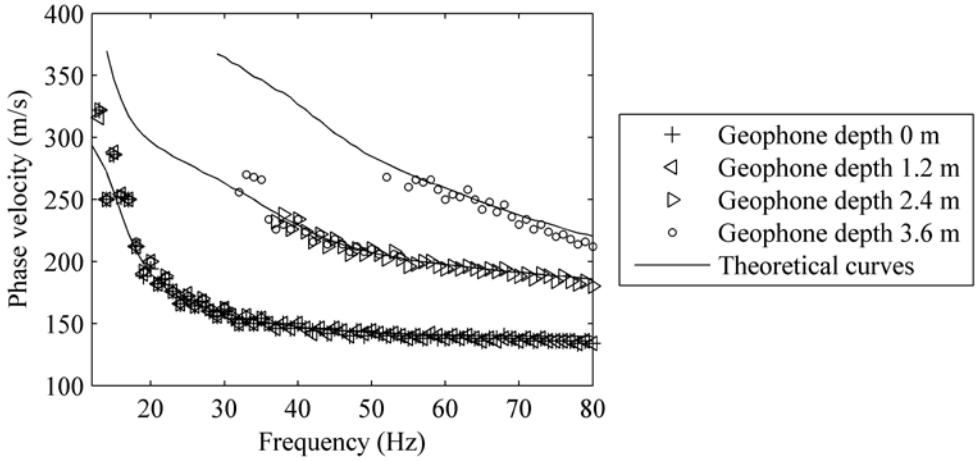

Figure 6.7 Multi-mode dispersion curves for the soil model of Table 6.1: simulated experimental (FEM) vs. theoretical (transfer matrix method).

6.5.2 Multi-mode inversion via genetic simulated-annealing optimization

In this thesis work, an optimization method was developed which combines the Genetic algorithm and Simulated Annealing algorithm for inversion of dispersion data. This inversion program was used to back-calculate the soil profile in terms of layer thickness and shear-wave velocity for the multi-modal simulated experimental dispersion curves of Figure 6.7. For each inversion trial, the first generation of starting models was randomly produced within a search space obtained by varying the parameters of the same initial model by ±50%. Figure 6.8a shows inversion results for six trials using only the fundamental mode as the inversion target, while Figure 6.8b shows results of using the first two modes in a multi-objective inversion. The two-mode inversion results in a greater number of V_S profiles close to the real profile in terms of both V_S and layer thickness.

To quantify the inversion accuracy, the inversion error (*IR*) was calculated in terms of the cumulative relative errors of the inverted profiles as

$$IR = \sum_{i=1}^{2} \sum_{L=1}^{N} \frac{\left| Inversion_{i,L} - Real_{i,L} \right|}{Real_{i,L}} \tag{6.1}$$

where i=1 represents layer thickness, i=2 represents shear-wave velocity, L represents the layer number, and N is the total number of layers. Use of the higher-mode dispersion data significantly improves the accuracy of the velocities and layer thicknesses, thus reducing the inversion error (Figure 6.8, Table 6.3), while a good match of the fundamental mode alone does not ensure a good match for the higher modes. For example, although the fundamental mode's root-mean-square error (RMS_0) of 3.85 for the fundamental-mode inversion (Figure 6.9a) is slightly smaller than the RMS_0 error of 4.17 for the two-mode inversion (Figure 6.9b), the corresponding errors RMS_1 and RMS_2 for the first- and second-higher modes as well as the average IR (Table 6.3) are nearly twice as high if only the fundamental mode is used. Switching from a two-mode to a three-mode inversion slightly increased the RMS error of all three dispersion curves (Figure 6.9), but decreased the minimum IR as well as the average IR (Table 6.3), thus increasing the accuracy of the inverted shear-wave velocity profiles (Figure 6.8). The multi-mode inversion provides a good balance between matching the fundamental and higher modes, leading to the more accurate inversion results.

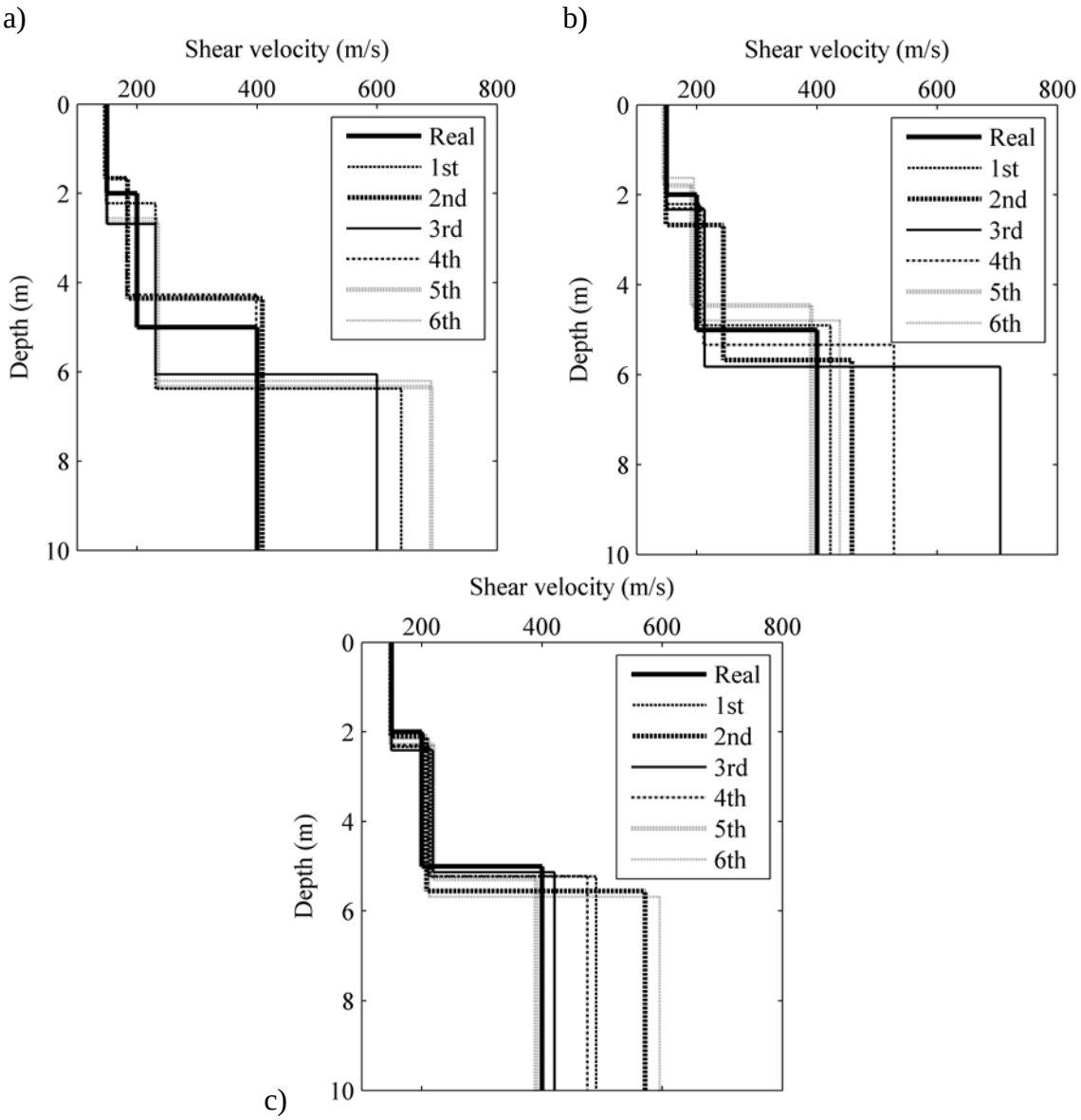

Figure 6.8 Six inversion results for dispersion data of Figure 6.7: a) fundamental-mode inversion, b) two-mode inversion, c) three-mode inversion.

Table 6.3 Inversion error (*IR*).

Modes used for inversion	Inversion trial						Average
	1st	2nd	3rd	4th	5th	6th	
Fundamental mode	1.264	**0.390**	1.122	0.409	1.457	1.388	1.001
Two-modes	**0.303**	0.716	1.158	0.545	**0.303**	0.407	0.572
Three modes	0.506	0.676	0.447	0.421	**0.281**	0.819	0.525

Note: Underlined values denote the minimum *IR*s.

a) b)

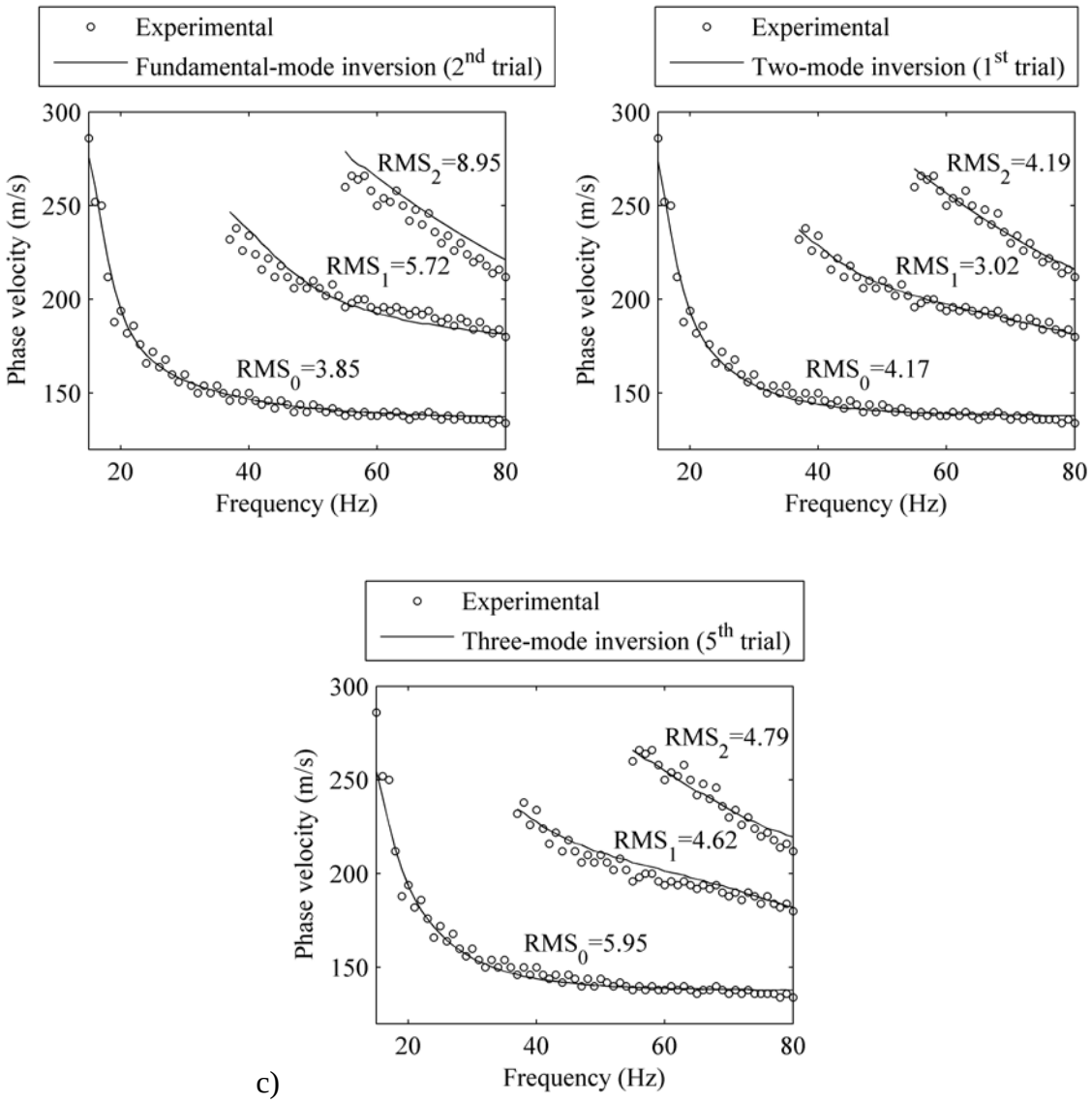

c)

Figure 6.9 Dispersion curves and RMS errors for inversion of FEM simulation data for profiles having smallest inversion errors in Table 6.3: a) fundamental-mode inversion, b) two-mode inversion, c) three-mode inversion.

6.6 Preliminary MMSW Field Testing with Shallow Borehole Measurements at East River Valley

The hybrid MMSW testing method described above was employed for preliminary tests at the East River Valley recreational site in Ames, Iowa (Figure 6.10). A 4.5 Hz vertical geophone was coupled to the soil surface using a ground spike, and a triggered 10 lb sledgehammer source was used to generate Rayleigh waves by impacting an aluminum plate resting on the ground surface. A 4-channel LDS Photon II dynamic signal analyzer was used for data acquisition, with a sampling interval of 0.78125 msec, sample size of 2,048 points, and anti-aliasing filtering for a maximum alias-free frequency of 500 Hz. A 3.66 m (12 ft) station separation was used over an offset range from 3.66 to 43.89 m (12 to 144 ft), and 10 impacts were performed at each station for signal stacking. As mentioned above, the dispersion data for the geophone depth of 0 m is theoretically equivalent to an MASW surface-wave test with 12 receivers. However, the source and geophone locations are reversed in the MSOR testing method. An 8.3 cm (3.25 inch) borehole was hand-augured to a depth of 0.91 m (3 ft) and the geophone was inserted into the bottom surface of the borehole using the ground spike and a specially constructed insertion and retrieval device (Figure 6.10). Similar tests were then performed with geophone depths of 1.83, 2.74, and 3.35 m (6, 9, and 11 ft), giving a total of five test depths.

a)  b) 

c) 

Figure 6.10 Borehole geophone preparation for MIBS field testing: (a) drilling borehole by hand-auger, (b) PVC pipe insertion device for borehole geophone, and (c) borehole geophone coupled to bottom of borehole by ground spike.

The experimental dispersion data for depths of 0 and 0.91 m show a consistent fundamental mode from 6 to 35 Hz (Figures 6.11b and 6.11d). As anticipated, with an increased geophone depth of 1.83 m, Figure 6.11f clearly shows the appearance of a higher mode around 30 Hz which becomes more prominent as sensor depth is increased,

and is also accompanied by possible additional higher modes (Figures 6.11h and 6.11j). By superimposing the five dispersion images shown in Figure 6.11, the multi-mode experimental dispersion curves in Figure 6.12 were obtained, similar to those from the FEM simulation. While the tests detailed herein are preliminary, it should be noted that the near-surface resolution may be improved by reducing the 3.66 m (12 ft) receiver spacing. This would minimize spatial aliasing and far-field effects, and improve the quality of dispersion data above 30 Hz. Additionally, dispersion data at frequencies below 8 to 10 Hz could be a result of ambient sources, which can result in high apparent phase velocities if originating off-line from the receiver spread. For simplicity, the clear trend from 6 to 35 Hz in Figure 6.11 will be referred to herein as the fundamental mode, but this might not be the true fundamental-mode dispersion trend for the site. This issue will be examined in future studies.

As expected, the presumed fundamental and possibly two higher modes were obtained using the embedded geophone (Figure 6.12), whereas the higher modes were less clearly defined in the surface-wave test with the geophone at a depth of 0 m (Figure 6.11b). However, the simple approach of inserting the geophone spike into the bottom of a borehole does not provide optimal coupling with the soil, and therefore may reduce the signal-to-noise ratio. It is anticipated that proper coupling of the geophone with the soil using either a pneumatic bladder, a commercially available borehole geophone, or a modified seismic CPT probe as described above will increase the measurement quality of the higher modes.

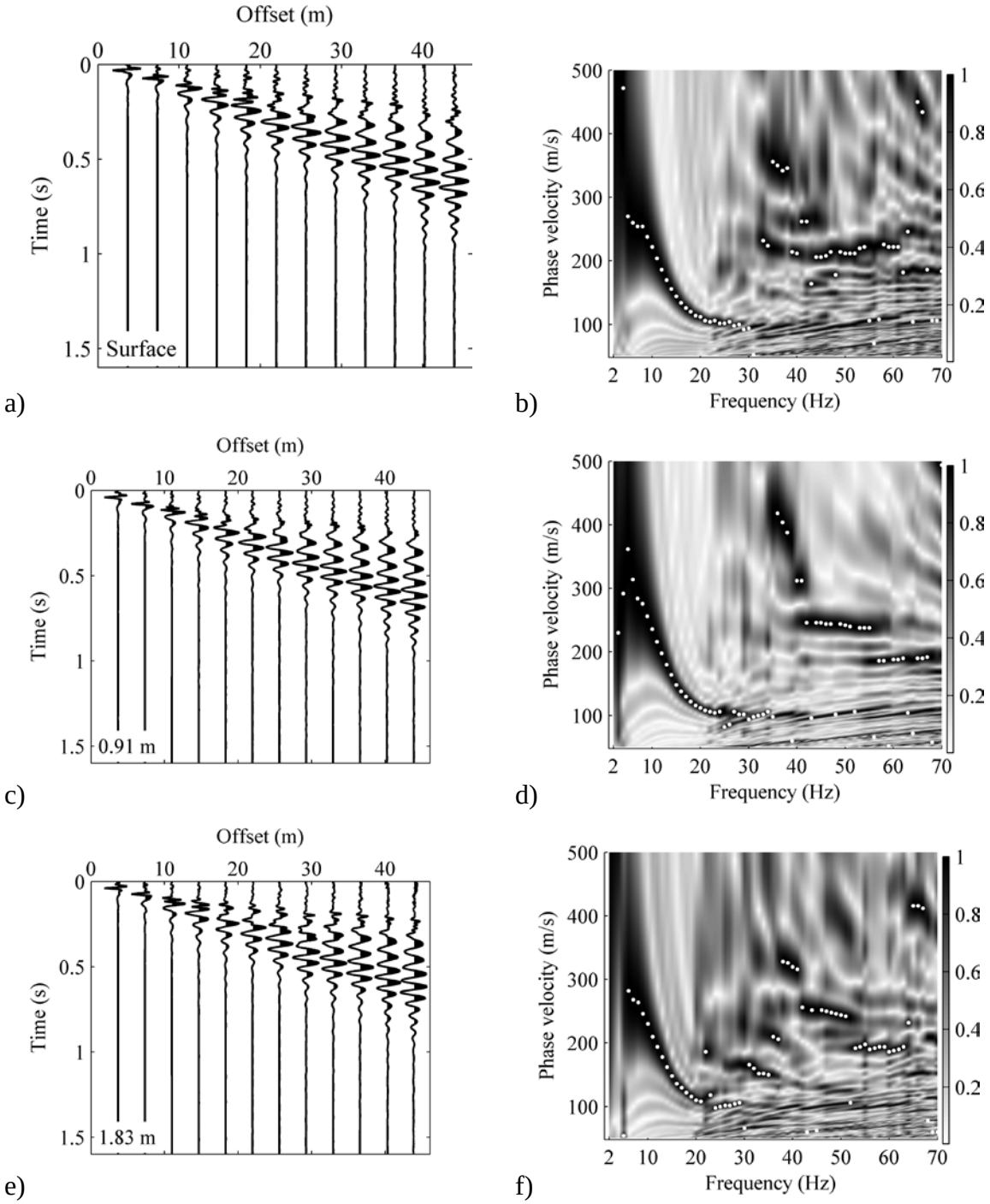

Figure 6.11 Stacked, normalized velocity traces from field tests and dispersion images obtained from MASW phase scanning method: a) and b) geophone at depth of 0 m, c) and d) geophone depth 0.91 m, e) and f) geophone depth 1.83 m, (continued on next page).

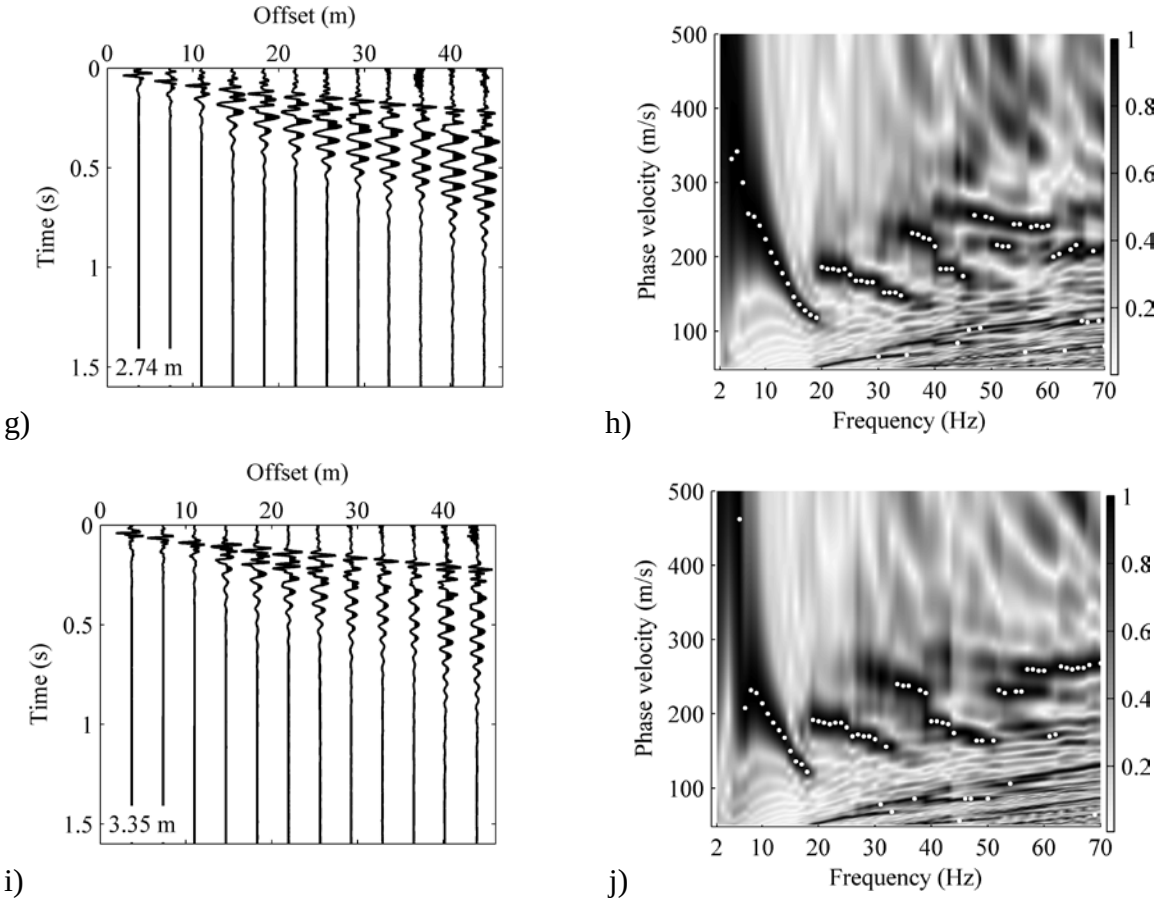

Figure 6.11 (continued) g) and h) geophone depth 2.74 m, i) and j) geophone depth 3.35 m. White dots are the maxima.

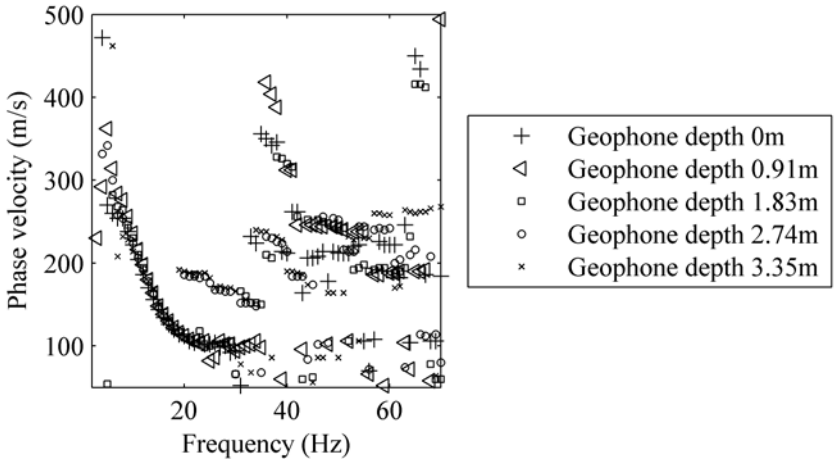

Figure 6.12 Multi-mode dispersion data obtained from preliminary MMSW tests.

To determine the near-surface shear-wave velocity profile of the test site, the first two modes of Figure 6.12 were used in the genetic-simulated-annealing inversion

program with a frequency range of 6 to 30 Hz. Two analyses were performed; the first using the fundamental-mode as the optimization objective function, and the second using the first two-modes. The two-mode inversion yielded final converged velocity profiles with a smaller scatter than the fundamental-mode inversion (Figure 6.13a). A statistical analysis of the depth-averaged shear-wave velocities was also performed for the profiles of Figure 6.13a, since the average shear-wave velocity in the upper 30 meters (V_{S30}) is used in the AASHTO (2009) specifications for bridge design and in many building codes for classification of sites according to soil type. The results show that the two-mode inversion gives a smaller standard deviation of average velocity than the fundamental-mode inversion (Figure 6.13b). The multi-mode inversion from the proposed hybrid test method thus has the potential to reduce the ambiguity and uncertainty of shear-wave velocity profiles used for seismic hazard assessment.

Similar to the FEM simulation results, a two-mode inversion was found to produce a better fit of the experimental first-higher mode than the fundamental-mode inversion (Figure 6.14). Furthermore, for both the fundamental and first-higher modes, the two-mode inversion resulted in a lower average RMS error and standard deviation than the fundamental-mode inversion (Figure 6.15). In particular, the RMS_1 error of the first-higher mode is significantly reduced for the two-mode inversion compared to the fundamental-mode inversion, in terms of both the average value and the distribution range (Figure 6.15b).

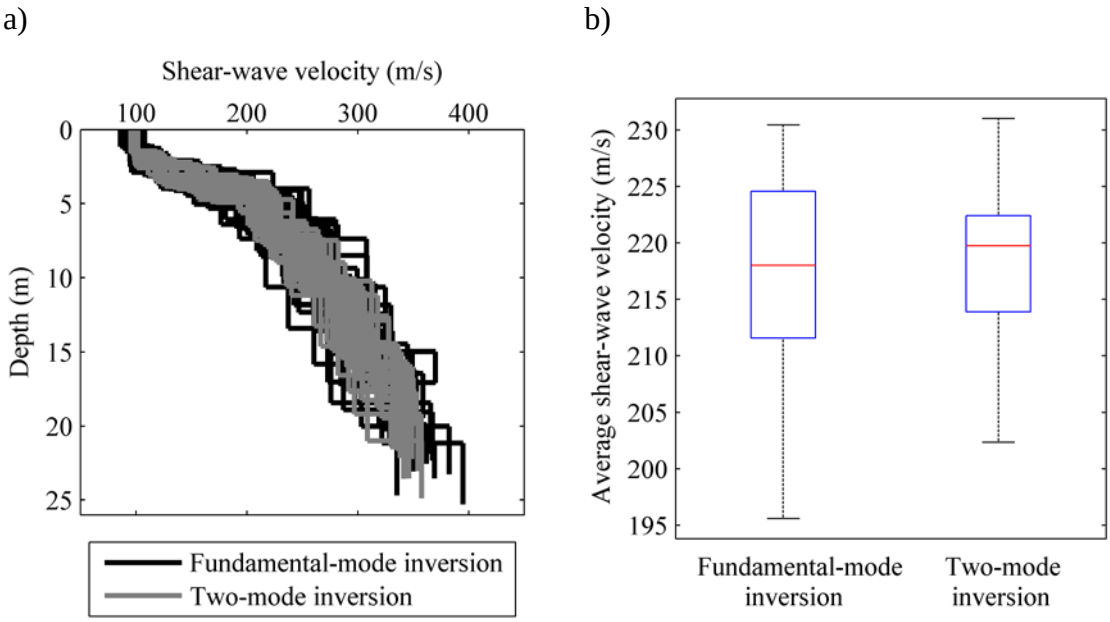

Figure 6.13 Fundamental-mode and two-mode inversions of field data: a) inverted profiles, b) box plots of average shear-wave velocity distributions (central mark is median, box edges are 25th and 75th percentiles, whiskers extend to most extreme data not considered outliers).

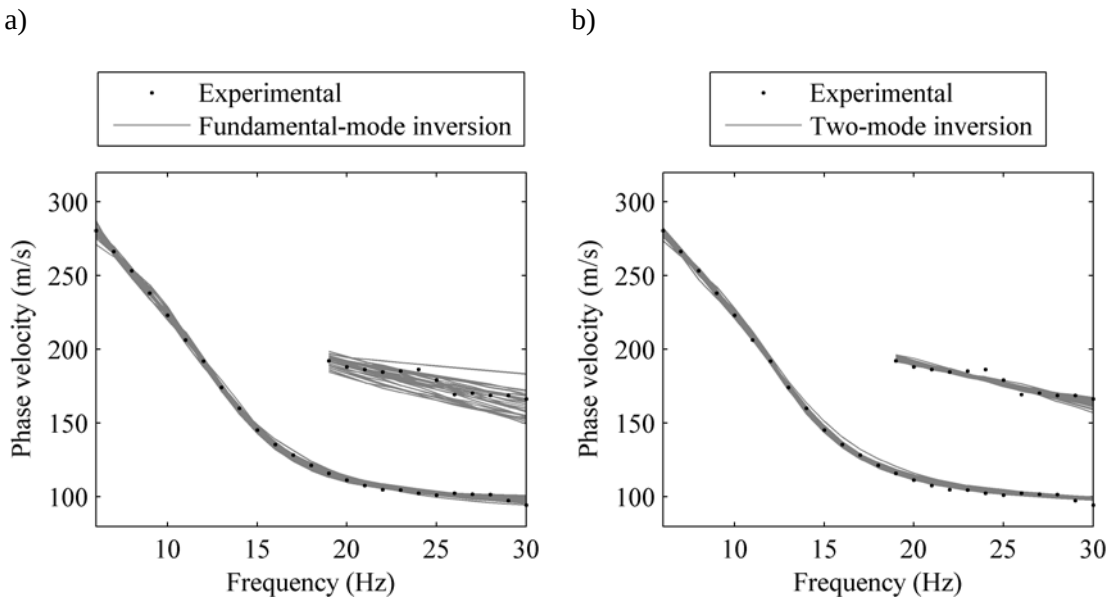

Figure 6.14 Experimental dispersion curves compared to theoretical dispersion curves of final inverted profiles: a) fundamental-mode inversion (30 trials), b) two-mode inversion (30 trials).

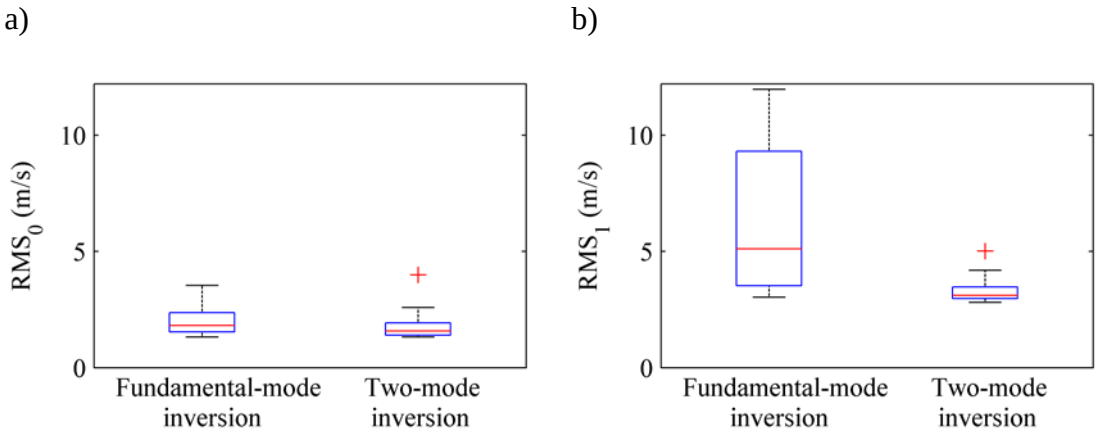

Figure 6.15 RMS error of inversion for Figure 6.14: a) error of fundamental mode, b) error of first-higher mode (central mark is median, box edges are 25th and 75th percentiles, whiskers extend to most extreme data not considered outliers, outliers shown as + marks).

Since the minimally invasive procedure employs sensors embedded in the soil, the attenuation of Rayleigh-wave motion with depth is a logical concern. To examine this aspect, the amplitude and signal-to-noise ratio of all field data shown in Figure 6.11 was analyzed for the range of sensor depths and impact offsets used. As shown in Figure 6.16a, the amplitude generally attenuates with offset and depth, with minor variations that might be attributable to variations in impact energy and ambient noise. Figure 6.16b shows the signal-to-noise ratio of all field data, which is affected by both the dominant surface waves in Figure 6.11, as well as the noise from the tail-end of the signal traces. The signal-to-noise ratio generally decreases with depth and offset distance, but is still significant at the greatest employed geophone depth of 3.35 m. This further indicates that it is feasible to measure the motion of Rayleigh waves within the soil via the hybrid MMSW testing procedure presented herein. It should be noted that the 3.35 m depth of the borehole is only 13.4% of the total depth of 25 m of the inverted profile.

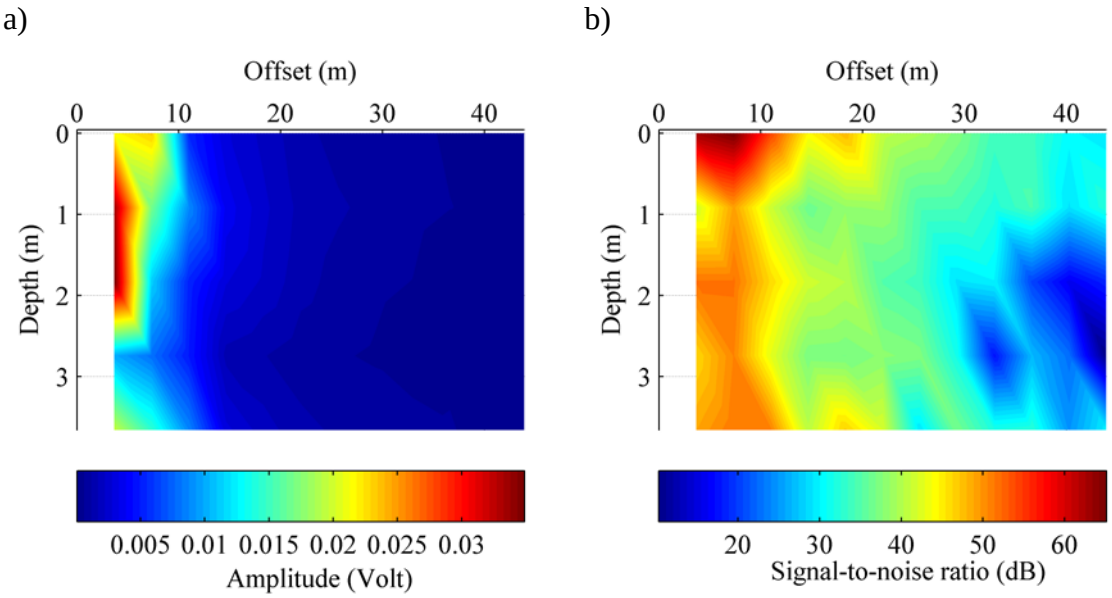

Figure 6.16 Field test data: a) amplitude, b) signal-to-noise ratio.

As shown in the numerical and physical examples above, a significant advantage of the hybrid MMSW method relative to borehole methods is that the sensor needs to be embedded to only a fraction of the total depth profiled. For example, a borehole or probe-insertion of roughly 4.5 m would be needed for a profile of the upper 30 m for typical seismic site classification purposes, compared to the entire 30 m for crosshole, downhole, or seismic CPT tests. Additionally, fewer tests would be required compared to the borehole and CPT methods, as the hybrid procedure gives global soil properties measured over a large receiver-spread area. Finally, the above analyses illustrate the enhanced clarity of multi-mode experimental dispersion images of Rayleigh waves by the hybrid MMSW method compared to surface-only methods, as well as the reduction in variability of the final inverted velocity profiles gained by multi-mode inversion.

6.7 Minimally-invasive MSOR Tests for Measuring Multi-mode Dispersion Curves

The preliminary tests in Section 6.6 and Lin and Ashlock (2014a) were achieved using a hand-augured borehole up to a maximum geophone depth of 3.35 m (11 ft) at the East River Valley site described in the previous section. To examine the method for greater depths, additional MSOR tests were conducted at the Geoprobe Systems test site in Salina, Kansas (Figure 6.17). A Geoprobe 8140LC direct-push drilling machine was used to drill a 8.3 cm (3.25 in) borehole with continuous sampling of the soil profile. A geophone was potted with silicone rubber gel inside a 46 mm (1.8 in) schedule 40 PVC threaded well-riser pipe to enable inserting the geophone into the bottom of the borehole at depths up to 7.62 m (25 ft) (Figure 6.18). The water table was at a depth of approximately 6.71 m (22 ft), and the geophone cable was routed through a series of threaded well-riser pipes with holes drilled in them to allow the water to pass through to minimize their buoyancy.

A four-channel LDS Photon II dynamic signal analyzer was used for data acquisition, with a sampling interval of 1.333 msec, a sample size of 2,048 points, and an anti-aliasing filtering for an alias-free bandwidth of 293 Hz. The borehole was advanced to depths of 0, 1.52, 3.05, 4.57, and 7.62 m (0, 5, 10, 15, and 25 ft) using a combination of vibratory and direct-push sampling using the Geoprobe rig. Drilling was stopped at each of the depths and the geophone was inserted into the bottom of the borehole using the ground spike. The PVC pipe was partially buoyant and was attached to the geophone during testing. A 3.66 m (12 ft) station separation over an offset range from 3.66 to 43.89 m (12 to 144 ft) was used for MSOR tests, with seven impacts performed on the soil

surface at each station for signal stacking. The MSOR tests were repeated in a similar manner for the five test depths.

a) b)

Figure 6.17 (a) borehole geophone potted in well-point PVC pipe, (b) MSOR impacts by 10 lb sledgehammer on aluminum plate

a) b)

Figure 6.18 (a) Geoprobe 8140LC, (b) attaching lengths of threaded PVC well-point riser pipes to install geophone in bottom of borehole.

The corresponding experimental data and dispersion images, obtained using the PIS method introduced in Chapter 3, are shown in Figure 6.19. Two clear modes are evident for a geophone depth of 0 m (i.e., the surface MSOR test). The first mode is the fundamental mode (M0), and the second mode could possibly be the first higher (M1) or

second higher (M2) mode. This data demonstrates the common problem with ambiguous and unclear higher modes in surface wave testing. The discontinuity at 18 Hz indicates that the testing site may have trapped soft layers or high damping soils near the surface. By superimposing five dispersion images of the field data for the five geophone depths, three modes are clearly revealed (Figure 6.20). From these minimally-invasive hybrid test procedure results, it can be concluded that the second mode in Figure 6.19b was actually the second higher mode (M2), and not the first higher mode (M1). Misidentification of this mode as M1 in an inversion analysis would result in significant errors in the inverted stiffness profile.

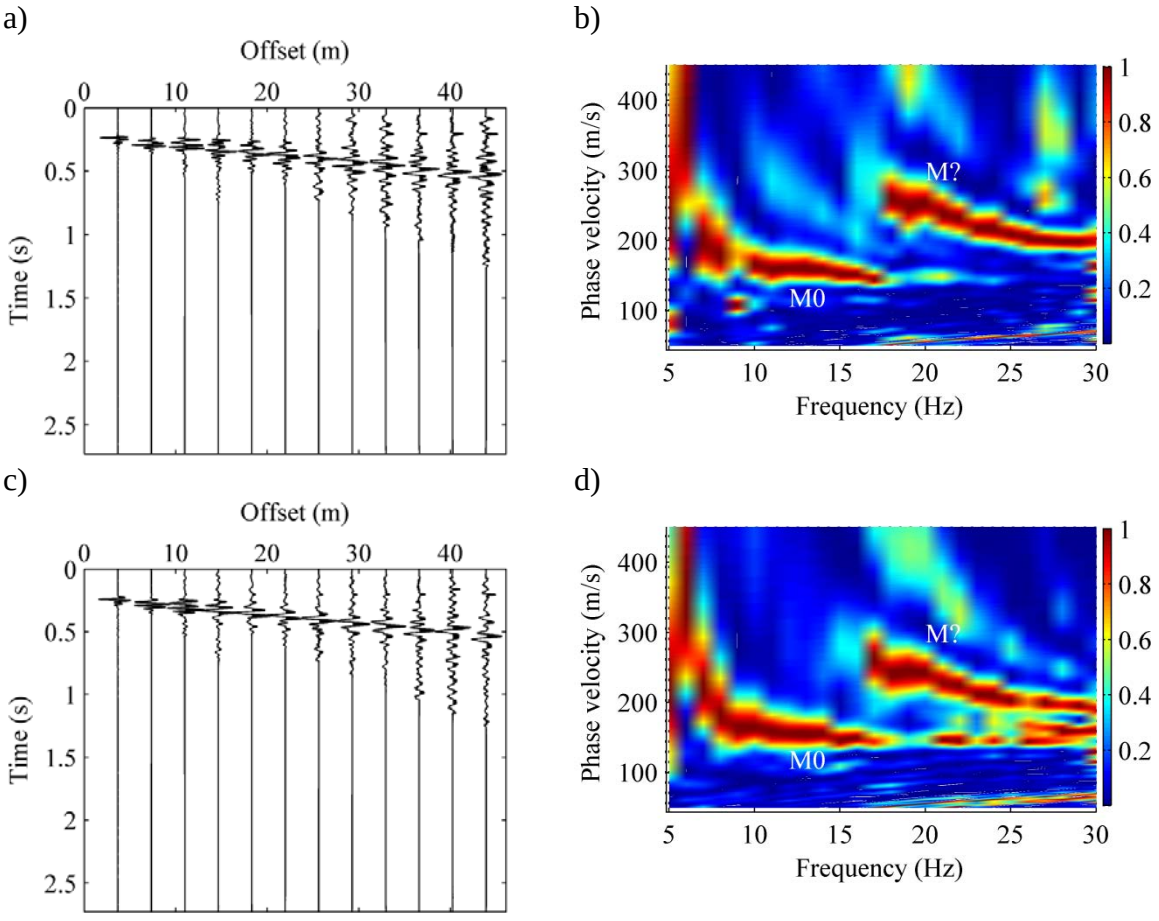

Figure 6.19 Field data and dispersion images: a) and b) geophone at soil surface, c) and d) geophone at 1.52m (5ft) depth, (continued on next page).

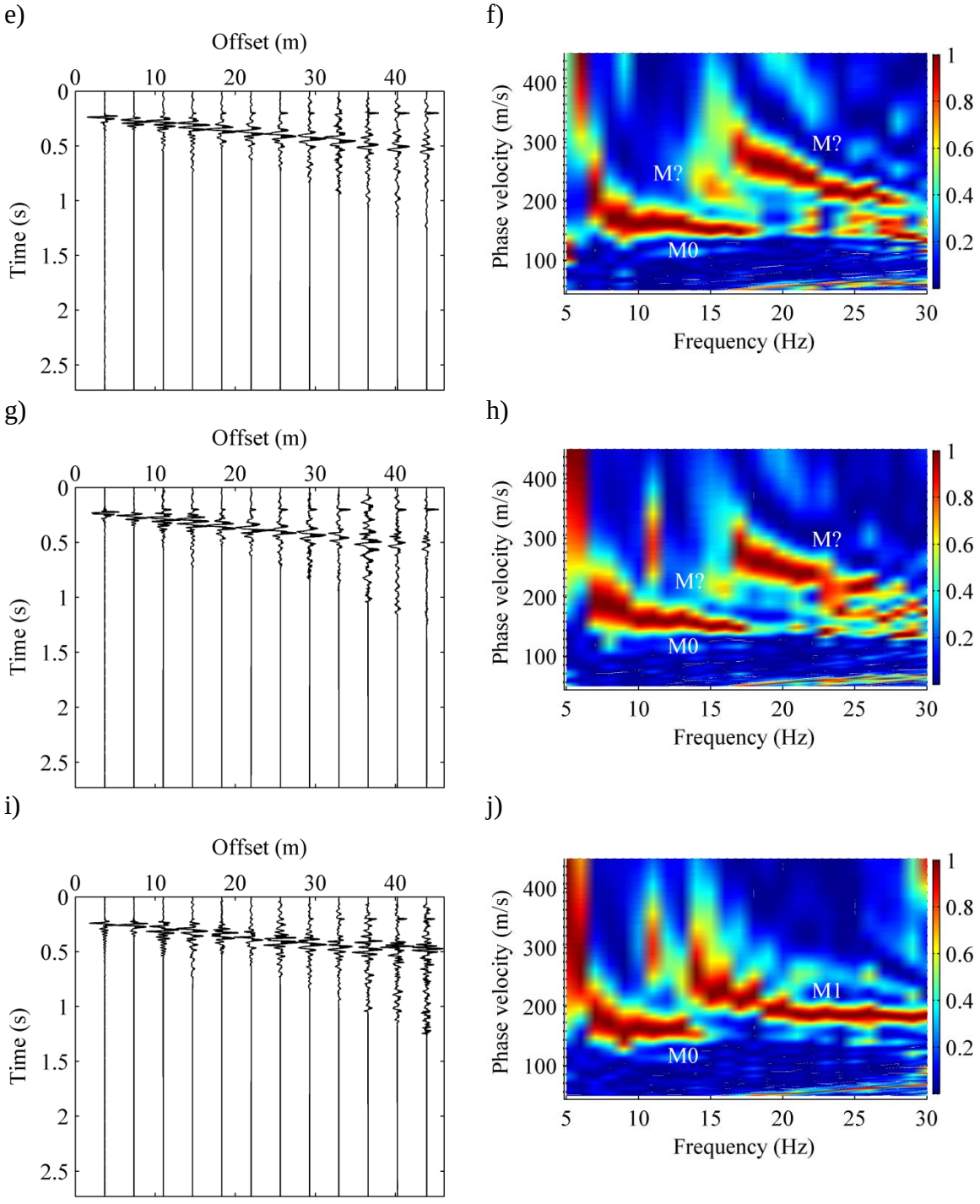

(**Figure 6.19** continued). Field data and dispersion images: e) and f) geophone at 3.05m (10ft) depth, g) and h) geophone at 4.57m (15ft) depth, i) and j) geophone at 7.62m (25ft) depth.

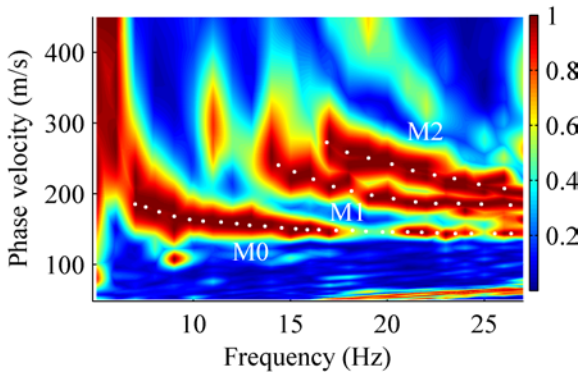

Figure 6.20 Multi-mode dispersion image obtained from minimally invasive shallow borehole measurements in MSOR tests at Geoprobe test site.

Since the vertical amplitude of Rayleigh-wave motion decays exponentially with depth (e.g., Chapter 2; Richart et al. 1970; Kramer 1996), and the minimally invasive testing employs geophones embedded at selected depths in the soil, the motion attenuation with depth is a key concern. To address this concern, all field data shown in Figure 6.19 were used to analyze the amplitude and signal-to-noise ratio for the range of sensor depths and impact offsets used. Figure 6.21a shows an attenuation of amplitude with offset and depth, with minor variations due to differences in impact energy and ambient noise. Based on this figure, the Rayleigh-wave appears to be relatively weak when offset increases beyond 10 m or depth increases beyond 3 m. However, the motion might be still detectable and useful if a certain signal-to-noise ratio can be obtained. The signal-to-noise ratio was calculated by considering the maximum voltage recorded and the noise level at the tail end of a given trace. As shown in Figure 6.21b, the signal-to-noise ratio of all field data generally decreases with depth and offset distance, but is still significant at the deepest geophone depth of 7.62 m for offsets up to 30 m. This further validates that it is feasible to measure the Rayleigh-wave motion within the soil via the minimally invasive testing procedure. For future study, it is suggested that an improved

borehole sensor coupling method be used, as the ground spike does not ensure a positive connection with the borehole walls. Additionally, the length of pipe resting on the geophone prevents it from measuring the unimpeded Rayleigh-wave motion and further attenuates the signal. Use of an expandable bladder, mechanical arm, or off-the-shelf borehole geophone is recommended. Alternatively, an accelerometer could be mounted in a cone penetration test (CPT) probe tip that can be uncoupled from the CPT rods. Some of these methods are being evaluated in a current USGS project.

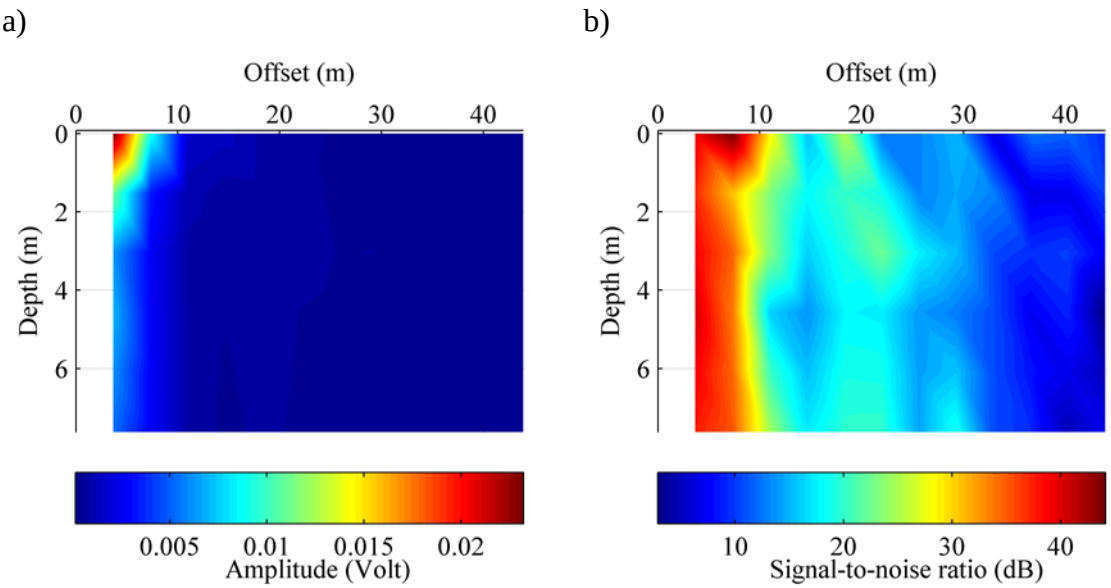

Figure 6.21 Field test data: a) amplitude, b) signal-to-noise ratio.

6.8 MMSW-SPT Method

Another form of the minimally-invasive hybrid surface-and-borehole method is proposed by reversing the roles of the surface impacts and borehole receiver in the MMSW method presented above, and using Standard Penetration Test (SPT) hammer blows as downhole impact sources. A multichannel seismograph is used to record shot gathers for an array of geophones on the soil surface due to the SPT hammer impacts in

the borehole. In the SPT test, a spit-spoon sampler with an external diameter of 50.8 mm (2 in.) and internal diameter of 34.9 mm (1.375 in.) is driven into the soil at the bottom of a borehole by a 63.5 kg (140 lb) hammer weight repeatedly dropped a distance of 0.76 m (30 in.), typically at a rate of 20 to 40 blows per minute. The number of blows to drive the sampler through each of three successive 0.15 m (6 in.) vertical increments is recorded, with the sum of the last two increments giving the blow count in blows per foot (blows per 0.3 m). Typical SPT hammer systems have an efficiency of 60%, yielding an energy of 285 N-m (210 ft-lb) per blow transferred to the soil, neglecting other sources of energy loss. Stiffer soils will result in a smaller sampler penetration per blow (higher blow count), and thus more effective transfer of stress waves through the soil.

Based on the reciprocity principle, the role of borehole impacts and surface receivers in the MMSW-SPT method should be equivalent to the surface impacts and borehole receivers of the MMSW method in terms of characterizing dispersion information. The impacts at different depths can excite different dominant modes propagating along the surface according to the generation of mode shapes of a lumped-mass structure based on structural dynamics theory (Chopra 2000). However, surface waves in a homogeneous half-space will only appear when the angle formed by the vertical and a line from the impact point to the surface receiver is larger than $\theta = \sin^{-1}(V_R / V_P)$, where V_R and V_P are speeds of Rayleigh waves and P-waves, respectively (Ewing et al. 1957), as shown in Figure 6.22. In other words, Rayleigh waves will only exist at the soil surface beyond a minimum horizontal distance $x = z_s \tan\theta$ from the borehole, where z_s is the depth of the borehole source. The

implications of this criteria for multi-layered soil profiles are recommended for further study.

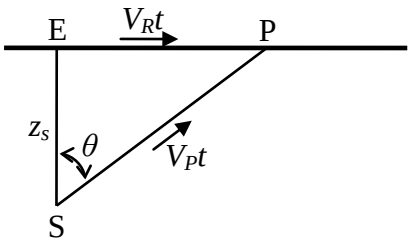

Figure 6.22 Minimum distance EP at which a Rayleigh surface wave appears for a source at depth z_s within a homogeneous half-space media (after Ewing et al. 1957).

To examine the feasibility of the proposed MMSW-SPT method, an FEM simulation was conducted for the soil model of Table 6.1, resulting in dispersion curves that agree fairly well with theoretical ones (Figure 6.23).A preliminary field test was then conducted using a geophone array at an SPT testing location, with vertical velocities recorded along the soil surface for borehole impacts at three selected depths, as detailed in the next section.

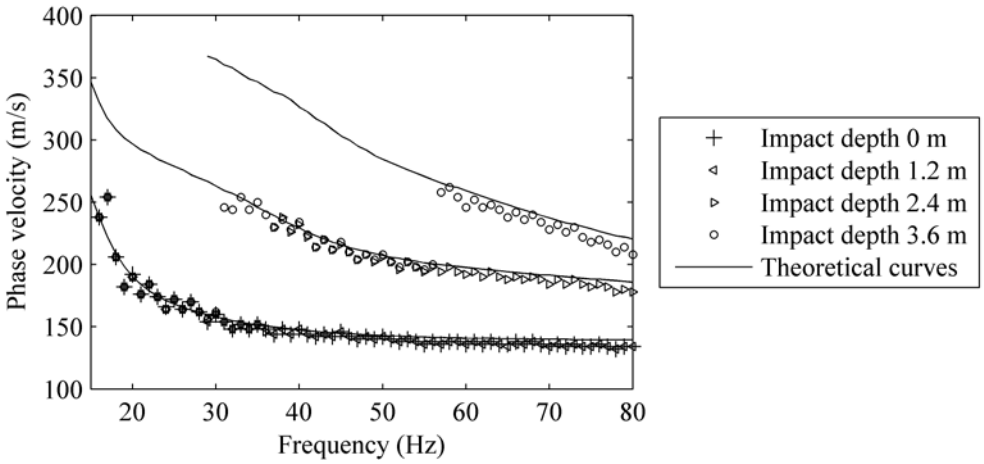

Figure 6.23 Dispersion curves for FEM simulation of MMSW-SPT test method (Theoretical curves from transfer matrix method).

6.8.1 Preliminary MMSW-SPT field test

Preliminary minimally-invasive hybrid surface-and-borehole tests with an SPT hammer source were conducted at the construction site for Fox Run Apartments Phase I, near East Iowa Avenue and North 7th Court, in Indianola, Iowa (Figure 6.24). SPT testing services were provided by Geotechnical Services, Inc. of Urbandale, Iowa. At the time of testing, the site was a former agricultural field saturated by recent rainfall. A Geometrics Geode seismograph was used with twenty-four 4.5 Hz vertical geophones at a spacing of 2 m and first offset of 6 m. A sampling interval of 0.5 msec was selected, with the recordings manually triggered before the SPT hammer was dropped. Shot gathers were recorded for single SPT impacts at depths of 0, 1.22, and 2.59 m (0, 4, and 8.5 ft). The impact on the soil surface at 0 m depth corresponds to a conventional MASW test. The 6-meter first offset was estimated to ensure that the first geophone at the surface would measure surface waves generated by the deepest impact at 2.59 m (8.5 ft) based on consideration of the minimum distance at which Rayleigh waves would first appear, as discussed above. A horizontal layered model illustrating the layout of the MMSW-SPT tests is shown in Figure 6.25.

a)

b)

Figure 6.24 Preliminary MMSW-SPT test: a) SPT drill rig and geophone layout, b) SPT hammer impacting aluminum plate on the soil surface.

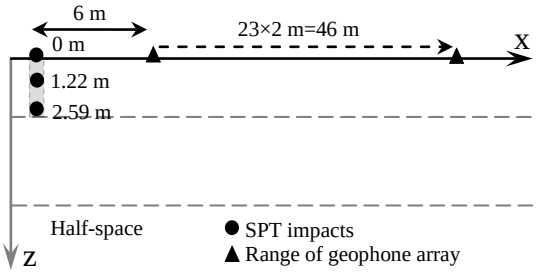

Figure 6.25 Schematic setup of the MMSW-SPT field test with layered earth model and impact/geophone locations.

Figures 6.26a, 6.26c, and 6.26e show the raw velocity field-data over a length of 1.2 seconds, which were manually extracted from a total record length of 4 seconds. The data were then filtered using a frequency-and-wave-speed filter to minimize signals above 70 Hz caused by the SPT drill rig motor, and to retain velocities in the analysis range of 50 to 600 m/s. Figures 6.26b, 6.26d, and 6.26f show three dispersion images extracted from the filtered data. The dispersion data of the surface impact in Figure 6.26b shows a strong mode from 10 to 40 Hz, and two potential fragmented modes or side lobes from 25 to 50 Hz at a velocity of approximately 120 m/s, and from 41 to 49 Hz at a velocity of approximately 180 m/s. If the traditional surface-only MASW were the only test performed at this site, the strong mode in Figure 6.26b would likely be incorrectly interpreted as the fundamental mode. The dispersion data of the impact at 1.22 m (4 ft) in Figure 6.26d, however, reveals a consistent fundamental mode from 10 to 53 Hz located below that of the MASW test, accompanied by strong dispersion information from 5 to 10 Hz and 15 to 20 Hz. Upon increasing the impact depth to 2.59 m (8.5 ft), the dispersion data in Figure 6.26f indicates the lowest mode from 10 to 35 Hz, a first-higher mode from 15 to 51 Hz, and second-higher mode from 30 to 65 Hz.

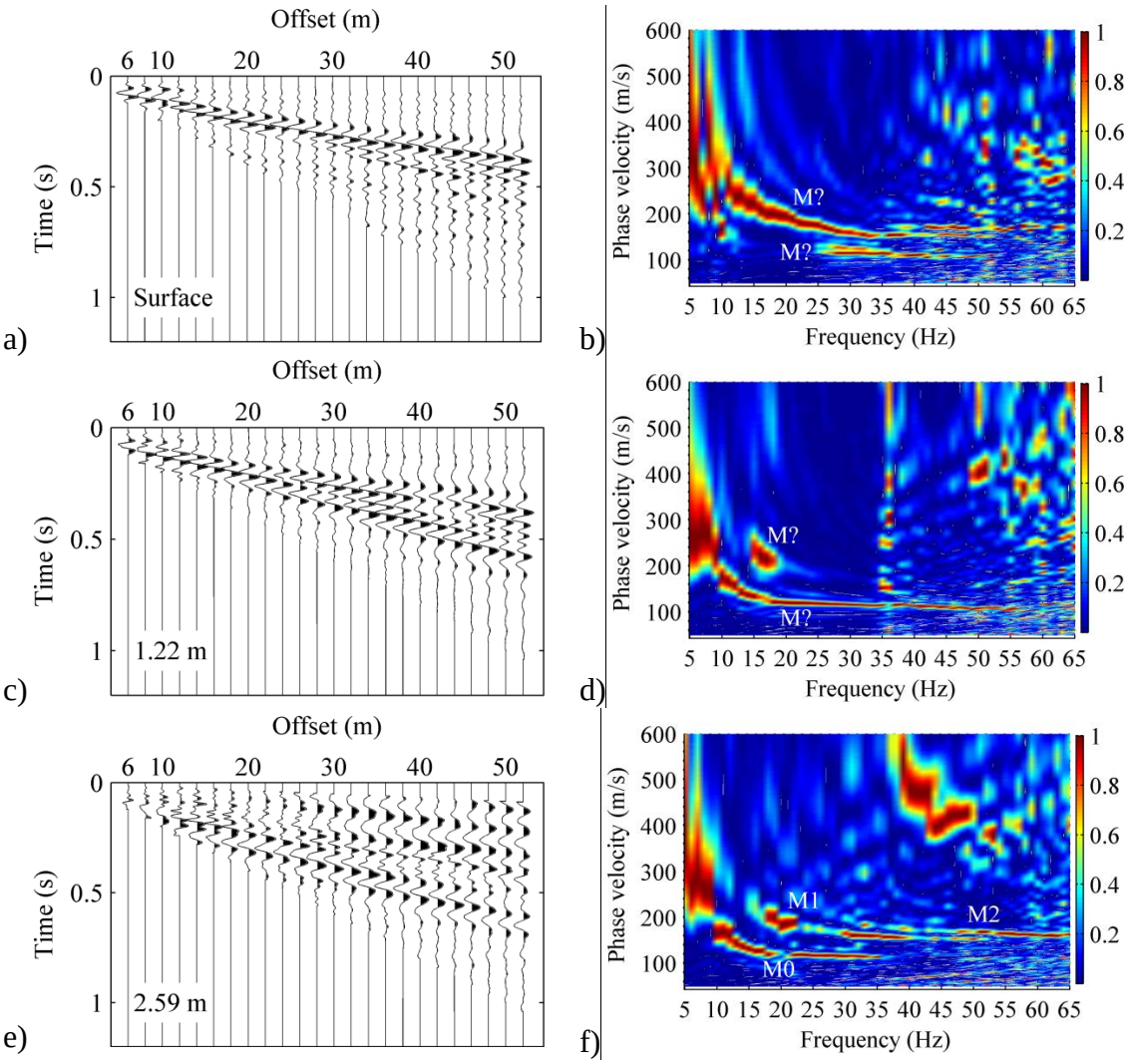

Figure 6.26 Stacked, normalized velocity traces from MMSW-SPT field tests and dispersion images from PIS analysis: a) and b) geophone at depth of 0 m, c) and d) geophone depth 1.22 m, e) and f) geophone depth 2.59 m.

By superimposing the three dispersion images of Figure 6.26, a three-mode composite experimental dispersion image is obtained (Figure 6.27). From this composite multi-mode dispersion image, the mode order of the surface-only MASW dispersion image in Figure 6.26b can correctly be identified as follows: the low-energy mode from 25 to 50 Hz is the fundamental mode (M0), the dominant-energy mode from 10 to 40 Hz is the first higher mode (M1), and the higher mode from 41 to 49 Hz is the second higher mode (M2).

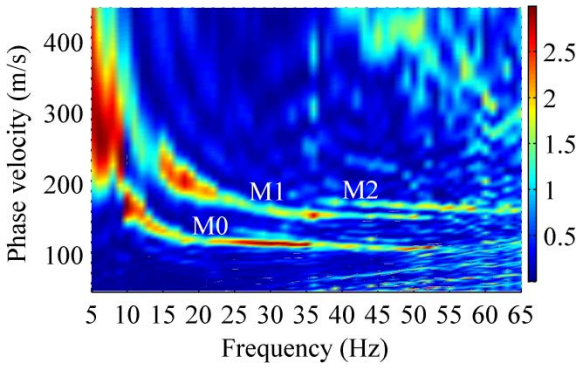

Figure 6.27 Superimposed multi-mode dispersion data obtained from MMSW-SPT tests with impacts at three depths.

6.8.2 Inversion results

To examine the potential error in the near-surface shear-wave velocity profile that would result from misidentification of the dominant mode in Figure 6.26b as the fundamental mode, this mode was selected as the fundamental mode in the SeisImager/SW inversion program from Geometrics, as well as the genetic-simulated-annealing (GSA) inversion program developed in this study. The three modes identified in Figure 6.27 were also used for a multi-mode inversion over a frequency range of 10 to 65 Hz in the GSA inversion program. A comparison of the inverted profiles is shown in Figure 6.28. The fundamental-mode inversion using the misidentified mode from the surface-only MASW test gives the shear-wave velocity profile shown as black dashed lines for SeisImager/SW and gray solid lines for the GSA program. The three-mode inversion from the hybrid MMSW-SPT test data gives the profile shown as black solid lines by the GSA program. As demonstrated in this figure, a likely inaccurate irregular profile with a velocity inversion is obtained if the apparent mode from the surface-only MASW test is misidentified as a fundamental mode, whereas the multi-mode inversion

from the MMSW-SPT method yields a more reasonable and likely more accurate regular profile.

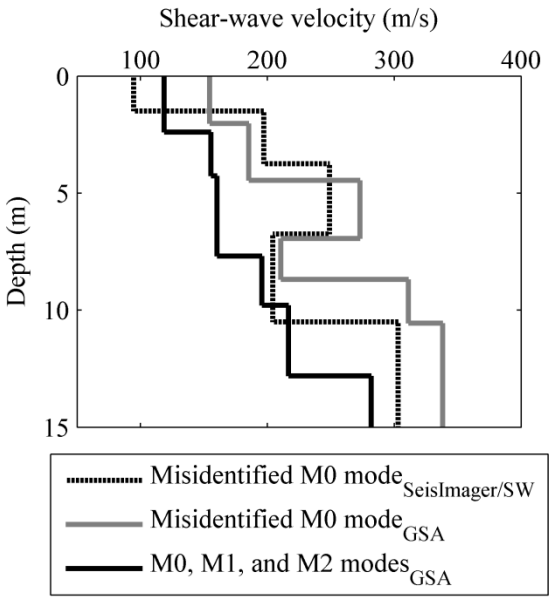

Figure 6.28 Comparison of inverted shear-wave velocity profiles from MMSW-SPT test.

Apparent dispersion trends with dominant higher modes, similar to the data of Figure 6.26b, are commonly encountered in conventional surface-only MASW tests of sites with velocity reversals or high-damping in near surface layers (e.g., Park et al. 2000, Xia et al. 2003, O'Neill and Matsuoka 2005, Lu et al. 2007, Moro and Ferigo 2011). For such sites, the dominant higher mode might be misidentified as the fundamental mode, the inversion of which can give erroneous results as demonstrated in Figure 6.28. The proposed MMSW-SPT method employs SPT hammer impacts at selected depths in the soil with the goal of exciting surface waves with dominant higher modes recorded by geophones at the surface. For unusual sites with highly damped layers near the surface, the MMSW-SPT procedure may actually result in a stronger excitation of the fundamental mode when the impacts are applied below the surface, as demonstrated by the field test detailed above.

The MASW data acquisition during SPT testing is fast and economical, and can be viewed as a beneficial byproduct for effectively estimating the average shear-wave velocity in the first 30 meters (V_{S30}). Additionally, SPT testing is already a very common component of site investigations for civil engineering projects. The machine-induced ambient vibration noise can be effectively reduced using a frequency-and-speed filter. As discussed above, the first receiver offset should be carefully chosen to ensure measurement of surface waves generated by the deepest impact.

6.9 Conclusions

The eigenvector analysis, numerical simulations, and preliminary field tests presented herein demonstrate the feasibility of using embedded sensors at various depths, or alternatively, impacts within a borehole, to more accurately measure higher-modes of Rayleigh waves in a minimally-invasive manner. As demonstrated in this study, the additional information offered by the higher modes can lead to more accurate models of the measured soil response as evidenced by improved fits of the higher-mode dispersion data, more accurate inverted soil profiles in numerical studies, and reduced variability in inverted profiles from field data. As in surface-wave methods, the use of Rayleigh waves enables measurement of geological properties well below the maximum sensor or impact depth. The advantages of greater accuracy commonly provided by borehole geophysical methods are thus combined with the benefit of sounding to depths below the sensor or impact elevations as provided by surface-wave methods. With refinements to improve the measurement accuracy of the field-testing technique presented herein, it is anticipated that the proposed methods can ultimately contribute to the goal of minimizing seismic hazard by improving the accuracy and reducing the ambiguity of shallow shear-wave

velocity profiles for site response analysis, seismic site classification, and soil-structure interaction analyses.

CHAPTER 7. CRITICAL DEPTHS FOR HIGHER MODES

7.1 Abstract

To measure more complete multi-mode dispersion data and thus improve the accuracy of inversion profiles, a minimally-invasive multimodal surface wave (MMSW) geophysical testing method was developed in the previous chapter. The new MMSW method employs a borehole geophone at selected depths to record seismic waves from a moving source on the soil surface. A variant called the MMSW-SPT method was also introduced, in which an SPT hammer is used as a borehole impact source while surface wave motion is recorded with a multichannel seismograph. The goal of this chapter is to develop a procedure for estimating the ranges of optimum geophone depths in MMSW tests or optimum depths of borehole impacts in MMSW-SPT tests to capture the higher modes. Stiffness matrix and finite element-based numerical simulations of the hybrid MMSW testing method are performed to identify the relationships between critical geophone depths and apparent cut-off frequencies. A preliminary field test is conducted using a vertical geophone placed at five depths while impacts are applied to the soil surface over a range of offsets. Dispersion images from the five geophone depths were superimposed to produce a dispersion image having three modes with improved clarity relative to the surface-only MASW method. A comparison of the experimental and theoretical apparent cut-off frequencies of higher modes is used to validate the prediction of critical depths by the stiffness matrix method. Matching of such experimental and theoretical apparent cut-off frequencies is proposed as additional optimization constraints to reduce the uncertainty of final inversion profiles.

7.2 Introduction

Data from geophysical surface wave test methods including spectral analysis of surface waves (SASW) and multichannel analysis of surface waves (MASW) has traditionally been analyzed in the form of a single apparent dispersion curve, comprised of the dominant component at each frequency (e.g., Nazarian 1984, Gucunski 1992, Stokoe et al. 1994, Park et al. 1999a, Xia et al. 1999, Cox and Wood 2011, Tran and Hiltunen 2011). However, it is well-known that apparent dispersion curves may be comprised of branches from multiple modes for irregular sites, such as those with velocity reversals. It has been shown that higher modes can have a deeper investigation depth than the fundamental mode, and their use can stabilize inversion procedures and increase the resolution of inverted S-wave velocities (Xia et al. 2003). A significant body of recent research has focused on measurement of higher modes of surface wave dispersion patterns and their use in simultaneous multi-objective inversion (e.g., Park et al. 1999b, Song et al. 2007, Bergamo et al. 2011).

Despite these advantages of higher modes, accurate measurement of multi-mode dispersion data using surface-only Rayleigh wave methods is challenging because higher modes are occasionally skipped, and are generally much less energetic at the surface than the fundamental mode (Socco et al. 2010). Long geophone arrays can separate higher modes with close phase velocities (Gabriels et al. 1987, Stokoe et al. 2004), but can potentially introduce significant lateral variation in near-surface profiles for the depth scale of interest (Park et al. 1999b). Although short geophone arrays sometimes record multi-mode dispersion data, the modes are generally incomplete in the frequency range of interest (e.g., Xia et al. 2003, Song et al. 2007, Bergamo et al. 2011).

To capture higher modes of dispersion data more completely and reliably, and thus improve the accuracy of near-surface profiling, the minimally-invasive multimodal surface wave (MMSW) hybrid testing method was developed as detailed in the previous chapter and in Lin and Ashlock (2014a). The new method employs a borehole geophone at selected depths to record seismic waves from a moving source on the soil surface. While the feasibility of the method has been demonstrated theoretically and experimentally in the previous chapter, guidance is needed on selection of the depths at which the geophone should be placed to most effectively measure the higher-mode Rayleigh waves.

To identify the critical minimum geophone depth for effective measurement of each higher mode, the stiffness matrix and finite element methods are employed in the following sections to simulate the minimally-invasive hybrid testing method. For each geophone depth analyzed, the stiffness matrix method yields an apparent dispersion curve, which is verified by the finite element simulation. The stiffness matrix method is used to calculate displacements in the wavenumber domain at selected depths, for multiple modes excited by loading applied at the free surface. At each geophone depth, the dominant mode is chosen as the one having the largest peak displacement amplitude. The critical depth for a given higher mode is then taken as the depth at which that mode's displacement becomes dominant. The hypothesis is that the energy of the first higher mode will become dominant in the dispersion data when the geophone is placed at or below the critical depth identified for the first higher mode, and so on. A real-word case study is carried out to measure multi-mode dispersion data and obtain a final profile upon multi-mode inversion. The final profile is then used for stiffness matrix simulation to

identify theoretically the critical depths and corresponding apparent cut-off frequencies, which are compared to the experimental results.

7.3 Numerical Simulation of Minimally-invasive Hybrid Method

A horizontal layered soil model is used to simulate the minimally-invasive hybrid testing method (Figure 7.1). Geophones are embedded at four depths of 0, 1.2, 2.4, and 3.6 meters, and a moving impact is applied sequentially at 24 locations on the soil surface with a spacing of 1 m and first offset of 2 m, as in the field tests of Lin and Ashlock (2011).

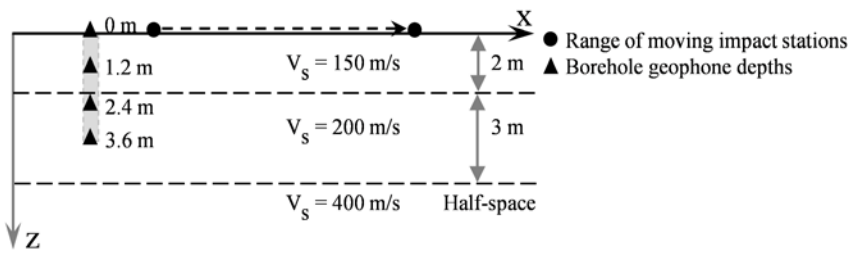

Figure 7.1 Layered earth model and impact/geophone locations for simulation of the hybrid minimally-invasive multimodal surface wave (MMSW) test.

The stiffness matrix method has previously been employed for Rayleigh-wave dispersion analysis by Kuasel and Roësset (1981), Gucunski and Woods (1992), Ganji *et al.* (1997), and Ryden and Park (2006), among others. The theory behind the stiffness matrix method was covered in detail in Chapter 2, and additional considerations needed for the numerical simulation are briefly reviewed here. The structural information of a layered soil model is used to compose a global stiffness matrix $\boldsymbol{K}$ by superposing the stiffness matrix of each layer, as detailed in Chapter 2. The displacement vector can be expressed as

$$\boldsymbol{U}(k,\omega) = \boldsymbol{K}(k,\omega)^{-1}\boldsymbol{P}(\omega) \tag{7.1}$$

where $\boldsymbol{K}(k, \omega)$ is a global stiffness matrix, $\boldsymbol{P}(\omega)$ is a unit loading vector, and $\boldsymbol{U}(k, \omega)$ is a displacement vector in the wavenumber (k) and frequency (ω) domains. When the applied loading is axisymmetric and vertical with uniform intensity P_0 and radius R_0, it can be transformed from the space and time domains $P(r,t)$ to the wavenumber and frequency domains $p(k,\omega)$ using Hankel and Fourier transforms, respectively, to give

$$p(k,\omega) = -\frac{P_0 R_0}{k} J_1(kR_0) \tag{7.2}$$

where J_1 is the Bessel function of the first kind of order 1. Denoting the vertical displacement at depth z due to a unit intensity loading P_0 at the surface as $\bar{\boldsymbol{U}}_z(k,\omega)$, the total displacement at depth z under the loading $p(k,\omega)$ may be written as

$$\boldsymbol{U}_z(k,\omega) = -\frac{P_0 R_0}{k} J_1(kR_0)\bar{\boldsymbol{U}}_z(k,\omega) \tag{7.3}$$

This displacement can then be transformed from the wavenumber-frequency domain back to the space-frequency domain using the inverse Hankel transform:

$$\boldsymbol{U}_z(x,\omega) = \int_0^\infty \boldsymbol{U}_z(k,\omega) k J_0(kr) dk = -P_0 R_0 \int_0^\infty J_1(kR_0) J_0(kr) \bar{\boldsymbol{U}}_z(k,\omega) dk \tag{7.4}$$

where J_0 is the Bessel function of the first kind of order 0. This displacement contains dispersion characteristics which can be extracted using the MASW phase-velocity scanning method detailed in Chapter 3 (Park et al. 1998, Ryden and Park 2006), i.e.

$$S_z(\omega, V_{ph}) = \int_{x_1}^{x_{end}} \boldsymbol{e}^{ix\omega/V_{ph}} \boldsymbol{U}_z(x,\omega) dx \tag{7.5}$$

where V_{ph} is the scanning phase-velocity, $x_1 \le x \le x_{end}$ is the horizontal impact-to-receiver offset, and S_z is the slant-stack amplitude for each frequency and velocity. Plotting Eq. (7.5) for a range of phase velocity and frequency values yields dispersion images, the

maxima of which give apparent dispersion curves which can consist of branches from multiple modes.

Dispersion images were calculated for each of the four geophone depths in the soil profile of Figure 7.1 using the stiffness matrix and phase-velocity scanning methods described above (Figures 7.2a, 7.2c, 7.2e, and 7.2g). Four dispersion images were also calculated by finite element simulation of the minimally-invasive hybrid testing method using Abaqus 6.10-1 (Figures 7.2b, 2d, 2f, 2h). The dispersion images obtained by the stiffness matrix simulation are in good agreement with those obtained by FEM. Both simulations yield dispersion images that agree well with theoretical dispersion curves calculated by the transfer matrix method (Haskell 1953), shown as solid purple lines in Figure 7.2. As discussed in Lin and Ashlock (2014a), the dispersion images for the individual geophone depths can be superimposed to obtain a more complete composite multi-mode dispersion image for the soil profile than would be obtained with the MASW method (represented by Figures 7.2a and 7.2b with the geophone at 0 m depth).

7.4 Critical Depths for Measurement of Higher Modes

Since the stiffness matrix method is able to accurately simulate the minimally-invasive hybrid testing method as demonstrated in Figure 7.2, the derived displacement $\boldsymbol{U}_z(k,\omega)$ can be used to monitor the transition of the dominant mode as geophone depth increases. The displacement $\boldsymbol{U}_z(k,\omega)$ in the wavenumber-frequency domain can be converted to the displacement $\boldsymbol{U}_z(\lambda,\omega)$ in the wavelength-frequency domain by the relation $\lambda=2\pi/k$. For example, Figure 7.3a shows the 60-Hz displacements $\boldsymbol{U}_z(\lambda,$ 60 Hz) at the four geophone depths of the profile of Figure 7.1. For a given frequency, a higher mode (higher phase velocity) has a longer wavelength than a lower mode (lower phase

velocity). Thus the dominant mode characterized by the largest displacement in Figure 7.3a shifts from the fundamental mode to the first-higher mode somewhere between geophone depths of 1.2 and 2.4 m, then to the second-higher mode between 2.4 and 3.6 m.

To more precisely locate the critical geophone depths at which the dominant mode shifts, the soil profile was divided into 0.1-m thick layers, and the normalized displacements were computed at all layer interfaces, as shown in Figure 7.3b. Using this data, the critical depth of the first-higher mode at 60 Hz was found to be 1.75 m, taken as the average of 1.7 m (where the fundamental mode is dominant) and 1.8 m (where the first-higher mode first becomes dominant). Similarly, the critical depths of the second-higher and third-higher modes at 60 Hz are 3.25 m and 5.75 m, respectively. A geophone should therefore be placed between 1.75 and 3.25 m depth for optimum measurement of the first-higher mode with an apparent cut-off frequency of 60 Hz, and between 3.25 and 5.75 m for optimum measurement of the second-higher mode with an apparent cutoff frequency of 60 Hz. That is, below the apparent cutoff frequency for the first-higher mode, the fundamental mode will be dominant in the dispersion image. At the apparent cutoff frequency for the first-higher mode, the dominant mode in the dispersion image will jump from the fundamental to the first-higher mode, and so on. The term “apparent cutoff frequency” is used because the higher mode may still exist below this frequency value, but it will no longer be the strongest (dominant) mode with the largest displacement. This avoids confusion with the term “cutoff frequency” which is defined as the lowest frequency for which a given mode can theoretically exist for a given soil profile.

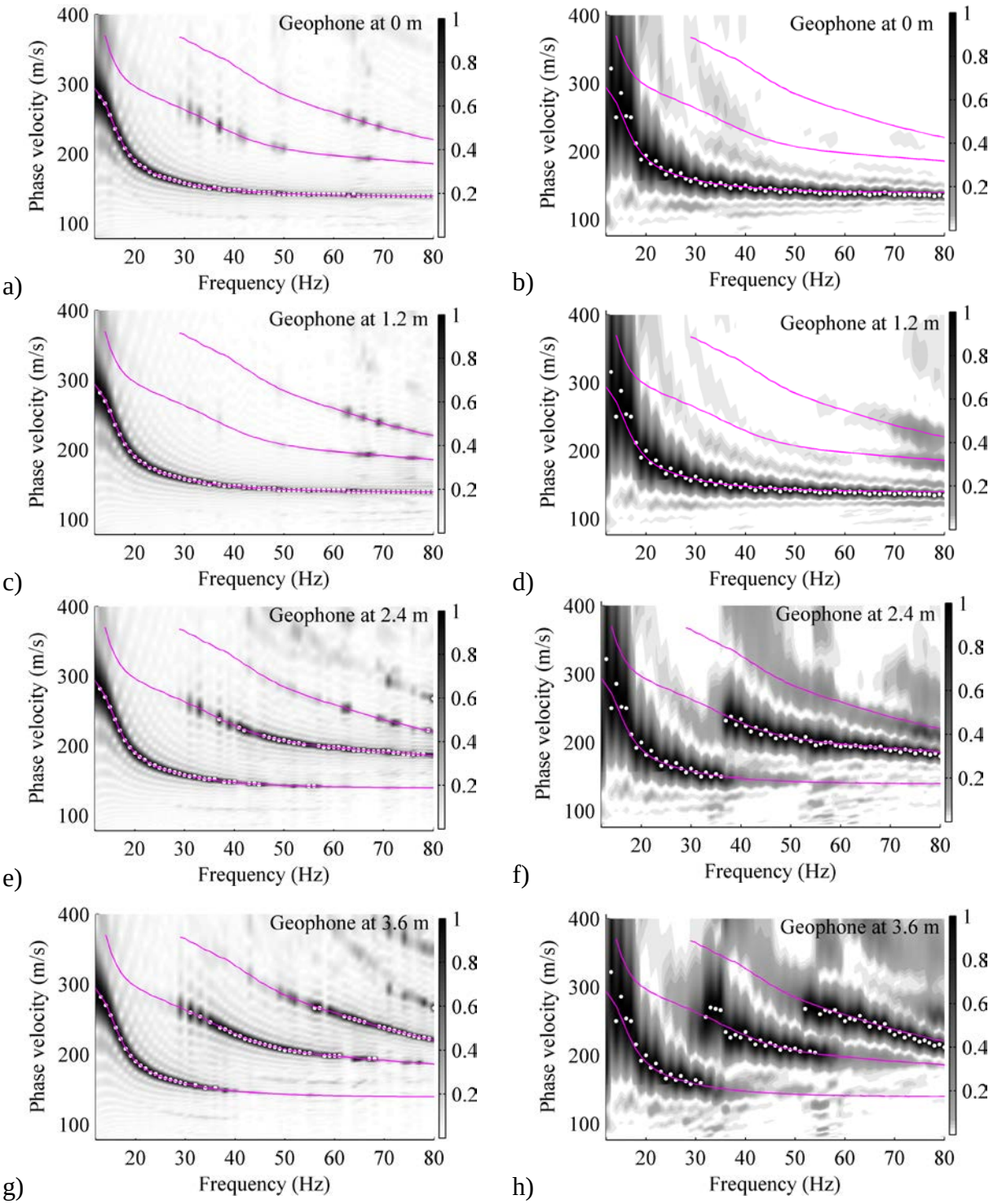

Figure 7.2 Dispersion images for layered soil model of Figure 7.1 by stiffness matrix (left column) and FEM simulations (right column) of geophone at depths of 0 m (a and b), 1.2 m (c and d), 2.4 m (e and f), and 3.6 m (g and h). White dots are maxima of the dispersion images. Solid purple dispersion curves by transfer matrix method.

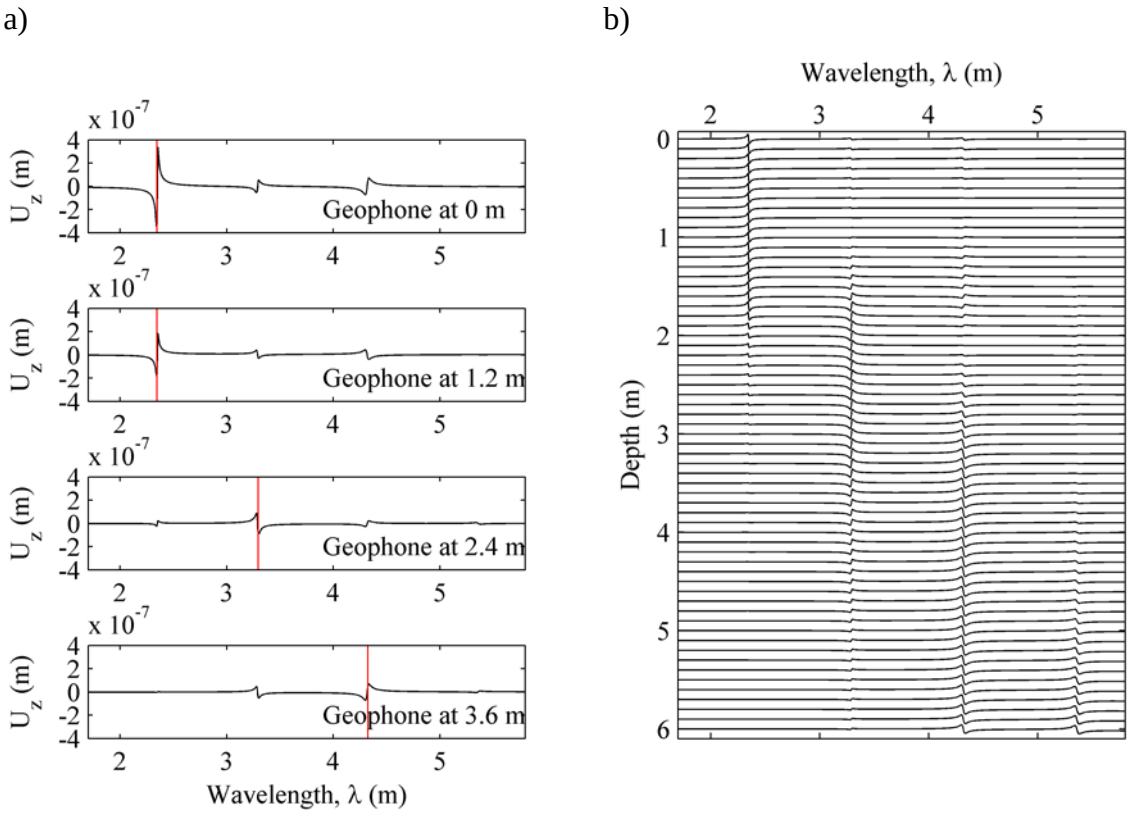

Figure 7.3 Vertical displacements versus wavelength at a frequency of 60 Hz: a) at four selected geophone depths (solid red line denotes the wavelength of the dominant mode having the maximum displacement amplitude); b) between 0 and 6 m depth at 0.1 m intervals.

By repeating the above procedure at different frequencies, the critical depths can be determined and plotted as a function of frequency, as shown in Figure 7.4 for the soil model of Figure 7.1. The three embedded geophone depths used in the simulation are also shown for reference. This figure can be used to determine either the required geophone depth range for a given higher mode's displacement to be dominant at a given frequency, or the lower apparent cut-off frequency below which the higher mode is no longer dominant for a given geophone depth. For example, geophone depths of 0 and 1.2 m for this soil model are not sufficient to measure a dominant first-higher mode below 80 Hz, which is consistent with the simulation results in Figures 7.2a through 7.2d. A geophone

depth of 2.4 m will result in a dominant first-higher mode above an apparent cut-off frequency of 36.5 Hz, also consistent with Figures 7.2e and 7.2f. Finally, a geophone depth of 3.6 m will give a dominant first-higher mode for frequencies between 30 and 55.5 Hz, and a dominant second-higher mode above 55.5 Hz, consistent with Figures 7.2g and 7.2h. These theoretical lower-bound apparent cut-off frequencies from the above stiffness-matrix-method displacement analysis compare well with those of the FEM simulation (Figures 7.2f and 7.2h), as detailed in Table 7.1.

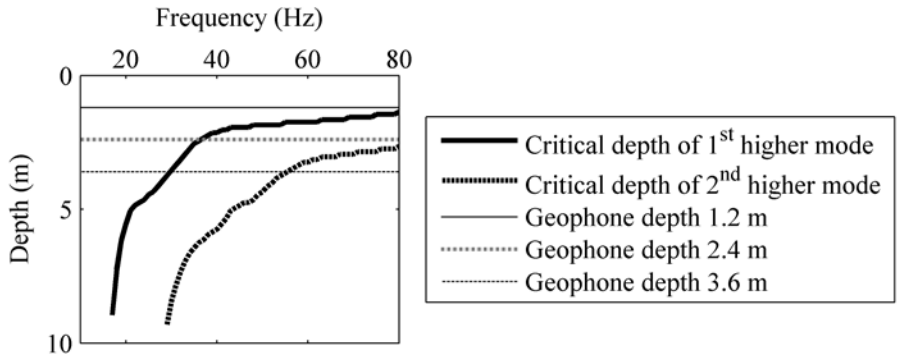

Figure 7.4 Critical geophone depths for measurement of 1st and 2nd higher modes for the layered soil model of Figure 7.1.

Table 7.1 Geophone depths and apparent cut-off frequencies.

Geophone depth (m)	Higher mode	Stiffness matrix analysis apparent cut-off frequency (Hz)	FEM simulation apparent cut-off frequency (Hz)
2.4	1st	36.5	37
3.6	1st	30	32
3.6	2nd	55.5	55

7.5 Field Case Study

To examine the critical depth for measuring higher modes, a real-word case study was carried out using the minimally-invasive hybrid surface-and-borehole method at the East River Valley recreational site in Ames, Iowa. A single 4.5 Hz vertical geophone with a ground spike was installed at the bottom of a hand-augured borehole at five depths

of 0 m, 0.91 m (3 ft), 1.83 m (6 ft), 2.74 m (9 ft), and 3.35 m (11 ft). A triggered 4.5 kg (10 lb) sledgehammer source impacting a 25 mm thick aluminum plate was used with a 3.66 m (12 ft) station separation over an offset range from 3.66 to 43.89 m (12 to 144 ft). Ten impacts were performed at each station for signal stacking. A 4-channel LDS Photon II dynamic signal analyzer was used for data acquisition, with a sampling interval of 0.78125 msec and anti-aliasing filtering for a maximum usable frequency of 500 Hz. Dispersion images were obtained for each of the five geophone depths using the MASW phase-velocity scanning technique. The individual dispersion images were then superposed to create a composite multi-mode dispersion image, as shown in Figure 7.5. A consistent fundamental mode can be seen from the data for geophone depths of 0 and 0.91 m. For a depth of 1.83 m, the first-higher mode appears above an apparent cut-off frequency of 31 Hz, which decreases to 20 Hz and 19 Hz as the geophone depth increases to 2.74 and 3.35 m, respectively. These trends are consistent with the numerical simulations presented above. The fundamental and first-higher modes in the frequency range of 6 to 30 Hz were used simultaneously in the GSA inversion algorithm of Chapter 8 to obtain the final shear-wave velocity profile for the site (Figure 7.6). The theoretical dispersion curves of the final profile are shown as purple curves in Figure 7.5.

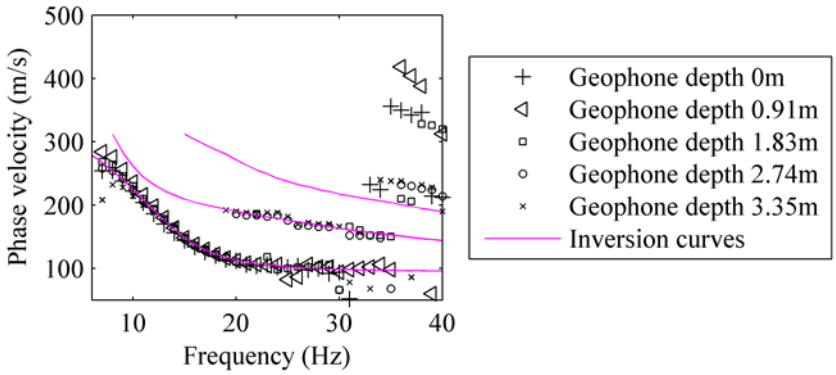

Figure 7.5 Multi-mode dispersion image obtained from MMSW field tests. Solid purple dispersion curves are for the inverted profile of Figure 7.6 by the transfer matrix method.

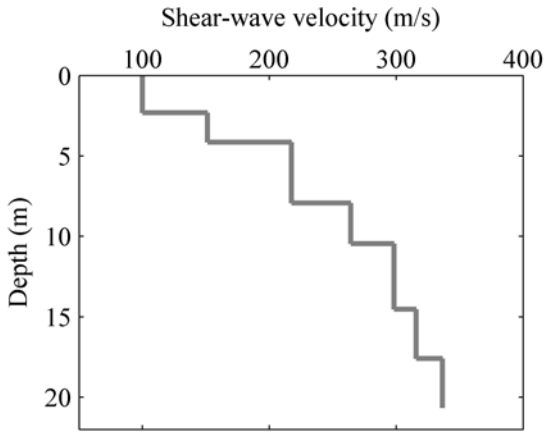

Figure 7.6 Final shear-wave velocity profile for field test site determined from two-mode inversion.

The final profile was then used in a stiffness matrix simulation as detailed above to identify the theoretical critical depths and corresponding theoretical apparent cut-off frequencies. For the first-higher mode, the theoretical cut-off frequencies are 28.5 Hz at a geophone depth of 1.83 m, 21 Hz at 2.74 m, and 18 Hz at 3.35 m (Figure 7.7). For the second-higher mode, the theoretical cut-off frequency is 36 Hz for the geophone depth of 3.35 m, while the experimental apparent cut-off frequencies from the dispersion data of Figure 7.5 are 36 Hz at a geophone depth of 2.74 m, and 34 Hz at 3.35 m. The experimental values generally agree well with the theoretical apparent cut-off frequencies, as summarized in Table 7.2. The geophone depth of 2.74 m does not intersect the theoretical second-higher mode curve in Figure 7.7, meaning that the theoretical apparent cut-off frequency for this depth is greater than 40 Hz. However, the experimental data of Figure 7.5 shows a second-higher mode with an apparent cut-off frequency of 36 Hz for a geophone depth of 2.74 m. The reason for this disagreement is that the inversion of the final profile used only the fundamental and first-higher modes between 6 and 30 Hz. Had the final inverted depth profile been determined using a three-

mode inversion between 6 and 40 Hz, the dispersion curve for the second-higher mode in Figure 7.5 would be expected to more closely match the experimental data.

It should be noted that the critical depth analysis as presented above requires an assumed layered soil model as input. Therefore, the comparison of experimental and theoretical apparent cut-off frequencies as shown above could be used as additional optimization constraints during inversion analyses to further reduce the uncertainty of final inversion profiles. However, such further application of the critical-depth analysis is beyond the scope of the present study.

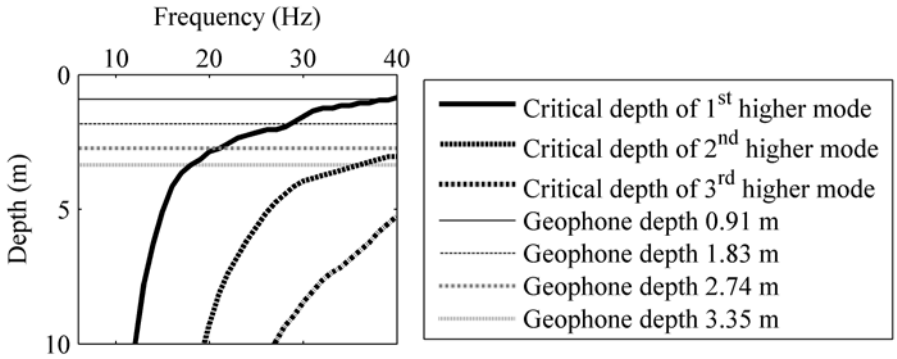

Figure 7.7 Theoretical critical depths for higher modes determined from the final profile of Figure 7.6.

Table 7.2 Geophone depths and apparent cut-off frequencies for 1st and 2nd higher modes.

Geophone depth (m)	Higher mode	Experimental apparent cut-off frequency (Hz)	Theoretical apparent cut-off frequency (Hz)
1.83	1st	31	28.5
2.74	1st	20	21
3.35	1st	19	18
2.74	2nd	36	NA
3.35	2nd	34	36

7.6 Conclusions

A procedure to determine the critical minimum geophone depths needed for capturing dominant higher modes of an assumed layered soil model was presented for use with a minimally-invasive hybrid surface-and-borehole method. The critical depth procedure employs stiffness matrix and phase-velocity scanning analyses, from which the critical depth is identified as the depth where the dominant peak of the displacement shifts to the next higher mode. The procedure was verified by numerical simulations and experimental data to give depths and corresponding apparent cut-off frequencies that agree well with those of both simulated and measured multi-mode dispersion images. For the regular soil profiles examined, the critical depth at a given frequency is deeper for higher modes than for lower modes, and the apparent cut-off frequency of a given higher mode decreases as the geophone depth increases. In general, a greater geophone depth can capture more dispersion information in terms of additional higher-modes with lower apparent cut-off frequencies. It is proposed that the comparison of experimental and theoretical apparent cut-off frequencies for embedded geophones could be used in inversion analyses for additional optimization constraints to further reduce the uncertainty of final inversion profiles.

CHAPTER 8. GENETIC-SIMULATED ANNEALING OPTIMIZATION FOR SURFACE WAVE INVERSION

8.1 Abstract

A new hybrid genetic-simulated-annealing (GSA) optimization algorithm is introduced to solve the multivariable minimization problem for surface wave inversion. The algorithm is effective for both global and local searches due to its combination of the reproduction and selective generation schemes from genetic algorithms (GA) with the nonlinear scaling fitness function and perturbation scheme from simulated annealing (SA). The hybrid GSA algorithm can reduce the risk of being trapped in a local minimum and improve global searching efficiency. A mathematical test function, as well as synthetic and real-world surface wave examples, is used to examine the advantages and performance of GSA. Comparison of GA, SA, and GSA inversion results demonstrates that GSA can yield the smallest uncertainty and greatest efficiency, and improve the confidence of using surface wave testing for stiffness profiling.

8.2 Introduction

Inversion is the final step in surface wave methods, by which stiffness profiles of testing sites are inferred by matching theoretical dispersion curves to their experimental counterparts (e.g., Nazarian 1995, Xia et al. 1999, Ryden and Park 2006). The theoretical dispersion curve is a nonlinear function of shear-wave velocities, thicknesses, densities, and Poisson's ratios of a horizontally-layered elastic structure. The nonlinear function can be solved using matrix methods to obtain the theoretical dispersion curves for a given soil profile, which is referred to as the forward problem (e.g., Haskell 1953, Kausel and Roësset 1981, Nazarian 1984, Stokoe et al. 1994, Lowe 1995, Gucunski and Maher 2002,

Ryden 2004). The experimental dispersion information can be extracted from raw offset-time field data by using the spectral analysis of surface waves (SASW) method (Nazarian 1984, Stokoe et al. 1994, Joh 1997), multichannel analysis of surface waves (MASW) method (Park et al. 1999a), refraction micrometer (ReMi) method (Louie 2001), MMSW-borehole geophone or MMSW-SPT methods presented in Chapter 6, or other multichannel transforms such as those described in Chapter 3.

The root mean square (RMS) error is employed herein to quantify the discrepancy between the theoretical and experimental curves (e.g., Nazarian 1995). Minimizing RMS error is a nonlinear and multivariable optimization procedure, because the theoretical dispersion curve is a nonlinear function of the stiffness profile (Yamanaka and Ishida 1996, Ryden and Park 2006). Thus, inversion is challenging and computationally intensive. Commonly used inversion methods include the Levenberg-Marquardt (L-M) method (e.g., Nazarian 1995, Xia et al. 1999), genetic algorithm (e.g., Yamanaka and Ishida 1996, Yamanaka 2005, Pezeshk and Zarrabi 2005), and simulated annealing algorithm (e.g., Iglesias et al. 2001, Ryden and Park 2006).

The L-M method, as a traditional minimization technique, is based on a linearized, damped least-squares method featuring a Jacobian matrix (i.e., partial derivatives of inverted parameters) and singular value decomposition (SVD) (Nazarian 1995). Although the L-M method has been widely applied in surface wave inversion (e.g., Nazarian 1995, Xia et al. 1999), it has some limitations, including the challenge of estimating an appropriate initial profile (Yamanaka and Ishida 1996, Yamanaka 2005), the risk of the solution becoming trapped in a local minimum (Yamanaka and Ishida 1996), unstable partial derivatives at jumps of apparent dispersion curves (Ryden and

Park 2006, Lin and Ashlock 2011), the requirement for choosing appropriate damping factors for SVD (Xia et al. 1999), and occasional numerical instabilities in calculating the Jacobian matrix (Yamanaka 2005).

To overcome the above limitations of the L-M method, global search algorithms such as the genetic algorithm (Holland 1975) and simulated annealing algorithm (Kirkpatrick et al. 1983, Szu and Hartley 1987), have been successfully applied for surface wave inversion by searching for the global minimum without the need for partial derivatives (e.g., Yamanaka and Ishida 1996, Iglesias et al. 2001, Yamanaka 2005, Pezeshk and Zarrabi 2005, Ryden and Park 2006, Lin and Ashlock 2011). The genetic algorithm is a search heuristic for optimization problems that mimics the process of natural selection, and tends to converge towards local minima. Simulated annealing is a probabilistic meta-heuristic for global optimizations that simulates the cooling of liquids to form crystals in metallurgy, with the convergence rate governed by a cooling temperature variable.

The GA and SA algorithms have different and complementary characteristics. The GA excels at global searches (Liang and Cui 2000, Yamanaka 2005) with a high efficiency (Liang and Cui 2000, Iglesias et al. 2001) and can use previous information to configure the search of the next generation effectively (Tang et al. 1996). However, its performance is not good for local searches, and it may possibly prematurely convergence to a local minimum (Liang and Cui 2000, Yamanaka 2005). The GA algorithm is complex due to three main aspects: (1) the requirements of binary conversion, reproduction, mutation, and crossover steps (Yamanaka 2005), (2) sensitivity to the choice of mutation probability and fitness functions (Franconi and Jennison 1997), (3)

and slow convergence for problems with many variables and large population sizes (Franconi and Jennison 1997, Li et al. 1999). The SA performance is good for local searches (Franconi and Jennison 1997, Liang and Cui 2000, Yamanaka 2005) and can achieve small RMS values at final iterations (Iglesias et al. 2001, Yamanaka 2005). The SA algorithm is comparatively simple (Yamanaka 2005), robust (Franconi and Jennison 1997), and has small computer memory requirements (Iglesias et al. 2001). However, its performance is not good for global searches (Franconi and Jennison 1997, Liang and Cui 2000, Yamanaka 2005).

To overcome the shortcomings of the GA and SA algorithms, a number of hybrid GA-SA optimization schemes have been proposed by other researchers as complementary strategies to combine the advantages of the two algorithms (e.g., Adler 1993, Jeong 1996, Tang et al. 1996, Franconi and Jennison 1997, Li et al. 1999, Liang and Cui 2000, Krahenbuhl and Li 2004, Zou and Kang 2005, Shan et al. 2006). Four main ways have been proposed to combine the GA and SA algorithms: (1) using the Metropolis criterion of SA to accept models yielded by GA with a specific probability to improve the diversity of searching models (e.g., Adler 1993, Jeong 1996, Tang et al. 1996, Li et al. 1999, Zou and Kang 2005, Shan et al. 2006); (2) parallel operation of GA and SA searches, then using two competing sets of searched models to gain a selective generation (Liang and Cui 2000); (3) a series connection of GA and SA with two searching steps, first operating a GA search, then passing GA models to SA for further searching (Li et al. 1999); and (4) applying the crossover of GA for mating offspring models of SA (Franconi and Jennison 1997). Each strategy can improve searching results,

but all require intensive computation due to conversion between model parameters and binary strings for the mutation and/or crossover steps of GA.

To improve searching efficiency and quality without increasing computational cost, selected aspects of GA and SA were combined in a new way in this investigation to formulate a hybrid genetic-simulated-annealing (GSA) optimization algorithm. The GSA algorithm combines the cooling and random perturbation schemes of SA with the reproduction scheme of GA, and employs the SA nonlinear scaling fitness as a control for the GA selection scheme. To improve speed, the GA crossover and mutation schemes were not included in the new GSA algorithm. The GA reproduction scheme was included in GSA to enable selection of good candidates from the previous generation of models, and guide further searches effectively without the need for converting between layer parameters and binary strings normally required by GA mutation and crossover schemes. The SA nonlinear scaling fitness, which varies with the cooling temperature, was used in GSA to improve the diversity of global searches at the beginning and speed up local searches at the end. GSA combines a global GA search, followed by the random perturbation scheme of SA for stable and efficient local searching. A selective-generation GA scheme is also used to select candidates from the reproduced and perturbed models to form a new generation while avoiding randomness and blindness of reproduction, and to speed up searching. The performance of GSA is demonstrated below using a test function and two case studies of surface wave inversion. As will be shown, GSA was found to perform well in global and local searches with a computational cost comparable to SA.

8.3 Genetic-Simulated Annealing Optimization Algorithm

Figure 8.1 shows a flowchart of the GSA algorithm for inversion problems, which contains the following steps:

Step 1) Set up the initial temperature and cooling schedule, and estimate bounds for inverted parameters; then randomly generate models as the first generation;

Step 2) Calculate dispersion curves and corresponding RMS errors for all models;

Step 3) Calculate the probability of reproduction; then reproduce a new generation of models (m_r);

Step 4) Randomly perturb the preceding models to provide a new set of models (m_p), and calculate their dispersion curves and corresponding RMS errors;

Step 5) Check whether any RMS meets the tolerance $RMS_{desired}$, or the iteration meets the maximum iteration limit;

Step 6) Obtain a selective generation from the two sets of models (m_r and m_p) according to their fitness;

Step 7) Return to Step 2 if the end condition is not met.

The procedures for reproduction using the nonlinear scaling fitness, simulated annealing perturbation, and selective generation schemes are introduced in detail in the following sections.

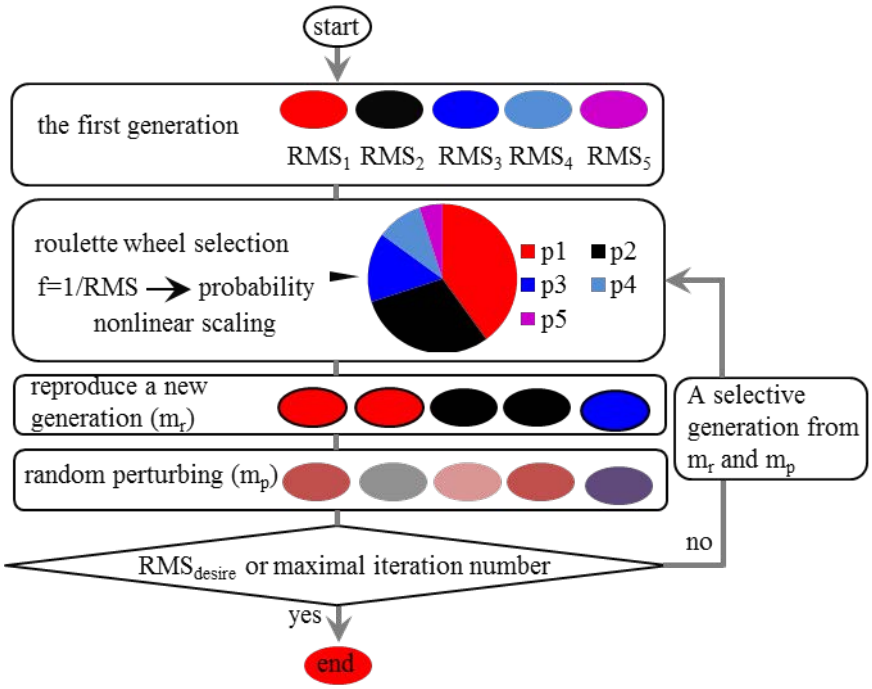

Figure 8.1 Flowchart of the genetic simulated annealing (GSA) algorithm.

8.3.1 Estimating bounds of inverted parameters

The bounds of the inverted parameters must first be estimated before a surface-wave inversion can be performed. The only known information at the starting point is the experimental dispersion curve, or set of curves for multi-mode inversions. A given point on the dispersion curve will correspond to the wavelength

$$\lambda = V_{ph} / f \tag{8.1}$$

where V_{ph} is the phase velocity of the Rayleigh wave component at the frequency f. Due to the decay of motion with depth, the majority of the Rayleigh wave energy occurs within a depth of one wavelength from the surface, and a representative measurement depth is usually recommended as one-half of the wavelength (Heukelom and Forster 1960, Park et al. 1999a). Surface wave methods are thus commonly viewed as measuring the average velocity of the layers in the medium within a depth proportional to the

surface wavelength at a given frequency. Therefore, initial profiles are commonly generated by assuming that V_{ph} represents the average Rayleigh-wave phase velocity within a depth equal to one-half of the Rayleigh wavelength for any point on the experimental dispersion curve. Note that the Rayleigh wavelength λ is defined in the horizontal direction of propagation, and the Rayleigh wave motion with depth is usually described in terms of z/λ, i.e. depth normalized by the horizontal wavelength.

The following procedure was developed in this study to generate initial profiles using a stronger theoretical basis than the above general guidelines of using one-half the wavelength as the depth for a given point on the dispersion curve. The average shear-wave velocity of the testing site within a depth one-half wavelength is:

$$\bar{V}_{Si} = \frac{\sum_{j=1}^{i-1} V_{Sj} h_j + V_{Si}\left(\lambda_i/2 - \sum_{j=1}^{i-1} h_j\right)}{\lambda_i/2} \tag{8.2}$$

where V_{Sj} and h_j are the shear-wave velocity and thickness of the j^{th} layer, and λ_i is the Rayleigh wavelength, the midpoint of which extends to some depth within the i^{th} layer. The shear-wave velocity in the i^{th} layer can be obtained from Eq. (8.2) as

$$V_{Si} = \frac{\bar{V}_{Si}\lambda_i/2 - \sum_{j=1}^{i-1} V_{Sj} h_j}{\lambda_i/2 - \sum_{j=1}^{i-1} h_j} \tag{8.3}$$

Denoting $V_{ph,i}$ as the average Rayleigh-wave velocity within a depth equal to one-half of the Rayleigh wavelength, which corresponds to a point inside layer i, $\bar{V}_{Si}$ can be expressed as

$$\bar{V}_{Si} = V_{ph,i}/\beta \tag{8.4}$$

where β is a factor to convert Rayleigh-wave phase velocity to shear-wave velocity, and is a function of Poisson's ratio. Substituting Eq. (8.4) into Eq. (8.3) gives

$$V_{Si} = \frac{\left(V_{ph,i}/\beta\right)\lambda_i/2 - \sum_{j=1}^{i-1} V_{Sj}h_j}{\lambda_i/2 - \sum_{j=1}^{i-1} h_j}, \quad i \geq 2. \tag{8.5}$$

where $V_{ph,i}$ and λ_i can be obtained from the experimental dispersion curve, h_j is layer thickness for the initial profile which can be assumed a small constant (e.g., 1 m for soils), β is a factor related to Poisson's ratio (e.g., approximately 0.9 for soils). As frequency increases, the wavelength decreases and the dispersion curves typically approach a constant and therefore become non-dispersive when the Rayleigh wavelength is smaller than the thickness of the first layer. Thus, the shear-wave velocity of the first layer can be estimated directly from the experimental dispersion curve as

$$V_{S1} = V_{ph}(f_{\max})/\beta \tag{8.6}$$

where $V_{ph}(f_{\max})$ is the phase-velocity at the maximum frequency from the experimental dispersion data. Substituting Eq. (8.6) into Eq. (8.5) then gives the shear-wave velocity of the second layer (V_{S2}), then using the known information of the first and second layer, the process is repeated to infer V_{S3} of the third layer, and so on. Using the known layer velocity recursively to infer the next unknown layer velocity for assumed constant layer thicknesses (e.g., 1 m) gives the initial shear-wave velocity profile. Adjacent layers found to have nearly equal shear-wave velocities can be merged into thicker layers. After building the estimated initial shear-wave velocity profile for inversion, the optimization search bounds for layer shear-wave velocity and thickness can be specified as

$$[1-\alpha \quad 1+\alpha]\times V_{Si} \ \textit{and} \ [1-\alpha \quad 1+\alpha]\times h_j, \ \ \alpha \in [0.1,\ 0.5] \tag{8.7}$$

where α is the searching range factor.

8.3.2 Probability of reproduction with nonlinear scaling fitness

In this section, a hybrid scheme is developed which uses the nonlinear scaling fitness scheme of SA to control the GA probability of reproduction. The convergence of the algorithm is monitored by the root-mean-square (RMS) error (Nazarian 1995):

$$RMS = \sum_{m=1}^{M} \sqrt{\frac{\sum_{i=1}^{N_{f,m}} \left(V_{ph,m,i} - V_{ph,m,i}^{e} \right)^2}{N_{f,m}}} \tag{8.8}$$

where M is the total number of modes used for inversion, V_{ph} is the phase velocity of the theoretical dispersion curve, V_{ph}^{e} is the phase velocity of the experimental dispersion curve, and $N_{f,m}$ is the number of frequency points for the m^{th} mode. In the genetic algorithm (Goldberg 1989), models are reproduced according to their fitness f, defined as

$$f = \frac{1}{RMS} \tag{8.9}$$

and the normal selection uses the probability of reproduction;

$$\mathrm{P}_j = \frac{f_j}{\sum_{k=1}^{N_g} f_k} \tag{8.10}$$

where N_{g} is the total number of models in a generation, and k refers to the k^{th} model. Equations (8.9) and (8.10) mean that a model will have a higher probability of reproduction to get passed down to the next generation when it has a smaller misfit (RMS) and therefore larger fitness. Although undesirable at the beginning of the search, it is possible to have some individuals with an extraordinary fitness, who will take over a significant part of the generation and lead to a premature convergence. Fitness scaling can help solve this problem using the approaches of linear scaling (Goldberg 1989) or nonlinear scaling (Li et al. 1999, Hui 2010). The application of annealing temperature in

the nonlinear scaling provides the "simulated annealing select" method (Li et al. 1999, Hui 2010), for which the probability of reproduction is

$$P_{ij} = \frac{e^{f_{ij}/T_i}}{\sum_{k=1}^{N_g} e^{f_{ik}/T_i}} \tag{8.11}$$

where i is the generation number, k refers to the k^{th} individual, f_{ij} is the fitness of the j^{th} individual in the i^{th} generation, and T_i is the annealing temperature in the i^{th} generation. When temperature is high, the reproduction probabilities between different individuals are close. This can guarantee that beginning generations have high diversity, which will help avoid the solution becoming trapped in a local minimum. When temperature decreases, the increasing difference among individuals' reproduction probabilities can speed up searching for the global minimum.

8.3.3 Simulated annealing perturbation schemes

In the GSA algorithm, the GA reproduction scheme is used to produce the first generation models (m_r), and then the SA cooling and random perturbation schemes are used to perturb all the models to generate a new generation of models (m_p). A common SA cooling schedule is

$$T_i = T_0 a^i \tag{8.12}$$

where a is the cooling parameter, and T_0 is the initial temperature (Ryden and Park 2006). The choices of a and T_0 are subjective and application dependent.

An effective random perturbation scheme for SA is to perturb all parameters once in each iteration (Ryden and Park 2006):

$$m_i^p = m_i + \Delta m_j \left(\frac{T_i}{T_0}\right)\left(\eta_1 \tan\left(\frac{\eta_2 \pi}{2}\right)\right) \tag{8.13}$$

where η_1 and η_2 are random variables in the interval [-1, 1], and Δm_j is the search interval of inverted parameter *j*.

8.4 Case Studies

8.4.1 Mathematical test function

In this section, the GSA algorithm is applied to search for the global minimum of a mathematical test function possessing multiple local minima, which represents the property of the misfit function in surface wave inversion (e.g., Ryden 2006, Moro and Ferigo 2011). The GA, SA, and GSA algorithms are utilized to search for the global minimum of the test function, shown in Figure 8.2 and defined as

$$f(x) = (x-6)^2 - 10\cos[2\pi(x-6)] + 10 \tag{8.14}$$

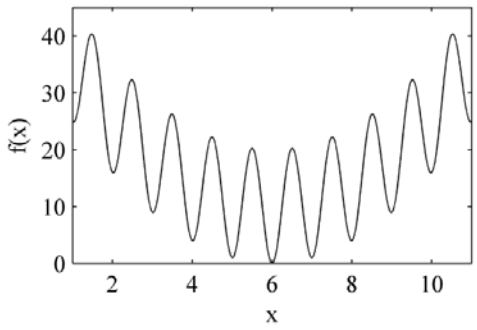

Figure 8.2 Mathematical test function for case study.

The abscissa of the exact global minimum of the test function in Figure 8.2 has a value of 6. The searching histories and results for 1,000 trials using the GA, SA, and GSA algorithms are shown in Figure 8.3. The results demonstrate that GA can converge to a value rapidly, then exhibits only a small improvement with further iterations, and has the lowest probability of converging to the true global minimum. SA has a strong fluctuation in error during searching, but a higher probability of converging to the true global minimum if a sufficient number of iterations are used. The GSA also exhibits a strong fluctuation of error at the beginning, because the simulated annealing selection is

utilized to ensure diversity of the generations. However, the GSA error consistently decreases with iteration number, while each generation retains some individuals having relatively high error to avoid premature convergence. At the end of iterations, GSA converges to the true global minimum of the test function with the highest probability of nearly 100%.

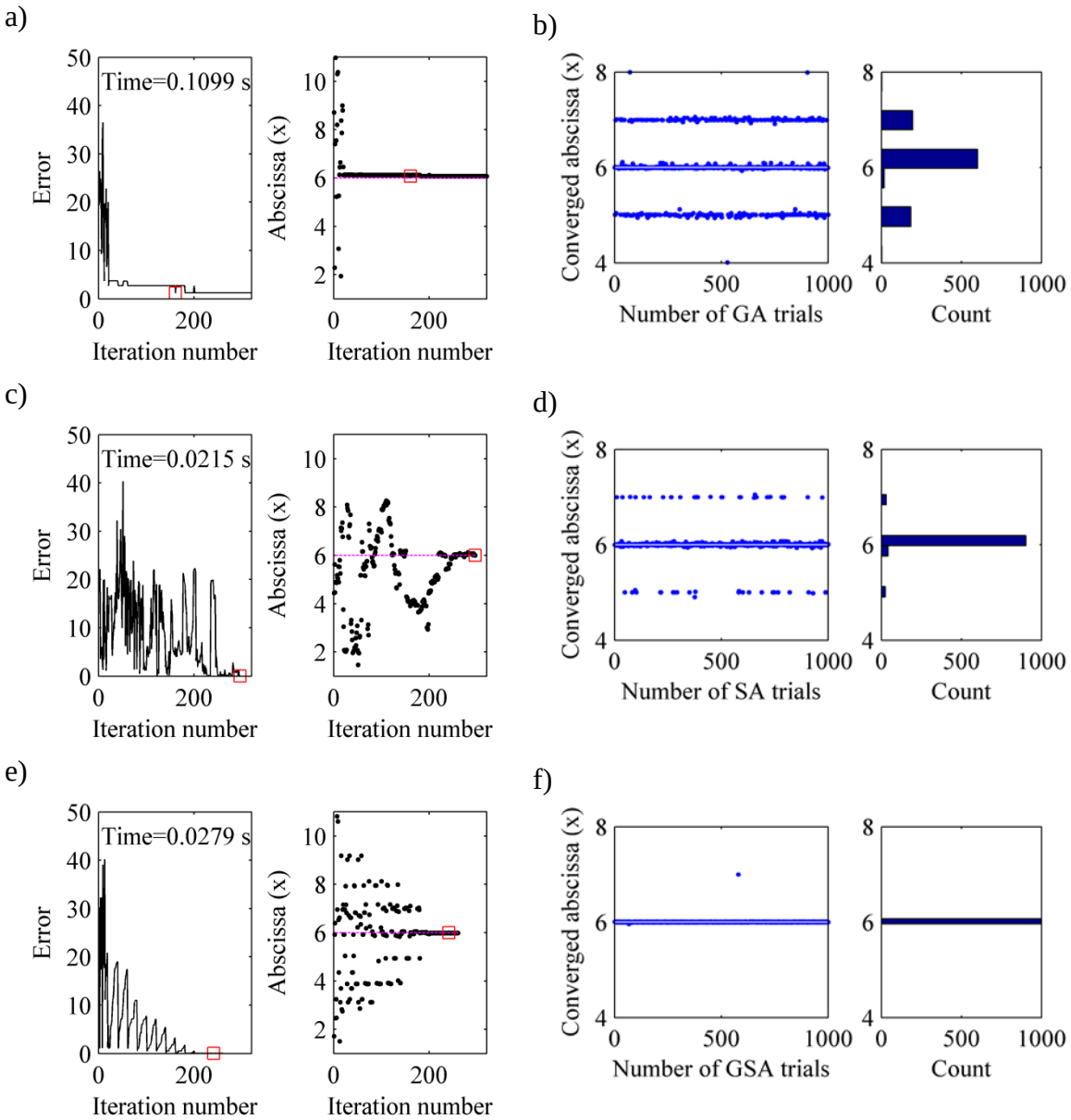

Figure 8.3 Convergence histories of GA (a), SA (c), and GSA (e), and converged abscissa values from 1,000 search trials with GA (b), SA (d), and GSA (f).

For GSA, a comparison of the normal and simulated annealing selections is shown in Figure 8.4 in terms of the reproduction probability versus fitness. The normal selection criterion provides different reproduction probabilities for individuals in a generation during the entire searching process. At the beginning, if an individual with a local minimum dominates one generation by having the highest fitness and reproduction probability, successive searching may be trapped in the local minimum. In contrast, the simulated annealing selection provides a more uniform reproduction probability at the beginning to give individuals a fair chance at becoming parents of a subsequent generation. As the annealing temperature decreases, the differences in reproduction probability between individuals increase to speed up searching for the global minimum.

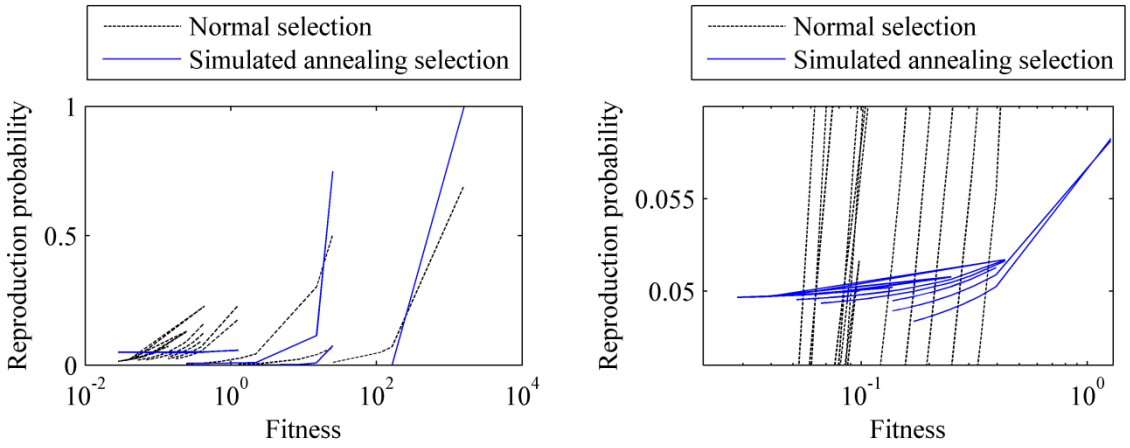

Figure 8.4 Comparison of normal and simulated annealing selections for GSA algorithm applied to test function. Left: full-range plot, right: close-up.

8.4.2 Surface wave inversion simulation example

A multi-layer profile with increasing stiffness (Table 8.1) was used to examine the efficiency and reliability of the GSA algorithm. The variation of RMS error with V_{S1} and V_{S2}, and with h_1 and h_2 is shown in Figures 8.5a and 8.5b, respectively. By varying only one set of parameters at a time (velocities or layer thicknesses), these figures do not

reveal the multiple minima of the RMS errors. If all parameters are simultaneously varied, the RMS error should exhibit multiple minima.

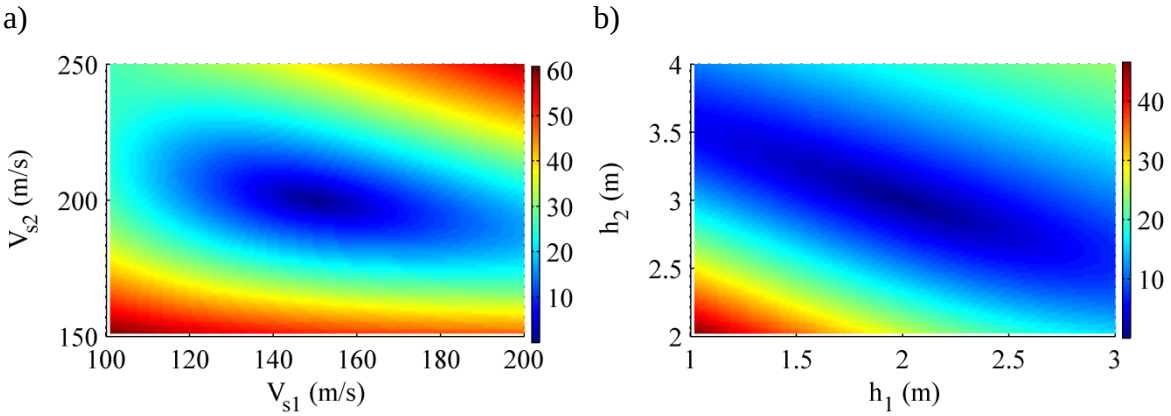

Figure 8.5 RMS error: (a) as a function of V_{S1} and V_{S2}, (b) as a function of h_1 and h_2.

Table 8.1 Parameters of layered soil model

Layer #	V_S (m/s)	V_P (m/s)	Density, ρ (kg/m^3)	Layer depth, h (m)
1	150	303	1800	2
2	200	403	1800	3
3	400	807	1900	∞ (half space)

To examine the performance of GA, SA, and GSA for the multiple minima surface-wave testing inversion problem, the fundamental mode theoretical dispersion curve of the soil profile defined in Table 8.1 was calculated using the transfer matrix method detailed in Chapter 2. The three optimization methods were then used with 68 inversion trials each, with a searching range factor $\alpha = 0.5$ applied to the initial profile generated by the procedure of Section 8.3.1. For the GA algorithm, the probabilities for the crossover and mutation were set to 0.9 and 0.03, respectively, and 50 generations consisting of 45 models each were used. The SA algorithm initial temperature was set to T_0=40, and an exponential cooling schedule of a=0.985 with 300 iterations was specified. For the GSA algorithm, an initial temperature of T_0=40 and an exponential cooling schedule of a=0.95 were used, with 50 generations consisting of 45 models in each

generation. The statistical properties of the inverted parameters from the three optimization methods are shown as box plots in Figure 8.6. In the box plots, the central horizontal line is the median value, the upper and lower box edges are the 25th and 75th percentiles, the whiskers extend vertically to the most extreme data not considered to be outliers, and the outliers are shown as + marks. Compared to GA and SA, the uncertainty of all five model parameters is lowest with GSA, especially for the three shear-wave velocities. Three sets of 68 inverted profiles from each of the GA, SA, and GSA search algorithms are shown in Figure 8.7 along with the real profile, from which GSA clearly results in the smallest uncertainty. The inversion error defined in Eq. (8.8) (i.e., the discrepancy between the final inverted and true profiles) is plotted versus RMS error (i.e., the discrepancy between dispersion curves for the inverted and real profiles) in Figure 8.8. The correlation is very scattered; the inversion error of some points decreases as RMS increases, indicating that RMS error in the dispersion curves is not a perfect indicator of how well the inverted profile agrees with the true profile. However, the overall trend exhibits a decrease in inversion error as the RMS error decreases.

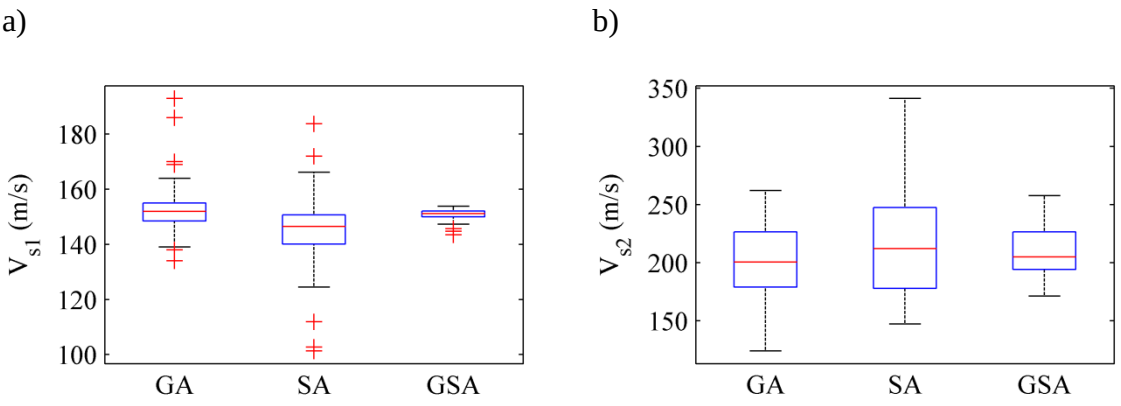

Figure 8.6 Box-plots of inverted model parameters from 68 trials using GA, SA, and GSA. (a) and (b): shear-wave velocities of the top two layers, (continued on next page)

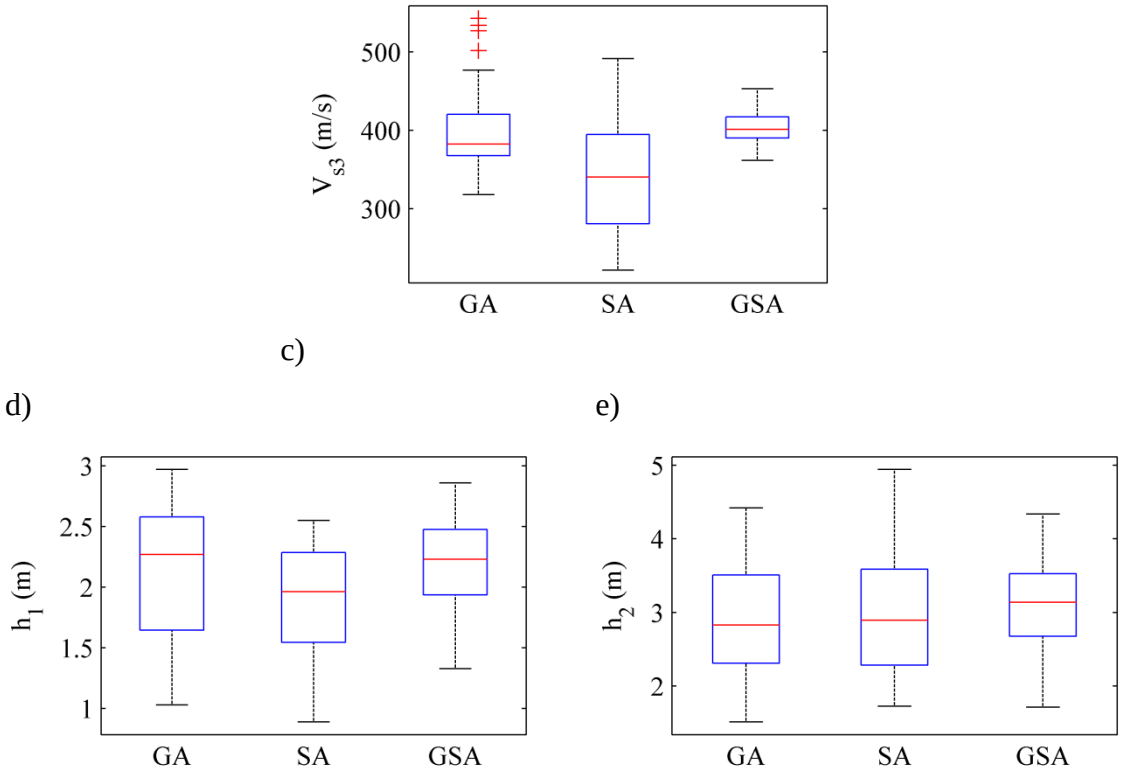

Figure 8.6 (continued) (c): shear-wave velocities of the third layers, (d) and (e): thicknesses of the top two layers.

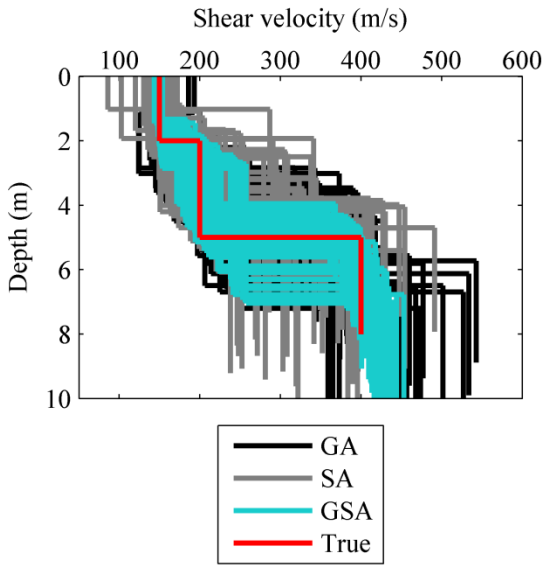

Figure 8.7 Inverted and true profiles.

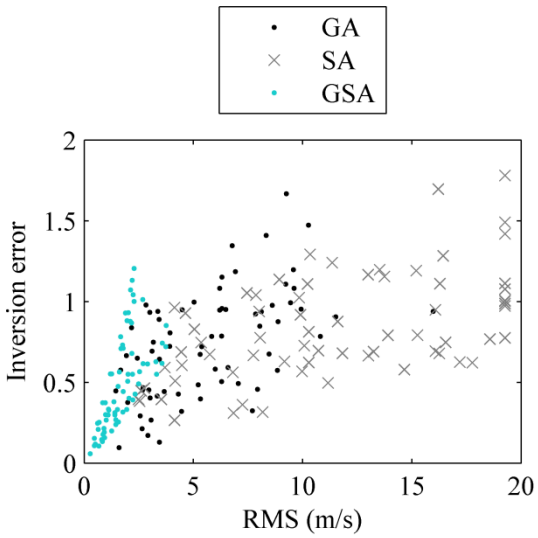

Figure 8.8 Inversion error vs. RMS.

8.4.3 Real-world surface wave inversion examples

8.4.3.1 SASW benchmarking data

The three optimization algorithms were applied to inversion of one set of field test data from the SASW benchmarking data set (Tran and Hiltunen 2011). The chosen test used geophone offsets from 98 to 220 ft in the site coordinate system, with the impact point at an offset coordinate of 88 ft. Data was collected using a multi-receiver with one impact (i.e., MASW) testing method with sixty-two 4.5-Hz vertical geophones, a sampling interval of 0.78125 msec, and a triggered sledgehammer. Geophones were placed along a straight-line with 10 ft source offset and 2 ft spacing. The pre-trigger delay was about 10% of the 12.8 sec total recorded time. A selected part of normalized signals are assembled in Figure 8.9a, and the experimental dispersion image with a fundamental mode is shown in Figure 8.9b.

The GA, SA, and GSA inversions all featured 50 trials with a searching range factor of $\alpha = 0.4$. For GA, the probabilities for the crossover and mutation were set to 0.9 and 0.05, respectively, with 55 generations and 20 models in each generation. For SA, an initial temperature of T_0=40 was used with an exponential cooling schedule of a=0.9962 with 1120 iterations. For the GSA algorithm, an initial temperature of T_0=40 was specified, with an exponential cooling schedule of a=0.95 with 55 generations and 20 models in each generation. The convergence histories of RMS error and V_{S30} are shown in Figures 8.9c and 8.9d. For GA, the RMS error rapidly reaches a minimum while V_{S30} rapidly converges to a value, and further searching does not reduce RMS or change V_{S30}. The values for SA fluctuate widely during the searching process and finally converge to a minimum RMS and a V_{S30} after many iterations. The GSA initially has a

diverse range of profiles and gradually converges to a minimum RMS below the minimum RMS values of GA and SA, while V_{S30} converges to a relatively stable value quickly.

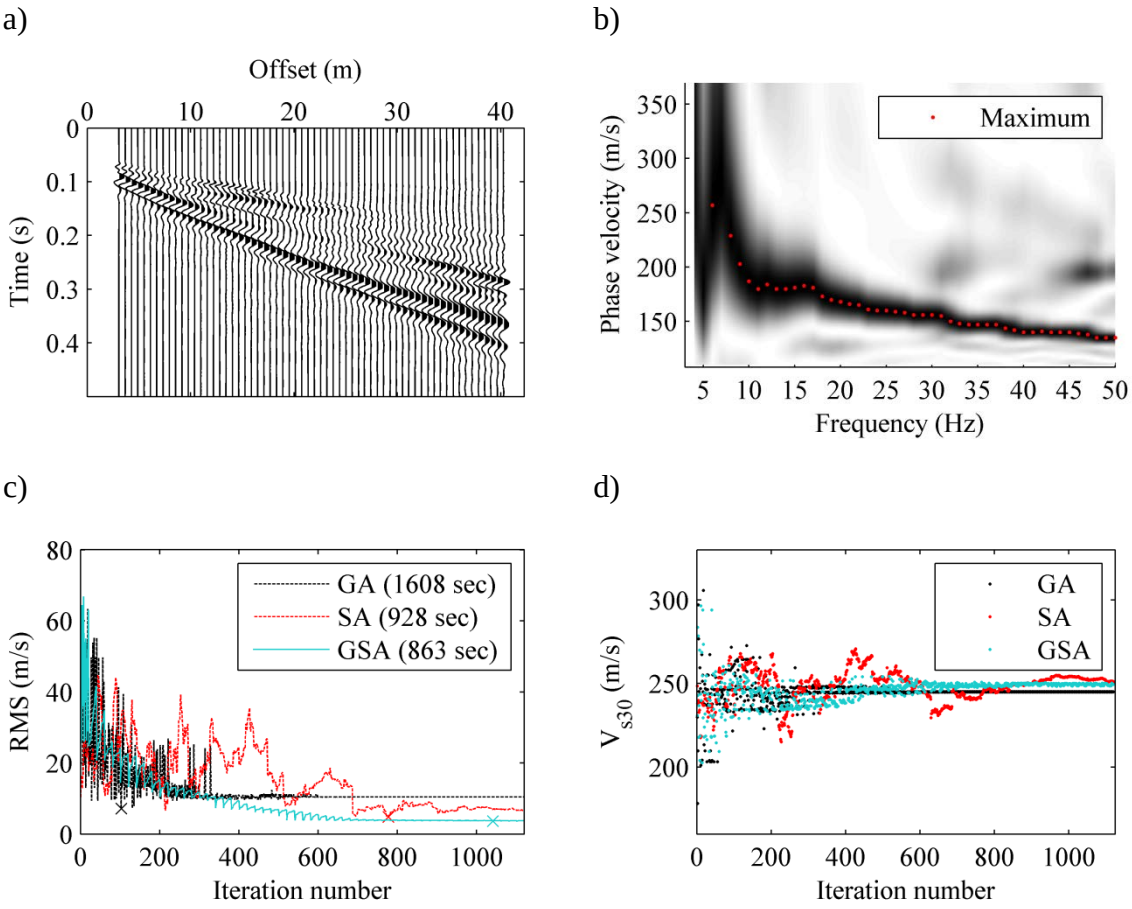

Figure 8.9 a) Field data; b) Experimental dispersion image and inversion dispersion curve; c) Convergence history of RMS; d) Convergence history of V_{S30}.

Figure 8.10 shows the final profiles of the GA, SA and GSA inversions along with profiles from other researchers (Martin 2011, Tran and Hiltunen 2011, Zhao 2011). All profiles are relatively close to each other in terms of V_{S30}, except the one from Tran. Figures 8.11 and 8.12 shows the boxplot of V_{S30} and RMS from 50 trials of GA, SA, and GSA inversions. The GSA algorithm significantly decreases the uncertainty of inversion

in terms of V_{S30}. Therefore, if the V_{S30} is close to a borderline limit for soil classification criteria, the GSA can significantly reduce the probability of misclassification.

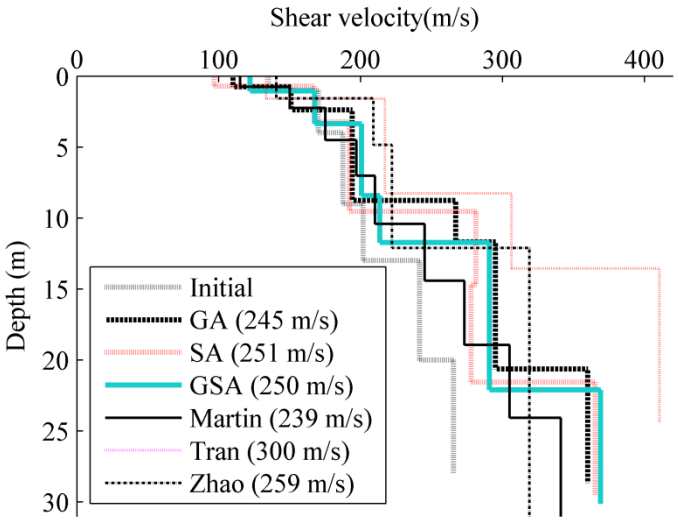

Figure 8.10 Final converged shear-wave velocity profiles.

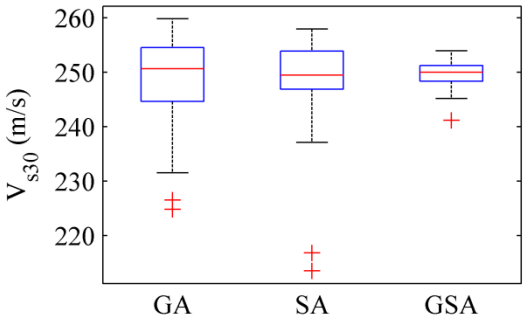

Figure 8.11 Boxplots of V_{S30} from 50-each GA, SA, and GSA inversions.

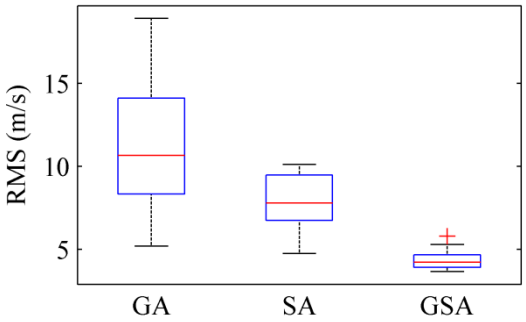

Figure 8.12 Boxplots of RMS error from 50-each GA, SA, and GSA inversions.

8.4.3.2 Data from MMSW-SPT tests

The multimode dispersion data of Figure 8.13 from the MMSW-SPT tests detailed in Chapter 6 were used for inversion analysis. During MMSW-SPT testing, seismic cone penetration tests (SCPT) were also performed by Geoprobe. The inverted shear-wave velocity profiles using single- and multi-mode inversions with GSA are shown in Figure 8.14. The fundamental-mode dispersion curve in Figure 8.13 was used from 7 Hz to 18 Hz. The fundamental mode (M_0) inversion gives a normal profile with increasing stiffness which does not identify the trapped slow layer identified in the SCPT profile. Misidentifying the second-higher mode (M_2) as the first-higher mode (M_1) and using the dispersion image up to 30 Hz, the two-mode (M_0-$M_{1,misidentified}$) inversion yields an irregular profile with an extraordinarily stiff layer. If the second-higher mode is correctly identified, the two-mode (M_0-M_1) inversion yields a profile having a trapped soft layer. However, the inverted soft layer is not in the correct position compared to the SCPT profile. Upon using the superimposed dispersion image in Figure 8.13, the three-mode (M_0-M_1-M_2) inversion gives a profile having a trapped soft-clay layer between 7 to 10 m, which is in good agreement with the SCPT profile (Figure 8.14). However, relative to the surface wave inversion profile, the SCPT data indicates a higher shear-wave velocity for the stiff layer overlying the soft layer.

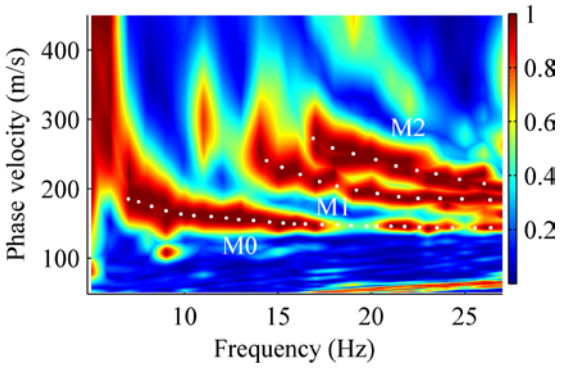

Figure 8.13 Multi-mode dispersion image obtained from MMSW-SPT tests.

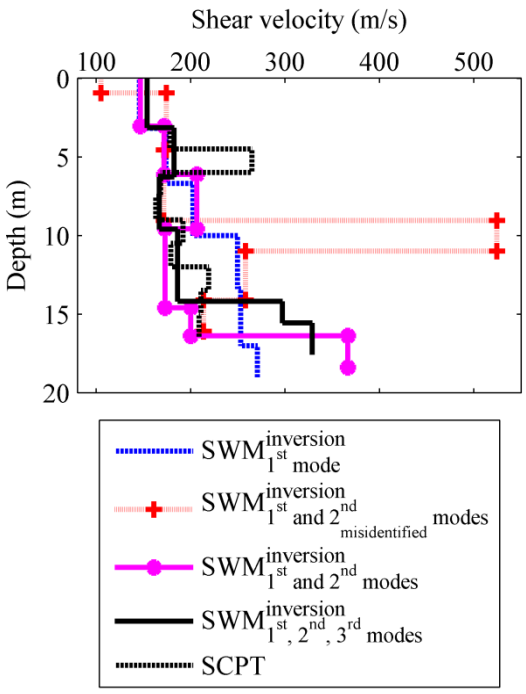

Figure 8.14 Shear-wave velocity profiles from 1, 2, and 3-mode surface wave inversions and SCPT test.

8.5 Conclusions

This chapter presents a new hybrid genetic-simulated annealing (GSA) optimization algorithm that combines the complementary advantages of genetic algorithms and simulated annealing algorithms. Incorporation of the GA reproduction scheme with the "simulated annealing select" method into the GSA algorithm can avoid premature convergence to a local minimum and speed up global searching, while use of the SA perturbation scheme can avoid slow searching performance over multiple parameters while assisting in local searches. Results from a mathematical test function demonstrate that the GSA algorithm is less likely to become trapped in local minima than the GA and SA algorithms. The elimination of GA crossover and mutation schemes along with their costly requirements of binary conversion gives GSA a faster speed than GA. Good performance of the GSA algorithm was demonstrated using numerical simulations

and real examples of surface wave inversion optimization problems. The results indicate that: (1) the GSA algorithm can provide stiffness profiles with lower uncertainty than SA or GA, (2) taking the average of multiple inversion results is more reliable than using the result of one inversion, and (3) the searching methods examined in this chapter appear unable to converge to an exact stiffness profile, but rather a profile near the exact one.

CHAPTER 9. CONCLUSIONS AND RECOMMENDATIONS

9.1 General Conclusions

Although active surface wave methods have developed and improved significantly during the past several decades, a wide range of concerns remain regarding the accuracy of test results due to issues such as complex 3D wave propagation, limitations of testing equipment and procedures, and uncertainty of inverted profiles results due to the non-uniqueness of the inversion problem. To advance knowledge for active surface wave testing in experimental, theoretical, and computational directions, this study developed a number of advancements in all three aspects of active surface wave methods: modeling, testing, and inversion. Chapter 2 in Part I presented a comprehensive overview of numerical modeling of Rayleigh surface waves by three matrix methods and a finite element method. The three matrix methods were programmed in MATLAB as forward theoretical dispersion programs for inversion analysis. These forward programs can handle not only regular soil structures, but also irregular soil structures with embedded high- or low-velocity layers, as well as pavement structures having inverse stiffness profiles. Surface-wave propagation was modeled in the time-domain utilizing the absorbing layers with increasing damping (ALID) FEM simulation technique to simulate half-space boundary conditions and minimize artificially reflected energy.

Surface wave testing results in field data in the space-time domain that contains dispersion information on the tested site. The experimental dispersion data are used to infer soil structures via inversion algorithms to solve nonlinear multi-variable optimization problems. Thus, accuracy in testing methods is essential for obtaining

accurate experimental dispersion data, which serves as the target for inversion. To this end, Part II dealt with various aspects of surface wave testing, including improvements in methods for experimental dispersion analysis, field data acquisition, and higher-mode measurement. The new phase-velocity and intercept-time scanning (PIS) method in Chapter 3 can extract dispersion information in the form of auto-power spectral values with increased resolution and a reduction in side lobes relative to the widely-practiced conventional MASW method. As a result, the PIS method can improve certainty and increase confidence when interpreting experimental dispersion images, and, in addition, require only a simple synchronized trigger, while eliminating the need for the ad-hoc assumption that the impact point is the generation point of Rayleigh waves.

In Chapter 4, the MSOR method is demonstrated to be equivalent to MASW in terms of characterizing dispersion information, provided consistent impacts can be achieved. The MSOR method is promising for reducing instrumentation costs and improving portability, especially for site investigation in remote areas or for post-disaster characterization immediately after earthquakes before ground conditions change. The hybrid minimally-invasive surface-and-borehole methods developed in this study enable improved measurement of multi-mode dispersion curves with a relatively short testing spread. Chapter 5 presents a computational and experimental study on seismic stiffness profiling of pavements using the MASW and MSOR testing procedures. A new custom-programmed data acquisition system for MASW and MSOR testing using MATLAB software and National Instruments hardware was developed. The system can enable surface wave testing of pavements with efficiency and relatively low cost. MASW was found to enable measurements of dispersion data for pavements to higher frequencies

than MSOR by avoiding significant degradation of high-frequency dispersion data due to slight variations in impact locations. As result, MASW was demonstrated to reduce uncertainty in characterizing the stiffness of the pavement surface layer relative to MSOR testing.

The hybrid MMSW-borehole geophone and MMSW-SPT methods were introduced in Chapter 6. These minimally-invasive testing methods can more accurately measure higher modes of Rayleigh waves by using embedded borehole geophones or SPT impacts at selected depths. Superimposing apparent dispersion modes recorded via the geophones at selected depths with moving surface impacts, or multichannel surface wave motion with SPT hammer impacts at selected depths, the resulting multi-mode dispersion data used in a multi-objective inverse analysis result in more accurate inverted profiles. Chapter 7 introduced a procedure to estimate the ranges of optimum geophone or impact depths for capturing the higher modes with these hybrid methods. Stiffness matrix and finite element-based numerical simulations of the hybrid testing method were used to identify the relationships between critical geophone depths and apparent cut-off frequencies. The critical depth at a given frequency was found to be deeper for higher modes than for lower modes, and the apparent cut-off frequency of a given higher mode shown to decrease as the geophone depth increases. In general, greater geophone depths were shown to capture more dispersion information in terms of additional higher-modes with lower apparent cut-off frequencies.

After field testing for experimental dispersion data collection and forward modeling to obtain theoretical dispersion data, the final step is surface wave inversion through matching the theoretical dispersion curves to experimental counterparts by

optimization methods. Chapter 8 presented a new hybrid GSA optimization algorithm to solve the multivariable minimization problem for surface wave inversion. Combining the advantages of genetic algorithms and simulated annealing while avoiding some of their drawbacks, the GSA algorithm can reduce the risk of being trapped in a local minimum and improve global searching efficiency. Case studies demonstrated that the hybrid method can yield inversion results with small uncertainty and high efficiency, and improve the confidence of using surface wave testing for stiffness profiling.

9.2 Recommendations for Future Work

Based on the results of the research in this dissertation, the following recommendations are proposed for future studies:

1. A more comprehensive modeling technique is needed to account for complex surface wave propagation accompanied with near/far field effects, circular wave fronts, and attenuation in both horizontal and vertical directions in a half space medium. Development of a fast and efficient forward modeling program for this purpose will require not only breakthroughs in modeling theory, but also increased computational power, including parallel computing using supercomputers or more economical desktop supercomputers incorporating general purpose computing on graphics processing units (GPU).

2. Measurement of multimode experimental dispersion data is of critical and fundamental importance for surface wave methods. Although this study already presents a preliminary study on measurement of multimode surface waves using the hybrid surface and borehole method, further efforts are needed to computationally and experimentally study higher-mode surface waves for easier and faster field testing.

Improved methods of coupling borehole receivers or the use of probe-mounted sensors which do not require a borehole should be examined. The promising MMSW-SPT method should be examined for a range of soil conditions and benchmarked against crosshole or downhole seismic tests such as SCPT. For success of this method, the minimum distance at which a borehole source results in a surface wave should be better understood for layered soil profiles. Additionally, the reciprocity of the MMSW-borehole geophone and MMSW-SPT methods should be examined in terms of the concepts of critical depth and apparent cutoff frequency presented herein.

3. Although a large number of inversion methods and programs are available for research and practice, the intrinsic non-unique nature of solutions for nondestructive testing technologies makes inversion one of the most challenging problems. Global searching algorithms have been applied to improve the certainty of final inversion results. However, intensive computation requirements and unexpected unreasonable inverted profiles prevent further development of the algorithms, especially for real-world applications needed by engineers. A faster, intelligent inversion algorithm should be developed to solve these challenges. In addition, computational efforts can be made to improve the efficiency of intensive global inversion algorithms using parallel programing and computing on GPUs.

4. Surface wave methods have specific applications with certain limitations on resolution, regardless of the number of advancements. A quantitative evaluation of the resolution of surface wave methods should be conducted to clearly delineate the exploration capabilities not only for researchers, but also to help engineers avoid misapplication of surface wave methods.

5. Uniform, open-access benchmarking databases for surface wave testing data should be built to unify the effort and intelligence of researchers and engineers throughout the world. The SASW Benchmarking Dataset (GEC 2011, Tran and Hiltunen 2011) and UTexas1 Surface Wave Dataset (Cox et al. 2014) are two available datasets contributing towards this goal. More datasets are needed from various site structures around the world. It is especially necessary to share the datasets from challenging sites and earthquake-affected sites to offer access to all interested researchers, who are willing to dedicate their research to the improvement of surface wave methods.

BIBLIOGRAPHY

AASHTO, 2009, *Guide Specifications for LRFD Seismic Bridge Design*, 1st ed., American Association of State Highway and Transportation Officials, Washington, DC.

Adler, D., 1993, Genetic algorithms and simulated annealing: a marriage proposal, *In IEEE International Conference on Neural Networks 1993*, Piscataway, NJ, pp. 1104-1109.

Alzate-diaz, S. P. and Popovics, J. S., Application of MASW to characterize top pavement layers, in *Proceedings of the 7th International Conference on Nondestructive Testing for Civil Engineering*, edited by X. Derobert and O. Abraham, COFREND, France. 2009.

Arntsen B., Carcione, J., 2000, A new insight into the reciprocity principle, *Geophysics*, **65** (5), pp. 1604–1612.

Ashlock, J. C. and Lin, S., 2014, Critical depths for higher modes by minimally-invasive seismic profiling: simulations and field test, *Proceedings of SAGEEP 2014*, Boston, MA.

Bardet, J. P., Ichii, K., and Lin, C. H., 2000, *User's Manual for EERA*, Department of Civil Engineering, University of Southern California.

Beaty, K. S., Schmitt, D. R., and Sacchi, M., 2002, Simulated annealing inversion of multimode Rayleigh wave dispersion curves for geological structure, *Geophys. J. Int.*, **151,** pp. 622–631.

Bendat, J. S. and Piersol, A. G., 1996, *Random data: Analysis and measurement procedures*, John Wiley, New York.

Berenger, J. P., 1994, A perfectly matched layer for the absorption of electromagnetic waves, *Journal of Computational Physics*, **114**, pp. 185–200.

Bergamo, P., Comina, C., Foti, S., and Maraschini, M., 2011, Seismic characterization of shallow bedrock sites with multimodal Monte Carlo inversion of surface wave data, *Soil Dynamics and Earthquake Engineering*, **31**, pp. 530–534.

Bian, X., Jin, W., and Jiang, H., 2012, Ground-borne vibrations due to dynamic loadings from moving trains in subway tunnels. *Journal of Zhejiang University SCIENCE A*, **13** (11), pp. 870–876.

Braile, L., Seismic Wave Demonstrations and Animations, accessed on Feburay 2014, http://web.ics.purdue.edu/~braile/edumod/waves/WaveDemo.htm

Burger, H. R., Sheehan, A. F., and Jones, C.H., 2006, *Introduction to applied geophysics:*

exploring the shallow subsurface, W. W. Norton & Company, New York.

Calderón-Macías, C. and Luke, B., 2007, Improved parameterization to invert Rayleigh wave-data for shallow profiles containing stiff inclusions, *Geophysics*, **72,** pp. U1–U10.

Casto, D. W., Calderón-Macías, C., Luke, B., and Kaufmann, R., 2010, Improving MASW Results for a Site with Shallow Bedrock Through the Use of Higher-Mode Data, in *Proceedings*, *GeoFlorida 2010*, pp. 1360–1368.

Chopra, A. K., 2000, *Dynamics of structure* -theory *and application to earthquake engineering*, New Jersey, Prentice Hall.

Cooley, J. W. and Tukey, J. W., 1965, An algorithm for the machine calculation of complex Fourier series, *Mathematics of Computation*, **19**, pp. 297–301.

Cox, B. R. and Wood, C. M., 2011, Surface wave benchmarking exercise: methodologies, results, and uncertainties: *in* Risk Assessment and Management in Geoengineering: *ASCE GeoRisk2011*, Atlanta, Georgia, pp. 845–852.

Cox, B .R. and Beekman, A.N., 2011, Intramethod Variability in ReMi Dispersion Measurements and V_S Estimates at Shallow Bedrock Sites. *J. Geotech. Geoenviron.*, **137** (4), pp. 354–362.

Crampin, S. and Bath, M., 1965, Higher Modes of Seismic Surface Waves: Mode Separation, *Geophys. J.*, **10,** pp. 81–92.

Dahlen, F. A., Tromp J., 1998, Theoretical *global seismology*. Princeton University Press, Princeton, New Jersey.

Das, B. M., 2011, *Fundamentals of* soil *dynamics*. 2nd ed. Stamford: Cengage Learning.

Drozdz, M. B., 2008, Efficient finite element modeling of ultrasound waves in elastic media, *PhD dissertation*, University of London, London, UK.

Dunkin, J. W., 1965, Computation of modal solutions in layered, elastic media at high frequencies, *Bulletin of Seismological* Society *of America*, **55** (2), pp. 335–358.

Ewing, W. M., W. S. Jardetsky, and F. Press, 1957, *Elastic waves in layered media*, New York, McGraw-Hill.

Foti, S., Sambuelli, L., Socco, L.V., and Strobbia, C., 2002, Spatial sampling issues in fk analysis of surface waves, *Proceedings of SAGEEP 2002*, Las Vegas, NV, February 10–14.

Franconi, L. and Jennison, C., 1997, Comparison of a genetic algorithm and simulated annealing in an application to statistical image reconstruction, *Statistics and*

Computing, **7**, pp. 193–207.

Gabriels, P., Snieder, R., and Nolet, G., 1987, In situ measurements of shear-wave velocity in sediments with higher-mode Rayleigh waves, *Geophysical Prospecting*, **35**, pp. 187–196.

Ganji, V., Gucunski, N., and Nazarian, S., 1998, Automated inversion procedure for spectral analysis of surface waves, *Journal of Geotechnical and Geoenvironmental Engineering*, **124** (8), pp. 757–770.

GEC (Geophysical Engineering Committee), 2011, SASW Wave Benchmarking Data Set, accessed June 20 2012. http://cgiss.boisestate.edu/~pm/geoph_cmty/data/

Geometrics, 2013, accessed April 2 2013, http://www.geometrics.com/geometrics-products/seismographs/download-seismograph-software/.

Goldberg, D. E., 1989, *Genetic algorithms in search, optimization, and machine learning*. Reading, MA: Addison-Wesley.

Gucunski, N. and Maher, A., 2002, Pavement dynamic response by stiffness matrix approach, *15th ASCE Engineering Mechanics* Conference, Columbia University, New York, NY, pp. 178–192.

Gucunski, N., and Woods, R. D., 1992, Numerical simulation of the SASW test, *Soil Dynamics and Earthquake Engineering*, **11 (**4), pp. 213–227.

Haskell, N. A., 1953, The dispersion of surface waves on multilayered media: Bull. Seismol. Soc. of Am., **43** (1), pp. 17–34.

Heisey, J. S., Stokoe, K. H. II, and Meyer, A. H., 1982, Moduli of pavement systems from Spectral Analysis of Surface Waves, *Transp. Res. Rec.*, 852, Washington D.C, pp. 22–31.

Heukelom, W. and Foster, C. R., 1960, Dynamic testing of pavements, *Journal of the Soil Mechanics and Foundations* division, ASCE, **86**, No. SM1, Part 1, pp. 2368–2372.

Holland, J. H., 1975, Adaptation *in natural and artificial systems*, Ann Arbor, the University of Michigan Press.

Horike, M., 1985, Inversion of phase velocity of long-period microtremors to the s-wave velocity structure down to the basement in urbanized areas, *J. Phys. Earth*, **33**, pp. 59-96.

Hui, S., 2010, Multi-objective optimization for hydraulic hybrid vehicle based on adaptive simulated annealing genetic algorithm, *Engineering Applications of Artificial Intelligence*, **23**, pp. 27–33.

Igel, H., *Introduction to Seismology: Surface waves and free oscillations* (website, accessed January, 2012), http://www.geophysik.unimuenchen.de/~igel/Lectures/Sedi /sedi_surface.pdf.

Iglesias, A., Cruz-Atienza, V. M., Shapiro, N. M., Singh, S. K., and Pacheco, J. F., 2001, Crustal structure of south-central Mexico estimated from the inversion of surface-wave dispersion curves using genetic and simulated annealing algorithms, *Geofísica Internacional*, **40**, pp. 181–190.

Ikelle, L. T. and Amundsen, L., 2005, *Introduction to petroleum seismology*, SEG Investigations in Geophysics No. 12

Jeong, I. K., Lee, J. J., 1996, Adaptive simulated annealing genetic algorithm for system identification, *Engineering* Applications *of Artificial Intelligence*, **9** (5), pp. 523–532.

Joh, S. H., 1997, Advanced in interpretation and analysis techniques for spectral-analysis-of-surface-waves measurements, *PhD Thesis*, The University of Texas at Austin, Austin, Texas.

Jones R., 1955, A vibration method for measuring the thickness of concrete road slabs in situ, *Mag. Concrete Res*., **7** (20), pp. 97–102.

Jones R., 1958, In-situ measurement of the dynamic properties of soil by vibration methods, *Géotechnique*, **8**, pp. 1–21.

Jones R., 1962, Surface wave technique for measuring the elastic properties and thickness of roads: Theoretical development, *British Journal of Applied Physics*, **13**, pp. 21–29.

Karray, M. and Lefebvre, G., 2010, The use of higher modes in surface wave testing, in *Proceedings*, *GeoFlorida* 2010, pp. 1379–1388.

Kausel, E. and Roësset, J. M., 1981, Stiffness matrices for layered soils, *Bull. Seism. Soc. Am.*, **71** (6), pp. 1743–1761.

Kirkpatrick, S., Gelatt, C. D. Jr., and Vecchi, M. P., 1983, Optimization by simulated annealing, *Science*, **220**, pp. 671–680.

Klein, G., Bohlen, T., Theilen, F., Kugler, S., and Forbriger, T., 2005, Acquisition and inversion of dispersive seismic waves in shallow marine environments, *Mar. Geophys. Res.*, **26,** pp. 287–315.

Knopoff, L., 1952, On Rayleigh wave velocities, *Bull. Seismol. Soc. Amer*., **42**, pp. 307-308.

Knopoff, L., 1964, A matrix method for elastic wave problems, *Bull. Seismol. Soc. Am.*, **54**, pp. 431–438.

Krahenbuhl, R., Li, Y., 2004, Hybrid optimization for a binary inverse problem, *74nd Ann.Internat. Mtg, Soc. Expl. Geophys*.

Kramer, S. L., 1996, Geotechnical *Earthquake Engineering*, Prentice-Hall, Upper Saddle River, NJ.

Lamb, H., 1917, On waves in an elastic plate, *Proceedings of the Royal Society*, London, pp. 114–128.

Levenberg, K., 1944, A method for the solution of certain non-linear problems in least squares, *Quart. Appl. Math.*, **2**, pp. 164–168.

Li, J., Feng, Z., Nishida, H., and Satofuka, N., 1999, Using whole annealing genetic algorithms for the turbine cascade inverse design problem, *Journal of Thermal Science*, **8**, pp. 32–37.

Liang, H. and Cui, J., 2000, Genetic simulated annealing algorithm with selective generation, *The 18th International Conference of The System Dynamics Society*, Bergen, Norway.

Lin, S. and Ashlock, J. C., 2011, A study on issues relating to testing of soils and pavements by surface wave methods, *38th Annual Review of Progress in Quantitative Nondestructive Evaluation (QNDE 2011)*, Burlington, VT, American Institute of Physics, Melville, NY, pp. 1532–1539.

Lin, S. and Ashlock, J. C., 2014a, Multi-mode Rayleigh wave profiling by hybrid surface and borehole methods, *Geophysical Journal International*, **197** (2), pp. 1184–1195.

Lin, S. and Ashlock, J. C., 2014b, Comparison of MASW and MSOR for surface wave testing of pavements, *Proceedings of SAGEEP 2014*, Boston, MA.

Liu, G. R. and Quek Jerry, S. S., 2003, A non-reflecting boundary for analyzing wave propagation using the finite element method, *Finite Eelements in Analysis and Design*, **39**, pp. 403–417.

Louie, J. N., 2001, Faster, better: shear-wave velocity to 100 meters depth from refraction microtremor arrays, *Bull. Seism. Soc. Am.*, **91**, pp. 347–364.

Lowe, M., 1995, Matrix techniques for ultrasonic waves in modeling multilayered media, *IEEE Transactions on ultrasonics,* ferroelectrics, *and frequency control*, **42** (4), pp. 525–542.

Lu, L., Wang, C., and Zhang, B., 2007, Inversion of multimode Rayleigh waves in the presence of a low-velocity layer-numerical and laboratory study, *Geophys. J. Int.*, **168,** pp. 1235–1246.

Luo, Y., Xia, J., Liu, J., Liu, Q., Xu, S., 2007, Joint inversion of high-frequency surface

waves with fundamental and higher modes, *J. appl. Geophys.*, **62,** pp. 375–384.

Luo, Y., Xia, J., Liu, J., Xu, Y., Liu, Q., 2009, Research on the middle-of-receiver-spread assumption of the MASW method, *Soil Dyn. Earthq. Eng.*, **29**, pp. 71–79.

Marquardt, D. W., 1963, An algorithm for least-squares estimation of nonlinear parameters, *J. Soc. Indust. Appl. Math.*, **11** (2), pp. 431–441.

Martin, A. J., 2011, Analysis of SASW, MASW, and passive surface wave data collected at the national geotechnical experimentation site at Texas A&M University, *GeoRisk 2011*, Atlanta, Geogia, pp. 886–893.

McMechan, G. A., and Yedlin, M. J., 1981, Analysis of dispersive waves by wave field transformation, *Geophysics*, **46**, pp. 869–874.

Moro, G. D., Ferigo, F., 2011, Joint analysis of Rayleigh- and Love-wave dispersion: Issues, criteria and improvements, *J. appl.* Geophys., **75**, pp. 573–589.

Motamed, R., Itoh, K., Hirose, S., Takahashi, A., Kusakabe, O., 2009, Evaluation of Wave Barriers on Ground Vibration Reduction through Numerical Modeling in Abaqus, *SIMULIA Customer Conference 2009*, May 18-21, London, England, pp. 402–419.

Nazarian, S., 1984, In situ determination of elastic moduli of soil deposits and pavement systems by spectral-analysis-of-surface-waves method, *PhD dissertation*, The University of Texas at Austin, Austin, Texas.

Nazarian, S., Yuan, D., and Baker, M. R., 1995, Rapid determination of pavement moduli with spectral-analysis of surface waves method, *Research Report 1243-1*, The Center for Geotechnical and Highway Materials Research, The University of Texas at Paso.

Nolet, G. and Panza, G. F., 1976, Array analysis of seismic surface waves: limits and possibilities, *Pure appl. Geophys.*, 114**,** pp. 776–790.

O'Connell, D. R. H. and Turner, J. P., 2011, Interferometric Multichannel Analysis of Surface Waves (IMASW), *Bulletin of the* Seismological *Society of American*, **101**, pp. 2122–2141.

O'Neill, A., Matsuoka, T., 2005, Dominant higher surface-wave modes and possible inversion pitfalls, *J. Environ. Eng.* Geoph., **10** (2), pp. 185–201.

Obando, E. A., Park, C. B., Ryden, N., and Ulriksen, P., 2010, Phase-scanning approach t ocorrect time-shift inaccuracies in the surface-wave walk-away method, *Soil Dynamics and Earthquake Engineering*, **30**, pp. 1528–1539.

Obrzud, R. F., 2010, On the use of the hardening soil small strain model in geotechnical practice, *Numerics in Geotechnics and Structures 2010*, Th. Zimmerman, A. Truty,

and K. Podles' Editors, Elme press International.

Olson, L. D. and Miller, P. K., 2010, Multiple Impact Surface Waves (MISW) – Improved Accuracy for Pavement System Thicknesses and Moduli vs. Spectral Analysis of Surface Waves (SASW), *GeoFlorida Conference*, 2010.

Park, C. B., Miller, R. D., and Xia, J., 1998, Imaging dispersion curves of surface waves on multichannel record, *Technical Program with biographies, SEG, 68th Annual Meeting*, New Orleans, Louisiana, pp. 1377–1380.

Park, C. B., Miller, R. D., and Xia, J., 1999a, Multichannel analysis of surface waves, Geophysics, **64** (3), pp. 800–808.

Park, C. B., Miller, R. D., Xia, J., Hunter, J. A., and Harris, J. B., 1999b, Higher mode observation by the MASW method, [Exp. Abs.]: *Soc. Explor. Geophys.*, pp. 524–527.

Park, C. B., Miller, R. D., and Xia, J., 2000, Detection of higher mode surface waves over unconsolidated sediments by the MASW method, *Proceedings of SAGEEP 2000*, Arlington, VA., February 20-24, pp. 1–9.

Park, C. B., Miller, R. D., and Xia, J., 2001a. Offset and resolution of dispersion curve in multichannel analysis of surface waves (MASW), *Proceedings of the SAGEEP 2001*, Denver, Colorado.

Park, C. B., Ivanov, J., Miller, R. D., Xia, J., and Ryden, N., 2001b, Seismic investigation of pavements by MASW method—geophone approach: *Proceedings of the SAGEEP 2001*, Denver, Colorado, RBA-6.

Park, C. B., Ryden, N., Miller, R. D., and Ulriksen, P., 2002, Time break correction in multichannel simulation with one receiver (MSOR), *Proceedings of SAGEEP 2002*, Las Vegas, NV, February 10–14.

Park, C. B., Miller, R. D., Ryden, N., Xia, J., and Ivanov, J., 2005. Combined use of active and passive surface waves, Journal *of Engineering and Environmental Geophysics*, **10(3)**, 323–334.

Park, C. B., 2011, Imaging dispersion of MASW data—full vs. selective offset scheme, *Journal of Environmental & Engineering* Geophysics, **16**, pp. 13–23

Park, C. B., 2012. Multichannel analysis of surface waves-short course, Geo-Congress 2012, Oakland, CA, March 25,

Pezeshk, S. and Zarrabi, M., 2005, A new inversion procedure for spectral analysis of surface waves using a genetic algorithm, *Bull. Seismol. Soc. Am.*, **95**, pp. 1801–1808.

Pickett, G., 1945, Dynamic testing of pavements, *Journal of the American Concrete*

Institute, **16** (5), pp. 473–489.

Press, F. and Dobrin, M. B., 1956, Seismic wave studies over a high-speed surface layer, *Geophysics*, **21** (2), pp. 285–298.

Rayleigh, L., 1885, On waves propagated along the plane surface of an elastic solid, *Proceedings of the London Mathematical Society*, **1**, pp. 4–11.

Richart, F. E., Hall, J. R., and Woods, R. D., 1970, *Vibrations of soils and foundations*, Prentice-Hall, Inc.

Rix, G. J., 1988, Experimental study of factors affecting the spectral-analysis-of-surface-waves method, *PhD dissertation*, The University of Texas at Austin, Austin, Texas.

Ryden, N., Ulriksen, P., Park, C. B., Miller, R. D., Xia, J., and Ivanov, J., 2001, High frequency MASW for non-destructive testing of pavements-accelerometer approach, *Proceedings of the SAGEEP 2001*, Denver, Colorado, RBA-5.

Ryden, N., Ulriksen, P., Park, C. B., and Miller, R. D., 2002a, Portable seismic acquisition system (PSAS) for pavement MASW, *Proceedings of* SAGEEP *2002*, Las Vegas, NV, 13IDA7.

Ryden, N., Park, C. B., Ulriksen, P., and Miller R. D., 2002b, Branching of dispersion curves in surface wave testing of pavements: *Proceedings of the* SAGEEP *2002*, Las Vegas, Nevada, 12SEI7.

Ryden, N., 2004, Surface wave testing of pavements, *PhD Dessertation*, Lund University, Lund, Sweden.

Ryden, N., Park, C. B., Ulriksen, P. and Miller, R. D., 2004, Multimodal approach to seismic pavement testing, *Journal of Geotechnical and Geoenvironmental Engineering*, ASCE, **130**(6), pp. 636–645.

Ryden, N. and Park, C.B., 2004, Surface waves in inversely dispersive media, *Near Surface Geophysics*, **2** (4), pp. 187–197.

Ryden, N., Lowe, M. J. S., Cawley, P., and Park, C. B., 2006, Evaluation of multilayered pavement structures from measurements of surface waves, In D. O. Thompson and D. E. Chimenti, Eds. *Review of progress in quantitative NDE 32nd Annual meeting*, AIP, New York, Vol. 25 (CP820), pp. 1616–1623.

Ryden, N. and Park, C. B., 2006, Fast simulated annealing inversion of surface waves on pavement using phase-velocity spectra, *Geophysics*,**71**, pp. 49–58.

Santamarina, J. C. and Fratta, D., 1998, *Introduction to discrete signals and inverse problems in civil engineering*, ASCE Press, Reston, VA.

Scholte, J. G., 1947, The range of existence of Rayleigh and Stoneley waves, *Royal Astronomical Society. Geo-physics*, supplement **5**, pp. 120–126.

Sezawa K., 1938, Anomalous dispersion of elastic surface waves II, *Bull. Earthq. Res. Inst.*, **16**, pp. 225–233.

Shan, H., Li, S., Gong, D., and Lou, P., 2006, Genetic simulated annealing algorithm-based assembly sequence planning, *International Technology and Innovation Conference 2006*, Hangzhou, China, pp. 1573–1579.

Sheriff, R. E., and Geldart, L. P., 1982, *Exploration seismology, Vol. 1: History, theory and data acquisition*: Cambridge University Press.

Socco, L.V., Foti, S., and Boiero, D., 2010, Surface-wave analysis for building near-surface velocity models — Established approaches and new perspectives, *Geophysics*, **75** (5), pp. 75A83–75A102.

Song, X., Gu, H., Liu, J., and Zhang, X., 2007, Estimation of shallow subsurface shear-wave velocity by inverting fundamental and higher-mode Rayleigh waves, *Soil Dyn. Earthq. Eng*., **27**, pp. 599–607.

Stokoe, K. H. II, Wright, G. W., James, A. B., and Jose, M. R., 1994, Characterization of geotechnical sites by SASW method, in Woods R. D., Ed., *Geophysical characterization of sites*: Oxford Publ, pp. 15–25.

Stokoe, K. H. II, Joh, S. H., and Woods, R. D., 2004, Some contributions of in situ geophysical measurements to solving geotechnical engineering problems, in Proceedings, *International Conference on Site Characterization* (ISC-2), Porto, Portugal, September 19-22.

Stoneley, R., 1924, Elastic waves at the surface of separation between two solids, *Proceedings of the Royal Society of London. Series A*, **106** (738), pp. 416–428.

Supranata, Y. E., 2006, Improving the uniqueness of shear wave velocity profiles derived from the inversion of multiple-mode surface wave dispersion data, *PhD dissertation*, University of Kentucky, Lexington, Kentucky.

KGS (Kansas Geological Survey), 2010, accessed April 2 2013, http://www.kgs.ku.edu/software/surfseis/.

Szu, H., Hartley, R., 1987, Fast simulated annealing, *Physics Letters A*, **122**, pp. 157-162.

Taghizadeh, S. R., 2000. *Digital Signal Processing*: Part 3 Discrete-Time Signals & Systems Case Studies, University of North London.

Tang, R., Yang, S., Li, Y., Wen, G., and Mei, T., 1996, Combined strategy of improved simulated annealing and genetic algorithm for inverse problem, *IEEE Transactions*

on Magnetics, **32**, pp. 1326–1329.

Tertre, A. D., Cascante, G., and Tighe, S. L., 2010, Combining portable falling weight deflectometer and surface wave measurements for evaluation of longitudinal joints in asphalt pavements, *Transportation Research Record*, No. 2152, pp. 28–36.

Thomson, W. T., 1950, Transmission of elastic waves through a stratified solid medium, *J. Appl. Phxs.*, **21**, pp. 89–93.

Thorson, R. J. and Claerbout, J. F., 1985, Velocity-stack and slant-stack stochastic inversion, *Geophysics*, **50**, pp. 2727–2741.

Tokimatsu, K., Tamura, S., and Kojima, H., 1992, Effects of multiple modes on Rayleigh wave dispersion characteristics, *J. Geotechn. Eng.*, **118**, pp. 1529–1543.

Tran, K. T., 2008, An appraisal of surface wave methods for soil characterization, *Master's thesis*, University of Florida, Gainesville, Florida.

Tran, K. T. and Hiltunen, D. R., 2008, A comparison of shear wave velocity profiles from SASW, MASW, and ReMi techniques, in Proceedings, *Geotechnical Earthquake Engineering and Soil Dynamics IV*, ASCE, Sacramento, California, May 18-22.

Tran, K. T. and Hiltunen, D. R., 2011, An assessment of surface wave techniques at the Texas A&M National Geotechnical Experimentation Site: *in* Risk Assessment and Management in Geoengineering: *ASCE GeoRisk2011*, Atlanta, Georgia, pp. 859–866.

Van Der Hilst, R. D., *Essentials of Geophysics*, MITOPEN COURSEWARE, Lecture Notes, p. 175. accessed on Feburary 2014, http://ocw.mit.edu/courses/earth-atmospheric-and-planetary-sciences/12-201-essentials-of-geophysics-fall-2004/lecture-notes/

Van der Poel C., 1951, Dynamic testing of road constructions, *Journal of Applied Chemistry*, **1**, pp. 281–290.

Vanneste, M., Madshus, C., Socco V. L., Maraschini, M., Sparrevik, P. M., Westerdahl, H., Duffaut, K., Skomedal, E., and Bjørnarå, T. I., 2011, On the use of the Norwegian Geotechnical Institute's prototype seabed-coupled shear wave vibrator for shallow soil characterization – I. Acquisition and processing of multimodal surface waves. *Geophys. J. Int.*, **185**, pp. 221–236.

Vidale, R. F., 1964, The dispersion of stress waves in layered media overlaying a half space of lesser acoustic rigidity, *PhD dissertation*, University of Wisconsin, Madison, Wisconsin.

Viktorov, I. A., 1967, *Rayleigh and Lamb waves: physical theory and applications*,

Plenum Press: New York.

Wapenaar K., 1997, Reciprocity properties of one-way propagators, *Geophysics*, **63** (4), pp. 1795–1798.

Wong, I. G., Stokoe, K. H. II, Cox, B. R., Lin, Y. C., and Menq, F. Y., 2011, Shear-wave velocity profiling of strong motion sites that recorded the 2001 Nisqually, Washington, Earthquake, *Earthq. Spectra.*, **27,** pp. 183–212.

Wylie, C. R. and Barrett, L. C., 1982, *Advanced engineering mathematics*. New York: McGraw-Hill.

Xia, J., Miller, R. D., and Park, C. B., 1999, Estimation of near-surface shear-wave velocity by inversion of Rayleigh waves, *Geophysics*, **64,** 691–700.

Xia, J., Miller, R. D., and Park, C. B., 2000, Advantages of calculating shear-wave velocity from surface waves with higher modes, [Exp. Abs.]: *Soc. Expl. Geophys*., pp. 1295–1298.

Xia, J., Miller, R.D., Park, C.B. & Tian, G., 2003. Inversion of high frequency surface waves with fundamental and higher modes, *J. appl. Geophys.*, **52,** 45–57.

Xia, J., Chen, C., Li, P. H., Lewis, M. J., 2004, Delineation of a collapse feature in a noisy environment using a multichannel surface wave technique, *Geotechnique*, **54** (1), pp. 17–27.

Yamanaka, H. and Ishida, H., 1996, Application of genetic algorithm to an inversion of surface wave dispersion data, *Bull. Seismol. Soc. Am.*, **86**, pp. 436–444.

Yamanaka, H., 2005, Comparison of performance of heuristic search methods for phase velocity inversion in shallow surface wave method, *Journal of Environmental and Engineering Geophysics*, **10**, pp. 163–173.

Zhao, D., 2011, Analysis of surface wave benchmarking data, *GeoRisk 2011*, Atlanta, Geogia, pp. 853–858.

Zou, X. and Kang L., 2005, Fast annealing genetic algorithm for muti-objective optimization problems, *International Journal of Computer Mathematics*, **82**, pp. 931–940.

Zywicki, D. J., Rix, G. J., 2005, Mitigation of near-field effects for seismic surface wave velocity estimation with cylindrical beamformers, *J. Geotech. Geoenviron.*, **131** (8), pp. 970–977.

APPENDIX: THE HANKEL TRANSFORM AND INVERSE HANKEL TRANSFORM

The two-dimensional Fourier transform and its inverse can be expressed as

$$f(x,y)=\frac{1}{2\pi}\int_{-\infty}^{\infty}\int_{-\infty}^{\infty}g(\xi,\eta)e^{i(x\xi+y\eta)}d\xi d\eta$$

$$g(\xi,\eta)=\frac{1}{2\pi}\int_{-\infty}^{\infty}\int_{-\infty}^{\infty}f(x,y)e^{-i(\xi x+\eta y)}dxdy$$

where $x=r\cos\theta,\ y=r\sin\theta,\ \xi=\rho\cos\phi,\eta=\rho\sin\phi.$

Note that

$$\xi x+\eta y=r\rho(\cos\theta\cos\phi+\sin\theta\sin\phi)=r\rho\cos(\theta-\phi)$$

Recalling that the differential area in polar coordinates is

$$dA=rdrd\theta$$

The above equation for $g(\xi,\eta)$ becomes

$$\begin{aligned}g(\xi,\eta)&=\frac{1}{2\pi}\int_{-\infty}^{\infty}\int_{-\infty}^{\infty}f(x,y)e^{-i(\xi x+\eta y)}dxdy\\&=\frac{1}{2\pi}\int_{0}^{\infty}\int_{0}^{2\pi}F(r)e^{-ir\rho\cos(\theta-\phi)}(rd\theta dr)\\&=\frac{1}{2\pi}\int_{0}^{\infty}rF(r)\left[\int_{0}^{2\pi}e^{-ir\rho\cos(\theta-\phi)}d\theta\right]dr\end{aligned}$$

Noting that the integral of a periodic function over one full period is the same regardless of the lower limit of integration and defining $u=\theta-\phi$, the inner integral above gives

$$\int_{0}^{2\pi}e^{-ir\rho\cos(\theta-\phi)}d\theta=\int_{-\phi}^{2\pi-\phi}e^{-ir\rho\cos u}du=\int_{0}^{2\pi}e^{-ir\rho\cos u}du$$

The last integral above may be evaluated as (Wylie and Barrett 1982, pp. 596)

$$\int_{0}^{2\pi}e^{-ir\rho\cos u}du=2\pi J_0(\rho r)$$

where J_0 is the Bessel function of the first kind of order 0. Substituting the above result into $g(\xi,\eta)$ gives

$$g(\xi,\eta) = \int_0^\infty rF(r)J_0(\rho r)dr$$

where $\rho = \sqrt{\xi^2 + \eta^2}$.

Based on the above derivation, the Hankel transform can be given as follows:

$$G(\rho) = \int_0^\infty rF(r)J_0(\rho r)dr$$

The corresponding inverse Hankel transform is

$$\begin{aligned} f(x,y) &= \frac{1}{2\pi}\int_{-\infty}^{\infty}\int_{-\infty}^{\infty} g(\xi,\eta)e^{i(x\xi+y\eta)}d\xi d\eta \\ &= \frac{1}{2\pi}\int_0^\infty\int_0^{2\pi} g(\xi,\eta)e^{ir\rho\cos(\theta-\phi)}(\rho d\rho d\phi) \\ &= \frac{1}{2\pi}\int_0^\infty \rho G(\rho)\left[\int_0^{2\pi} e^{ir\rho\cos(\theta-\phi)}d\phi\right]d\rho \\ &= \int_0^\infty \rho G(\rho)J_0(\rho r)d\rho \end{aligned}$$